Ion-Pair Effects on Molecular Photocatalysis

Dissertation

Zur Erlangung des Doktorgrades der Naturwissenschaften
(Dr. rer. nat.)
an der Fakultät für Chemie und Pharmazie
der Universität Regensburg

vorgelegt von

Elina K. Taskinen

aus Hollola, Finnland

2025

The experimental work was carried out between January 2021 and December 2024 under the supervision of Prof. Dr. Burkhard König at the University of Regensburg, Institute of Organic Chemistry.

Date of submission:	23.05.2025
Date of colloquium:	04.09.2025

Board of examiners:

Apl. Prof. Dr. Rainer Müller	(chair)
Prof. Dr. Burkhard König	(1st referee)
Prof. Dr. Alexander Breder	(2nd referee)
Prof. Dr. Patrick Nürnberger	(examiner)

“I want to know why. Why everything.
I don’t know the answers but a few days ago
I didn’t know there were questions”
– Terry Pratchett –

TABLE OF CONTENTS

CHAPTER 1

1 Ionic Effects in Photocatalysis

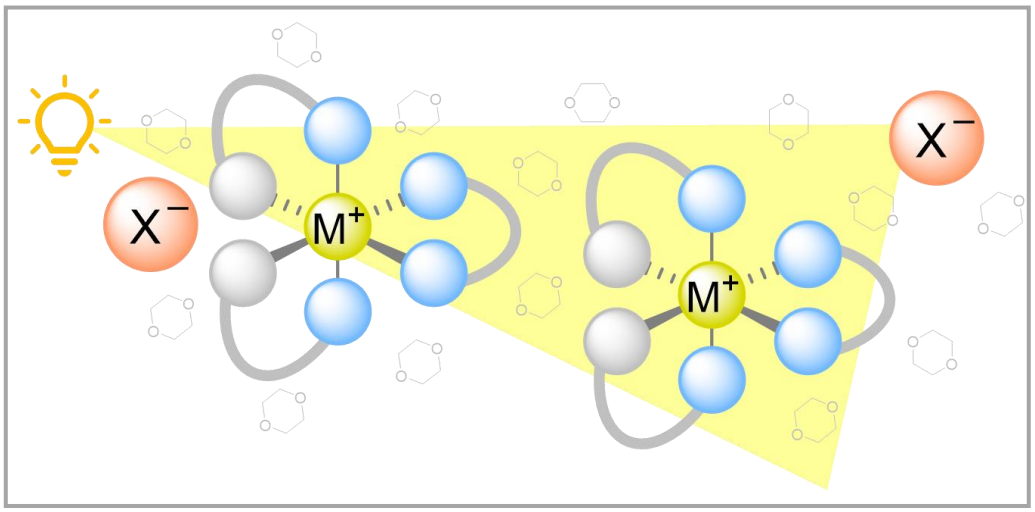

Abstract: Ionic attraction is the strongest intermolecular force present. This introductory chapter presents the most important terminology, concepts, and challenges related to ion-pairs, preparing the reader for the experimental research chapters ahead. While this chapter is mainly written from the point of view of an organic chemist, some of the underlying physicochemical principles are touched upon to clarify the concept. By summarizing the previous research, we hope to put our own contribution to the field in context.

Author contributions: E.K.T. developed the concept of the chapter, searched the references, drew the graphical elements and wrote the manuscript. B.K. supervised the work.

1.1 Motivation

"...counterion effect may be an under-appreciated but important phenomenon in many photoredox reactions".

– Yoon *et. al*, 2019 –

The role of the ionic compounds in the field of photocatalysis should certainly not be underestimated. In fact, $Ru(bpy)_3$ and Eosin Y, the first molecules to be repurposed to photoredox catalysis from their original uses, represent two very different examples of ionic photocatalysts. While the ruthenium polypyridyl complexes possess a metal centre and a cationic charge, Eosin Y is a fully organic molecule which easily forms mono- and dianionic species. Over the years the portfolio of charged photocatalysts has significantly broadened for example with iridium polypyridyl compounds, cationic acridinium and pyrylium salts and LMCT-active metal complexes. Although many of these catalysts are ion-paired compounds by nature, the majority of the research activity has focused on the structure and properties of the light-harvesting redox-active part, whereas the accompanying counterion has been mostly neglected – at least until recently.

1.2 Introduction

Electrostatic interactions are the strongest intermolecular forces present, the attractive forces ranging from 600 kJ/mol to 1500 kJ/mol. While the highest strengths are achieved between two units with permanent opposite charges, another relatively strong interaction can be achieved between one permanently charged ion and a highly polarizable counterpart. In recent years, the electrostatic environment of the reaction has received more attention, ranging broadly from enzymatic and enzyme mimetic catalysis[1] into reactions in ionic liquids[2] and under an external electric field.[3,4] While similar approaches are undoubtedly making their way to photocatalysis,[5] the idea of "charge matters" has definitely been around much longer.

In the context of photocatalysis, the ion-pair formation can take place either in the ground-state or between the reactive intermediates (Figure 1.1). For example, a plethora of reports have utilized the ground-state ion-pairing between two weakly absorbing species to form strongly light-harvesting electron donor-acceptor (EDA) complexes where two neutral radicals are formed swiftly after excitation and single-electron transfer (left, above).[6–9] Furthermore, Breslow, Rajagopalan, and Schwarz reported as early as 1981 a regioselective hydrogen atom abstraction (HAT) from decanedioic acid dianion ion-paired with 3,3'-carbonylbis(phenyltrimethylammonium)dication followed by direct excitation of the latter.[10] Whilst in the preceding reports the ion-pairing could be achieved between two native starting materials, ion-pair formation between reactive intermediates often requires pre-functionalization of one of the reaction partners. For example, the group of Taylor cleverly utilized a covalently-bound diphenylboronate group to achieve a regioselective functionalization of sugars,[11] while the group of Luo has used ionic auxiliaries to realize asymmetric allylic alkylations (left, below).[12] Despite these[13,14] and many other inspiring approaches,[15,16] the remaining this review will focus on the ion-pairs formed between the light-harvesting photocatalytic species and their counter-ion (with the exception of chiral countercations discussed in Section 1.3.6). Hence, the readers interested in the other approaches are encouraged to read the publications referenced above.

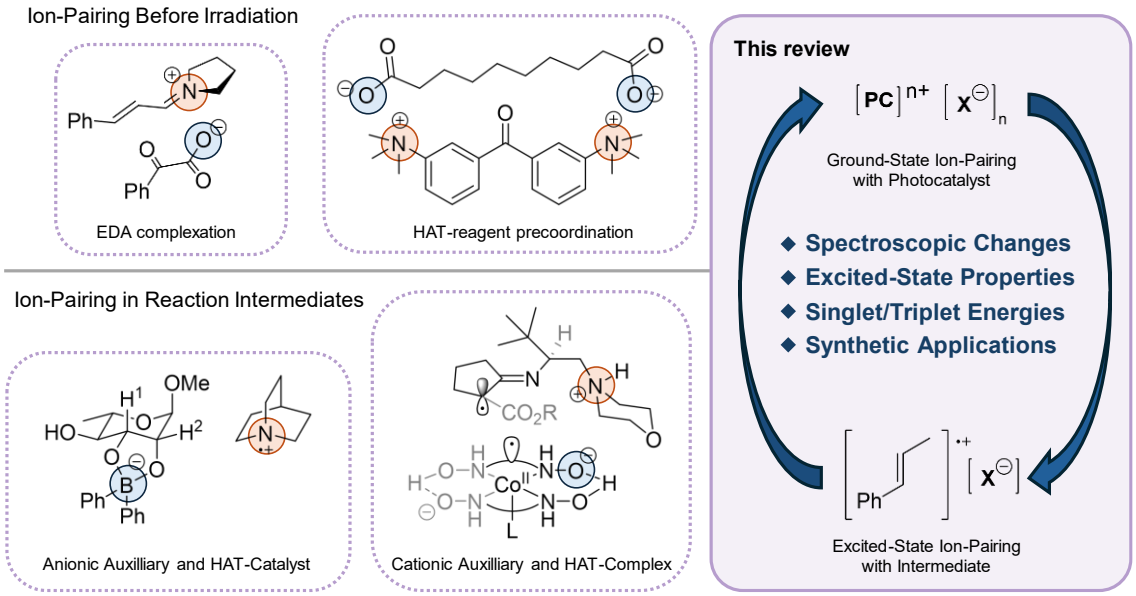

Figure 1.1. Possible ion-pairing in photocatalysis: ion-pairing in ground-state before irradiation (above left)[6–10], ion-pairing between reactive intermediates (below left)[11,12], and the scope of this review (right).

While researching for this review, it soon became obvious that the majority of studies focusing on characterization and reactivity of ion-pairs were mainly done on systems comprising of a cationic photocatalyst and its counter anion. While the reasoning behind this choice was typically not clearly described, one could assume that the broad availability and well-defined behavior of the positively charged photocatalysts (for example ruthenium and iridium polypyridyl complexes, acridinium and pyrylium salts) might play a role in the decision (Figure 1.2, a). Furthermore, the charged unit in those cationic molecules is often persistent in nature, whereas the anionic photocatalysts (such as Fluorescein derivatives, anthraquinones/napthaquinones and phenolates) are often in acid-base equilibrium with their neutral counterparts (Figure 1.2, b).

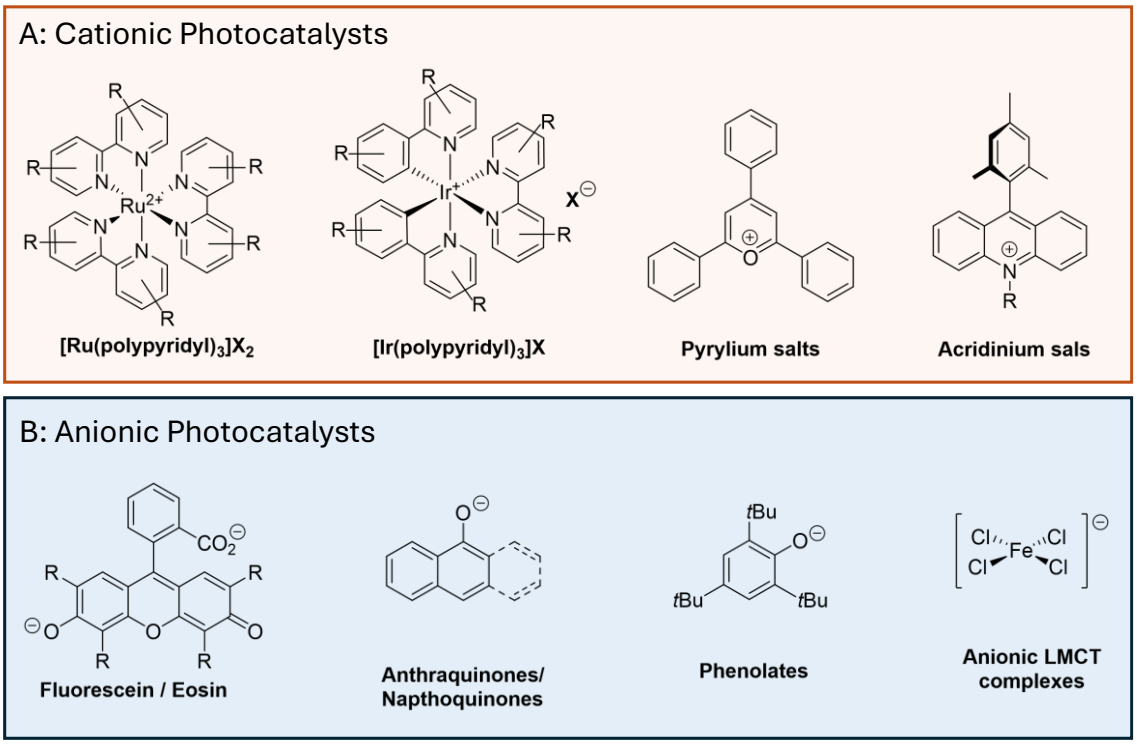

Figure 1.2. Examples of cationic and anionic photocatalysts/photoactive compounds.

Another important factor, and one which is repeatedly encountered in assessing the counterion effect, is solubility. Whereas the research in ion-pair catalysis (or ion-pairs in catalysis) often focuses on the characterization and reactivity of an *intermediate ion-pair*, which typically arises from *dissociation of a primary ion-pair*. Deprotonation can be a key step and is often carried out with an inorganic base, such as Cs_2CO_3, dissociation of this ion-pair must occur to enable the formation of the deprotonated substrate – cesium ion-pair.

For the aforementioned reasons, the variables governing the solvation of the ion-pairs play crucial roles in the synthetic applications of ionic compounds. Herein, the four major contributors (pressure, temperature, concentration and polarity of solvent and solute) are often strongly interconnected. In the following examples, the roles of solvent polarity, and the nature of the solute are particularly emphasized. Although highly polar solvents (Figure 1.3, above) allow for efficient solvation and fast reactions due to the high activity coefficient of the reactants, ion-pair interactions are typically lost. The proportion of contact ion-pairs can be maximized with the use of non-polar solvents (hydrocarbons being the best), but the pool of compounds soluble in such media is rather limited. Thus, the choice of the solvent in ion-pair catalysis is always a compromise between adequate solubility and ion-pairing interactions. As a further factor, the nature of the counterion also affects the solubility. Small anions, such as chloride, form tightly bound ion-pairs with the photocatalyst whereas an increase in counter anion size and polarizability leads to easier dissociation from the catalyst (Figure 1.3, below). Importantly, the choice of counterion and solvent goes hand-in-hand, and for example, the most tightly bound ion-pair can be achieved with a small counterion in non-polar solvents.

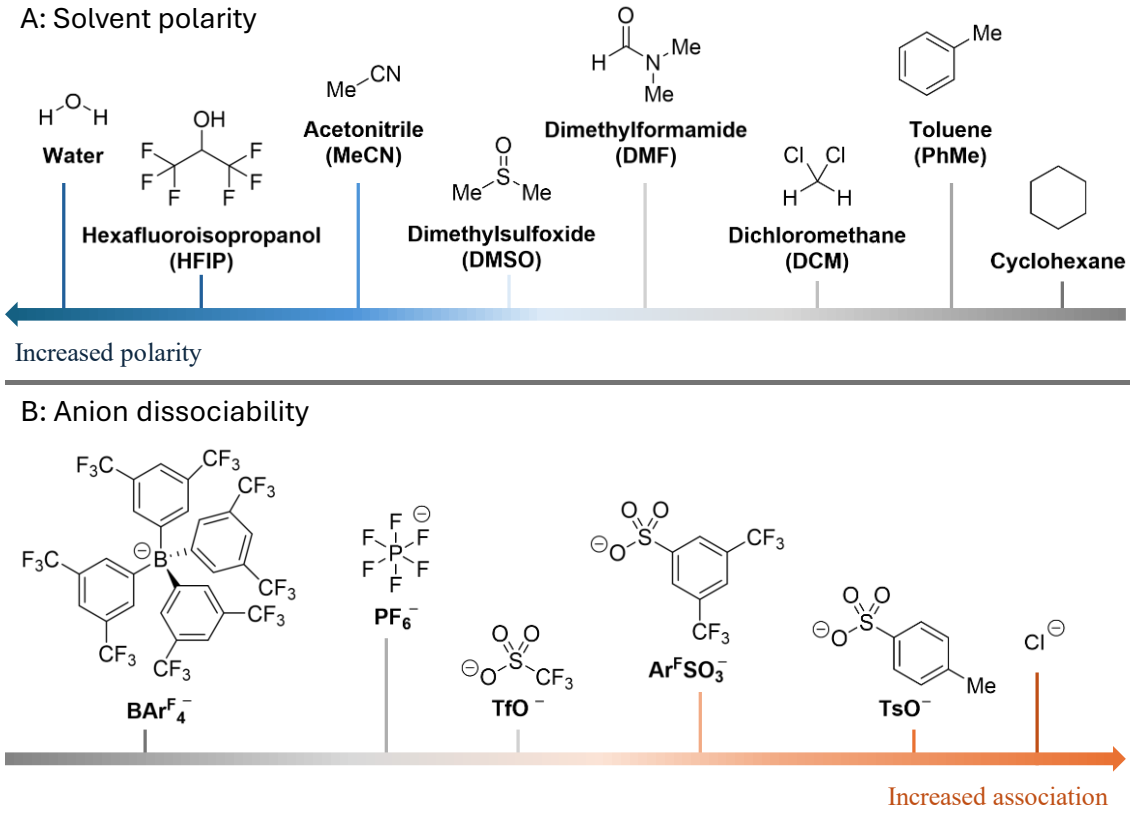

Figure 1.3. Depiction of the order of solvent polarities based on normalized solvent polarization parameter E_T^N (a)[17] and anion dissociabilities (b)[18].

A final point to be discussed before moving on to examining specific examples of the structure and reactivity of ion-pairs is the fluidity of the definition itself. For instance, Brønsted acid-base systems can exist somewhere in a continuum between hydrogen-bonded species and ion-pairs depending on the exact position of the proton (Figure 1.4, a). This paradigm has also been identified by chemists working in several fields, and new classifications of interactions, such as hydrogen-bond assisted ion-pairs and charge-assisted hydrogen bonds, have recently been coined.[19] Due to the widespread use of chiral phosphoric acids (CPAs) in particular, readers are encouraged to make their own assessments on reports describing either hydrogen-bonding or ion-pairing as the means of interactions between CPAs and other reaction components. At the time of this thesis, whether and to what extent Brønsted-acid catalysis should be considered in the terms of ion-pairing is a topic for ongoing debate in the chemistry community. However, from a strategic point of view, the added hydrogen-bonding nature is often welcomed as it makes up for the lack of directionality in purely electrostatic interactions. Moreover, in addition to the contact ion-pairs and solvent-separated ion-pairs discussed above, two further types of ion-pairs can be defined based on the involvement of the solvent (Figure 1.4, b).[20] In solvent-assisted ion-pairs the ions lie at a slightly prolonged interunit distance, while solvent molecules aid in holding them together, whereas in solvent-shared ion-pairs, one layer of solvent molecules exists between the oppositely charged ions.

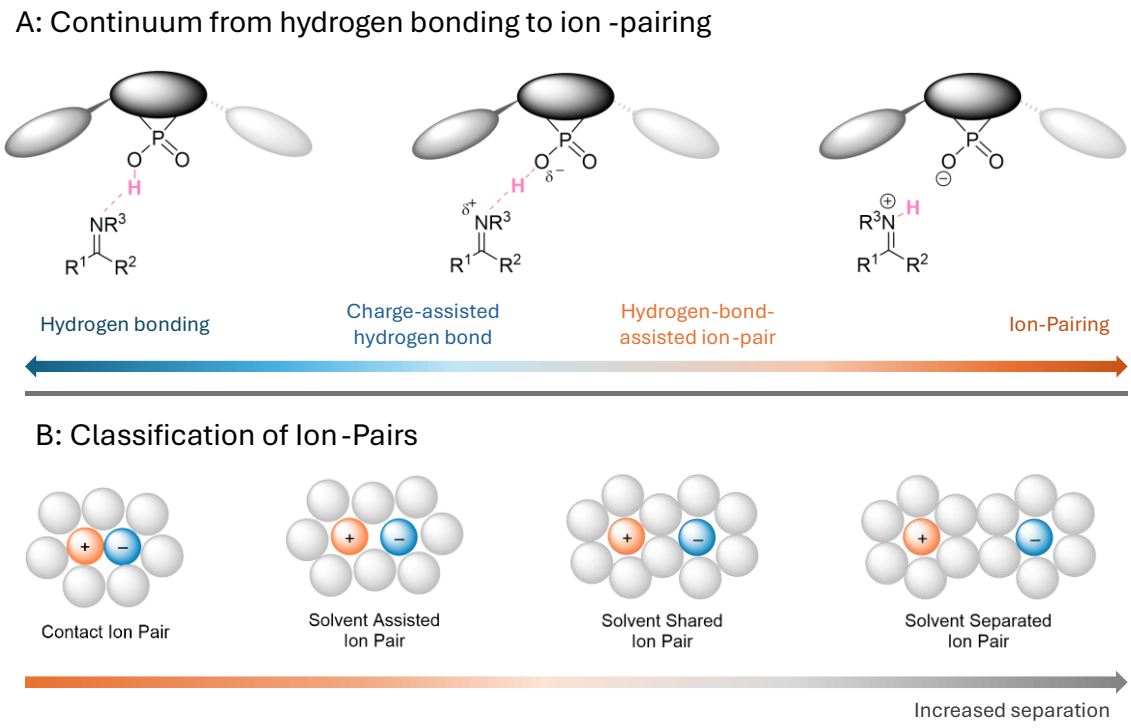

Figure 1.4. Continuum from hydrogen bonding to ion-pairing (a)[19] and classification of ion-pairs in solution (b)[20].

1.3 From neutral to ionic to ion-pairs – Background

Before we can start to evaluate the effect of counterions on the structure and reactivity of photocatalysts, we first have to understand the changes emerging when moving from neutral compounds to ionic ones. The first identification of chemical species as charge carriers was reported by Michael Faraday in the 1800s, when he also coined the terms ion, cation and anion based on his studies in electrochemistry.[21] Ion-pairing, by definition, describes a (partial) association of oppositely charged ions to form a distinct chemical species, an ion-pair.[22,23] Furthermore, in solution, the two oppositely charged species are expected to stay together at a certain separation (r) for a longer time than it would take to diffuse further than the distance R signifying free ions. Despite this rather straightforward definition, theoretical treatment of ion-pairs is notoriously more difficult, giving rise to various equations often describing ion-pairing under certain, tightly limited, conditions.[23] One of the first description of ion-pairs, Bjerrum handled ion-pairs with probability of finding the oppositely charged ions at a given distance of each other and noted that their separation would require electrostatic work. On another end, the free ions have been often depicted by the activities of electrolytes. Experimentally, though, the presence of ion-pairs can be measured with conductometry, potentiometry, salt/solvent activity measurements and spectroscopy. Importantly, while the classical understanding of ion-pairing only accounts for the formation of 1:1 ion-pairs in dilute solutions, recent experimental results highlight the possibility for higher aggregates even under such conditions.[24]

In the realm of photochemistry, ionic photocatalysts significantly differ from the neutral ones. From an orbital point of view, the presence of an electron-deficient site typically lowers the energy of the lowest unoccupied molecular orbital (LUMO), thus lowering the energy needed to promote an electron to this orbital (Figure 1.5, left).[25] In contrast, an excess electron density tends to raise the energy of the highest occupied molecular orbital

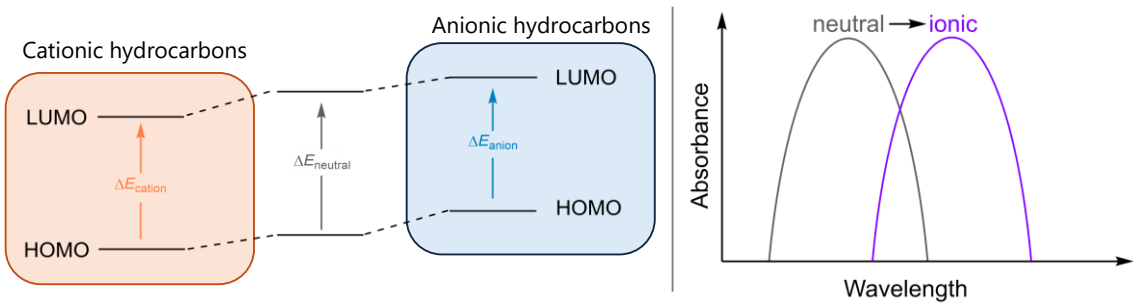

Figure 1.5. Effects of ionization to HOMO-LUMO energies (left) and UV-vis absorption spectra (right).[25]

(HOMO), again lowering the needed energy for photoexcitation. These changes in the HOMO-LUMO gap can be experimentally observed with UV-vis spectroscopy where the absorbance of the ionic compounds is often bathochromically shifted compared to their neutral counterparts.

Lastly, ionization has notable effects on the reactivity of molecules. For example, cationic molecules are often more Lewis acidic and anionic compounds are more basic and nucleophilic than the neutral ones.[26] Similar reactivity changes can also be seen in photocatalysis: anionic photocatalysts tend to be more reducing and cationic catalysts more oxidizing than their neutral counterparts.[27] In some cases, the neutral and ionic forms of the photocatalyst also exhibit different reactivities; for example, the neutral Eosin Y has been established as a HAT-catalyst while its anionic form engages in photoredox chemistry.[28,29] As a result, deliberate changes in the catalyst's structure can be used to tune its reactivity in a well-predictable manner. Furthermore, as an alternative to directly introducing a charged group to the catalyst, an *in-situ* protonation or deprotonation of suitable functional groups can also be harnessed to generate the charged species.[30] The behaviour and reactivity of ionic catalysts in comparison to their neutral forms are exemplified in Figure 1.6.

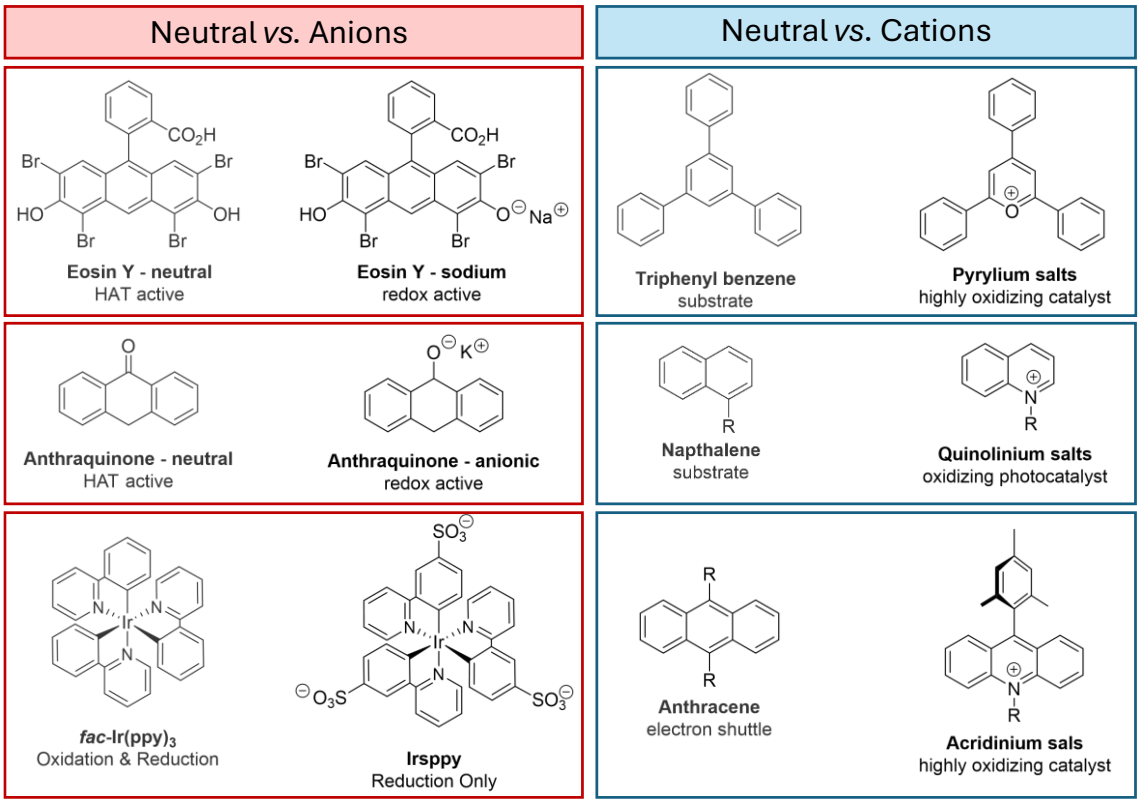

Figure 1.6. Examples of differing reactivities on neutral and ionic compounds.

1.4 Harnessing the counterion effect

The counterion can be harnessed in many ways, to support the desired reactivity or suppress an undesired one. As a first taste of why considering the counterion matters, representative examples can be drawn from the group of G. J. Meyer. Over the years, the group has elucidated the structure and photophysical behavior of various ion-pairs consisting of Ru(II) polypyridyl cation and halide anions (for example Cl^-, Br^-, I^-).[31–34] These reports represent important findings of what could happen with redox-active counterions. Indeed, excited-state quenching of the $[Ru(deep)(bpz)_2]^{2+}$ could be observed with bromide[33] and iodide[34,35,32] anions combined with single-electron reduction of the halide anion. In both cases, the ground-state ion exchange from PF_6^- to the halide was found to take place in DCM. With iodide, the formation of the $[Ru]I_2$ ion-pair could be forged even in MeCN, although the iodide concentration (stemming from TBAI) had to be increased by two orders of magnitude. While in these reports the intrasystem electron transfer was desired providing novel entries towards HBr and HI splitting reactions, it also serves as a stark reminder of the importance of choosing a redox-innocent counterion when activating other substrates.

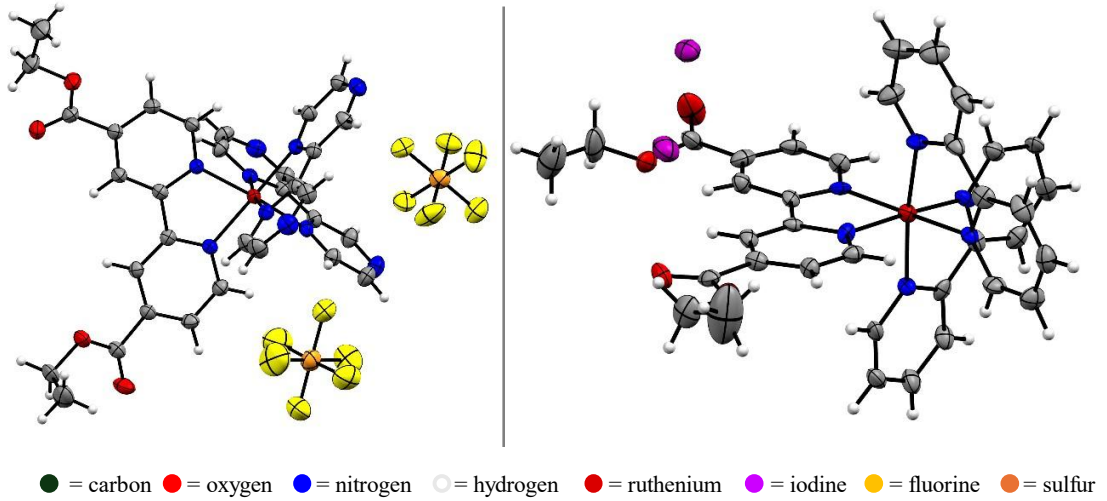

Figure 1.7. Single crystal structures of $[Ru(deep)(bpz)_2][PF_6]_2$ and $[Ru(deep)(bpz)_2]I_2$.[34,36] For clarity, two molecules of co-crystallized acetone (right complex) and one oxygen atom (most likely from acetone, left complex), omitted for clarity.

1.4.1 Spectroscopical Changes

Changes in the UV-vis absorption und fluorescence emission spectra give usually first hints about the ion-pair formation or counter-ion exchange. Based on multiple experimental reports, a generalized trend suggests that the contact ion-pair has its absorption maximum at lower wavelengths and that a bathochromic shift takes place upon ion-pair dissociation (Figure 1.8, left).[25,27] This spectral change corresponds to the differences in HOMO-LUMO energy gap, meaning that the gap is larger in contact ion-pairs and is reduced when no ionic contact is present. These shifts are often explained by the Franck–Condon factors: as the electrostatic interactions between the two ions are tighter in the ground-state than in the excited-state, the increased interionic separation destabilizes particularly the ground-state, thus raising its energy and causing the smaller HOMO-LUMO energy gap. As the solvent and the nature of the counterion bear an important effect on the dissociation and association of the ions, both factors influence the UV-vis absorption spectra as well.

Despite the easily understandable rationale, the experimental changes recorded for UV-vis absorption spectra often show relatively small changes ($\Delta\lambda_{max} \approx 10$ nm) between associated and dissociated ion-pairs.[18,37] While this shift has little to no effect on the irradiation wavelength used in reactions, it can still provide an assessment of the extent of ion-pairing upon careful inspection. Indeed, the group of G. J. Meyer demonstrated this in 2017 by titrating *n*-tetrabutylammonium bromide (TBABr) into a solution of $[Ru(deep)(bpz)_2][PF_6]_2$ in DCM.[36] During the portionwise addition of the first equivalent, a slight decrease in the intensity of the low-energy MLCT band at 460 nm was

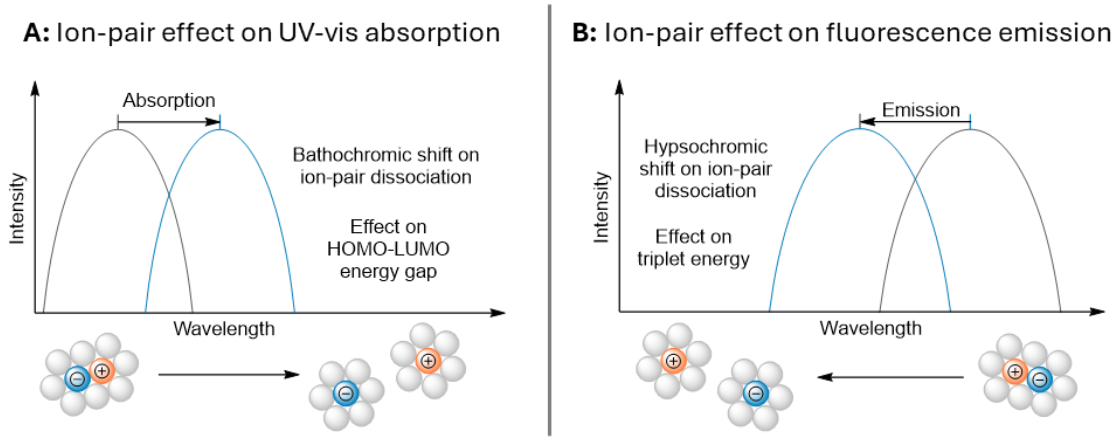

Figure 1.8. The effect of ion-pair dissociation in UV-vis absorption spectrum (left) and fluorescence emission spectrum (right).[25,27]

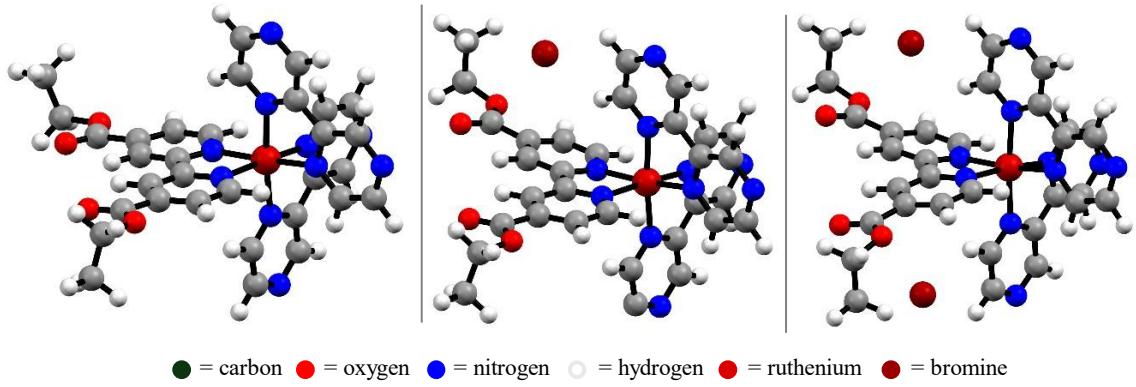

Figure 1.9. Computed structures for [Ru(deep)(bpz)$_2$] photocatalyst with no counteranions (left), with one bromide anion (middle) and with two bromides (right).[36]

observed. Upon titration of the second equivalent the formerly diminished peak at 460 nm remained rather unchanged yet another peak on its shoulder (445 nm) decreased in intensity. Isobestic points for the formation of [Ru^{2+}, Br^{-}]$^{+}$ were found at 411, 430 and 460 nm and for the [Ru^{2+}, $2Br^{2-}$] at 402 and 466 nm. Computational modelling of the catalysts with different equivalents of bromide anions (zero to two) proposed an energetically favorable location(s) for the bromides above the deep-ligands (Figure 1.9). Furthermore, the same group has reported similar spectral changes when the titration was done with chloride or iodide anions instead.[31,35] In all cases the spectral changes could be reversed by the addition of excess $TBAPF_6$.

In the fluorescence emission spectrum, the dissociation of a tightly bound ion-pair results in a hypsochromic shift (Figure 1.8, right). In contrast to the modest changes often seen in the UV-vis absorption, spectral changes in the fluorescence emission are usually more prominent. In an early report (1985), the group of T. J. Meyer identified the counterion effect in the photophysical properties of osmium polypyridyl complexes [Os(phen)$_3$]$^{2+}$ and [Os(4,4'-Ph_2phen)$_3$]$^{2+}$.[38] In their systematic study, five counteranions were combined at a time with each osmium photocatalyst, and their fluorescence emission spectra were recorded, revealing a difference in emission maximum up to 18 nm (Table 1.2). However, utilizing ruthenium polypyridyls [Ru(btfmb)$_3$]$^{2+}$ and [Ru(bpy)$_3$]$^{2+}$, counteranion-induced emission differences as large as 29 nm and 52 nm have been reported.[18,37]

Table 1.2. Emission maxima of different osmium photocatalyst ion-pairs.[38]

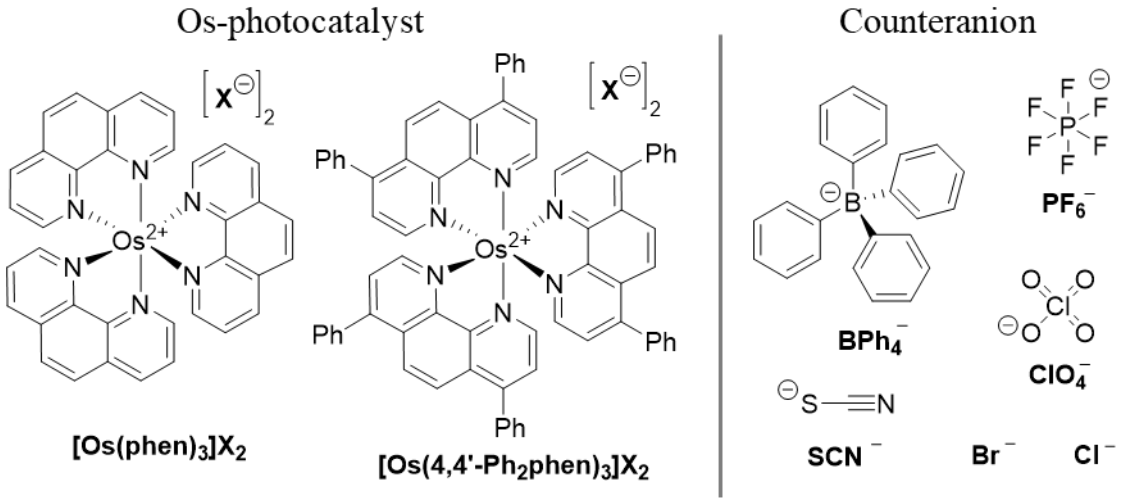

X^- / $\lambda_{em,max}$ (nm)	Cl^-	Br^-	SCN^-	ClO_4^-	PF_6^-	BPh_4^-
$[Os(phen)_3]X_2$	714	714	708	705	700	696
$[Os(4,4'\text{-}Ph_2phen)_3]X_2$	744	741	739	741	734	–

The shifts in the fluorescence emission maximum can be explained by the changes in excited-state triplet energies.[38] The experimental results presented above can be summarized as follows: The tightly coordinating counterion stabilizes the ground-state, thus increasing the HOMO-LUMO energy gap in contact ion-pairs. Furthermore, the tightly bound counterion can act as a stabilizing force in the triplet excited state, thus lowering its energy. Experimentally, these effects can be seen as a hypsochromic shift in the UV-vis absorption and bathochromic shift in fluorescence emission, respectively, although the former effect is sometimes less prominent.

1.4.2 Excited-State Redox-Potentials, Energies and Lifetimes

In 2019, the Yoon group reported their study on counterion effects with the $[Ru(btfmb)_3]^{2+}$ complex, intending to identify trends between the counterion association and photophysical properties of the catalyst in DCM.[37] Interestingly, a notable enhancement of the excited-state redox potentials (+1.04 V to +1.52 V) was found when moving from the most-coordinating TsO^- anion to the least coordinating $BAr^F{}_4^-$ (Table 1.3). Importantly, this series places the complex with $BAr^F{}_4^-$ anion +0.36 V higher in excited-state oxidation potential than the standardly used PF_6^- salt (Entries 1 and 2). The trend observed with excited-state redox-potentials was rationalized as a synergistic effect of ground-state reduction potentials $E(Ru^{2+/+})$ and the triplet-state energies (the latter estimated from the

Table 1.3. Effect of counteranion to the photophysical properties of $[Ru(btfmb)_3]^{2+}$.[37]

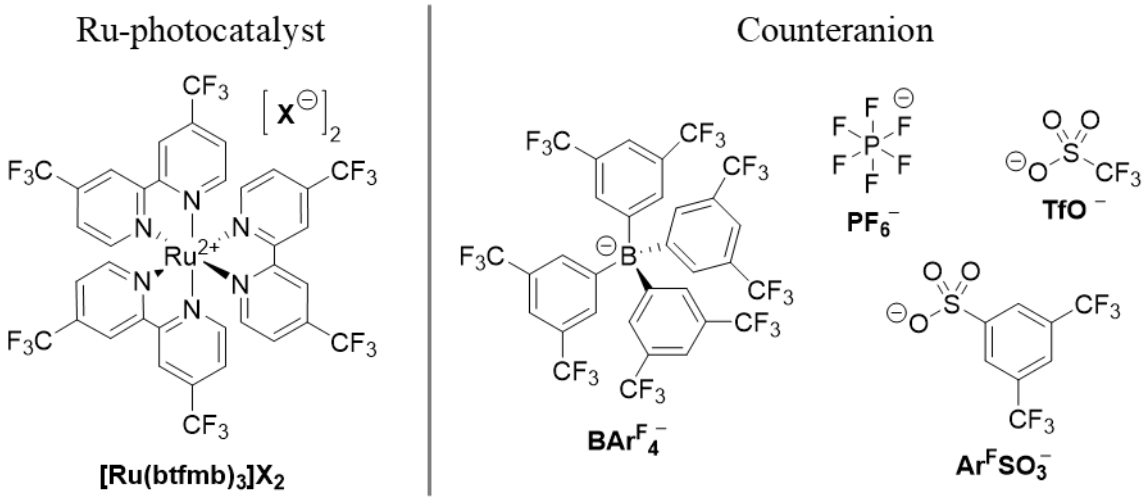

Entry	X^-	ΔG_{ES} (eV)	$E(Ru^{2+/+})$ (eV)	$^*E(Ru^{2+/+})$ (V)	τ_0 (ns)
1	$BAr^F{}_4^-$	2.17	– 0.65	+1.52	520
2	PF_6^-	2.05	– 0.89	+1.16	860
3	$Ar^FSO_3^-$	2.01	– 0.93	+1.08	950
4	TsO^-	1.99	– 0.95	+1.04	–

cross-point energy of normalized UV-vis absorption and fluorescence emission spectra). For instance, the borate salts possess the lowest ground-state reduction potential combined with the highest (estimated) triplet-state energy summing up to a high excited-state redox-potential (Entry 1). The opposite holds true for the triflate anion (Entry 4). While the theoretical background for the ion-pairing effect on triplet-state energies was explained in the previous section, the lowered ground-state reduction potential was proposed to stem from a facilitated one-electron transfer to the least electrostatically stabilized complex, i.e. when the counteranion is possibly far dissociated.

In 2024, the groups of Dixon, Canac, Smietana and Baslé published a similar work this time with $[Ru(bpy)_3]^{2+}$ photocatalyst. The triplet-state energies of catalysts with different counter anions were calculated based on experimental benchmarking (Table 1.4).[18] Comparison of the trend between the nature of the counteranion and the triplet-state energy can be found to follow the same trend as those reported by Yoon.[37] The least coordinating $BAr^F{}_4^-$ was calculated to have the lowest excited triplet-state 46.6 kcal/mol, while the most coordinating TsO^- had the triplet-state energy 44.1 kcal/mol. This computational result also places the borate-salt higher in triplet-state energy (+1.1 kcal/mol) than the PF_6-salt.

Table 1.4. Effect of counteranion to the photophysical properties of $[Ru(bpy)_3]^{2+}$.[18]

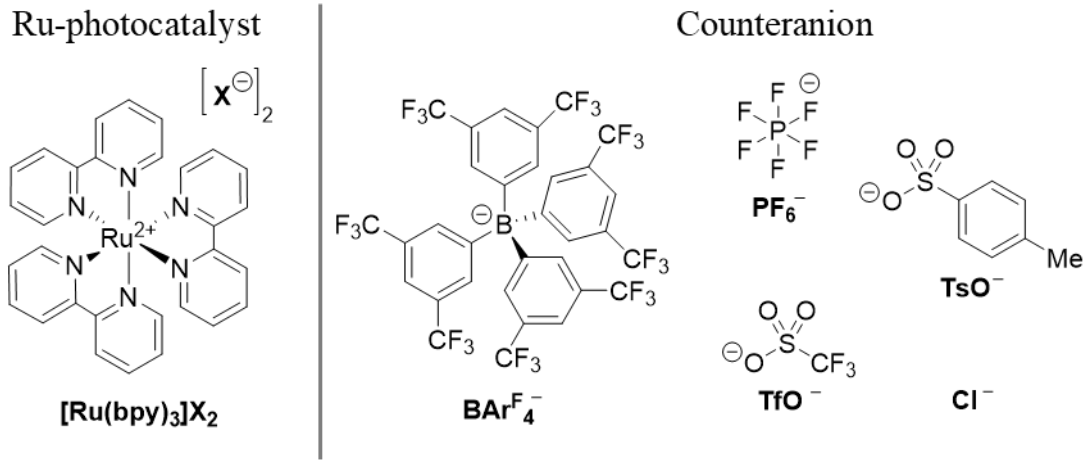

Entry	X^-	λ_{em} (nm)	GS-^{3}MLCT (kcal/mol)	τ_0 (ns)
1	$BAr^F{}_4^-$	575	46.6	231
2	PF_6^-	596	45.5	675
3	TfO^-	598	44.4	694
4	TsO^-	604	44.1	804

Excited triplet-state lifetimes (τ_0) were also found to vary depending on the counteranion, and usually decrease with increasingly dissociated counteranion (Tables 1.3 and 1.4).[18,37] Hence, both the $BAr^F{}_4^-$ salts were found to have excited-state lifetimes significantly shorter (520 ns for $[Ru(btfmb)_3]^{2+}$ and 231 ns for $[Ru(bpy)_3]^{2+}$ than the generally utilized PF_6^- salts (860 ns and 675 ns, respectively). In turn, with the most coordinating $Ar^FSO_3^-$ counteranion the $[Ru(btfmb)_3]^{2+}$ chromophore displayed its longest excited-state lifetime of 950 ns. This trend has been explained with the energy gap law. Especially in non-hydroxylic solvents, the counterion notably influences the vibrational overlap or Franck-Condon factors for the acceptor vibrations.[38] The increased energy separation between the ground-state and excited-state results in decreased overlap terms between donor and acceptor vibrations, thus lowering the rate of non-radiative decay. Perhaps most strikingly (yet as predicted by energy gap law), the logarithm of non-radiative rate-constant for excited-state decay (ln k_{nr}) and emission energy (E_{em}) have been found to display a linear relationship as demonstrated by T. J. Meyer on the osmium polypyridyl photocatalysts.[38] For ruthenium photocatalysts, the energy gap between excited-state and ground-state is generally proposed to come in the form of ^{3}MLCT and ^{3}MC states.[18] This internal conversion has been recognized as an important nonradiative deactivation pathway.

1.4.3 Changes in Molecular Orbitals and Excited-State Dipole Moments

The excitation of a single electron from its ground-state to an excited-state has a considerable effect on the electronic properties of metal polypyridyl photocatalysts. In metal chelates bearing three identical bidentate ligands, as best described by T. J. Meyer in the context of $[Os(phen)_3]^{2+}$, the excited electron is typically localized on a single polypyridyl ligand (at least on a vibrational time scale).[38] Even though EPR studies on related, singly reduced $[Ru(bpy)_3]^{+}$ and $[Fe(phen)_3]^{+}$ indicate a fast electron hopping between ligands in acetonitrile, in less polar solvents this phenomenon is mostly absent. This was proposed to result from the formed contact ion-pair since, unlike the ground-state which is D_3-symmetric, the excited state can be best described as C_2-symmetric and therefore able to support a permanent dipole moment (Figure 1.10, a).[18] In a contact ion-pair the anions are most likely positioned on the side of the complex opposite to the dipole, hence stabilizing the excited-state and lowering the energies of excited triplet-states. In addition to the stabilization, an energy barrier to the interligand electron transfer is created stemming from the need for accompanying anion translocation. This theoretical rationalization was experimentally verified by measurements on flash-photolysis time-resolved dielectric-loss (fp-TRDL) spectroscopy by Rumbles and Reid in 2022.[39] By using their custom-made setup, $[Ir[dF(CF_3)ppy]_2(dtbpy)]^{2+}$ catalyst bearing either PF_6^- or $BAr^F{}_4^-$ counter anion was exposed to microwave irradiation and the changes in phase and amplitude of the transmitted waveforms were recorded. In the measurement the presence of a contact ion-pair could be observed by a strong dielectric-loss signal, whereas no changes appear in solvent-separated ion-pairs as ion diffusion is too slow.

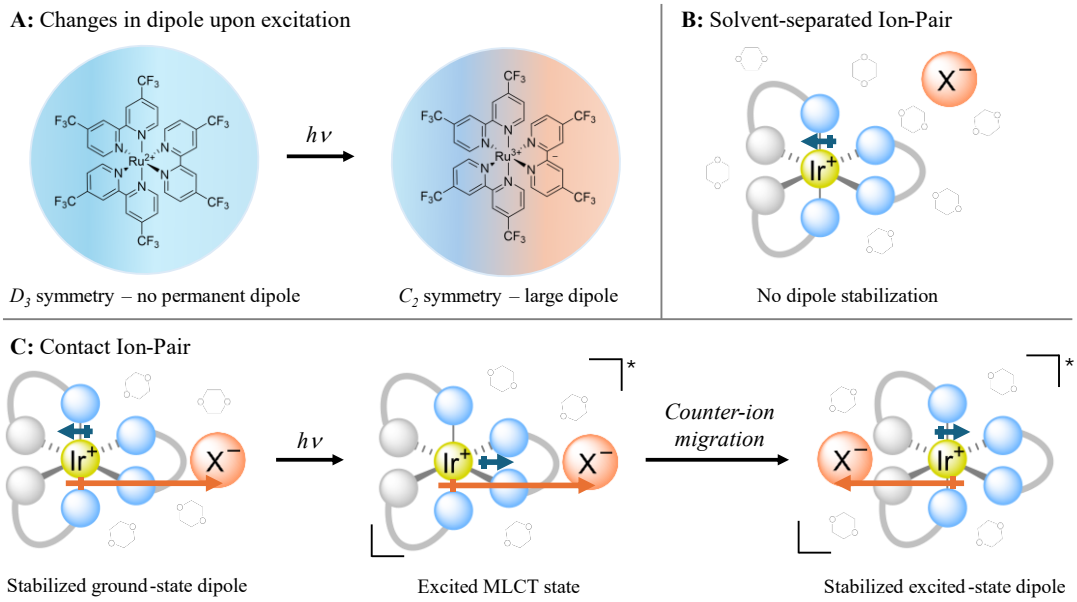

Figure 1.10. Dipole moments in ruthenium and iridium photocatalysts.[39]

Based on these experimental results, several previously formed hypotheses were confirmed. Firstly, in the ground-state the $[Ir]^{+}PF_6^{-}$ complex was found to form a tightly-bound ion-pair while the $[Ir]^{+}BAr^{F}{}_4^{-}$ was characterized to be solvent-separated, thus the dipole-moment of the latter was equal to the dipole moment of the iridium polypyridyl complex (Figure 1.10, b).[39] The transient dipole moment, a key factor in the stabilization of triplet-state dipole, was found to indeed stem from the migration of the counterion from the initial electron-donating site (dtbpy) to the excited-state electron donating site (dF(CF_3)ppy). This effect is typically explained by the reduced energy gap between ^{3}MLCT excited-state and the low-lying ^{3}MC state, which facilitates the internal conversion leading to more efficient nonradiative deactivation pathways.[40,41]

As a further notice, the nature of the counter anion also exhibits great influence on the photostability of the $[Ru(bpy)_3]^{2+}$ catalysts.[18] Under irradiation with 460 nm LED in DCM, over 85% decomposition of the (TsO^{-}) ion-paired ruthenium catalyst was observed in just 10 minutes. In the other extreme, 70% of the ($BAr^{F}{}_4^{-}$) complex was found to be present even after one hour in these conditions. Notably, the stability of the borate salt compares favorably to the typically used (PF_6^{-})-salt, being almost twice as stable. The differences in photostability were rationalized as follows: Strongly coordinating anions, such as TsO^{-}, can increase the decomposition rate by substituting a bipyridine ligand. This becomes particularly notable in solvents with low dielectric constants. At the orbital level, the ligand dissociation has been proposed to proceed *via* $^3MC_{cis}$ states rather than $^3MC_{trans}$ states as the former involves population of $d_{x^2-y^2}$ type of orbital elongating Ru–N bonds of the same ligand (Figure 1.11, a). With $[Ru]BAr^{F}{}_4^{-}$ these MC states are higher in energy than with $[Ru]PF_6^{-}$, disfavouring their population (Figure 1.11, b).

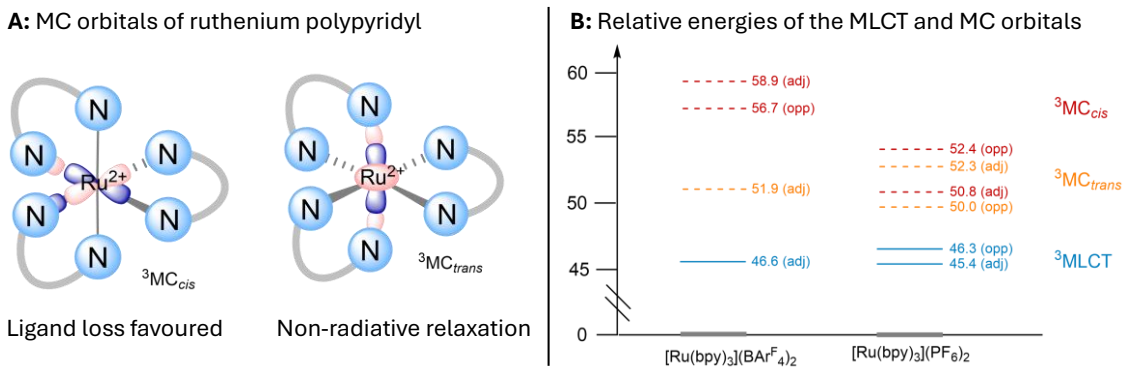

Figure 1.11. ^{3}MC orbitals of $Ru(bpy)_3$ (a) and their relative energies (b).[18]

1.4.4 Effects on the reactivity

The combination of the factors described in earlier sections eventually translates into notable differences in the catalystic abilities. As a remarkable example, the Yoon group reported in 2019 that the $[Ru(btfmb)_3][BAr^F{}_4^-]_2$ complex efficiently catalyzed the Diels–Alder reaction between the dienophile **1.1** and diene **1.2**, giving almost quantitative yield of the product **1.3** in 20 minutes (Scheme 1.1, upper part).[37] The other counter anions (TfO^-, TsO^-, $Ar^FSO_3^-$ and $Ar^FCO_2^-$) resulted in under 60% yields even after 24 hours. Furthermore, significant amounts of starting material could be recovered from the low-yielding reactions, thus showing that low conversion correlated with the low yields.

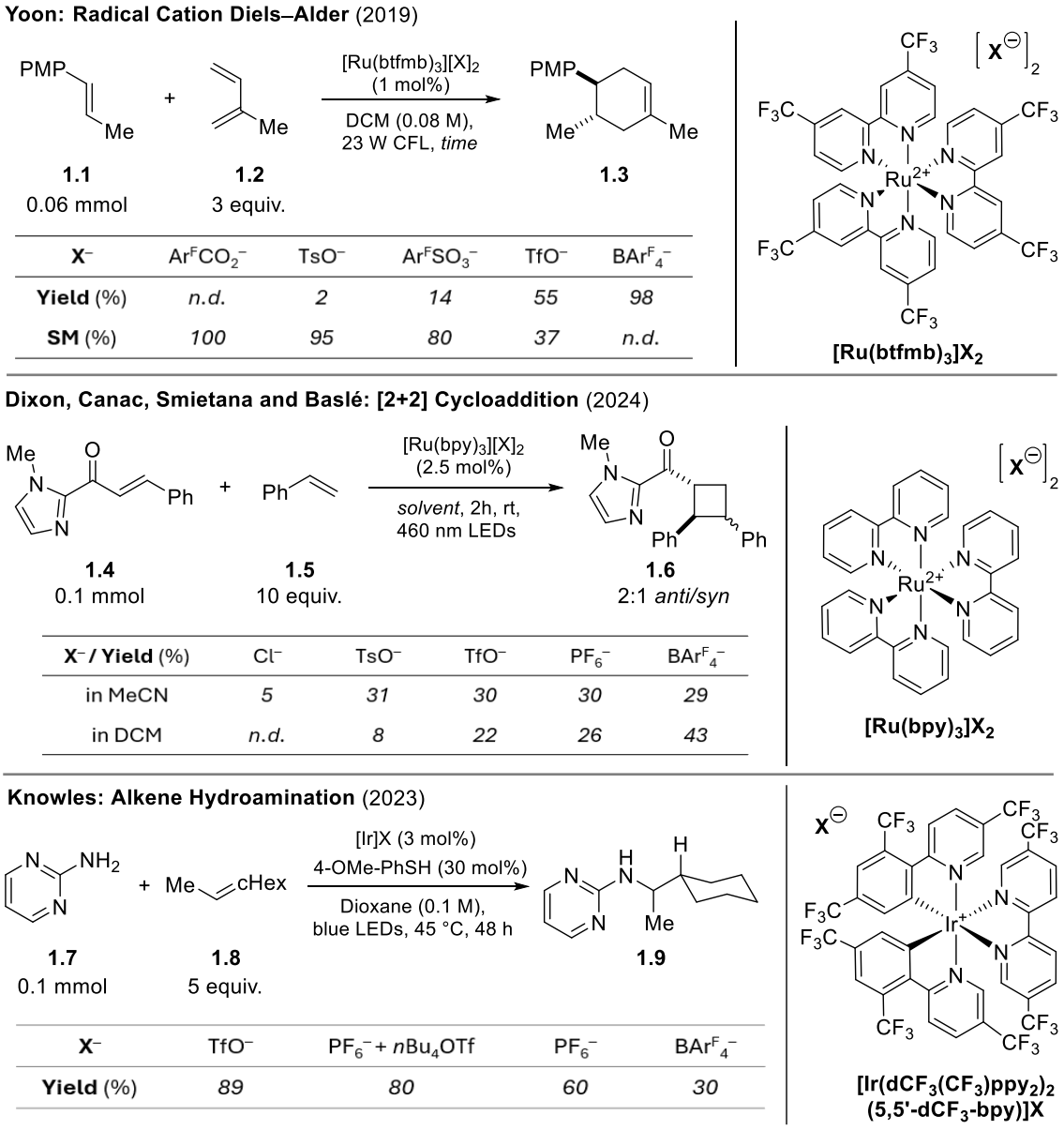

Scheme 1.1. Counter anion effect on reactivity: Radical cation Diels–Alder reaction (upper part),[37] [2+2] cycloaddition (middle)[18] and alkene hydroamination (lower part)[42].

The group explained the experimental observations as a sum of two factors: Firstly, as discussed in Section 1.4.2, the dissociation of the counter anion from the photocatalyst tends to raise its excited-state oxidation potential, leading to the more facile substrate activation. Secondly, the radical cation intermediates formed by the olefin oxidation and [4+2] cycloaddition are also likely to form ion-pairs, meaning that the anion originating from the Ru-ion-pair could affect subsequent reaction steps. The latter point was further supported by measurements of the quantum yield of the reaction (Φ). After taking into account the different rates of catalyst quenching, the estimated chain lengths (CL) became CL = 26 for $BAr^F{}_4^-$ and CL = 0.42 for $Ar^FSO_3^-$. It was thus deduced that the nature of the counteranion also impacts the efficiency of radical chain reactions.

In 2024, similar effects to the reactivity were reported in a classical [2+2] cycloaddition proceeding *via* triplet-triplet energy transfer catalysis (TTEnT) (Scheme 1.1, middle).[18] Using $[Ru(bpy)_3]^{2+}$ as a photocatalyst, the yield of the reaction was measured in two solvents. In acetonitrile, where general dissociation of ions could be expected, identical yields were obtained almost regardless of the counter anion. In dichloromethane, significant differences depending on the anion were observed, and the highest yield was obtained with the most easily dissociating aryl borate. Importantly, the $[Ru(bpy)_3][BAr^F{}_4^-]_2$ catalyst gave almost twice the yield as typically utilized PF_6^--salt. Resulting from the enhanced stabilization explained in Section 1.4.3, the loading of the $[Ru][BAr^F{}_4^-]_2$ could be lowered to 0.5 mol% without affecting the yield, giving a catalyst turnover number of 144. In the other extreme, the overall poor performance of chloride might be explained by a possible electron transfer from the catalyst to the redox-active counterion.[31]

In 2023, the group of Knowles in turn reported a strong counter-ion dependence on the $[Ir(dCF_3(CF_3)ppy)_2(5,5'\text{-}dCF_3\text{-}bpy)]$ photocatalyst.[42] In the context of their alkene hydroamination reaction, the opposite trend to the previous examples was observed; the tightly-bound TfO^- anion gave the highest yield whereas the $[Ir]BAr^F{}_4^-$ was the least suitable to catalyze this reaction. Interestingly, an *in situ*- anion exchange from $[Ir]BAr^F{}_4^-$ to TfO^- could restore the yield to the same level as with the pre-formed TfO^- salt. Preliminary mechanistic studies revealed that the longer excited-state lifetime of the photocatalyst ion-pair was beneficial for the reaction. However, as the C–N bond formation has been proposed to be the rate-determining step for such amination reactions, the possibility of triflate stabilizing other reaction intermediates becomes likely.

1.4.5 Ion-Pairing with Acids and Bases

In addition to peculiarly chosen counterions, some photocatalysts may also form ion-pairs with (Brønsted) acidic or basic reaction components. In 2023, the group of Ritter utilized the *in situ* protonation of an acridine **1.11** for the formation of a photoactive ion-pair between the acridinium cation and the anion from the mineral acid HCl or HNO_3 (Scheme 1.2, upper part).[43] Upon irradiation, a photoinduced electron transfer (PET) takes place between the acridinium catalyst and its counter anion to generate either chlorine or nitrate radicals, similarly to the report of Meyers (see Section 1.4). The generated radical then adds to a terminal alkene, and after HAT from a thiol, *anti*-Markovnikov hydrochlorination and hydronitrooxylation products are accessed in one step. Speaking for the importance of the ion-pair formation, the reaction was significantly hampered by addition of a redox-inert salt ($(n\text{Bu})_4\text{NBF}_4$) which competes with the mineral acid anion for the ion-pairing with the photocatalyst. Furthermore, fluorescence quenching of the photocatalyst was observed with both HCl and HNO_3, whereas 1-dodecene alone had no effect on the emission spectrum, thus excluding the alternative alkene oxidation mechanism.

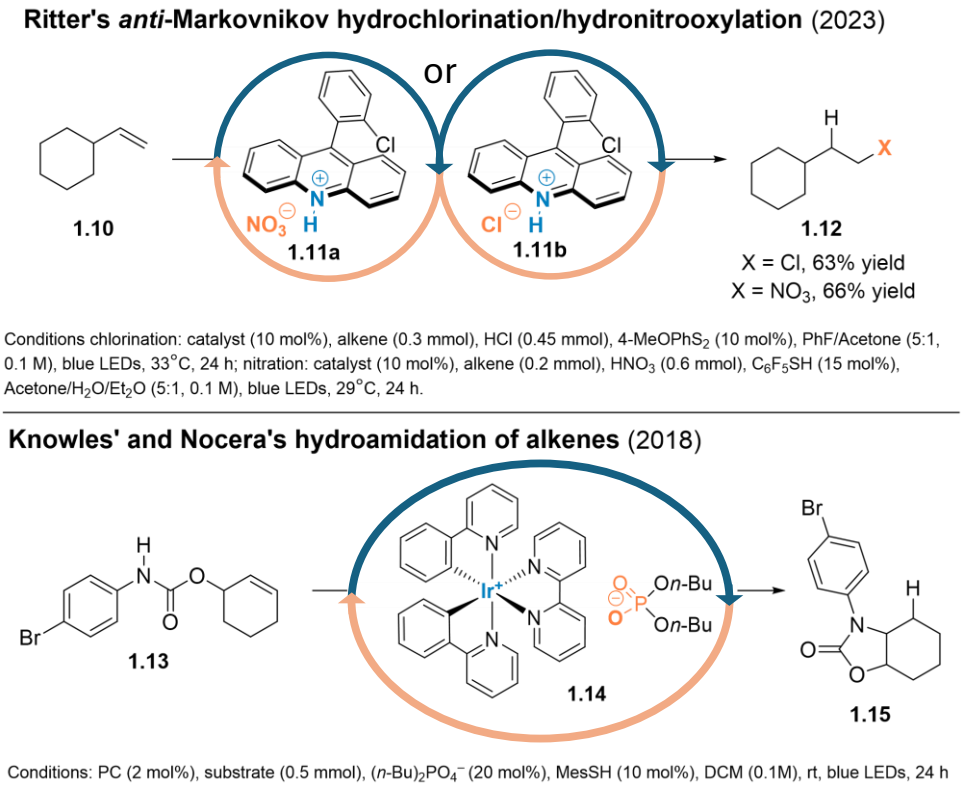

Scheme 1.2. Ion-pairing of the protonated acridinium cation and nitrate/chloride counter anions (upper part)[43] and in PCET-driven hydroamination (below).[44,45]

Ion-pair formation between a cationic photocatalyst and an anionic base has also recently been identified as a prerequisite for in proton-coupled electron transfer (PCET). Based on the initially described system of Knowles, the group of Nocera decided to take a deeper look at the underlying mechanism in 2018 (Scheme 1.2, lower part).[44,45] First, Stern–Volmer quenching studies ruled out the possible quenching of the excited-state photocatalyst by the phosphate base. However, a fine structure appeared in the emission spectrum together with a marginally increased excited-state lifetime of the iridium catalyst. Importantly, both changes could be reversed by the addition of excess $TBAPF_6$, which led to the suggestion of ground-state ion-pairing between the photocatalyst and the phosphate. Further quenching studies established that the amide substrate **1.13** could not alone quench the excited-state photocatalyst, therefore highlighting the necessity for all three components of the PCET step. In this direction, the ion-pairing between the photocatalyst and phosphate anion could be advantageous as it would ensure constant proximity of two of the three reagents. However, as the amide could also attach to the phosphate by hydrogen bonding, the full extent of the PC-phosphate interaction becomes difficult to assess. Importantly, this study raises an important consideration to all PCET reactions, and prominent, yet less acknowledged, ion-pairing interactions could be found in other systems as well.

1.4.6 Regioselective HAT *via* Ion-Pairing

Developing the idea of electrostatic-directed HAT of Breslow[10] further, the group of Davies reported in 2017 their photocatalytic procedure for the synthesis of pyrrolidine-3-one and related cyclic 1,3-carbonylated amines.[46] Their design was based on previously established trends in C–H activation towards radical-driven HAT upon amine protonation (Scheme 1.3, above).[47] Thus, protonation with pyrrolidine (**1.16**) with sulfuric acid rendered the α-C–H bonds acidic and the hydrogen atom abstraction took place on the β-positions instead yielding **1.17** after oxidation with H_2O_2. Although in this example the nature of the C–H bond overrides the possible ion-pairing, other examples have later verified the possibility for both rate enhancement and regioselectivity control by ionic attraction.[48,49] Indeed, in 2022 the groups of Torigoe and Kuninobu reported a regioselective functionalization of methylated anilines **1.18**.[49] In this system the change in the acidity of the neighboring methyl substituents is not a problem, and impressively the CH_3-substituent closest to the protonated aniline undergoes HAT selectively even in a protic polar solvent giving the *ortho*-functionalized product **1.20** with high regioselectivity.

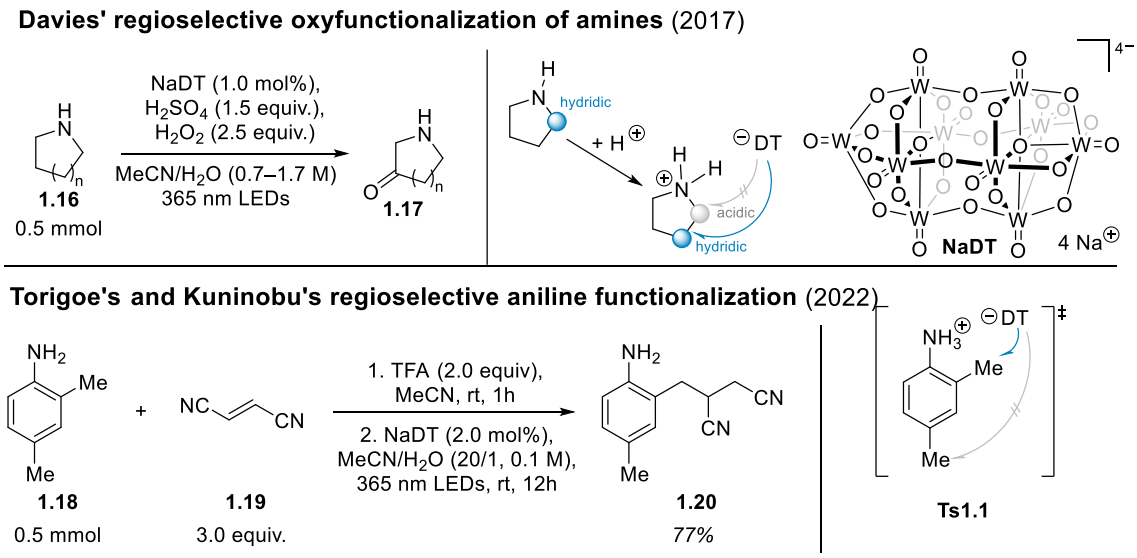

Scheme 1.3. Electrostatic-directed regioselective HAT with decatungstate anion.[46,49]

1.4.7 Imposing chirality *via* Asymmetric Counterions

In the previous section many studies postulated that the counterion of the photocatalyst might affect reaction steps beyond the first electron transfer by the formation of a secondary ion-pair with the substrate-derived ion. Indeed, recent studies have not only confirmed this interaction but also harnessed it to transfer chirality from the counterion to the products. While this topic has been recently reviewed by our group[16] and others,[15] a few selected examples are discussed below to establish some general trends and challenges.

An early example came from the group of Ooi in 2015 in a form of an enantioselective coupling of aldimines (**1.21**) with *N*-arylaminometanes (**1.22**) (Scheme 1.4, upper part).[50] Chiral tetraaminophosphonium cation **1.23**, derived from binol, was identified as an efficient catalyst for not only the asymmetric induction but also for the formation of the desired heterocoupling products. The proposed attractive interactions in intermediate **TS1.1**, formed after single-electron reduction of the aldimine, is perhaps best-described by ion-pair assisted hydrogen-bonding or hydrogen-bonding assisted ion-pairing. In a similar style, the group of Jiang reported an enantioselective photoreduction of 1,2-diketones **1.25** and α-keto ketimines (Scheme 1.4, middle).[51] Also in their case the key chiral intermediate is an ion-pair supported by two hydrogen bonds (**TS1.2**), which efficiently traps the reduced diketone intermediate and, after second reduction into carbanion allows the protonation only from the less hindered side.

Unlike the chiral cations, which are typically added to the reaction mixtures as their bromide or borate salts, the chiral anions are most often complexed with the active photocatalyst prior to the reaction. While the pre-complexation removes the possibility for tuning the loading of the photocatalyst and the chiral anion separately from one another, significant success has been achieved with as little as 2.5 mol% of the asymmetric ion-pair.[52] One of the key factors behind this success might be the fast transfer of the chiral anion from the photocatalyst to the (radical) cation intermediate due to continuous spatial proximity. The typical reaction conditions for asymmetric reactions, namely non-polar solvents and low temperatures, amplify the significance of minimal diffusion. In 2017, the group of Luo applied this strategy towards enantioselective *anti*-Markovnikov hydroetherification of alkenols such as **1.28** (Scheme 1.5, above).[53] The key catalytic ion-pair **1.29** was formed by an ion-exchange reaction between the sodium phosphates and acridinium tetrafluoroborate. Upon screening the different substitution pattern on the

CPA, slightly electron-poor 3,3'-aryl substituents combined with 6,6'-triisopropyl silyl groups were found to give the best results at room temperature (83% yield, 22% *ee*). Lowering the temperature first to −15 °C improved the chiral induction, while cooling down further to −25 °C started to notably hamper the reactivity (70% yield, 60% *ee*). The optimal conditions were hence established at −15 °C giving 83% yield of **1.30** with 56% *ee*.

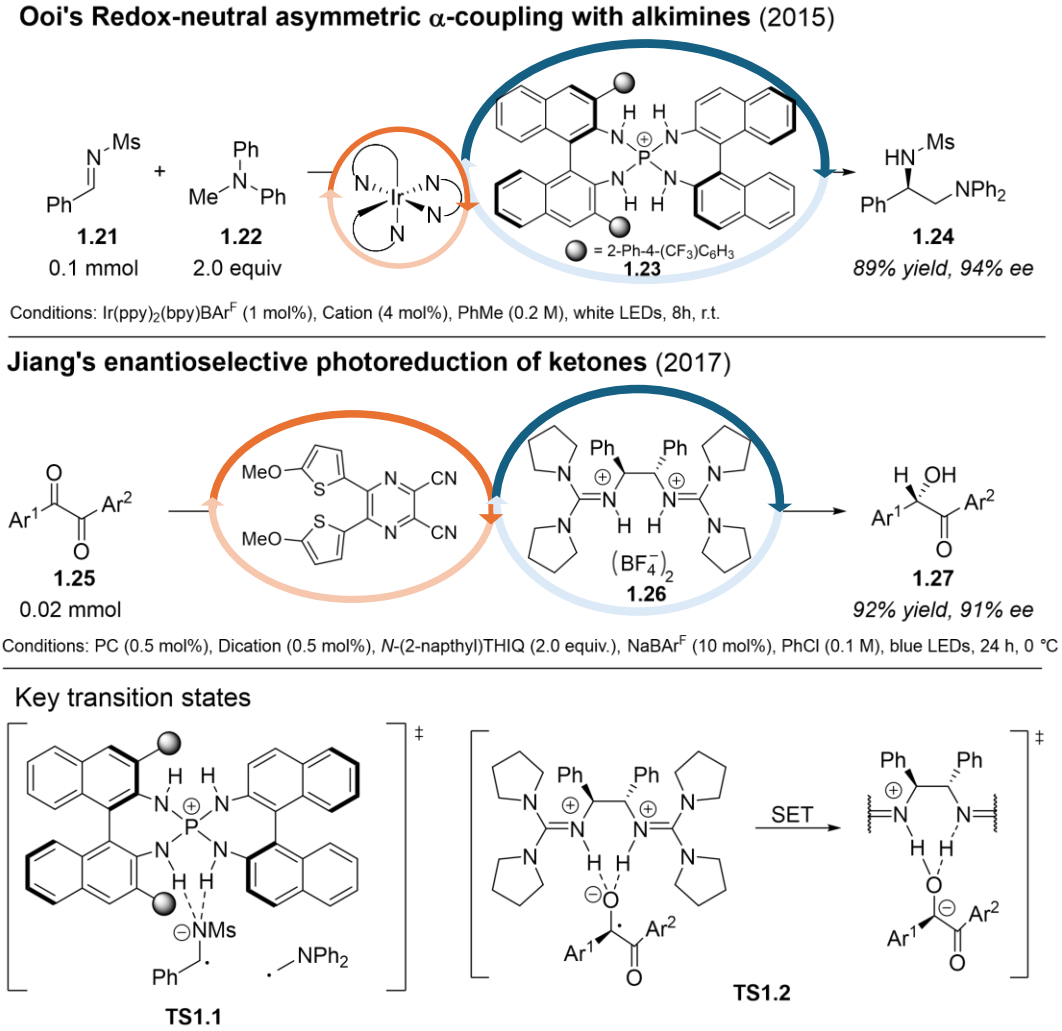

Scheme 1.4. Enantioselective reduction of aldimines (upper part) and diketones/ ketimines (lower part) induced by chiral cations.[50,51]

A year later the group of Nicewicz reported a similar approach towards chiral induction in a radical cation Diels–Alder reaction (Scheme 1.4, middle).[54] In contrast to the phosphoric acid derivative used by Luo, less nucleophilic *N*-trifylphosphoric acids (introduced as salt **1.32**) were needed to drive the product formation. In addition, triphenylsilyl groups at the 3,3'-position also contributed to the yield improvement despite them being

detrimental to the reactivity in Luo's system. Taken together, this highlights the importance of systematic evaluation of different substitution patterns on CPAs upon changing from one reaction to another. Under the optimized conditions an intramolecular enantioselective Diels–Alder reaction could convert the starting materials such as **1.31** to products **1.33** with 72% yield, 6:1 dr and 75:25 er. The differences between the CPAs were further reflected in the proposed transition states, Luo's being described as hydrogen-bond assisted ion-pair **TS1.3** and Nicewicz's a pure ion-pair **TS1.4** in nature (Scheme 1.4, below).[53,54]

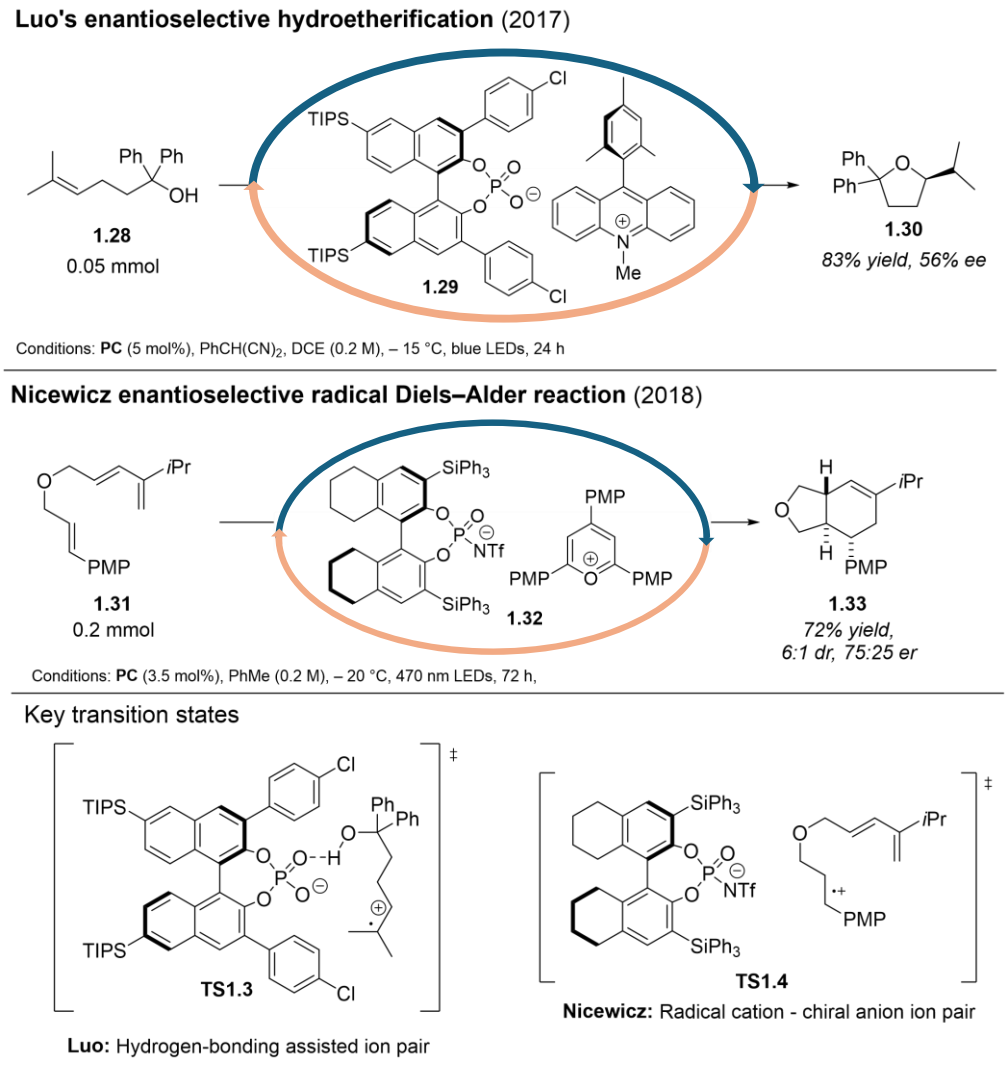

Scheme 1.5. CPA and chiral *N*-trifylphosphoric acids as chirality transfer reagents.[53,54] TIPS = triisopropyl silyl, PMP = *para*-methoxyphenyl.

The group of List managed to improve the enantioselectivity to a very high level (> 95:5 er) in 2022 with a photocatalytic [2+2]-cycloaddition as a model reaction (Scheme 1.6).[52] Herein, the key to their success was the broad screening of a library of phosphoric acid, imidodiphosphoric acid and imidodiphosphorimidate acid derived chiral anions. Importantly, their best-performing imidodiphosphorimidate anion (**1.36**) combined a relatively high acidity (pK_a of the acid dissociation ~ 4) and significant structural confinement. Although necessary for the high er, the high steric bulk together with the low temperatures (– 100 °C) resulted into very long reaction times (from 5 days up to a week). The absence of acidic protons in either of the starting materials led to ionic attraction being proposed as main interaction in transition states (**TS1.5** to **TS1.7**). These interactions combined with the tight confinements of the CPA catalyst most likely folded the open-chain substates/intermediates to a certain conformation resulting into an efficient chirality transfer.

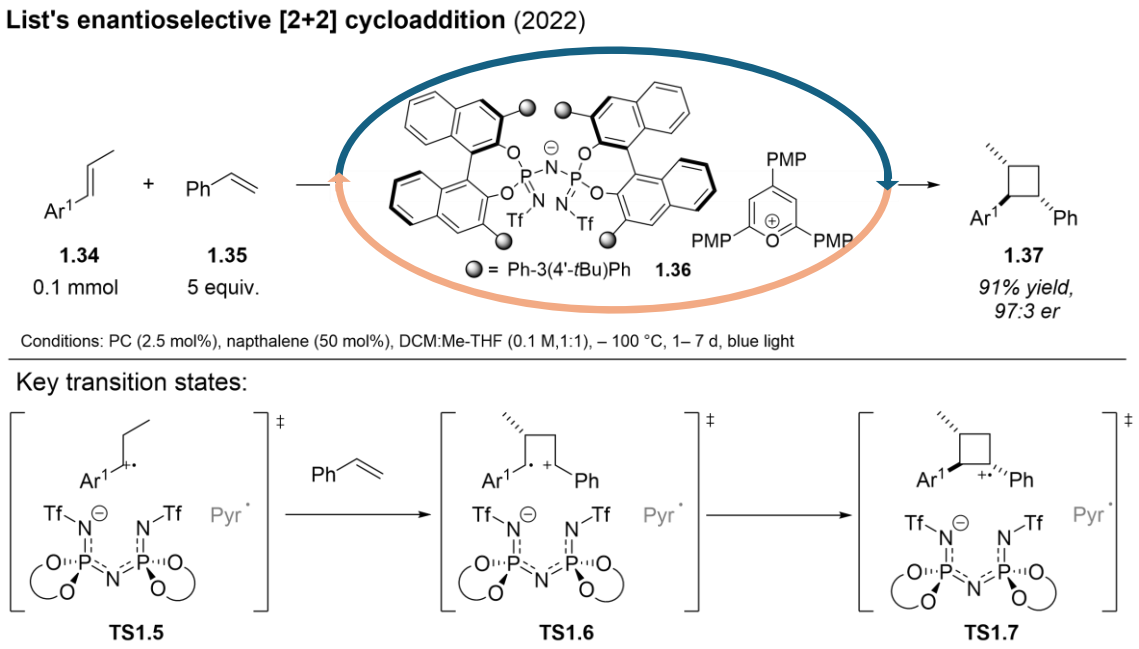

Scheme 1.6. Chiral imidodiphosphorimidate anions as a chiral transfer reagent.[52] PMP = *para*-methoxyphenyl, Tf = trifluoromethane sulfonate.

1.4.8 Ionic Bifunctional Catalysts

As a relatively new addition to the repertoire of photocatalyst ion-pairs are the bifunctional photocatalysts covalently bound to a chiral backbone. Herein, the key design principles include the electric interaction often comprising of hydrogen bonding and ionic interactions between the catalyst and substrate. In 2021, the group of Bach reported their bifunctional catalyst **1.40** where the chiral phosphoric acid backbone was utilized to covalently link two thioxanthone photocatalysts (Scheme 1.7, a).[55] Catalytic potential of this compound was demonstrated with an enantioselective [2+2]-photocycloaddition between an oxazolidine (**1.38**) and 2,3-dimethylbutadiene (**1.39**) which gave the aldehyde (**1.41**) after hydrolysis. From the mechanistic point of view, an *in situ*- ring opening of the oxazolidine generates an imine, which can be protonated to iminium ion by the CPA, ensuring the spatial proximity of the reactants leading to chirality transfer.

During their studies towards enantioselective photooxygenation of β-keto esters, the group of Meng rendered their cinchona alkaloid-based chiral phase-transfer catalyst into a bifunctional photocatalyst **1.43** by binding tetraphenylporphyrin photocatalyst to its core structure (Scheme 1.7, b).[56,57] As for the substrate, deprotonation of the β-keto ester **1.42** was employed for the generation of the delocalized enolate, which would then form

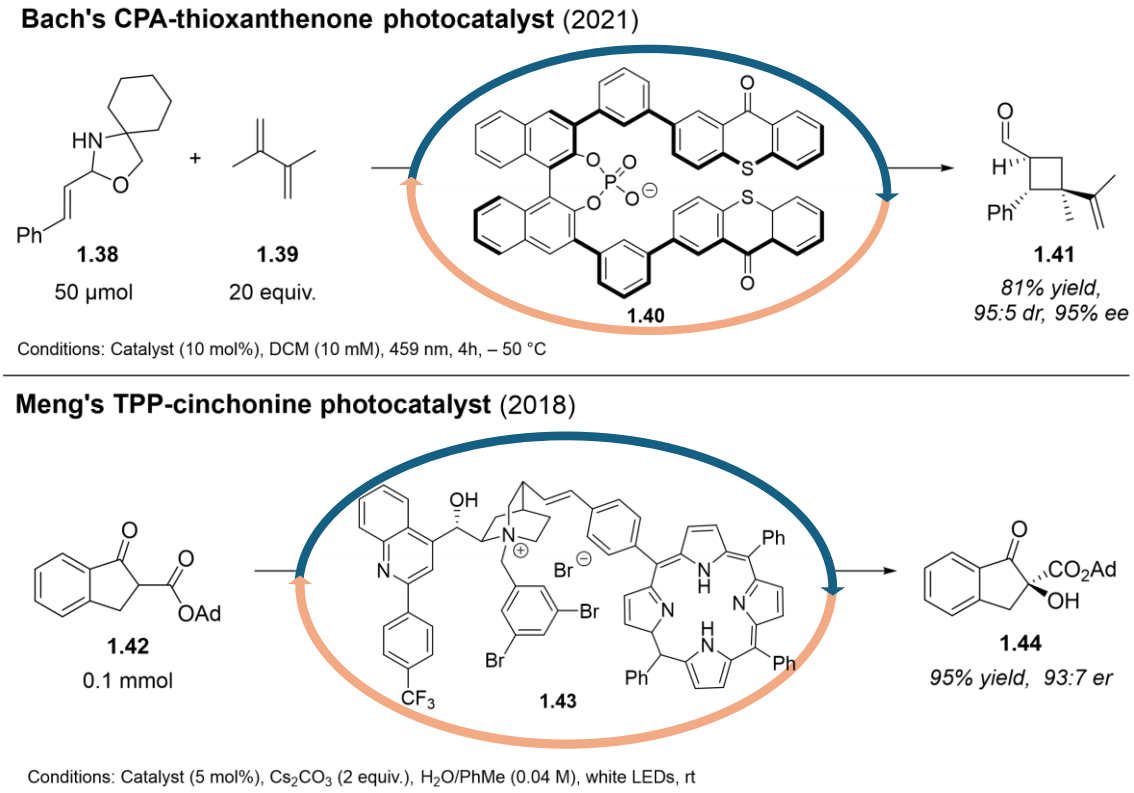

Scheme 1.7. Chiral bifunctional photocatalysts bearing an ionic moiety.[55,57]

an ion-pair with the catalyst. Following photoirradiation generated singlet oxygen, which acted as an oxidizing agent in the asymmetric environment to yield the β-hydroxyester **1.44** as product with high er.

In the past few years, the group of Ooi has further expanded the strategic use of charge throughout their research in zwitterionic HAT/photocatalysts.[58–60] Their firstly developed zwitterionic 1,2,3-triazolium amidates and phosphinylamidates were established as potent HAT catalysts when utilized together with light-harvesting iridium polypyridyl complexes (Scheme 1.8, upper part).[58,59] However, the newest generation of these phenylamidates are in turn covalently bound to acridinium core, giving novel catalytic species capable of both light-harvesting and HAT activation of substrates (Scheme 1.8, lower part).[60] Under irradiation, the excited-state zwitterionic photocatalyst **1.51** could undergo an intramolecular single-electron transfer to a biradical. The amidyl-derived *N*-centred radical represent a strong HAT reagent, easily abstracting hydrogen atom from fully unactivated hydrocarbon substrates. As a result, very high yields of the Giese coupling products (up to 99%) can be achieved with just 1 mol% of the catalyst.

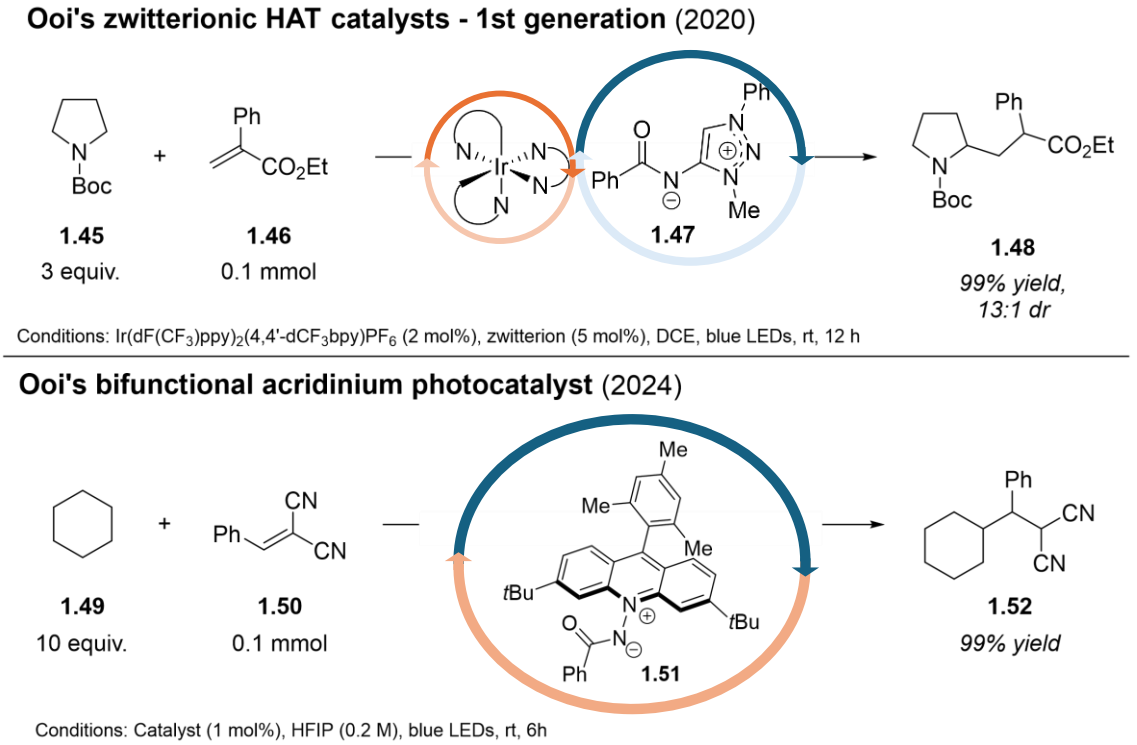

Scheme 1.8. Utilization of zwitterionic HAT-catalysts (a)[58] and bifunctional zwitterionic photo/HAT catalysts (b)[60] for Giese-coupling reactions.

1.5 Summary and Outlook

Despite ions and ion-pairing being known for more than a hundred years, in the field of photochemistry this intermolecular force has remained mainly unrecognized until recently. What in many cases started as the search for redox-inert counterions and better-soluble photocatalyst complexes turned out to reveal much more significant and intricate ion-pairing effects. Among the most important ones, changes in the UV-vis absorption, fluorescence emission, excited-state energies and lifetimes are all affected by the counterion. Furthermore, reactivities and stabilities of the catalysts are also modified. To date, these reports of the counterion effects have been obtained with numerous photocatalysts (both metal polypyridyls and fully organic ones) and with widely varying reaction conditions demonstrating the generality of this concept.

After recognition of the importance of the counterions, several reports detailing their uses in transferring stereoinformation have emerged. The requirement for the formation of a contact ion-pair for chirality transfer can be clearly seen by the optimal reaction conditions, where nonpolar solvents, particularly hydrocarbons, are used. While this is certainly justifiable from the ion-pairing point of view, it does limit the starting materials to compounds bearing large hydrophobic skeletons with few hydrophilic functionalities. In addition, cooling of the reaction mixture below 0 °C is often needed to diminish the rate of the racemic background reaction. However, this typically also prolongs reaction times. Upon comparing the reactions with chiral cations to the ones using chiral anions, a clear distinction can be seen in the way in which the chirality-bearing ion is introduced into the reaction mixture. While an ion-pair comprising of the photocatalyst and chiral anions is often made before the reactions, a similar strategy with the chiral cations has remained elusive. While this might be in part due to the easy accessibility of chiral phosphoric acid anions and cationic photocatalysts, interesting applications could be achieved by reversing the charges of the chiral unit and the catalyst

1.6 References

(1) Riuttamäki, S.; Laczkó, G.; Madarász, Á.; Földes, T.; Pápai, I.; Bannykh, A.; Pihko, P. M. Carboxylate Catalyzed Isomerization of β,γ-Unsaturated N-Acetylcysteamine Thioesters. *Chem. Eur. J.* **2022**, *28* (45), e202201030.

(2) Pârvulescu, V. I.; Hardacre, C. Catalysis in Ionic Liquids. *Chem. Rev.* **2007**, *107* (6), 2615–2665.

(3) Che, F.; Gray, J. T.; Ha, S.; Kruse, N.; Scott, S. L.; McEwen, J.-S. Elucidating the Roles of Electric Fields in Catalysis: A Perspective. *ACS Catal.* **2018**, *8* (6), 5153–5174.

(4) Léonard, N. G.; Dhaoui, R.; Chantarojsiri, T.; Yang, J. Y. Electric Fields in Catalysis: From Enzymes to Molecular Catalysts. *ACS Catal.* **2021**, *11* (17), 10923–10932.

(5) Nugmanova, A. G.; Sokolov, M. R.; Alexandrov, A. E.; Kniazeva, M. A.; Eremchev, I. Y.; Naumov, A. V.; Boukhvalov, D. W.; König, B.; Kalinina, M. A. Electric Field-Induced Amplification of Graphene Oxide's Visible Light Photocatalytic Activity. *J. Mater. Chem. A*, **2024**, *13* (1), 200–204.

(6) Fu, M.-C.; Shang, R.; Zhao, B.; Wang, B.; Fu, Y. Photocatalytic Decarboxylative Alkylations Mediated by Triphenylphosphine and Sodium Iodide. *Science*, **2019**, *363* (6434), 1429–1434.

(7) Quint, V.; Morlet-Savary, F.; Lohier, J.-F.; Lalevée, J.; Gaumont, A.-C.; Lakhdar, S. Metal-Free, Visible Light-Photocatalyzed Synthesis of Benzo[b]Phosphole Oxides: Synthetic and Mechanistic Investigations. *J. Am. Chem. Soc.* **2016**, *138* (23), 7436–7441.

(8) Morack, T.; Mück-Lichtenfeld, C.; Gilmour, R. Bioinspired Radical Stetter Reaction: Radical Umpolung Enabled by Ion-Pair Photocatalysis. *Angew. Chem. Int. Ed.* **2019**, *58* (4), 1208–1212.

(9) Woźniak, Ł.; Murphy, J. J.; Melchiorre, P. Photo-Organocatalytic Enantioselective Perfluoroalkylation of β-Ketoesters. *J. Am. Chem. Soc.* **2015**, *137* (17), 5678–5681.

(10) Breslow, R.; Rajagopalan, R.; Schwarz, J. Selective Functionalization of Doubly Coordinated Flexible Chains. *J. Am. Chem. Soc.* **1981**, *103* (10), 2905–2907.

(11) Dimakos, V.; Su, H. Y.; Garrett, G. E.; Taylor, M. S. Site-Selective and Stereoselective C–H Alkylations of Carbohydrates via Combined Diarylborinic Acid and Photoredox Catalysis. *J. Am. Chem. Soc.* **2019**, *141* (13), 5149–5153.

(12) Jia, Z.; Zhang, L.; Luo, S. Asymmetric C–H Dehydrogenative Allylic Alkylation by Ternary Photoredox-Cobalt-Chiral Primary Amine Catalysis under Visible Light. *J. Am. Chem. Soc.* **2022**, *144* (24), 10705–10710.

(13) Ye, J.; Kalvet, I.; Schoenebeck, F.; Rovis, T. Direct α-Alkylation of Primary Aliphatic Amines Enabled by CO2 and Electrostatics. *Nat. Chem.* **2018**, *10* (10), 1037–1041.

(14) Jia, Z.; Cheng, L.; Zhang, L.; Luo, S. Asymmetric C–H Dehydrogenative Alkenylation via a Photo-Induced Chiral α-Imino Radical Intermediate. *Nat. Commun.* **2024**, *15* (1), 4044.

(15) Gillespie, J. E.; Fanourakis, A.; Phipps, R. J. Strategies That Utilize Ion Pairing Interactions to Exert Selectivity Control in the Functionalization of C–H Bonds. *J. Am. Chem. Soc.* **2022**, *144* (40), 18195–18211.

(16) Schirmer, T. E.; König, B. Ion-Pairing Catalysis in Stereoselective, Light-Induced Transformations. *J. Am. Chem. Soc.* **2022**, *144* (42), 19207–19218.

(17) Dutkiewicz, M. Classification of Organic Solvents Based on Correlation between Dielectric β-Parameter and Empirical Solvent Polarity Parameter E^N_T, *J. Chem. Soc., Faraday Trans.*, **1990**, *86*, 2237–2241.

(18) Zanzi, J.; Pastorel, Z.; Duhayon, C.; Lognon, E.; Coudret, C.; Monari, A.; Dixon, I. M.; Canac, Y.; Smietana, M.; Baslé, O. Counterion Effects in [Ru(Bpy)3](X)2-Photocatalyzed Energy Transfer Reactions. *JACS Au* **2024**, *4* (8), 3049–3057.

(19) Iribarren, I.; Mates-Torres, E.; Trujillo, C. Revisiting Ion-Pair Interactions in Phase Transfer Catalysis: From Ionic Compounds to Real Catalyst Systems. *Dalton Trans.* **2024**, *53* (3), 1322–1335.

(20) Macchioni, A. Ion Pairing in Transition-Metal Organometallic Chemistry. *Chem. Rev.* **2005**, *105* (6), 2039–2074.

(21) Faraday, M. VI. Experimental Researches in Electricity.-Seventh Series. *Phil. Trans. R. Soc.* **1834**, *124*, 77–122.

(22) Kraus, C. A. The Ion-Pair Concept, Its Evolution and Some Applications. *J. Phys. Chem.* **1956**, *60* (2), 129–141.

(23) Marcus, Y.; Hefter, G. Ion Pairing. *Chem. Rev.* **2006**, *106* (11), 4585–4621.

(24) Burger, V.; Franta, M.; Ofial, A. R.; Gschwind, R. M.; Zipse, H. Highly Nucleophilic Pyridinamide Anions in Apolar Organic Solvents Due to Asymmetric Ion Pair Association. *J. Am. Chem. Soc.* **2025**, *147* (6), 5043–5050.

(25) Fox, M. A. The Photoexcited States of Organic Anions. *Chem. Rev.* **1979**, *79* (3), 253–273.

(26) Heine, J.; Peerless, B.; Dehnen, S.; Lichtenberg, C. Charge Makes a Difference: Molecular Ionic Bismuth Compounds. *Angew. Chem. Int. Ed.* **2023**, *62* (24), e202218771.

(27) Schmalzbauer, M.; Marcon, M.; König, B. Excited State Anions in Organic Transformations. *Angew. Chem. Int. Ed.* **2021**, *60* (12), 6270–6292.

(28) Majek, M.; Filace, F.; Wangelin, A. J. V. On the Mechanism of Photocatalytic Reactions with Eosin Y. *Beilstein J. Org. Chem.* **2014**, *10*, 981–989.

(29) Fan, X.-Z.; Rong, J.-W.; Wu, H.-L.; Zhou, Q.; Deng, H.-P.; Tan, J. D.; Xue, C.-W.; Wu, L.-Z.; Tao, H.-R.; Wu, J. Eosin Y as a Direct Hydrogen-Atom Transfer Photocatalyst for the Functionalization of C−H Bonds. *Angew. Chem. Int. Ed.* **2018**, *57* (28), 8514–8518.

(30) Schmalzbauer, M.; Svejstrup, T. D.; Fricke, F.; Brandt, P.; Johansson, M. J.; Bergonzini, G.; König, B. Redox-Neutral Photocatalytic C−H Carboxylation of Arenes and Styrenes with CO2. *Chem*, **2020**, *6* (10), 2658–2672.

(31) Ward, W. M.; Farnum, B. H.; Siegler, M.; Meyer, G. J. Chloride Ion-Pairing with Ru(II) Polypyridyl Compounds in Dichloromethane. *J. Phys. Chem. A*, **2013**, *117* (36), 8883–8894.

(32) Troian-Gautier, L.; Wehlin, S. A. M.; Meyer, G. J. Photophysical Properties of Tetracationic Ruthenium Complexes and Their Ter-Ionic Assemblies with Chloride. *Inorg. Chem.* **2018**, *57* (19), 12232–12244.

(33) Swords, W. B.; Meyer, G. J.; Hammarström, L. Excited-State Proton-Coupled Electron Transfer within Ion Pairs. *Chem. Sci.* **2020**, *11* (13), 3460–3473.

(34) Marton, A.; Clark, C. C.; Srinivasan, R.; Freundlich, R. E.; Narducci Sarjeant, A. A.; Meyer, G. J. Static and Dynamic Quenching of Ru(II) Polypyridyl Excited States by Iodide. *Inorg. Chem.* **2006**, *45* (1), 362–369.

(35) Clark, C. C.; Marton, A.; Meyer, G. J. Evidence for Static Quenching of MLCT Excited States by Iodide. *Inorg. Chem.* **2005**, *44* (10), 3383–3385.

(36) Li, G.; Swords, W. B.; Meyer, G. J. Bromide Photo-Oxidation Sensitized to Visible Light in Consecutive Ion Pairs. *J. Am. Chem. Soc.* **2017**, *139* (42), 14983–14991.

(37) Farney, E. P.; Chapman, S. J.; Swords, W. B.; Torelli, M. D.; Hamers, R. J.; Yoon, T. P. Discovery and Elucidation of Counteranion Dependence in Photoredox Catalysis. *J. Am. Chem. Soc.* **2019**, *141* (15), 6385–6391.

(38) Vining, W. J.; Caspar, J. V.; Meyer, T. J. The Influence of Environmental Effects on Excited-State Lifetimes. The Effect of Ion Pairing on Metal-to-Ligand Charge Transfer Excited States. *J. Phys. Chem.* **1985**, *89* (7), 1095–1099.

(39) Earley, J. D.; Zieleniewska, A.; Ripberger, H. H.; Shin, N. Y.; Lazorski, M. S.; Mast, Z. J.; Sayre, H. J.; McCusker, J. K.; Scholes, G. D.; Knowles, R. R.; Reid, O. G.; Rumbles, G. Ion-Pair Reorganization Regulates Reactivity in Photoredox Catalysts. *Nat. Chem.* **2022**, *14* (7), 746–753.

(40) Schmid, L.; Kerzig, C.; Prescimone, A.; Wenger, O. S. Photostable Ruthenium(II) Isocyanoborato Luminophores and Their Use in Energy Transfer and Photoredox Catalysis. *JACS Au* **2021**, *1* (6), 819–832.

(41) Soupart, A.; Dixon, I. M.; Alary, F.; Heully, J.-L. DFT Rationalization of the Room-Temperature Luminescence Properties of Ru(Bpy)32+and Ru(Tpy)22+: 3MLCT–3MC Minimum Energy Path from NEB Calculations and Emission Spectra from VRES Calculations. *Theor. Chem. Acc.* **2018**, *137* (3), 37.

(42) Geunes, E. P.; Meinhardt, J. M.; Wu, E. J.; Knowles, R. R. Photocatalytic Anti-Markovnikov Hydroamination of Alkenes with Primary Heteroaryl Amines. *J. Am. Chem. Soc.* **2023**, *145* (40), 21738–21744.

(43) Kim, J.; Sun, X.; Van Der Worp, B. A.; Ritter, T. Anti-Markovnikov Hydrochlorination and Hydronitrooxylation of α-Olefins via Visible-Light Photocatalysis. *Nat. Catal.* **2023**, *6* (2), 196–203.

(44) Miller, D. C.; Choi, G. J.; Orbe, H. S.; Knowles, R. R. Catalytic Olefin Hydroamidation Enabled by Proton-Coupled Electron Transfer. *J. Am. Chem. Soc.* **2015**, *137* (42), 13492–13495.

(45) Ruccolo, S.; Qin, Y.; Schnedermann, C.; Nocera, D. G. General Strategy for Improving the Quantum Efficiency of Photoredox Hydroamidation Catalysis. *J. Am. Chem. Soc.* **2018**, *140* (44), 14926–14937.

(46) Schultz, D. M.; Lévesque, F.; DiRocco, D. A.; Reibarkh, M.; Ji, Y.; Joyce, L. A.; Dropinski, J. F.; Sheng, H.; Sherry, B. D.; Davies, I. W. Oxyfunctionalization of the Remote C−H Bonds of Aliphatic Amines by Decatungstate Photocatalysis. *Angew. Chem. Int. Ed.* **2017**, *56* (48), 15274–15278.

(47) Salamone, M.; Carboni, G.; Bietti, M. Fine Control over Site and Substrate Selectivity in Hydrogen Atom Transfer-Based Functionalization of Aliphatic C–H Bonds. *J. Org. Chem.* **2016**, *81* (19), 9269–9278.

(48) Yuan, Z.; Yang, H.; Malik, N.; Čolović, M.; Weber, D. S.; Wilson, D.; Bénard, F.; Martin, R. E.; Warren, J. J.; Schaffer, P.; Britton, R. Electrostatic Effects Accelerate Decatungstate-Catalyzed C–H Fluorination Using [18F]- and [19F]NFSI in Small Molecules and Peptide Mimics. *ACS Catal.* **2019**, *9* (9), 8276–8284.

(49) Zeng, J.; Torigoe, T.; Kuninobu, Y. Control of Site-Selectivity in Hydrogen Atom Transfer by Electrostatic Interaction: Proximal-Selective C(Sp3)–H Alkylation of 2-Methylanilinium Salts Using a Decatungstate Photocatalyst. *ACS Catal.* **2022**, *12* (5), 3058–3062.

(50) Uraguchi, D.; Kinoshita, N.; Kizu, T.; Ooi, T. Synergistic Catalysis of Ionic Brønsted Acid and Photosensitizer for a Redox Neutral Asymmetric α-Coupling of N-Arylaminomethanes with Aldimines. *J. Am. Chem. Soc.* **2015**, *137* (43), 13768–13771.

(51) Lin, L.; Bai, X.; Ye, X.; Zhao, X.; Tan, C.-H.; Jiang, Z. Organocatalytic Enantioselective Protonation for Photoreduction of Activated Ketones and Ketimines Induced by Visible Light. *Angew. Chem. Int. Ed.* **2017**, *56* (44), 13842–13846.

(52) Das, S.; Zhu, C.; Demirbas, D.; Bill, E.; De, C. K.; List, B. Asymmetric Counteranion-Directed Photoredox Catalysis. *Science*, **2023**, *379* (6631), 494–499.

(53) Yang, Z.; Li, H.; Li, S.; Zhang, M.-T.; Luo, S. A Chiral Ion-Pair Photoredox Organocatalyst: Enantioselective Anti-Markovnikov Hydroetherification of Alkenols. *Org. Chem. Front.* **2017**, *4* (6), 1037–1041.

(54) Morse, P. D.; Nguyen, T. M.; Cruz, C. L.; Nicewicz, D. A. Enantioselective Counter-Anions in Photoredox Catalysis: The Asymmetric Cation Radical Diels-Alder Reaction. *Tetrahedron*, **2018**, *74* (26), 3266–3272.

(55) Pecho, F.; Sempere, Y.; Gramüller, J.; Hörmann, F. M.; Gschwind, R. M.; Bach, T. Enantioselective [2 + 2] Photocycloaddition via Iminium Ions: Catalysis by a Sensitizing Chiral Brønsted Acid. *J. Am. Chem. Soc.* **2021**, *143* (25), 9350–9354.

(56) Lian, M.; Li, Z.; Cai, Y.; Meng, Q.; Gao, Z. Enantioselective Photooxygenation of β-Keto Esters by Chiral Phase-Transfer Catalysis Using Molecular Oxygen. *Chem. Asian J.* **2012**, *7* (9), 2019–2023.

(57) Tang, X.; Feng, S.; Wang, Y.; Yang, F.; Zheng, Z.; Zhao, J.; Wu, Y.; Yin, H.; Liu, G.; Meng, Q. Bifunctional Metal-Free Photo-Organocatalysts for Enantioselective Aerobic Oxidation of β-Dicarbonyl Compounds. *Tetrahedron*, **2018**, *74* (27), 3624–3633.

(58) Ohmatsu, K.; Suzuki, R.; Furukawa, Y.; Sato, M.; Ooi, T. Zwitterionic 1,2,3-Triazolium Amidate as a Catalyst for Photoinduced Hydrogen-Atom Transfer Radical Alkylation. *ACS Catal.* **2020**, *10* (4), 2627–2632.

(59) Ohmatsu, K.; Suzuki, R.; Fujita, H.; Ooi, T. Zwitterionic Diphenylphosphinyl Amidate as a Powerful Photoinduced Hydrogen-Atom-Transfer Catalyst for C–H Alkylation of Simple Alkanes. *J. Org. Chem.* **2023**, *88* (10), 6553–6556.

(60) Entgelmeier, L.-M.; Mori, S.; Sendo, S.; Yamaguchi, R.; Suzuki, R.; Yanai, T.; García Mancheño, O.; Ohmatsu, K.; Ooi, T. Zwitterionic Acridinium Amidate: A Nitrogen-Centered Radical Catalyst for Photoinduced Direct Hydrogen Atom Transfer. *Angew. Chem. Int. Ed.* **2024**, *63* (43), e202404890.

CHAPTER 2

2 Eosin Y Catalyzed Dehydration of Aryl-1,2-diols

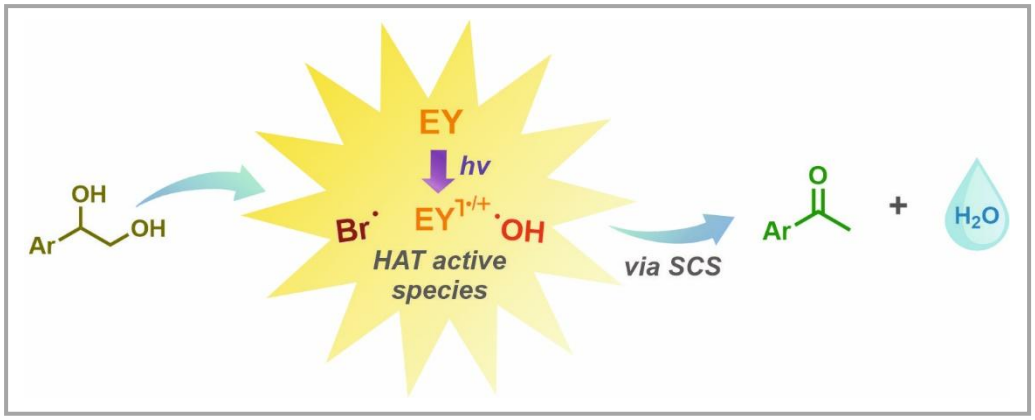

Abstract: Herein, we report a photocatalytic redox-neutral dehydration of aryl-1,2-ethanediols to the respective methyl ketones. Originally, we envisioned that Eosin Y, an organophotocatalyst with easily accessible neutral and anionic forms, could act as a dual Brønsted acid/HAT catalyst to initiate the key 1,2-spin centre shift (SCS) sequence. However, our mechanistic studies hint towards photodegradation of the catalyst prior to the onset of the reaction. Regardless, the desired transformation was achieved with high functional group tolerance and water as the sole by-product.

Modified version of this chapter has been published. For reference, see:
E. K. Taskinen, D. Kolb, M. Morgenstern and B. König*, Photocatalyzed Dehydration of 1-Aryl-1,2-ethanediols to Methyl Ketones Driven by Eosin Y Fragmentation Products, *Chem. Eur. J.*, **2024**, e202404200.

Author contributions: E.K.T and M.M. formed the concept of the study. D.K. optimized the reaction, and E.K.T. and D.K. synthetized the starting materials and formed the scope. E.K.T. planned and carried out mechanistic studies. E.K.T. wrote the manuscript with input from all authors. B.K. supervised the work.

2.1 Motivation

While some photocatalysts are already added to the reaction mixtures as their ion-pairs (for example, the ruthenium and iridium polypyridyls, acridinium and pyryliuym cations), a few of them can be converted to their ionic forms by *in situ* protonation/deprotonation. This shuttling between neutral and ionic forms opens possibilities for flexible modification of the catalyst's properties (such as UV-vis absorption) and reaction modes. Towards this goal we envisioned that Eosin Y could offer us a pronounced platform to evaluate its neutral and ionic forms obtained commercially or accessed *in situ*.

However, the ease of proton transfer also presents challenges in identifying the nature of the photoactive species.[1] Indeed, several factors need to be considered. Firstly, many literature reports simply use the notion "Eosin Y" when referring to any form of the catalyst, leading to difficulties in properly evaluating these reports and possible challenges upon reproducing such work. Secondly, even when the neutral form of Eosin Y is used, deprotonation can readily take place due to minor impurities in reagents or with solvents such as DMSO acting as a base. Furthermore, the use of irradiation sources such as compact fluorescence lamps (CFLs) or white LEDs emit over a broad range, giving no hints as to which wavelength is absorbed. As concluded by the group of von Wangelin, the photoredox reactions of Eosin Y cannot be discussed without strict specification of the form of the dye used and the accompanying reaction conditions.

To address these issues, we decided to take several measures to help us identify and unequivocally describe our findings. Firstly, we set out to test and clearly label the neutral Eosin Y (referred to as "Eosin Y") and its monoanionic ("Eosin Y sodium") and dianionic ("Eosin Y disodium") forms as catalysts in our reaction. Secondly, a thorough solvent screening was carried out. The nature of the catalyst in our reaction mixture was additionally characterized with UV-vis absorption spectroscopy, where the prominent peak around 535 nm is often labelled as characteristic for the anionic Eosin Y. Lastly, we chose to utilize commercial narrow-band LEDs and measure their emission spectra (see Section 2.5.1) to better monitor the irradiation wavelength absorbed during our reaction. While the inadequate description of experimental conditions has been particularly detrimental with Eosin Y, careful detailing of the reagents, catalysts and reaction conditions is certainly beneficial for all scientific reporting and should be hold as a golden standard for publishing.

2.2 Introduction

Eosin Y (EY, Eosin yellowish), a tetrabrominated fluorescein-derivative, was first synthetized in 1874 by Heinrich Caro in the Badische Anilin und Soda-Fabrik (currently known as BASF).[2] It was first employed as a dyeing agent in textile industry, and shortly afterwards as an artistic dye used by the likes of Vincent van Gogh and Paul Gauguin.[3] Intriguingly, both artists are said to have noticed discoloration of their paintings just a few months after completion, stemming from what is now known as Eosin Y photodegradation. Furthermore, the dyeing properties of Eosin Y have been and are still extensively employed in biological staining, in particular when used together with hematoxylin to generate the so-called H&E stain.[4–6]

The chemistry of Eosin Y is strongly influenced by pH, giving rise to various forms of the dye (Scheme 2.1).[1] In its neutral, "spirit soluble" form, Eosin Y exists in an equilibrium between its cyclic lactone form and a ring-opened acid form. Sequential deprotonation of the phenolic hydroxy group and benzoic acid moiety lead to water-soluble mono-and dianionic compounds with sodium countercation coming from the base. A cationic form of Eosin Y has also been accessed recently *via* protonation with strong Brønsted acids.[7] Importantly, the neutral and charged forms of the dye behave very differently under photochemical settings. The neutral form of Eosin Y is established as hydrogen-atom abstracting species, reported to abstract a hydrogen atom from slightly weakened *alpha*-heteroatom (O, N, S) positions, benzylic positions and aldehydes.[8,9] While the neutral Eosin Y only gave

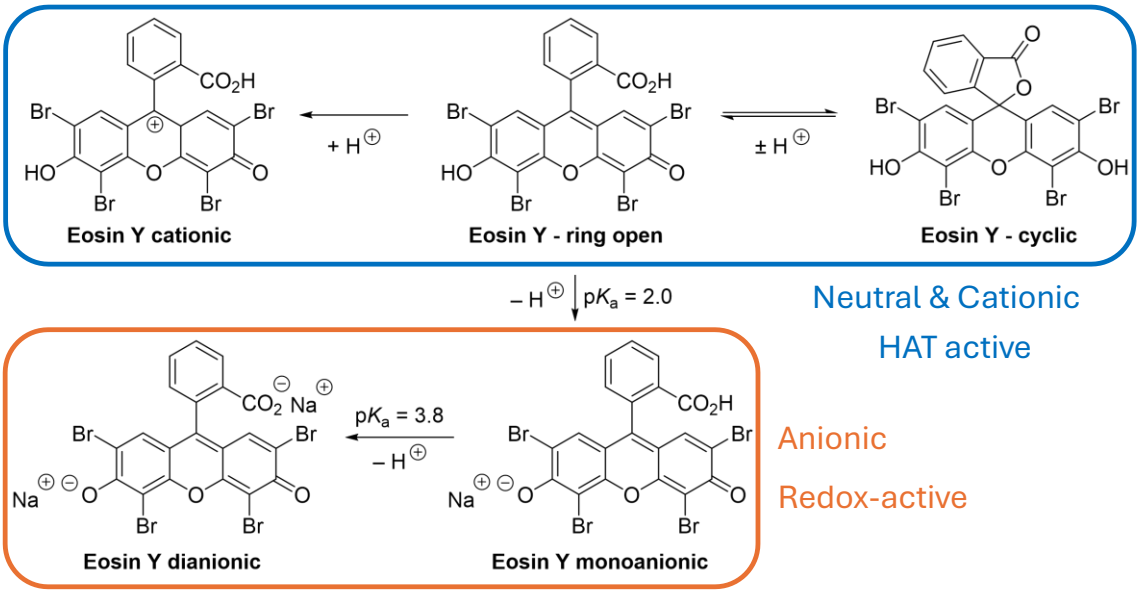

Scheme 2.1. Different forms of Eosin Y: cationic, neutral and anionic.

moderate yields with hydrocarbon substrates,[8] the cationic EY has been found to be a stronger hydrogen-atom abstracting reagent, giving high yields even from fully unactivated starting materials.[7] In photoredox catalysis, Eosin Y, as many anionic photocatalysts, is particularly active towards excited-state reductions with a potential of –1.58 V vs SHE (for the pair $E_{ox}(EY^{-}/{}^{*}EY^{2})$).[10] Hence, many of the redox-reactions of Eosin Y employ the photoinduced one-electron reduction as a first step.[11]

For our study we were particularly inspired by the possibility of dual Eosin Y catalysis, on one hand activating the substrates with protonation and on the other hand as a photocatalyst. In addition to the afore-described ground-state acidity, recent reports also suggest that photoexcitation of the neutral form of the catalyst might enhance its deprotonation, enabling proton transfer to weakly basic substrates.[12–14] Hence, we envisioned that this protonation could be harnessed in enhancing the leaving group ability as a part of a productive photocatalytic transformation. For these endeavours, we chose aryl-1,2-diols as starting materials as they can undergo various reaction pathways depending on the reaction conditions. For example, subjecting the aryl-1,2-ethanediol to cerium ligand-to-metal charge transfer (LMCT) conditions results into a formation of oxygen-centred radical (grey) which swiftly undergoes a β-scission to yield two aldehydes as products (Scheme 2.2, a).[15] In turn, abstraction of the benzylic hydrogen atom generated the benzylic radical (grey), and in the presence of a suitable leaving group, benzophenones are formed as products (Scheme 2.2, b). This interesting reaction sequence comprising of a concomitant carbonyl group formation, 1,2-radical shift and leaving group elimination was first defined by Wessig and Muehlin as 1,2-spin centre shift (SCS)

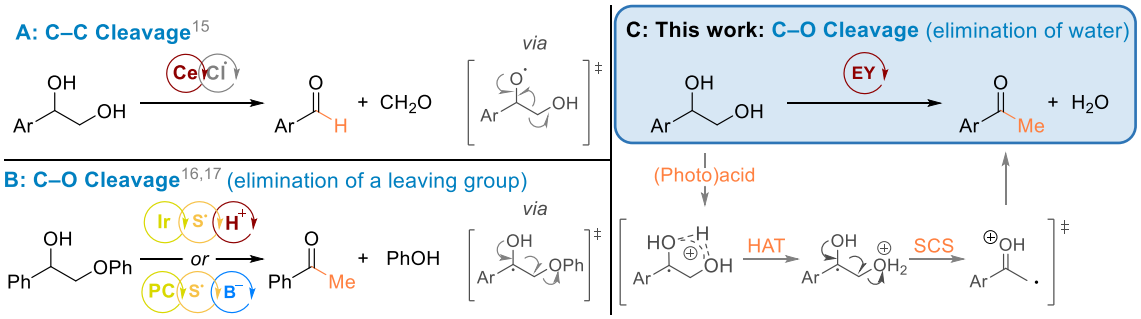

Scheme 2.2. Previously reported photocatalytic reactions of vicinal diols with cerium LMCT catalysis (a)[15], HAT-driven SCS process (b)[16–18] and this work (c).

in their biochemical review.[19] While the SCS was first observed inside living cells as a mechanism for biosynthesis and repair of DNA, it has also later found uses in synthetic laboratories for degradation of lignin model compounds and pyridine alkylations to name a few.[19–21] Despite the successful reaction of 2-phenoxy-1-arylethan-1-ols under the conditions developed separately by König and Nocera, no reaction could be observed with native diols.[16–18] Indeed, as summarized by Houk and Wang in their recent review, the general limitation still suppressing the broader applicability of the SCS is its requirement for a good leaving group and/or for additives to assist the leaving group elimination.[20] As converting the β-functionality to a good leaving group adds to the number of synthetic steps and increases the waste generated, the use of strong acids or bases severely limits the functional group tolerance. Hence, we questioned whether we could employ the dual catalytic nature of Eosin Y to first activate the diol substrate by a (photocatalyzed) protonation followed by HAT to initiate the SCS sequence (Scheme 2.2, c). This reaction design would notably simplify the reaction mixture needed for the reaction and eliminate the use for strong acids and bases. Herein, successful implementation of this strategy is discussed.

2.3 Results and Discussion

2.3.1 Reaction Optimization

We commenced our efforts towards the development of a mild dehydration protocol by choosing the commercially available 1-phenyl-1,2-ethanediol (**2.1**) as a starting material (Table 2.1). Upon screening various HAT catalysts, we were pleased to observe that Eosin Y gave an excellent conversion of the starting material into the product within one hour. With further optimization, the loading of Eosin Y could be reduced to 2 mol% while obtaining the product in 91% yield (Entry 1). Intriguingly, the structurally related fluorescein and product-resembling benzophenone were unable to catalyse the desired transformation (Entries 2 and 3). Bismuth and iron chloride, known to generate chlorine radicals *via* LMCT mechanism,[22,23] also furnished the product albeit in lowered yields (32% and 11% yield, respectively, Entries 4 and 5). Moving on to solvents, acetonitrile turned out to be the best option, although ethyl acetate also gave good yields despite the reaction was proceeding slightly slower (Entry 6). Unexpectedly, irradiation with 385 nm LEDs

Table 2.1. Screening of reaction conditions.

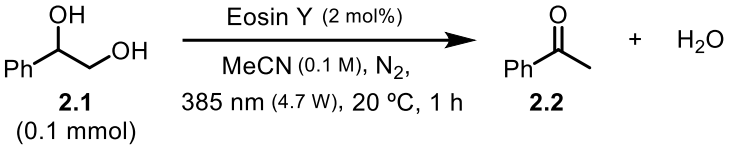

Entry	Deviation from optimal	Yield (%)[a]
1	None	91
2	Fluorescein	0
3	Benzophenone	0
4[b]	$BiCl_3$ (20 mol%)	32
5[c]	$FeCl_3$ (20 mol%)	11
6[d]	EtOAc instead of MeCN	73
7	420 nm or 520 nm LEDs	*traces*
	Control Experiments	
8	Under air	*traces*
9	No light or Photocatalyst	0

[a] Yields calibrated GC-FID yields. [b] $BiCl_3$ (20 mol%) + TBACl (40 mol%). [c] $FeCl_3$ (20 mol%) + TBACl (20 mol%). [d] Reaction time 3 h. TBACl = tetra-*n*-butylammonium chloride.

gave the highest yield, whereas 520 nm or 420 nm irradiation resulted in trace amounts of product (Entry 7). Finally, control experiments proved the necessity of an inert atmosphere, light and photocatalyst for the transformation (Entries 8 and 9).

2.3.2 Substrate Scope

Having established the optimal reaction conditions, we moved on to study the scope of the transformation. Some trends across the reaction scope were identified (Scheme 2.3). With respect to the steric effects, a methyl substituent on the *para*-and *meta*-positions gave essentially identical yields (71% and 70%), whereas shifting the methyl group to the *ortho*-position decreased the yield to 21% (compound **2.3** + **2.4** vs. **2.5**). These results suggest some degree of sensitivity towards steric hindrance near the reaction centre. Further away on the ring, though, a smooth conversion to the product could be achieved even with a *tert*-butyl group in place (compound **2.6**). With respect to the electronic effects, a clear preference was observed for electron-poor groups placed in the *para*-position and electron donating groups located in the *meta*-position (*vide infra*). For example, the *para*-

fluorinated diol furnished the corresponding acetophenone **2.7** in a 72% yield whereas the *meta*-fluorinated diol reacted to the product in a mere 32% yield (**2.8**). In addition to fluorine, *para*-trifluoromethyl and *para*-chlorine substituents were also well tolerated, both giving the desired products with over 70% yields (compounds **2.9** and **2.10**). In contrast, a methoxy group in a *para*-position led to 15% yield of product **2.11** but a methoxy group as the *meta*-substituent gave the acetophenone derivative **2.12** in an excellent yield (90%). Furthermore, a highly electron-rich and acid-labile TBS group could be used to protect the phenolic hydroxy group in the *meta*-position, thus forming the corresponding OH-protected acetophenone **2.13** in a 68% yield. A MOM-protected phenol, in turn, gave the product **2.14** in 11% yield. Mechanistically speaking, the observed electronic preference seems to support the HAT as a mechanism for the initial radical generation as the alternative aryl oxidation-deprotonation pathway would operate better on electron-rich aromatic systems.[24,25]

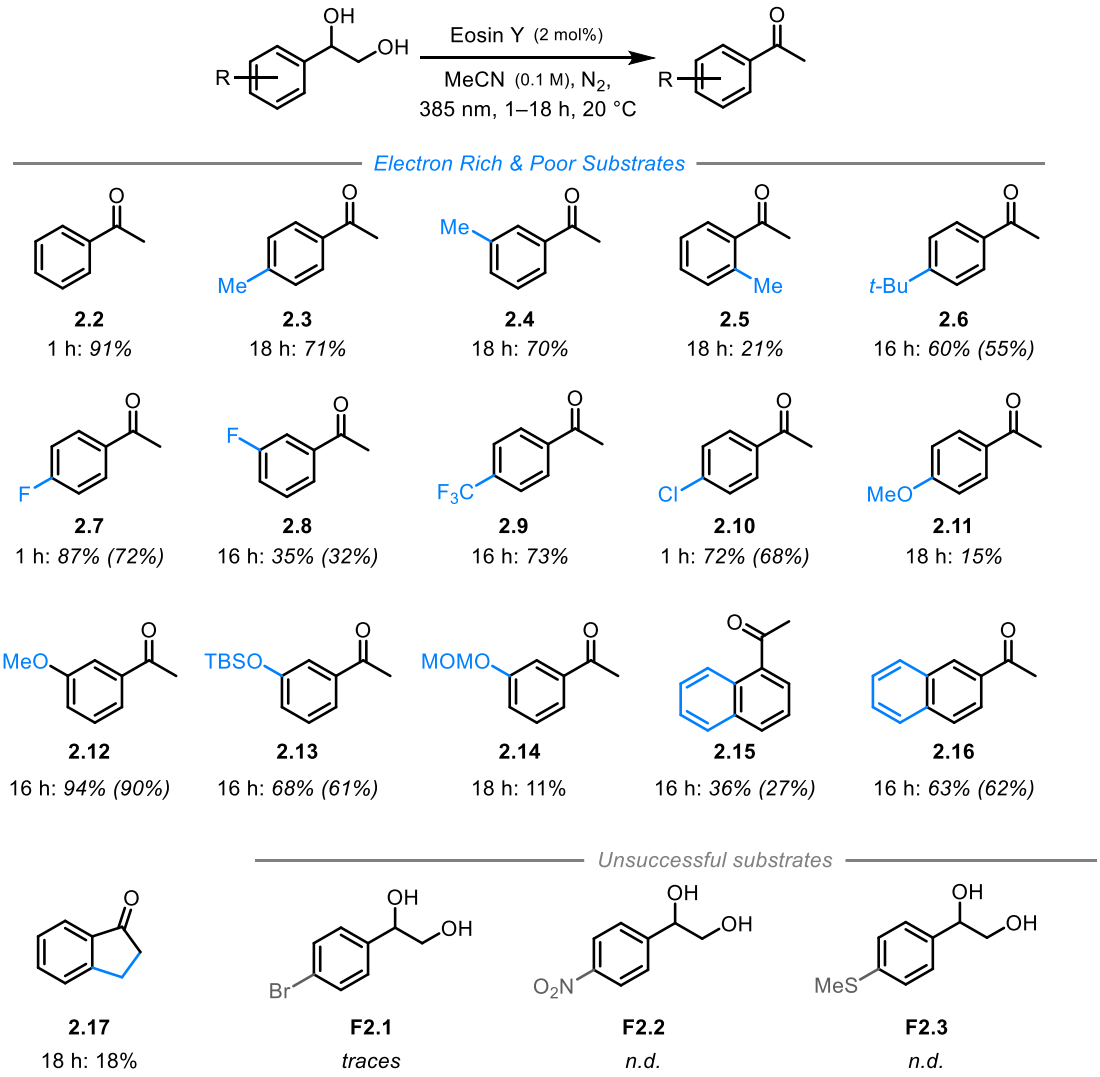

Scheme 2.3. Scope for the photocatalytic dehydration of diols. Yields reported as calibrated GC-FID yields, isolated yields in parenthesis.

Moving on to the naphthyl system, the sterically hindered 1-napthyl diol reacted to the corresponding acetophenone product **2.15** more sluggishly than its 2-napthyl counterpart **2.16**. Lastly, the importance of free rotation and antiperiplanar relationship between the leaving group and the benzylic radical were showcased by the thwarting of the reaction with substrate **2.17** where the leaving group is located on a secondary carbon (see also SI). Regarding limitations, the bromine-containing substrate **F2.1** decomposed under the reaction conditions, whereas cyano-, nitro- and sulfur-containing groups completely prevented the reaction progress (substrates **F2.2**, **F2.3** and SI).

2.3.3 Mechanistic studies

To gain a deeper understanding of our reaction, a set of mechanistic experiments were carried out. Our initial hypothesis was that the neutral Eosin Y, which has been well-established as a HAT catalyst, would possibly activate the leaving group while certainly initiating the SCS sequence.[1,8,26] However, we were puzzled by the identification of 385 nm LEDs as optimal irradiation source and the lack of reactivity with 420 nm and 520 nm irradiation (Table 2.1 and Table S2.4). Therefore, we started out by tracking down the light-absorbing species in our reaction mixture. When dissolved into acetonitrile, the main absorption band of the Eosin Y was found around 540 nm (Figure 2.1, a). As this absorption band has been further assigned to the monoanionic Eosin Y, our observation further demonstrates the dynamic, solvent-dependent acid-base equilibrium of this photocatalyst.[1,26] Although protonation of Eosin Y with Brønsted acids has been reported to enhance the HAT-activity of the catalyst, in our system, the addition of acetic acid, hydrochloric acid or sulfuric acid did not enable the conversion *trans*-cyclohexane-1,2-diol to cyclohexanone.[7] We found these results puzzling as they would indicate the absence of the neutral, HAT-active form of EY in our reaction mixture. Upon careful inspection, an additional absorption feature could be observed around 380 nm. This band was unambiguously identified to stem from Eosin Y (dark orange line), since the diol **2.1** did not show any absorbance above 300 nm (grey dotted line). However, the addition of **2.1** to a solution of Eosin Y resulted in small changes in the absorption spectrum below 320 nm and above 500 nm, thus indicating a possible hydrogen bonding and/or π-π-stacking interactions between these reactants.

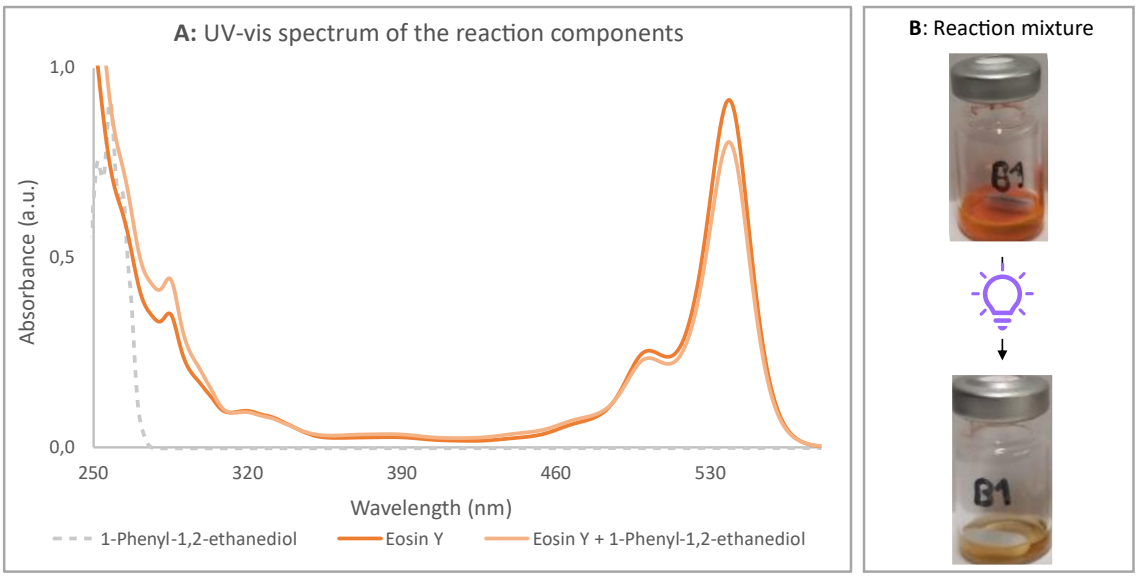

Figure 2.1 UV-vis spectrum of the reactants (a) and colour change during reaction (b).

To better characterize the observed colour change of the reaction mixture from bright pink to pale yellow under irradiation (Figure 2.1, b), an *ex-situ* UV-vis monitoring of the reaction was carried out. Herein, irradiation with a 385 nm LED resulted in a smooth decrease in the main absorption band at 520 nm, followed by the rise of a broad absorption band in the blue-light region (Scheme 2.4, a). Notably, the diol **2.1** had a significant impact on the rate of the spectral changes: a solution containing only Eosin Y retained its green-light absorption feature for almost 45 minutes, whereas in the presence of the diol, this band disappeared after just 10 minutes of irradiation. Although faster, these spectral changes are in good agreement with those observed by the group of Janssen during their study on the Eosin Y photodegradation under green laser irradiation.[3] Under a green-light LED, however, our spectral changes were significantly slower and without the diol **2.1**, no new absorption features could be observed (Scheme 2.4, b). These differences observed with irradiation sources might stem either from the higher energy and higher light intensity of the 385 nm LEDs and 520 nm laser as compared to 520 nm LEDs or, alternatively, hint towards excitation of an electron to a higher laying orbital when using a lower wavelength irradiation (anti-Kasha behaviour).[27] Further support of Eosin Y photolysis was obtained from HPLC-MS analysis of the reaction mixture which revealed the emergence of numerous compounds after a 10-minute irradiation period (Scheme 2.4, c). Based on the HRMS, most of these molecules could be categorized into a) debromination, b) dehydration, and c) radical adducts of Eosin Y. In this context, it is also worth mentioning that stirring Eosin Y at 60 °C in the dark did not result in any degradation even after prolonged periods of time, thus confirming the photochemical nature of this process.

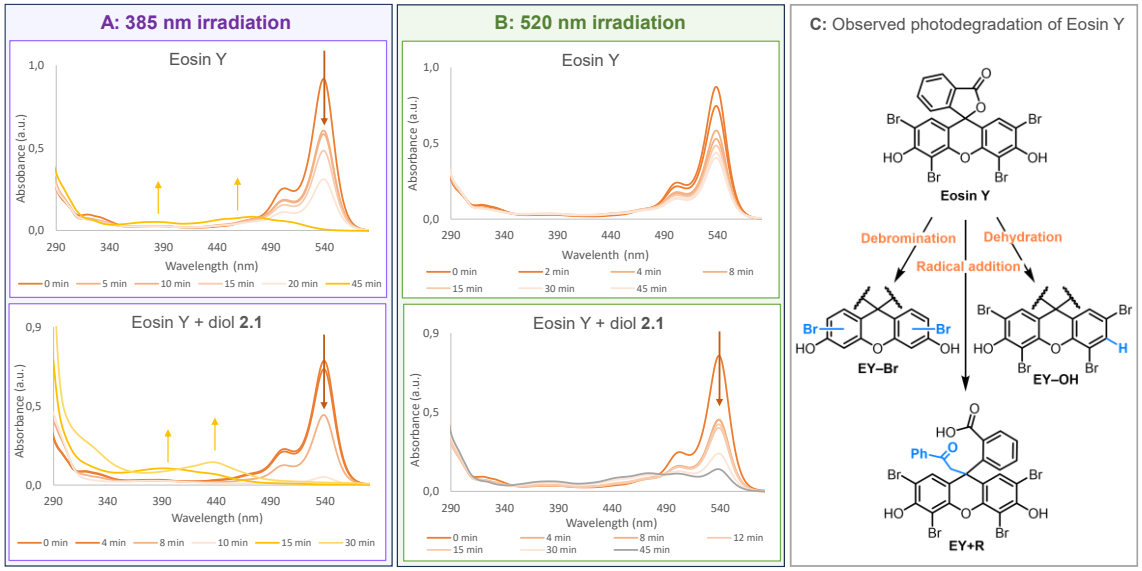

Scheme 2.4. *Ex-situ* irradiation of Eosin Y with and without the diol **2.1** with 385 nm (a), with 520 nm (b), and photodegradation products observed by HPLC-MS (c).

We then turned our attention to the product-forming events. The kinetic profile of the reaction was measured and was found to display a sigmoidal curve (Scheme 2.5, a). Furthermore, three different stages could be separated from this curve: the reaction starts with an induction period (stage I, 0–10 min), followed by rapid consumption of the substrate (stage II, 10–15 min) and ending with a prolonged period of continuous product formation (stage III, 15–60 min). Strikingly, when comparing the reaction kinetics with the UV-vis studies on Eosin Y degradation discussed above, the time frame for the induction period and photodissociation of the catalyst seem to perfectly align. This synchronism explains the unusual combination of Eosin Y with violet light: the reaction does not proceed *via* the triplet state of Eosin Y, but Eosin Y is rather a precatalyst whose photodissociation forms the actual catalytically active mixture. Interestingly, even though the photolysis of Eosin Y has been previously well characterized together with the establishment of the catalytic activity of other photocatalysts' decomposition products, to our knowledge, this is the first report detailing the synthetic utilization of Eosin Y degradation products.[3,28–30] Out of the previously discussed dissociation products, especially the bromine radicals are well known as HAT active species.[31,32] To test whether the bromine radicals could indeed catalyse our transformation, we set up control experiments using catalytic amounts of tetra-*n*-butylammonium bromide (TBABr) in combination with a photocatalyst capable of oxidizing the bromide anion into a bromine radical (Scheme 2.5, b).[31,32] Indeed, the combination of TBABr with an acridinium-derived photocatalyst gave the desired product **2.2** in a 36% yield, whereas the acridinium dye alone was not able to catalyse the

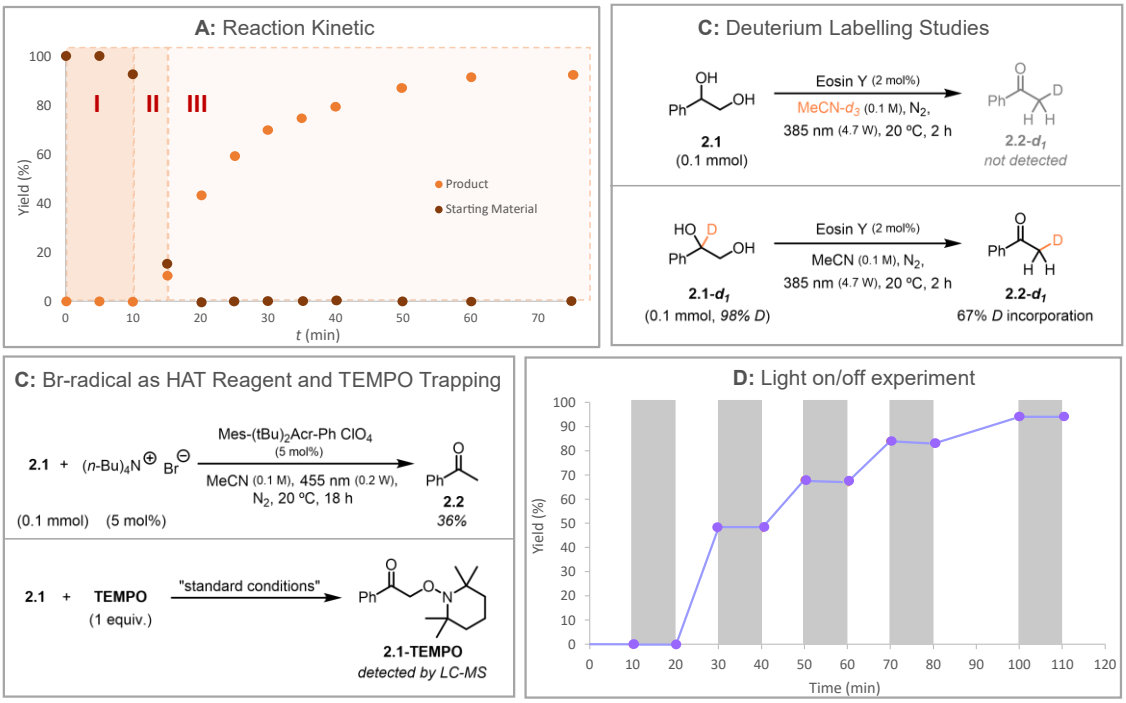

Scheme 2.5. Key mechanistic studies.

reaction. On one hand, this result confirms the feasibility of the bromine radical as the HAT catalyst, but on the other hand, it leaves room for the coexistence of other catalytically active species to reach the efficiency observed under the optimal reaction conditions. Finally, the autocatalytic mechanism was ruled out as the addition of acetophenone to the reaction mixture before irradiation was found to thwart the reaction (see Table S2.7).

Next, we investigated the processes taking place during the starting material conversion and the product formation phases (stages II + III of the kinetic curve). Although a clear discrepancy could be observed in the rates of these two events, no intermediates could be detected by GC-FID or ^{1}H-NMR analysis of the reaction progress (see Figure S2.8). However, a radical trapping experiment with TEMPO was able to identify the adduct stemming from the *alpha*-carbonyl radical (**2.2-TEMPO**) supporting the 1,2-spin center shift as a viable reaction pathway (Scheme 2.5, b). Further insights into the behaviour of this radical came from deuterium labelling experiments (Scheme 2.5, c). Running the reaction in deuterated acetonitrile did not result in any deuterium incorporation into the product, which indicates that the solvent does not play any active role in the reaction.[33] Interestingly, a high level of deuterium transfer between the benzylic position and the α-carbonyl position was observed, suggesting that the abstracted hydrogen (or deuterium) atom might end up in the terminal position of the product. This deuteration process could

occur either through a back deuterium atom transfer (bDAT) or, through a reductive radical polar crossover, followed by deuteration of the enolate intermediate. Importantly, the former mechanistic pathway, where the *alpha*-carbonyl radical is proposed to abstract a deuterium atom would imminently regenerate the original HAT active species, thus making the process a radical chain reaction. Although the free carbanions have been in turn described as superbasic intermediates able to deprotonate acetonitrile, in our reaction, the possibility for enolate formation would significantly reduce the basicity of these reduced species. Moreover, the performed light on/off experiment verified the necessity of continuous irradiation for the reaction, thus hinting against a radical chain mechanism as the main product-forming pathway (Scheme 2.5, d).

Based on our mechanistic studies and the previous literature on 1,2-spin center shift discussed above, the following reaction mechanism is proposed (Scheme 2.6). During the induction period of the reaction (stage I), the high energy irradiation forms a highly active catalytic mixture of Eosin Y derivatives **I** and their corresponding elimination products (such as bromine radicals). These HAT active species initiate the product-forming cycle (stages II and III) by abstracting a hydrogen atom from the aryl-1,2-diols **2.1** forming the benzylic radical **II**. This radical undergoes a rapid 1,2-spin center shift generating an α-

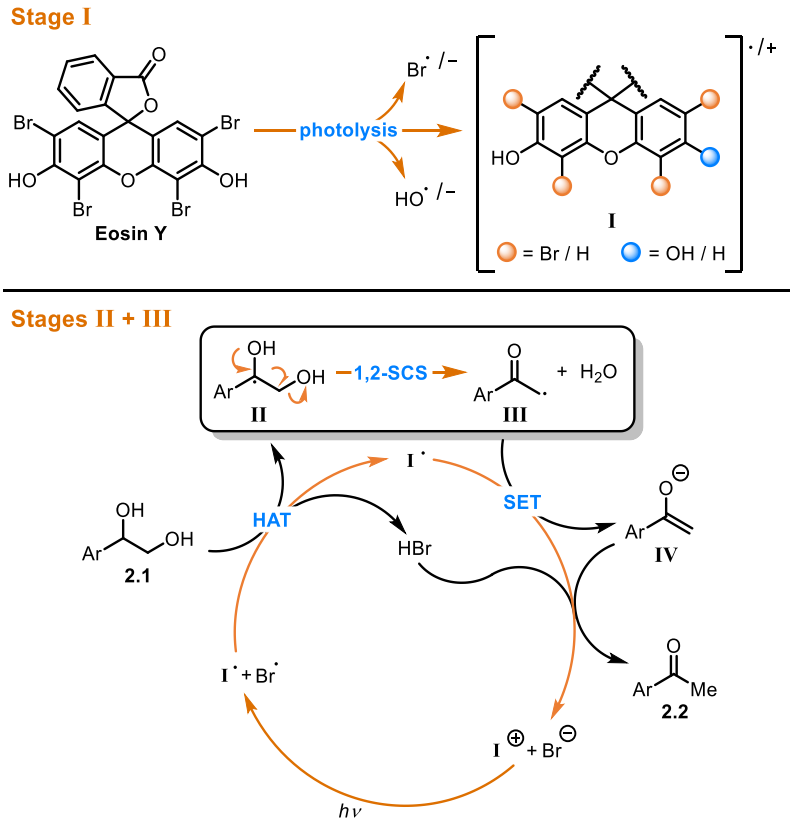

Scheme 2.6. Proposed reaction mechanism.

carbonyl radical **III** and releasing a molecule of water. The radical intermediate **III** is then reduced to the corresponding enolate **IV**, followed by protonation to product **2.2**, for example, by the initial hydrogen atom abstracting species. Although the final steps of the mechanism could not be fully ascertained, a photocatalytic regeneration step, such as a SET between $\mathbf{I}^{+}$ and Br^{-}, is needed to close the catalytic cycle.

2.4 Conclusions and Outlook

In summary, we have developed a protocol for the photocatalytic dehydration of aryl-1,2-diols to the corresponding methyl ketone derivatives. While our initial plan was to harness the dual catalytic nature of Eosin Y as a mild Brønsted acid and HAT catalyst, mechanistic studies indicated that the reaction is in fact driven by a highly active mixture of Eosin Y photodegradation products. Nevertheless, the efficiency of this mixture allowed us to carry out dehydration of the starting materials under simplified reaction conditions and without activating reagents or pre-functionalization steps. The product-forming cycle features a benzylic hydrogen atom abstraction followed by a 1,2-spin center shift, after which the carbonyl radical is reduced to its enolate form and is finally protonated. Considering the sensitivity of complex (bio)molecules and the conditions typically required in dehydration protocols, we hope that our contribution will inspire further development towards improved methods for elimination reactions.

2.5 Experimental

2.5.1 General Information

Chemicals and solvents: all commercially available chemicals were purchased in high quality and used without further purification. Solvents for column chromatography were distilled prior to use. Petrol ether is abbreviated as PE while ethyl acetate as EtOAc. Moisture and oxygen-sensitive reactions were carried out using dry solvents in oven-dried glassware under inert atmosphere of pre-dried nitrogen. The evaporation of solvents was carried out in a rotary evaporator at temperatures below 40 ºC, under reduced pressure. The water content of acetonitrile (245 ± 7 ppm water) used for photocatalyzed reactions was determined by Karl-Fischer titration.

Flash Column Chromatography (FCC): flash silica gel (Merck, 40-63 μm) was used as the stationary phase. Binary eluent mixtures are reported as v/v solutions normalized to 100 volume units. Purification by automated flash column chromatography was performed on a Biotage® IsoleraTM Spektra One device using either pre-packed Biotage® columns or silica gel 60 M (particle size 40–63 μm, 230–440 mesh, Merck) self-packed columns.

Analytical TLC: performed on silica gel pre-coated aluminium sheets (Machery-Nagel, silica gel 60 G/UV254, 0.2 mm). Visualization was accomplished by exposure to UV-light (254 nm). Eluent mixtures for TLC are reported as v/v solutions normalized to 100 volume units.

Nuclear magnetic resonance (NMR): spectra were recorded at room temperature using a Bruker Avance 400 (400 MHz for ^{1}H, 101 MHz for ^{13}C, 376 MHz for ^{19}F) NMR spectrometer. Chemical shifts are reported in δ-scale as parts per million [ppm] relative to the solvent residual peaks as internal standard. Coupling constants *J* are given in Hertz [Hz] and the multiplicity of the signals is abbreviated as: singlet (s), broad singlet (br. s), doublet (d), doublet of doublets (dd), triplet (t), doublet of triplets (dt), triplet of doublets (td), quadruplet (q), or multiplet (m). Signals are reported as follows: (multiplicity, coupling constant *J*, number of protons). Spectra were analyzed using MestReNova 6.0.2.

High Resolution Mass Spectrometry (HRMS): spectra were obtained from the central analytical mass spectrometry facilities of the Faculty of Chemistry and Pharmacy, University of Regensburg. All mass spectra were recorded on a Finnigan MAT 95, Thermo

Quest Finnigan TSQ 7000, Finnigan MATSSQ 710 A or an Agilent Q-TOF 6540 UHD instrument.

GC-FID and GC-MS: GC measurements were performed on a GC 7890 from Agilent Technologies. Data acquisition and evaluation was done with Agilent Chem Station Rev.C.01.04. GC–MS measurements were performed on a 7890A GC system from Agilent Technologies with an Agilent 5975 MSD Detector. Data acquisition and evaluation was done with MSD Chem Station E.02.02.1431. A capillary column HP-5MS/30 m x 0.25 mm/0.25 µM film and helium as carrier gas (flow rate of 1 mL/min) were used. The injector temperature (split injection: 40:1 split) was 280 ºC, detection temperature 300 ºC (FID). GC measurements were made and investigated via integration of the signal obtained. The GC oven temperature program was adjusted as follows: initial temperature 40 ºC was kept for 3 minutes, the temperature was increased at a rate of 15 ºC/min over a period of 16 minutes until 280 ºC was reached and kept for 5 minutes, the temperature was again increased at a rate of 25 ºC/min over a period of 48 seconds until the final temperature (300 ºC) was reached and kept for 5 minutes.

Photoreactor setup in batch: photoreactions were irradiated with LEDs (Engine LZ4-40UB00-00U5, λ = 385 nm (± 28), average radiant flux 4702 ± 70 mW, 90 V, 900 mA). Reaction mixtures were exposed to light under stirring (400 rpm, magnetic stirrer) from the bottom side of the vial. The temperature of the system was controlled by a water-cooling circuit consisting of an aluminium cooling block connected to a thermostat (Figure S2.1).

Figure S2.1. Photoreactor setup. A: Thermostat connected to the aluminium cooling block. B: Cooling block and LED on top of stirrer. C: LED module.

The optical power of the LEDs was determined using a FieldMaxII-TOTM laser power meter equipped with a PM3 sensor. The emission spectrum of the LEDs (Figure S2.2) was recorded using an Ocean Optics HR4000CG-UV-NIR Glass fibre and diffusor.

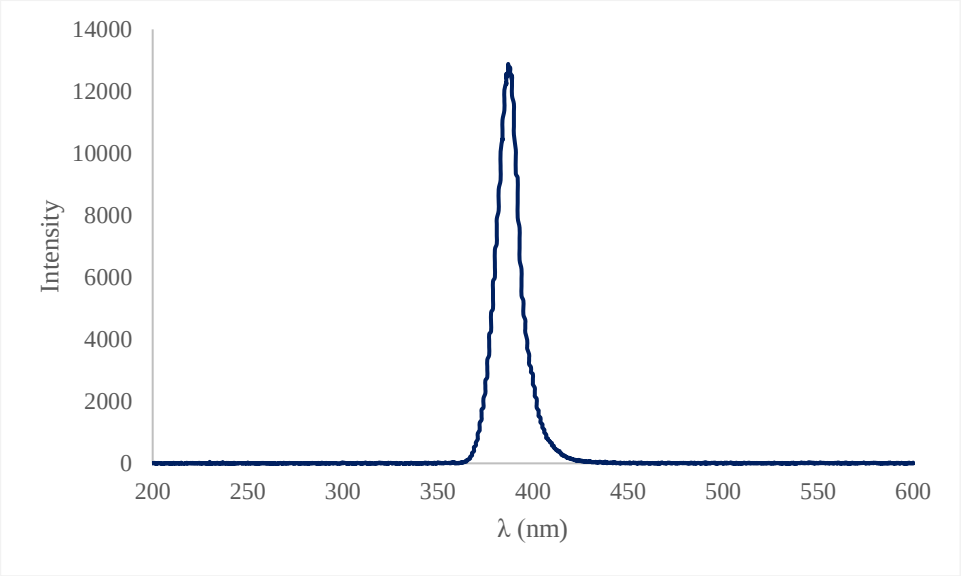

Figure S2.2. Led emission spectrum of the LED used for the photoreactions.

Glassware absorption: photoreactions were carried out in WICOM 20 mm crimp-cap vials (5 mL, 38.5 x 22.0 mm) made of borosilicate glass. The vials transmit 100% of incident light above 350 nm (Figure S2.3).

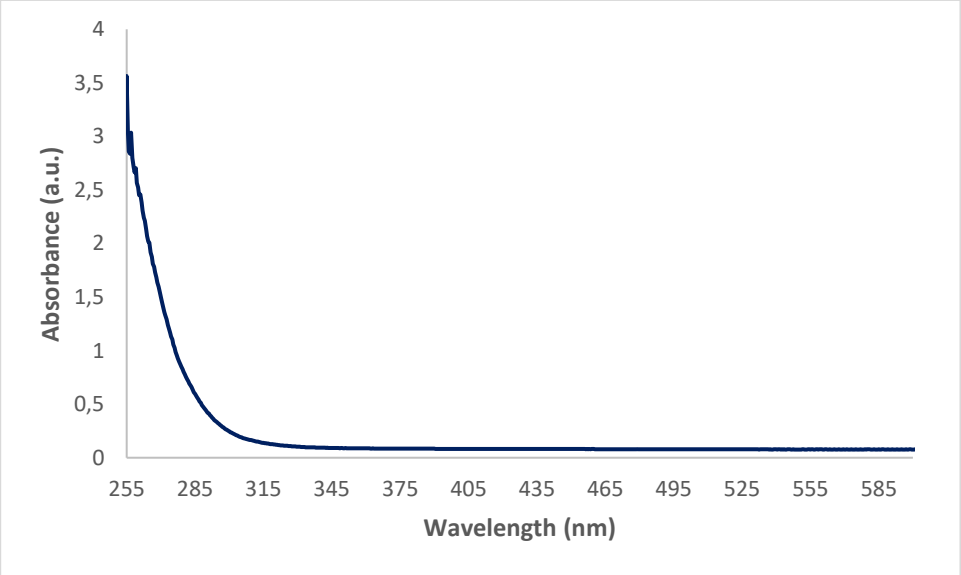

Figure S2.3. Absorption spectrum of vials used for photoreactions.

2.5.2 Photocatalytic dehydration of 1,2-diols

GP1: General Procedure for the photocatalytic dehydration reaction

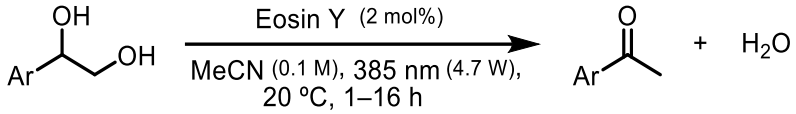

A 5 mL crimp-cap vial equipped with a Teflon-coated stirring bar, was loaded with the corresponding 1,2-ethanediol (0.1 mmol, 1.0 equiv.) and Eosin Y (1.4 mg, 2.0 µmol, 2 mol%). The vial was sealed, evacuated, and back filled with N_2 before adding MeCN (1 mL). Then, the resulting mixture was sonicated for 15 s, purged with N_2 for 5 min and subsequently stirred under irradiation using a 4.7 W 385 nm (± 25 nm) LED set-up for 1 to 18 hours at 20 °C (temperature controlled by a cryostat). Reaction progress was monitored by GC analysis. For the determination of the GC-FID yields, mesitylene (250 µL of 0.4 M stock solution) was added to the crude reaction mixtures, which were then filtered through a syringe filter before subjecting to GC-FID analysis. Final GC-FID yields were calculated with a five-point calibration curve made with each product.

For isolation, two to four identical vials (see exact details from section 2.5.2.2) were set parallel according to the **GP1**. After completion, the vials were combined, and major impurities were removed by filtering the mixture through a short silica plug using DCM as eluent. The volume of the crude was then carefully reduced to around 10 mL, which was then subjected to flash column chromatography using a mixture of Et_2O/PE as eluent. Careful solvent evaporation yielded the desired products.

2.5.2.1 Full Optimization Studies

All optimization studies were carried out using the conditions described in **GP1** as standard conditions, changes to these conditions are given in each table. The yields reported are calculated from a five-point GC-FID calibration curve of acetophenone using mesitylene (250 μL of 0.4 M stock solution) as internal standard.

Optimization of Photocatalyst

Table S2.1. Full optimization of photocatalyst.

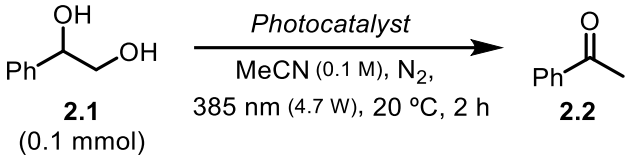

Entry	Photocatalyst	Yield (%)
1	$FeCl_3$ (20 mol%) + TBACl (20 mol%)	11
2	$BiCl_3$ (20 mol%) + TBACl (40 mol%)	32
3	$BiBr_3$ (20 mol%) + TBABr (40 mol%)	46
4	Eosin Y (2 mol%)	91
5	Eosin Y (1 mol%)	79
6	Eosin Y (5 mol%)	87
7	Eosin Y disodium salt (2 mol%)	0
8	Eosin B (2 mol%)	0
9	Eosin B disodium salt (2 mol%)	0
10	Fluorescein (2 mol%)	0
11	Fluorescein Na-salt (2 mol%)	0
12	Thioxanthone (5 mol%)	*traces*
13	Benzophenone (5 mol%)	*traces*
14	TBADT (2 mol%)	*traces*
15	Xanthone (5 mol%)	0
16	4-Methoxyacetophenone (5 mol%)	0

Yields determined with calibrated GC-FID using mesitylene as internal standard.
TBACl = Tetrabutylammonium chloride, TBABr = Tetrabutylammonium bromide, TBADT = Tetrabutylammonium decatungstate.

Optimization of Catalyst Loading

Table S2.2. Optimization of Eosin Y loading.

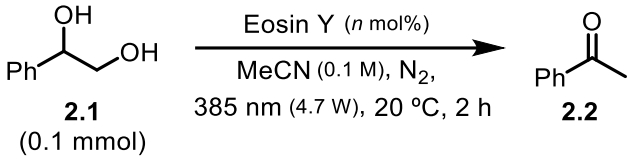

Entry	Eosin Y (mol%)	Yield (%)
1	0.2	0
2	0.5	23
3	1.0	42
4	2.0	89
5	3.0	89
6	4.0	87

Yields determined with calibrated GC-FID using mesitylene as internal standard.

Optimization of Solvent

Table S2.3. Full optimization of solvent.

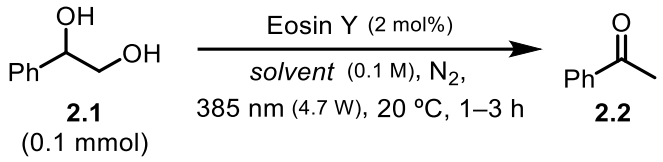

Entry	Solvent (1 mL, 0.1 mM)	Time (h)	Yield (%)
1	MeCN	1	89
2	EtOAc	1	22
3	EtOAc	3	73
4	Acetone	1	*traces*
5	DMSO	1	0
6	DMF	1	0
7	DMA	1	0
8	DCM	1	46
10	$CHCl_3$	1	12
11	MeOH	1	0

Yields determined with calibrated GC-FID using mesitylene as internal standard.

Optimization of Irradiation Wavelength

Table S2.4. Optimization of irradiation wavelength.

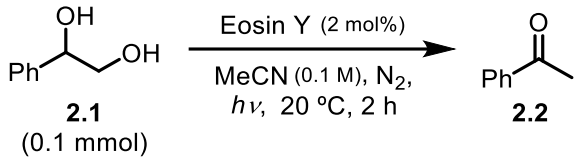

Entry	Light source (LEDs)	Yield (%)
1	365 nm	*traces*
2	385 nm (4.7 W)	79
3	420 nm (0.6 W)	2
4	520 nm	n.r.

Yields determined with calibrated GC-FID using mesitylene as internal standard.

Optimization of Reaction Time and Concentration

Table S2.5. Optimization of reaction time and concentration.

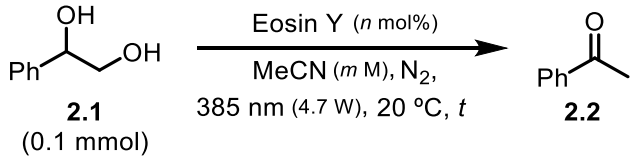

Entry	c (M)	Eosin Y (mol%)	*t* (min)	Yield (%)
1	0.1	1	15	3
2	0.1	2	60	89
3	0.1	2	70	91
4	0.1	4	90	89
5	0.1	3	120	92
6	0.15	2	120	78
7	0.20	2	120	73

Yields determined with calibrated GC-FID using mesitylene as internal standard.

Control Experiments

Table S2.6. Control experiments

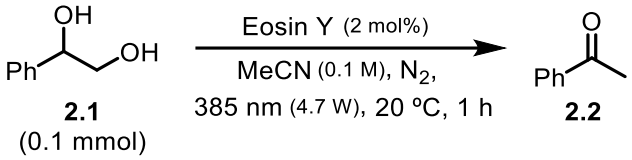

Entry	Deviation from standard	Yield (%)
1	none	89
2	no light	0
3	no Eosin Y	0
4	under air	*traces*
5	with TEMPO	*traces*

Yields determined with calibrated GC using mesitylene as internal standard.

2.5.2.2 Details and Characterization of Products

Synthesis of acetophenone (2.2)

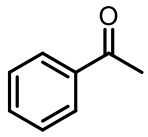

2.2

Prepared according to **GP1** from 1-phenylethane-1,2-diol (13.8 mg, 0.10 mmol, 1.00 equiv.), reaction time 1 h. Calibrated GC-FID yield 91%.

Synthesis of 1-(*p*-tolyl)ethan-1-one (2.3)

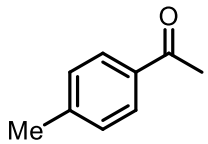

2.3

Prepared according to **GP1** from 1-((*p*-tolyl)ethane)-1,2-diol (15.2 mg, 0.10 mmol, 1.00 equiv.), reaction time 18 h. Calibrated GC-FID yield 71%.

Synthesis of 1-(*m*-tolyl)ethan-1-one (2.4)

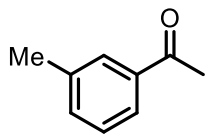

2.4

Prepared according to **GP1** from 1-(*m*-tolyl)ethane)-1,2-diol (15.2 mg, 0.10 mmol, 1.00 equiv.), reaction time 18 h. Calibrated GC-FID yield 70%.

Synthesis of 1-(*o*-tolyl)ethan-1-one (2.5)

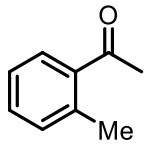

2.5

Prepared according to **GP1** from 1-(*o*-tolyl)ethane)-1,2-diol (15.2 mg, 0.10 mmol, 1.00 equiv.), reaction time 18 h. Calibrated GC-FID yield 21%.

Synthesis of 1-(4-(*tert*-butyl)phenyl)ethan-1-one (2.6)

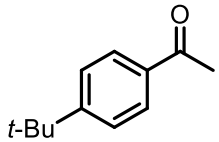

2.6

Prepared according to **GP1** from 1-(4-(*tert*-butyl)phenyl)ethane-1,2-diol (58.3 mg, 0.30 mmol, 1.00 equiv.), reaction time 18 h. After the silica plug and evaporation, the crude was purified with flash column chromatography with flash column chromatography (5 % Et_2O/PE) giving the title compound as a pale oil. Calibrated GC-FID yield 60%, isolated yield 29 mg, 55%.

$\mathbf{R}_f$ = 0.55 (PE/Et_2O = 90/10), UV

^{1}H-NMR (400 MHz, $CDCl_3$): δ (ppm) = 7.84–7.80 (m, 2H), 7.41–7.38 (m, 2H), 2.50 (s, 3H), 1.26 (s, 9H);

^{13}C-NMR (101 MHz, $CDCl_3$): δ (ppm) = 197.6, 156.8, 134.6, 128.3, 125.5, 35.1, 31.1, 26.6;

HRMS (EI+): calc. [$M^{\cdot+}$] for $[C_{12}H_{18}O_2]^{\cdot+}$ 176.11957, found 176.11966, Δ = – 0.09 mDa.

Synthesis of 1-(4-fluorophenyl)ethan-1-one (2.7)

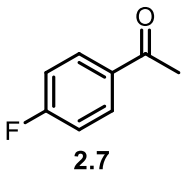

2.7

Prepared according to **GP1** from 1-(4-fluorophenyl)ethane)-1,2-diol (62.5 mg, 0.40 mmol, 1.00 equiv.), reaction time 16 h. The crude was purified with flash column chromatography (10% Et_2O/PE) to give the title compound as a pale oil. Calibrated GC-FID yield 87%, isolated yield 30 mg, 72%.

R_f = 0.59 (PE/Et_2O = 90/10), UV

^{1}H-NMR (400 MHz, $CDCl_3$): δ (ppm) = 8.01–7.95 (m, 2H), 7.16–7.10 (m, 2H), 2.59 (s, 3H);

^{13}C-NMR (101 MHz, $CDCl_3$): δ (ppm) = 196.5, 165.7 (d, *J* = 255 Hz), 133.6 (d, *J* = 3.0 Hz), 130.9 (d, *J* = 9.4 Hz), 115.6 (d, *J* = 21.9 Hz), 26.5;

^{19}F-NMR (376 MHz, $CDCl_3$, $PhCF_3$ as internal standard): δ (ppm) = –106.3 – (–)106.4 (m)

HRMS (APCI+): calc. [M^{+}] for $[C_8H_7FO+H]^{+}$ 139.0559, found 139.0553, Δ = 0.6 mDa.

Synthesis of 1-(3-fluorophenyl)ethan-1-one (2.8)

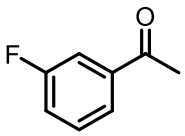

2.8

Prepared according to **GP1** from 1-(3-fluorophenyl)ethane)-1,2-diol (62.5 mg, 0.40 mmol, 1.00 equiv.), reaction time 16 h. The crude was purified with flash column chromatography (10% Et_2O/PE) to give the title compound as a pale oil. Calibrated GC-FID yield 35%, isolated yield 18 mg, 32%.

R_f = 0.45 (PE/Et_2O = 90/10), UV

^{1}H-NMR (400 MHz, $CDCl_3$): δ (ppm) = 7.72 (ddd, *J* = 7.8, 1.6, 0.9 Hz, 1H), 7.62 (ddd, *J* = 9.5, 2.6, 1.6 Hz, 1H), 7.43 (app. dt, *J* = 8.2, 5.5 Hz, 1H), 7.25 (dtd, *J* = 8.2, 2.6, 0.9 Hz, 1H), 2.58 (s, 3H);

^{13}C-NMR (101 MHz, $CDCl_3$): δ (ppm) = 196.8 (d, *J* = 2.1 Hz), 162.7 (d, *J* = 248.0 Hz) 139.2 (d, *J* = 6.1 Hz), 130.3 (d, *J* = 7.6 Hz), 124.1 (d, *J* = 3.0 Hz), 120.1 (d, *J* = 21.5 Hz), 114.9 (d, *J* = 22.2 Hz), 26.7;

^{19}F-NMR (376 MHz, $CDCl_3$, $PhCF_3$ as internal standard): δ (ppm) = −112.93 – (–)113.01 (m)

HRMS (EI+): calc. [$M^{\cdot+}$] for $[C_8H_7FO]^{\cdot+}$ 138.04754, found 138.04756, Δ = 0.02 mDa.

Synthesis of 1-(4-(trifluoromethyl)phenyl)ethan-1-one (2.9)

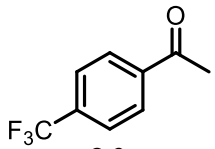

2.9

Prepared according to **GP1** from 1-(4-(trifluoromethyl)phenyl)ethane-1,2-diol (20.6 mg, 0.10 mmol, 1.00 equiv.), reaction time 16 h. Calibrated GC-FID yield 73%.

Synthesis of 1-(4-chlorophenyl)ethan-1-one (2.10)

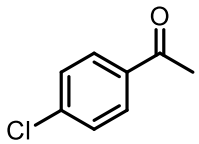

2.10

Prepared according to **GP1** from 1-(4-chlorophenyl)ethane-1,2-diol (34.5 mg, 0.20 mmol, 1.00 equiv.), reaction time 1 h. The crude was purified with flash column chromatography (10% Et_2O/PE) giving the title compound as a pale-yellow oil. Calibrated GC-FID yield 72%, isolated yield 21 mg, 68%.

R_f = 0.41 (PE/Et_2O = 90/10), UV

^{1}H-NMR (400 MHz, $CDCl_3$): δ (ppm) = 7.85–7.81 (m, 2H), 7.39–7.35 (m, 2H), 2.52 (s, 3H);

^{13}C-NMR (101 MHz, $CDCl_3$): δ (ppm) = 196.8, 139.6, 135.4, 129.7, 128.9, 26.6;

HRMS (EI+): calc. [$M^{\cdot+}$] for $[C_8H_7OCl]^{\cdot+}$ 154.01799, found 154.01789, Δ = 0.1 mDa.

Synthesis of 1-(4-methoxyphenyl)ethan-1-one (2.11)

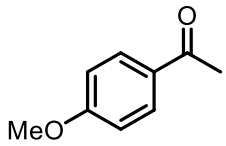

2.11

Prepared according to **GP1** from 1-(4-methoxyphenyl)ethane)-1,2-diol (16.8 mg, 0.10 mmol, 1.00 equiv.), reaction time 18 h. Calibrated GC-FID yield 15%.

Synthesis of 1-(3-methoxyphenyl)ethan-1-one (2.12)

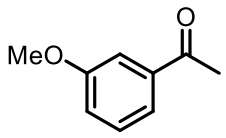

2.12

Prepared according to **GP1** from 1-(3-methoxyphenyl)ethane)-1,2-diol (67.3 mg, 0.40 mmol, 1.00 equiv.), reaction time 16 h. The crude was purified with flash column chromatography (15% Et_2O/DCM) giving the title compound as a pale-yellow oil. Calibrated GC-FID yield 94%, isolated yield 54 mg, 90%.

R_f = 0.46 (PE/Et_2O = 90/10), UV

^{1}H-NMR (400 MHz, $CDCl_3$): δ (ppm) = 7.52 (ddd, *J* = 7.6, 1.7, 1.0 Hz, 1H), 7.47 (dd, *J* = 2.8, 1.7 Hz, 1H), 7.35 (t, *J* = 8.2 Hz, 1H), 7.09 (ddd, *J* = 8.2, 2.8, 1.0 Hz, 1H), 3.84 (s, 3H), 2.58 (s, 3H);

^{13}C-NMR (101 MHz, $CDCl_3$): δ (ppm) = 196.9, 158.8, 137.5, 128.5, 120.1, 118.6, 111.3, 54.4, 25.7;

HRMS (EI+): calc. [$M^{\cdot+}$] for $[C_9H_{12}O_2]^{\cdot+}$ 150.06753, found 150.06714, Δ = 0.39 mDa.

Synthesis of 1-(3-((*tert*-butyldimethylsilyl)oxy)phenyl)ethan-1-one (2.13)

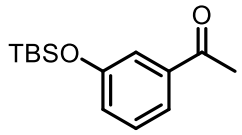

2.13

Prepared according to **GP1** from 1-(3-((*tert*-butyldimethylsilyl)oxy)phenyl) ethan-1,2-diol (80.5 mg, 0.30 mmol, 1.00 equiv.), reaction. The crude was purified with flash column chromatography (10% Et_2O/PE) giving the title compound as a pale-yellow oil. Calibrated GC-FID yield 68%, isolated yield 46 mg, 61%.

R_f = 0.40 (Et_2O/PE, 10%), UV

^{1}H-NMR (400 MHz, $CDCl_3$): δ (ppm) = 7.54 (ddd, *J* = 7.7, 1.8, 1.0 Hz, 1H), 7.42 (dd, *J* = 2.6, 1.8 Hz, 1H), 7.31 (t, *J* = 8.0 Hz, 1H), 7.04 (ddd, *J* = 8.0, 2.6, 1.0 Hz, 1H), 2.57 (s, 3H), 0.99 (s, 9H), 0.21 (s, 6H);

^{13}C-NMR (101 MHz, $CDCl_3$): δ (ppm) = 197.8, 156.0, 138.6, 129.5, 124.9, 121.6, 119.5, 26.7, 25.6, 18.2, – 4.4;

HRMS (APCI+): calc. $[M+H]^+$ for $[C_{14}H_{22}O_2Si+H]^+$ 251.1467, found 251.1464, Δ = 0.3 mDa.

Synthesis of 1-(3-(methoxymethoxy)phenyl)ethan-1-one (2.14)

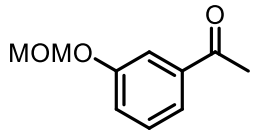

2.14

Prepared according to **GP1** from 1-(3-(methoxymethoxy)phenyl) ethane-1,2-diol (18.1 mg, 0.10 mmol, 1.00 equiv.) reaction time 18 h. Calibrated GC-FID yield 11%.

Synthesis of 1-(naphthalen-1-yl)ethan-1-one (2.15)

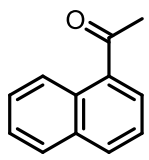

2.15

Prepared according to **GP1** from 1-(naphthalen-1-yl)ethane)-1,2-diol (56.5 mg, 0.30 mmol, 1.00 equiv.), reaction time 16 h. After the silica plug and evaporation, the crude was purified with flash column chromatography (10% Et_2O/PE) giving the title compound as brownish oil. Calibrated GC-FID yield 36%, isolated yield 14 mg, 27%.

R_f = 0.44 (PE/Et_2O = 90/10), UV

^{1}H-NMR (400 MHz, $CDCl_3$): δ (ppm) = 8.75 (dd, *J* = 8.7, 0.5 Hz, 1H), 8.02–7.87 (m, 4H), 7.63–7.49 (m, 4H), 2.76 (s, 3H);

^{13}C-NMR (101 MHz, $CDCl_3$): δ (ppm) = 201.9, 135.5, 134.0, 133.0, 130.2, 128.7, 128.4, 128.1, 126.5, 126.0, 124.3, 29.7;

HRMS (EI+): calc. [$M^{\cdot+}$] for [$C_9H_{12}O_2$]$^{\cdot+}$ 170.07262, found 170.07228, Δ = 0.33 mDa.

Synthesis of 1-(naphthalen-2-yl)ethan-1-one (2.16)

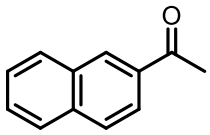

2.16

Prepared according to **GP1** from 1-(naphthalen-2-yl)ethane)-1,2-diol (37.6 mg, 0.20 mmol, 1.00 equiv.), reaction time 16 h. The crude was purified with flash column chromatography (10% Et_2O/PE) giving the title compound as a pale solid. Calibrated GC-FID yield 63%, isolated yield 21 mg, 62%.

R_f = 0.38 (PE/Et_2O = 90/10), UV

^{1}H-NMR (400 MHz, $CDCl_3$): δ (ppm) = 8.47 (br. s., 1H), 8.04 (dd, *J* = 8.7, 1.8 Hz, 1H), 7.97 (d, *J* = 8.1 Hz, 1H), 7.91–7.87 (m, 2H), 7.63–7.59 (m, 1H), 7.58–7.54 (m, 1H), 2.73 (s, 3H);

^{13}C-NMR (101 MHz, $CDCl_3$): δ (ppm) = 198.1, 135.6, 134.5, 132.5, 130.2, 129.6, 128.5, 128.4, 127.8, 126.8, 123.9, 26.7;

HRMS (EI+): calc. [$M^{\cdot+}$] for [$C_{12}H_{10}O$]$^{\cdot+}$ 170.07262, found 170.07221, Δ = 0.41 mDa.

Synthesis of 2,3-dihydro-1*H*-inden-1-one (2.17)

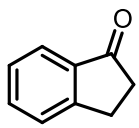

2.17

Prepared according to **GP1** from a commercially available 2,3-dihydro-1*H*-inden-1,2-diol (15.0 mg, 0.10 mmol, 1.00 equiv.) reaction time 18 h. Calibrated GC-FID yield 18%.

3.5.3 List of Unsuccessful Substrates

With respect to the limitations of the current method, certain functional groups were found to be incompatible (Figure S2.4).

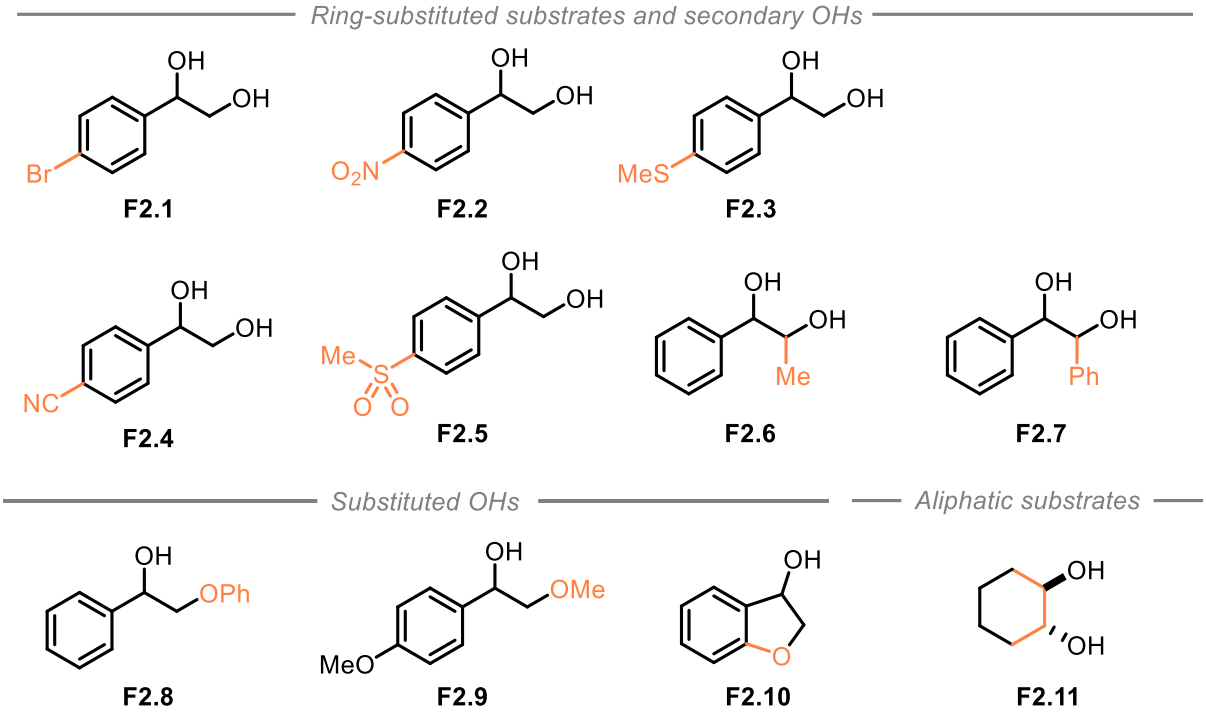

Figure 2.4. Unsuccessful substrates.

Firstly, brominated starting materials (such as **F2.1**) underwent debrominative degradation, leading to a complex mixture of products. On the other hand, nitro-(**F2.2**) and cyano-(**F2.4**) substituents and sulfur-containing functional groups (as in **F2.3** and **F2.5**) fully hindered the conversion of starting material. Furthermore, steric hindrance around the leaving group, as demonstrated with **F2.6** and **F2.7** seemed to thwart the transformation. In stark contrast to many previously reported methods, a hydroxy group was found to be the best-performing leaving group whereas phenoxy (**F2.8**), methoxy (**F2.9**) and phenolic (**F2.10**) containing substrates were mostly unreactive under our reaction conditions. Finally, aliphatic substrates (such as commercially available **F2.11**) could not be engaged to the transformation most likely due to the stronger aliphatic α-oxygen C–H bond.

2.5.4 Synthesis and Characterization of Starting Materials

The model compound **2.1** was commercially purchased and used without further purification. Other diols were synthetized according to the following procedures.

Synthesis of diols *via* alkene oxidation (GP2)

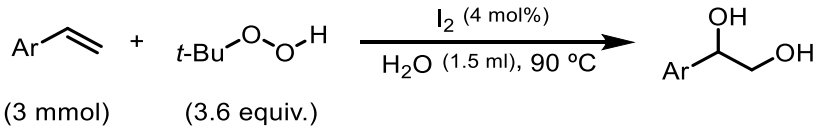

According to a procedure of Liu *et al.*[34]; the styrene derivative (3.0 mmol, 1.0 equiv.), I_2 (30 mg, 16 µmol, 4 mol%), distilled water (1.5 mL) and *tert*-butylhydroperoxide (70% solution in H_2O, 1.5 mL, 10.8 mmol, 3.6 equiv.) were added to a 15 ml crimp-cap vial. The vial was sealed, and the reaction mixture was heated at 90 ºC for 24 h. The reaction was quenched with a 2 M $Na_2S_2O_3$ (4 mL) and the product was extracted with EtOAc (5 x 10 mL). The combined organic layers were dried over $MgSO_4$, and the solvent was removed under reduced pressure. The crude product was purified by flash column chromatography using PE/Acetone as eluent.

Synthesis of diols *via* oxidation of acetophenones (GP3)

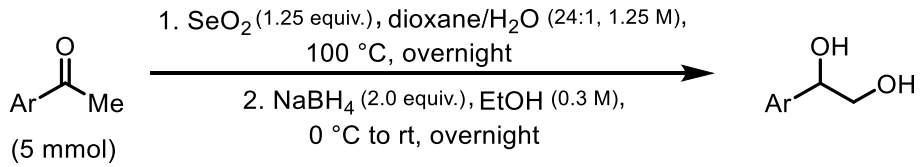

According to a detailed literature procedure by Rygus and Hall[35]: SeO_2 (1.25 equiv.) was suspended into a mixture of 1,4-dioxane and water (24:1, 1.25 M), and warmed to 55 °C until fully dissolved. The mixture was then cooled to room temperature, the acetophenone derivative (5 mmol, 1.0 equiv.) was added and the reaction was heated at reflux (100 °C) overnight. Dark (often green) colored reaction mixture with black precipitate at the bottom often indicated a successful oxidation. After cooling to ambient temperature, the mixture was filtered and concentrated under reduced pressure. The crude was then pressed through a silica plug with EtOAc/PE (1:1) and evaporated. The crude product was then dissolved in EtOH (0.3 M) and cooled to 0 °C. $NaBH_4$ (2.0 equiv.) was added portionwise, and the reaction was stirred overnight while allowing to warm to rt. The reaction was quenched with 2M HCl (or sat. NH_4Cl for acid sensitive substrates), ethanol was removed under reduced pressure and the remaining aqueous mixture was extracted with EtOAc (×3). After drying with $MgSO_4$, the mixture was filtered, and the solvent evaporated. Purification with flash column chromatography (PE/Acetone) yielded the final products.

CAUTION: Selenium-containing waste (solids, filterpaper etc.) need to be disposed carefully!

2.5.4.1 Synthetized successful diols

Synthesis of 1-(*p*-tolyl)ethane-1,2-diol (2.18)

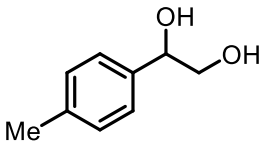

2.18

Prepared according to **GP2** from 1-methyl-4-vinylbenzene (350 µL, 2.5 mmol, 1.0 equiv.). The crude product was purified with flash column chromatography (PE/Acetone = 70/30), giving the title compound as a white solid (204 mg, 60%).

R_f = 0.26 (PE/Acetone = 70/30) [phosphomolybdic acid];

^{1}H-NMR (400 MHz, $CDCl_3$): δ (ppm) = 7.25 (d, *J* = 7.9 Hz, 2H), 7.17 (d, *J* = 7.9 Hz, 2H), 4.78 (dd, *J* = 8.1, 3.6 Hz, 1H), 3.72 (dd, *J* = 11.5, 3.6 Hz, 1H), 3.64 (dd, *J* = 11.5, 8.1 Hz, 1H), 2.63 (br. s., 2H), 2.34 (s, 3H);

^{13}C-NMR (101 MHz, $CDCl_3$): δ (ppm) = 137.8, 137.5, 129.3, 126.0, 74.6, 68.1, 21.1;

HRMS (EI+): calc. [$M^{\cdot+}$] for $[C_9H_{12}O_2]^{\cdot+}$ 152.08318, found 152.08343, Δ = **–** 0.25 mDa.

Synthesis of 1-(*m*-tolyl)ethane-1,2-diol (2.19)

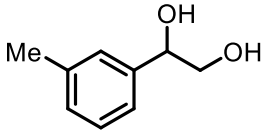

2.19

Prepared according to **GP3** from 1-(*m*-tolyl)ethan-1-one (1.3 g, 10 mmol, 1.0 equiv.). The crude product was purified with flash column chromatography (PE/Acetone 60/40), giving the title compound as a white solid (668 mg, 44%).

R_f = 0.47 (PE/Acetone = 60/40) [phosphomolybdic acid];

^{1}H-NMR (400 MHz, $CDCl_3$): δ (ppm) = 7.23 (d, *J* = 7.6 Hz, 1H), 7.17**–**7.09 (m, 3H), 4.77 (dd, *J* = 8.2, 2.5 Hz, 1H), 3.72 (dd, *J* = 11.4, 2.5 Hz, 1H), 3.64 (dd, *J* = 11.4, 8.2 Hz, 1H), 2.97**–**2.70 (br. s., 2H), 2.35 (s, 3H);

^{13}C-NMR (101 MHz, $CDCl_3$): δ (ppm) = 140.4, 138.2, 128.7, 128.4, 126.7, 123.1, 74.7, 68.1, 21.4;

HRMS (EI+): calc. [$M^{\cdot+}$] for $[C_9H_{12}O_2]^{\cdot+}$ 152.08318, found 152.08282, Δ = 0.34 mDa.

Synthesis of 1-(*o*-tolyl)ethane-1,2-diol (2.20)

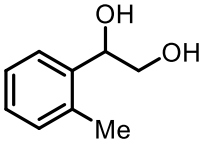

2.20

Prepared according to **GP3** from 1-(*o*-tolyl)ethan-1-one (1.3 g, 10 mmol, 1.0 equiv.). The crude product was purified with flash column chromatography (PE/Acetone 70/30), giving the title compound as a colorless oil (624 mg, 41%).

R_f = 0.48 (PE/Acetone = 60/40) [phosphomolybdic acid];

^{1}H-NMR (400 MHz, $CDCl_3$): δ (ppm) = 7.49 (dd, *J* = 7.4,1.2 Hz, 1H), 7.25–7.13 (m, 3H), 5.06 (dd, *J* = 8.4, 3.0 Hz, 1H), 3.73 (dd, *J* = 11.4, 3.0 Hz, 1H), 3.62 (dd, *J* = 11.4, 8.4, 1H), 2.35 (s, 3H), 2.29 (br.s., 2H);

^{13}C-NMR (101 MHz, $CDCl_3$): δ (ppm) = 138.4, 134.7, 130.5, 127.8, 126.3, 125.7, 71.4, 66.9, 19.0;

HRMS (EI+): calc. [$M^{\cdot+}$] for $[C_9H_{12}O_2]^{\cdot+}$ 152.08318, found 152.08315, Δ = 0.03 mDa.

Synthesis of 1-(4-(*tert*-butyl)phenyl)ethane-1,2-diol (2.21)

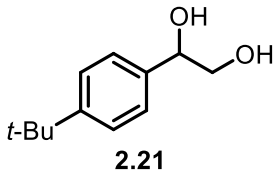

2.21

Prepared according to **GP2** from 1-(*tert*-butyl)-4-vinylbenzene (690 µL, 5.0 mmol, 1.0 equiv.). The crude product was purified with flash column chromatography (PE/Acetone = 60/40) giving the title compound as an off-white solid (702 mg, 72%).

R_f = 0.28 (PE/Acetone = 70/30) [phosphomolybdic acid];

^{1}H-NMR (400 MHz, $CDCl_3$): δ (ppm) = 7.41–7.38 (m, 2H), 7.32–7.29 (m, 2H), 4.81 (dd, *J* = 8.0, 3.5 Hz, 1H), 3.77 (dd, *J* = 11.3, 3.5 Hz, 1H), 3.69 (dd, *J* = 11.3, 8.0 Hz, 1H), 2.30 (br. s., 2H), 1.32 (s, 9H);

^{13}C-NMR (101 MHz, $CDCl_3$): δ (ppm) = 151.1, 137.5, 125.8, 125.5, 74.5, 68.0, 34.6, 31.3;

HRMS (EI+): calc. [$M^{\cdot+}$] for $[C_{12}H_{18}O_2]^{\cdot+}$ 194.13013, found 194.13046, Δ = – 0.33 mDa.

Synthesis of 1-(4-fluorophenyl)ethane-1,2-diol (2.22)

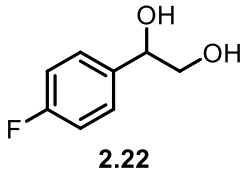

2.22

Prepared according to **GP2** from 1-fluoro-4-vinylbenzene (600 µL, 5.0 mmol, 1.0 equiv.). The crude product was purified with flash column chromatography (PE/Acetone 70/30), giving the title compound as a white solid (548 mg, 70%).

R_f = 0.30 (PE/EtOAc = 80/20) [phosphomolybdic acid];

^{1}H-NMR (400 MHz, $CDCl_3$): δ (ppm) = 7.37–7.31 (m, 2H), 7.08–7.01 (m, 2H), 4.81 (dd, *J* = 8.2, 3.1 Hz, 1H), 3.75 (dd, *J* = 11.3, 3.1 Hz, 1H), 3.63 (dd, *J* = 11.3, 8.2 Hz, 1H), 2.50 (br. s., 2H);

^{13}C-NMR (101 MHz, $CDCl_3$): δ (ppm) = 162.5 (d, *J* = 247 Hz), 136.1 (d, *J* = 3.1 Hz), 127.7 (d, *J* = 8.1 Hz), 115.4 (d, *J* = 21.5 Hz), 74.0, 68.1;

^{19}F-NMR (376 MHz, $CDCl_3$, $PhCF_3$ as internal standard): δ (ppm) = –115.25 – (–)115.34 (m)

HRMS (APCI+): calc. $[M+NH_4]^+$ for $[C_8H_9FO_2+NH_4]^+$ 174.0930, found 174.0928, Δ = 0.2 mDa.

Synthesis of 1-(3-fluorophenyl)ethane-1,2-diol (2.23)

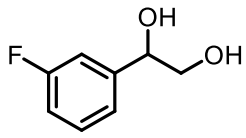

2.23

Prepared according to **GP2** from 1-(3-fluorophenyl)ethan-1-one (690 mg, 5.0 mmol, 1.0 equiv.). The crude product was purified with flash column chromatography (PE/Acetone 70/30), giving the title compound as a pale yellow solid (286 mg, 37%).

$\mathbf{R_f}$ = 0.57 (PE/Acetone = 60/40) [phosphomolybdic acid];

^{1}H-NMR (400 MHz, $CDCl_3$): δ (ppm) = 7.29–7.23 (m, 1H), 7.04–7.00 (m, 2H), 6.98–6.93 (m, 1H), 4.73 (dd, *J* = 8.5, 3.1 Hz, 1H), 4.37 (br. s., 2H), 3.64 (dd, *J* = 11.7, 3.1 Hz, 1H), 3.54 (dd, *J* = 11.7, 8.5 Hz, 1H);

^{13}C-NMR (101 MHz, $CDCl_3$): δ (ppm) = 162.8 (d, *J* = 246.2 Hz) 143.1 (d, *J* = 6.8 Hz), 130.0 (d, *J*= 8.2 Hz), 121.6 (d, *J* = 2.9 Hz), 114.7 (d, *J* = 21.2 Hz), 113.0 (d, *J* = 21.7 Hz), 74.1 (d, *J* = 1.5 Hz), 67.7;

^{19}F-NMR (376 MHz, $CDCl_3$, $PhCF_3$ as internal standard): δ (ppm) = –113.59 – (–)113.67 (m)

HRMS (EI+): calc. $[M^{\cdot+}]$ for $[C_8H_9FO_2]^{\cdot+}$ 156.0587, found 136.0585, Δ = 0.2 mDa.

Synthesis of 1-(4-(trifluoromethyl)phenyl)ethane-1,2-diol (2.24)

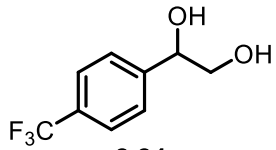

2.24

Prepared according to **GP3** from 1-(4-(trifluoromethyl)phenyl)ethan-1-one (1.9 g, 10 mmol, 1.0 equiv.). The crude product was purified with flash column chromatography (PE/Acetone 60/40), giving the title compound as an off-white solid (797 mg, 39%). The product was sparingly soluble in $CHCl_3$.

$\mathbf{R_f}$ = 0.58 (PE/Acetone = 60/40) [phosphomolybdic acid];

^{1}H-NMR (400 MHz, DMSO-d_6): δ (ppm) = 7.67 (d, *J* = 8.1 Hz, 2H), 7.57 (d, *J* = 8.1 Hz, 2H), 5.46 (d, *J* = 4.4 Hz, 1H), 4.80 (app. t., *J* = 5.5 Hz, 1H), 4.63 (dd, *J* = 11.9, 5.5 Hz, 1H), 3.52–3.41 (m, 2H);

^{13}C-NMR (101 MHz, DMSO-d_6): δ (ppm) = 148.8 (app. d, *J* = 1.2 Hz), 127.9 (q, *J* = 31.8 Hz), 127.5, 125.1 (q, *J* = 3.8 Hz), 124.9 (q, *J* = 271 Hz), 73.6, 67.5;

^{19}F-NMR (376 MHz, DMSO-d_6, $PhCF_3$ as standard): δ (ppm) = –63.32;

HRMS (EI+): calc. $[M+NH_4]^+$ for $[C_9H_9F_3O_2+NH_4]^+$ 224.0898, found 224.0896, Δ = 0.2 mDa.

Synthesis of 1-(4-chlorophenyl)ethane-1,2-diol (2.25)

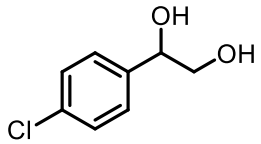

2.25

Prepared according to **GP2** from 1-chloro-4-vinylbenzene (600 µL, 5.0 mmol, 1.0 equiv.). The crude product was purified with flash column chromatography (PE/Acetone = 70/30), giving the title compound as a pale brown solid (370 mg, 43%).

R_f = 0.27 (PE/Acetone = 70/30) [phosphomolybdic acid];

^{1}H-NMR (400 MHz, $CDCl_3$): δ (ppm) = 7.35 – 7.31 (m, 2H), 7.31 – 7.27 (m, 2H), 4.79 (dd, *J* = 8.2, 3.5 Hz, 1H), 3.73 (dd, *J* = 11.3, 3.5 Hz, 1H), 3.60 (dd, *J* = 11.3, 8.2 Hz, 1H), 2.72 (bs, 2H).

^{13}C-NMR (101 MHz, $CDCl_3$): δ (ppm) = 138.9, 133.8, 128.7, 127.5, 74.0, 67.9.

HRMS (EI+): calc. $[M^{\cdot+}]$ for $[C_8H_9O_2Cl]^{\cdot+}$ 172.02856, found 172.02844, Δ = 0.12 mDa.

Synthesis of 1-(4-methoxyphenyl)ethane-1,2-diol (2.26)

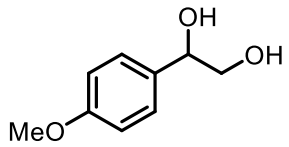

2.26

Prepared according to **GP3** from 1-(4-methoxyphenyl)ethan-1-one (1.5 g, 10 mmol, 1.0 equiv.). The 2-oxoacetaldehyde was reduced in wet THF as solvent according to literature[36] under diluted conditions (M = 0.1 M). NOTE: Typical concentration (M = 0.3 M) on the reduction leads to polymerization indicated by the formation of milky mixture. The crude was purified with flash column chromatography (PE/Acetone 70/30), giving the title compound as a white solid (1.34 g, 53%).

R_f = 0.37 (PE/Acetone = 60/40) [phosphomolybdic acid];

^{1}H-NMR (400 MHz, DMSO-d_6): δ (ppm) = 7.25 (d, *J* = 8.6 Hz, 2H), 6.87 (d, *J* = 8.6 Hz, 2H), 5.11 (d, *J* = 4.1 Hz, 1H), 4.66 (app. t., *J* = 5.7 Hz, 1H), 4.49 (dd, *J* = 12.2, 5.6 Hz, 1H), 3.73 (s, 3H);

^{13}C-NMR (101 MHz, $CDCl_3$): δ (ppm) = 158.7, 135.9, 127.8, 113.7, 73.8, 68.0, 55.5;

HRMS (ESI+): cal. $[M+Na]^+$ for $[C_9H_{12}O_3+Na]^+$ 191.0684, found: 191.0677, Δ = 0.7 mDa.

Synthesis of 1-(3-methoxyphenyl)ethane-1,2-diol (2.27)

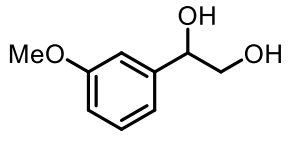

2.27

Prepared according to **GP3** from 1-(3-methoxyphenyl)ethan-1-one (1.5 g, 10 mmol, 1.0 equiv.). The crude product was purified with flash column chromatography (PE/Acetone 70/30), giving the title compound as a cream-white solid (1.8 g, 79 %).

R_f = 0.36 (PE/Acetone = 60/40) [phosphomolybdic acid];

^{1}H-NMR (400 MHz, $CDCl_3$): δ (ppm) = 7.29 (app. t., *J* = 8.1 Hz, 1H), 6.96–6.93 (m, 2H), 6.87–6.84 (m, 1H), 4.81 (dd, *J* = 8.2, 2.4 Hz, 1H), 3.83 (s, 3H), 3.77 (dd, *J* = 11.5, 2.4 Hz, 1H), 3.67 (dd, *J* = 11.5, 8.2 Hz, 1H), 2.72 (br. s., 2H);

^{13}C-NMR (101 MHz, $CDCl_3$): δ (ppm) = 159.8, 142.2, 129.6, 118.3, 113.4, 111.7, 74.6, 68.0, 55.3;

HRMS (EI+): calc. [$M^{\cdot+}$] for $[C_9H_{12}O_2]^{\cdot+}$ 168.07810, found 168.07827, Δ = – 0.18 mDa.

Synthesis of 1-(3-((*tert*-butyldimethylsilyl)oxy)phenyl)ethane-1,2-diol (2.28)

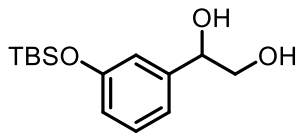

2.28

1-(3-((*tert*-butyldimethylsilyl)oxy)phenyl)ethan-1-one was prepared *via* TBS-protection of 3'-hydroxyacetophenone following a literature reported procedure.[37] The title compound was then prepared according to **GP3** from using the protected alcohol (1.25 g, 5 mmol, 1.0 equiv.). The crude was purified with flash column chromatography (PE/Acetone 70/30), giving the title compound as a pale solid (677 mg, 50%).

R_f = 0.66 (PE/Acetone = 60/40) [phosphomolybdic acid];

^{1}H-NMR (400 MHz, $CDCl_3$): δ (ppm) = 7.21 (app. t., *J* = 7.8 Hz, 1H), 6.95–9.92 (m, 1H), 6.86–6.84 (m, 1H), 6.77 (dd, *J* = 8.0, 0.8 Hz, 1H), 4.76 (dd, *J* = 8.2, 3.5 Hz, 1H), 3.73 (dd, *J* = 11.4, 3.5 Hz, 1H), 3.63 (dd, *J* = 11.4, 8.2 Hz, 1H), 2.42 (br. s., 2H), 0.98 (s, 9H), 0.19 (s, 6H);

^{13}C-NMR (101 MHz, $CDCl_3$): δ (ppm) = 155.8, 142.1, 129.5, 119.6, 118.9, 117.8, 74.5, 68.1, 25.7, 18.2, – 4.4;

HRMS (APCI+): calc. $[M+NH_4]^+$ for $[C_{14}H_{24}O_3Si+NH_4]^+$ 286.1839, found 286.1838, Δ = 0.1 mDa.

Synthesis of 1-(3-(methoxymethoxy)phenyl)ethane-1,2-diol (2.29)

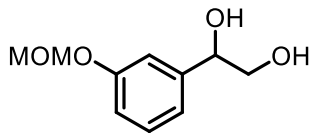

2.29

1-(3-methoxymethoxy)phenyl)ethan-1-one was synthetized *via* MOM-protection of 3'-hydroxyacetophenone following a literature reported procedure.[38] The title compound was then prepared according to **GP3** from using the protected alcohol (1.80 g, 10 mmol, 1.0 equiv.). The crude was purified with flash column chromatography (PE/Acetone 70/30), giving the title compound as a viscous yellow oil (785 mg, 40%).

R_f = 0.34 (PE/Acetone = 60/40) [phosphomolybdic acid];

^{1}H-NMR (400 MHz, $CDCl_3$): δ (ppm) = 7.28 (t, *J* = 7.8 Hz, 1H), 7.07–7.05 (m, 1H), 7.02–6.96 (m, 2H), 5.81 (s, 2H), 4.80 (dd, *J* = 8.0, 3.5 Hz, 1H), 3.77 (dd, *J* = 11.2, 3.5 Hz, 1H), 3.66 (dd, *J* = 11.2, 8.0 Hz, 1H), 3.47 (s, 3H), 2.19 (br. s., 2H);

^{13}C-NMR (101 MHz, $CDCl_3$): δ (ppm) = 157.5, 142.2, 129.7, 119.5, 115.8, 114.0, 94.4, 74.5, 68.0, 56.1;

HRMS (APCI+): calc. $[M+NH_4]^+$ for $[C_{10}H_{14}O_4+NH_4]^+$ 216.1236, found 216.1235, Δ = 0.1 mDa.

Synthesis of 1-(naphthalen-1-yl)ethane-1,2-diol (2.30)

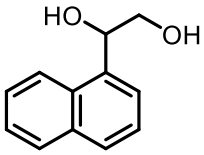

2.30

Prepared according to **GP3** from 1-(naphthalen-1-yl)ethan-1-one (1.7 g, 10 mmol, 1.0 equiv.). The crude product was purified with flash column chromatography (PE/Acetone 70/30), giving the title compound as an off-white solid (1,4 g, 73%). The product was sparingly soluble in $CHCl_3$.

R_f = 0.74 (PE/Acetone = 60/40) [phosphomolybdic acid];

^{1}H-NMR (400 MHz, DMSO-d_6): δ (ppm) = 8.16 (d, *J* = 8.2 Hz, 1H), 7.93 (dd, *J* = 7.8, 1.6 Hz, 1H), 7.82 (d, *J* = 8.1 Hz, 1H), 7.66 (d, *J* = 7.1 Hz, 1H), 7.57–7.48 (m, 3H), 5.45–5.42 (m, 1H), 5.37–5.32 (m, 1H), 3.67 (ddd, *J* = 11.1, 6.0, 3.8 Hz, 1H), 3.52 (ddd, *J* = 11.2, 6.9, 3.8 Hz, 1H), 3.37 (br.s, 2H);

^{13}C-NMR (101 MHz, DMSO-d_6): δ (ppm) = 139.4, 133.6, 130.9, 129.0, 127.6, 126.2, 125.8, 125.8, 124.1, 123.9, 71.6, 67.6;

HRMS (EI+): calc. $[M^{\cdot+}]$ for $[C_9H_{12}O_2]^{\cdot+}$ 188.08318, found 188.08300, Δ = 0.18 mDa.

Synthesis of 1-(naphthalen-2-yl)ethane-1,2-diol (2.31)

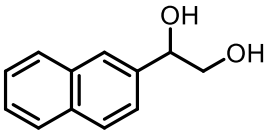

2.31

Prepared according to **GP2** from 2-vinylnaphthalene (771 mg, 5.0 mmol, 1.0 equiv.). The crude product was purified by flash column chromatography (PE/EtOAc = 60/40), obtaining the title compound as a white solid (586 mg, 62%). The product was sparingly soluble in chloroform.

R_f = 0.37 (PE/EtOAc = 60/40) [phosphomolybdic acid];

^{1}H-NMR (400 MHz, DMSO-d_6): δ (ppm) = 7.91–7.84 (m, 4H), 7.53–7.46 (m, 3H), 5.37 (d, *J* = 4.2 Hz, 1H), 4.76 (app. t., *J* = 5.8 Hz, 1H), 4.71 (dd, *J* = 11.8, 5.8 Hz, 1H), 3.53 (t, *J* = 5.8 Hz, 2H);

^{13}C-NMR (101 MHz, DMSO-d_6): δ (ppm) = 141.6, 133.2, 132.8, 128.1, 127.9, 127.7, 126.3, 125.9, 125.5, 125.1, 74.4, 67.8;

HRMS (EI+): calc. [$M^{\cdot+}$] for $[C_{12}H_{12}O_2]^{\cdot+}$ 188.08318, found 188.08317, Δ = 0.01 mDa.

2.5.4.2 Synthetized unsuccessful diols

Synthesis of 1-(4-bromophenyl)ethane-1,2-diol (F2.1)

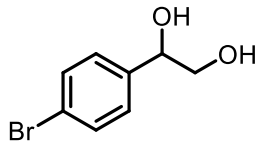

F2.1

Prepared according to **GP3** from 1-(4-bromophenyl)ethan-1-one (2.0 g, 10 mmol, 1.0 equiv.). The crude product was purified with flash column chromatography (PE/Acetone 70/30), giving the title compound as an off-white solid (80 mg, 6 %).

R_f = 0.69 (PE/Acetone = 60/40) [phosphomolybdic acid];

^{1}H-NMR (400 MHz, $CDCl_3$): δ (ppm) = 7.49 (d, *J* = 8.4 Hz, 2H), 7.25 (d, *J* = 8.4 Hz, 2H), 4.79 (dd, *J* = 8.0, 3.0 Hz, 1H), 3.75 (dd, *J* = 11.4, 3.0 Hz, 1H), 3.62 (dd, *J* = 11.4, 8.0 Hz, 1H), 2.28 (br. s., 2H);

^{13}C-NMR (101 MHz, $CDCl_3$): δ (ppm) = 139.4, 131.65, 127.8,121.9, 74.0, 67.9;

HRMS (APCI+): calc. $[M+NH_4]^+$ for $[C_8H_9BrO_2 + NH_4]^+$ 234.0129, found 234.0121, Δ = 0.8 mDa.

Synthesis of 1-(4-nitrophenyl)ethane-1,2-diol (F2.2)

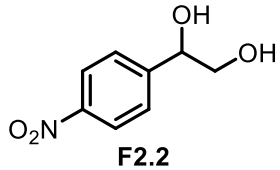

F2.2

Prepared according to **GP3** from 1-(4-nitrophenyl)ethan-1-one (1.6 g, 10 mmol, 1.0 equiv.). The crude product was first purified with flash column chromatography (PE/Acetone 60/40), and the orange oil obtained was further subjected to reverse-phase column (C18, H_2O+0.5 % TFA / MeCN). After evaporation of the solvent and lyophilization product the title compound was obtained as a yellow solid (244 mg, 13%).

R_f = 0.42 (PE/Acetone = 60/40) [phosphomolybdic acid];

^{1}H-NMR (400 MHz, $CDCl_3$): δ (ppm) = 8.20–8.24 (m, 2H), 7.54–7.58 (m, 2H), 4.95 (dd, *J* = 7.9, 3.4 Hz, 1H), 3.84 (dd, *J* = 11.3, 3.4 Hz, 1H), 3.64 (dd, *J* = 11.3, 7.9 Hz, 1H), 2.62 (br. s., 2H);

^{13}C-NMR (101 MHz, $CDCl_3$): δ (ppm) = 147.7, 147.6, 126.9, 123.7, 73.7, 67.7;

HRMS (APCI+): calc. $[M+NH_4]^+$ for $[C_8H_9NO_4+NH_4]^+$ 201.0875, found 201.0868, Δ = 0.07 mDa.

Synthesis of 1-(4-(methylthio)phenyl)ethane-1,2-diol (F2.3)

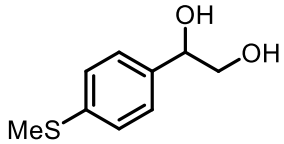

F2.3

1-(4-methylthio)phenyl)ethan-1-one was synthetized *via* Friedel–Crafts acylation of methylthiophenol ether following a literature reported procedure.[39] Title compound was then prepared according to **GP3** from 4'-(methylthio)-acetophenone (831 mg, 5 mmol, 1.0 equiv.). Purification with flash column chromatography (PE/Acetone 60/40), gave the title compound as a cream-white solid (314 mg, 34%).

$\mathbf{R_f}$ = 0.26 (PE/Acetone = 60/40) [phosphomolybdic acid];

^{1}H-NMR (400 MHz, DMSO-d_6): δ (ppm) = 7.31 (d, J = 8.3 Hz, 2H), 7.23 (d, J = 8.3 Hz, 2H), 4.65 (br. s., 2H), 4.54 (app. t., J = 5.9 Hz, 1H), 3.46–3.43 (m, 2H), 2.45 (s, 3H);

^{13}C-NMR (101 MHz, DMSO-d_6): δ (ppm) = 140.3, 136.2, 127.0, 125.8, 73.5, 67.5, 15.1;

HRMS (APCI+): calc. $[M+NH_4]^+$ for $([C_9H_{12}O_2S]+NH_4)^+$ 202.0902, found 202.0894, Δ = 0.8 mDa.

Synthesis of 4-(1,2-dihydroxyethyl)benzonitrile (F2.4)

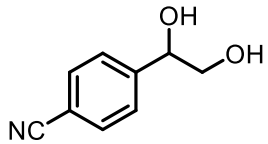

F2.4

Prepared according to **GP3** from 4-acetylbenzonitrile (1.4 g, 10 mmol, 1.0 equiv.). The crude product was purified with flash column chromatography (PE/Acetone 60/40), giving the title compound as a pale oil (784 mg, 48%).

$\mathbf{R_f}$ = 0.43 (PE/Acetone = 60/40) [phosphomolybdic acid];

^{1}H-NMR (400 MHz, $CDCl_3$): δ (ppm) = 7.70–7.67 (m, 2H), 7.55–7.52 (m, 2H), 4.92 (dd, J = 7.8, 3.4 Hz, 1H), 3.84 (dd, J = 11.2, 3.4 Hz, 1H), 3.65 (dd, J = 11.2, 7.8 Hz, 1H), 1.56 (br. s., 2H);

^{13}C-NMR (101 MHz, $CDCl_3$): δ (ppm) = 146.0, 132.3, 126.8, 118.7, 111.5, 73.9, 67.6;

HRMS (APCI+): calc. $[M+NH_4]^+$ for $[C_9H_9NO_2+NH_4]^+$ 181.0977, found 181.0973, Δ = 0.4 mDa.

Synthesis of 1-(4-(methylsulfonyl)phenyl)ethane-1,2-diol (F2.5)

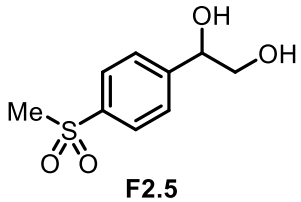

F2.5

Prepared according to **GP3** from 1-(4-(methylsulfonyl)phenyl)ethan-1-one (1.98 g, 10 mmol, 1.0 equiv.). The crude was purified with flash column chromatography (PE/Acetone 70/30), giving the title compound as a white solid (450 mg, 21%). The product was sparingly soluble in $CHCl_3$.

$\mathbf{R_f}$ = 0.09 (PE/Acetone = 60/40) [phosphomolybdic acid];

^{1}H-NMR (400 MHz, DMSO-d_6): δ (ppm) = 7.88 (d, J = 8.0 Hz, 2H), 7.62 (d, J = 8.0 Hz, 2H), 5.51 (br. s., 1H), 4.83 (br. s., 1H), 4.66 (br. s., 1H), 3.49 (br. s., 2H), 3.19 (s, 3H);
^{13}C-NMR (101 MHz, DMSO-d_6): δ (ppm) = 149.7, 139.3, 127.3, 126.6, 73.2, 67.1, 43.7;
HRMS (ESI+): calc. $[M+H]^+$ for $([C_9H_{12}O_4S]+H)^+$ 217.0535, found 217.0530, Δ = 0.5 mDa.

Synthesis of 1-phenylpropane-1,2-diol (F2.6)

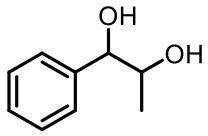

F2.6

Prepared according to a literature reported procedure.[40] 1-Phenylpropane-1,2-dione (600 mg, 4.0 mmol, 1.0 equiv.) was dissolved in EtOH (10 mL) and cooled to 0 °C. $NaBH_4$ (180 mg, 2.5 mmol, 1.2 equiv.) was added portionwise over 10 minutes, after which the reaction mixture was stirred for 30 minutes at 0 °C and 1 h at room temperature. Reaction was quenched with H_2O, extracted with EtOAc (×3), combined organic layers dried over $MgSO_4$, followed by filtration and evaporation of solvent. Crude was purified with flash column chromatography (Acetone/PE, 5% → 25%) and after solvent evaporation, the product was obtained as pale solid (564 mg, 92%). The ratios of *cis* and *trans* – isomers in the 1H-NMR spectrum were determined using Karplus analysis on the dublets at 4.68 and 4.36 ppm.
$\mathbf{R}_f$ = 0.51 (PE/Acetone = 60/40) [phosphomolybdic acid];
^{1}H-NMR (400 MHz, $CDCl_3$): δ (ppm) = 7.38–7.28 (br. m., 8.5H), 4.68 (*cis*, d, J = 4.2 Hz, 1H), 4.36 (*trans*, d, J = 7.8 Hz, 0.6H), 4.01 (*cis*, dq, J = 6.6, 4.2 Hz, 1H), 3.87 (*trans*, dq., J = 7.8, 6.4 Hz, 0.6H), 2.82 (br. s., 3H), 1.08 (*cis*, d, J = 6.4 Hz, 3H), 1.06 (*trans*, d, J = 6.4 Hz, 1.8H);
^{13}C-NMR (101 MHz, $CDCl_3$): δ (ppm) = 141.0 (*trans*), 140.3 (*cis*), 128.5 (*trans*), 128.3 (*cis*), 128.1 (*trans*), 127.8 (*cis*), 126.9 (*trans*), 126.6 (*cis*), 79.5 (*trans*), 77.4 (*cis*), 72.2 (*trans*), 71.3 (*cis*), 18.7 (*trans*), 17.1 (*cis*);
HRMS (APCI+): calc. $[M+NH_4]^+$ for $[C_9H_{12}O_2+NH_4]^+$ 170.1181, found 170.1176, Δ = 0.5 mDa.

Synthesis of 2-phenoxy-1-phenylethan-1-ol (F2.8)

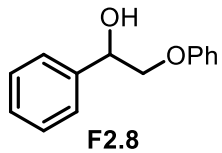

F2.8

Prepared according to a literature reported procedure.[16] Phenol (1.45 mL, 16.5 mmol, 1.1 equiv.) and K_2CO_3 (3.0 g, 22.5 mmol, 1.5 equiv.) were dissolved in acetone (150 mL) at room temperature. 2-bromo-1-phenyl-ethan-1-one (3.0 g, 15.0 mmol, 1.0 equiv.) was added portionwise to the mixture, and the reaction was refluxed for 4 h. After cooling to room temperature, the

suspension was filtered, and the solvent removed under reduced pressure. The obtained crude product was then used in the next step without further purification.

For the reduction, crude 2-phenoxy-1-phenylethan-1-one (1.5 g, 15.0 mmol, 1.0 equiv.) was dissolved in the mixture of THF/water (75 mL, 4/1) and cooled to 0 °C. $NaBH_4$ (681 mg, 18.0 mmol, 1.2 equiv.) was added portionwise at 0 °C, after which the reaction was stirred at room temperature for 2 h. The reaction was quenched with sat. NH_4Cl (30 mL) and the aqueous phase was extracted with ethyl acetate (3×). Combined organic phases were dried over $MgSO_4$, filtered and concentrated. Finally, purification with flash column chromatography (EtOAc/PE, 10% → 50%) yielded the product as cream-white solid (1.08 g, 72 %).

R_f = 0.83 (PE/Acetone = 60/40) [phosphomolybdic acid];

^{1}H-NMR (400 MHz, DMSO-d_6): δ (ppm) = 7.52–7.48 (m, 2H), 7.40–7.35 (m, 2H), 7.32–7.26 (m, 3H), 6.97–6.91 (m, 3H), 5.70 (d, *J* = 4.6 Hz, 1H), 4.07–4.03 (m, 2H), 3.46 (br. s., 1H);

^{13}C-NMR (101 MHz, DMSO-d_6): δ (ppm) = 159.0, 142.9, 129.9, 128.5, 127.7, 126.9, 121.0, 115.0, 73.5, 71.4;

HRMS (EI+): calc. $[M+H]^{+\cdot}$ for $[C_{14}H_{14}O_2]^{+\cdot}$ 214.0993, found 214.0990, Δ = 0.03 mDa.

Synthesis of 2-methoxy-1-(4-methoxyphenyl)ethan-1-ol (F2.9)

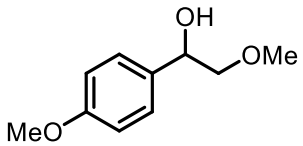

F2.9

Prepared according to **GP3** from 1-(4-methoxyphenyl)ethan-1-one (1.5 g, 10 mmol, 1.0 equiv.). Reduction of the 2-oxoacetaldehyde intermediate in MeOH led to fortuitous addition of methanol to the terminal carbon. Purification with flash column chromatography (PE/Acetone 60/40), giving the title compound as a cream-white solid (480 mg, 26%).

R_f = 0.61 (PE/Acetone = 60/40) [phosphomolybdic acid];

^{1}H-NMR (400 MHz, $CDCl_3$): δ (ppm) = 7.24–7.20 (m, 2H), 6.92–6.88 (m, 2H), 4.25 (dd, *J* = 8.6, 3.8 Hz, 1H), 3.80 (s, 3H), 3.67 (dd, *J* = 11.6, 8.6 Hz, 1H), 3.57 (dd, *J* = 11.6, 3.8 Hz, 1H), 3.27 (s, 3H), 2.34 (br. s., 1H);

^{13}C-NMR (101 MHz, $CDCl_3$): δ (ppm) = 159.5, 130.2, 128.1, 114.0, 84.1, 67.4, 56.7, 55.3;

HRMS (EI+): calc. $[M]^+$ for $[C_{10}H_{14}O_3]^+$ 182.0943, found 182.0942, Δ = 0.1 mDa

Synthesis of 1-phenylpropane-1,2-diol (F2.10)

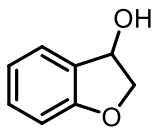

F2.10

Prepared according to a literature reported procedure.[16] 3-Coumaranone (0.54 g, 4.0 mmol, 1.0 equiv.) was disolved in MeOH (10 mL) and the mixture was cooled to 0 °C. $NaBH_4$ (1.6 g, 42 mmol, 11.4 equiv.) was added portionwise during 1 h. After the addition, the reaction was stirred for 30 minutes at 0 °C, after which it was allowed to warm to room temperature. The reaction was quenched with aqueous HCl (15 mL, 0.2 M) and the aqueous phase was extracted with chloroform (3×). The combined organic phases were dried over $MgSO_4$, filtered and concentrated. Purification by flash column chromatography (*tert*-butyl methyl ether) gave the title compound as a pale oil (529 mg, 97%).

R_f = 0.62 (PE/Acetone = 60/40) [phosphomolybdic acid];

^{1}H-NMR (400 MHz, $CDCl_3$): δ (ppm) = 7.22 (d, *J* = 7.5 Hz, 1H), 7.12 (app, td, *J* = 7.5, 1.0 Hz, 1H), 6.80 (app. td, *J* = 8.1, 1.0 Hz, 1H), 6.71 (d, *J* = 8.1 Hz, 1H), 5.02 (dd, *J* = 6.6, 2.5 Hz, 1H), 4.26 (dd, *J* = 10.7, 6.6 Hz, 1H), 4.15 (dd, *J* = 10.7, 2.5 Hz, 1H), 3.07 (br. s., 1H);

^{13}C-NMR (101 MHz, $CDCl_3$): δ (ppm) = 160.1, 130.7, 128.2, 125.6, 121.0, 110.5, 79.0, 71.8;

HRMS (EI+): calc. $[M]^{\cdot+}$ for $[C_8H_8O_2]^{\cdot+}$ 136.0523, found 136.0517, Δ = 0.6 mDa.

2.5.4.3 Synthetized diols for mechanistic studies

Synthesis of 1-phenylthane-1-*d*-1,2-diol (2.1_d_1)

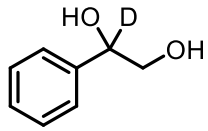

2.1_d_1

2-Hydroxy-1-phenylethan-1-one (163 mg, 1.20 mmol, 1.00 equiv.) was dissolved in CD_3OD (5 mL) and the resulting mixture was cooled to 0 °C. Then, sodium borodeuteride (98% *D*-atom, 167 mg, 4.00 mmol, 3.33 equiv.) was added portionwise over 10 minutes. The reaction was allowed to slowly warm towards room temperature while stirring for 2h, after which TLC analysis of the reaction showed full consumption of the starting material. The reaction was quenched by adding a few drops of 1M HCl, and methanol was evaporated under reduced pressure. Water (10 mL) was added to the residue and the aqueous phase was extracted with DCM (5×10 mL). The combined organic layers were dried over $MgSO_4$, filtered and the solvents evaporated. The product was dried under high vacuo overnight which afforded the title compound as white solid (29 mg, 17%, 98%-*D*-atom).

^{1}H-NMR (400 MHz, $CDCl_3$): δ (ppm) = 7.37–7.27 (m, 5H), 4.79 (br.s., 0.02H, residual 1H), 3.70 (br. s., 1H), 3.64 (br. s., 1H), 3.16 (br.s., 2H);

^{13}C-NMR (101 MHz, $CDCl_3$): δ (ppm) = 140.4, 128.5, 128.0, 126.1, 74.3, 67.9.

2.5.5 Mechanistic studies and discussions

2.5.5.1 UV-vis Studies

The mechanistic studies were commenced with attempts to identify the light-absorbing species in this photochemical transformation. For this, UV-vis spectra were recorded from the 1-phenylethane-1,2-diol (**2.1**, 0.1 mM), Eosin Y (0.25 mM) and a combination of Eosin Y (0.25 mM) and the diol **2.1** (0.1 M) and the results are shown in Figure S2.5. The spectra were recorded using a 10 mm × 1 mm quartz cuvette with 10 mm pathlength at 25 °C. The spectral window was chosen to be from 800 nm to 200 nm, data interval of 1 nm and scan rate 600 nm/min. Baseline spectrum of pure non-dried MeCN was subtracted from each spectra before measurement.

NOTE: Due to the low absorption coefficient of the absorption band around 390 nm, the combination of indicated concentration with 10 mm light pathlength were found crucial for separating this small absorbance from the baseline.

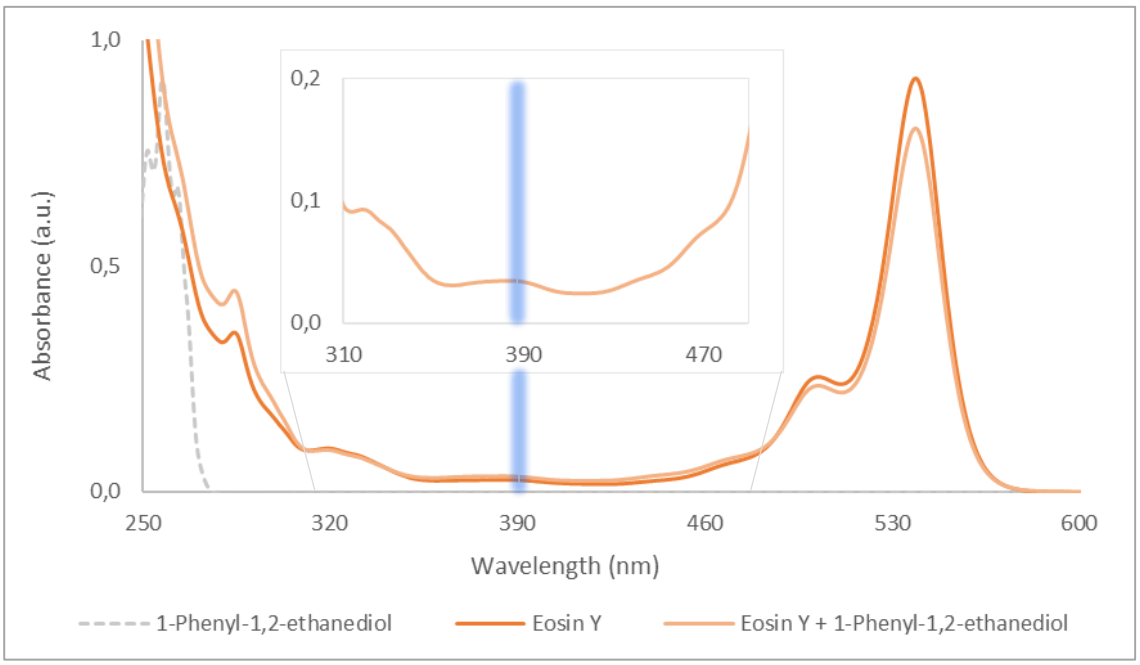

Figure S2.5. UV-vis spectrum of Eosin Y (0.25 mM), 1-phenylethane-1,2-diol (**2.1**, 0.1 M) and a combination of the two (0.25 mM for EY and 0.1 M for diol) in a non-dried MeCN (V = 1 mL).

As can be seen from Figure S2.5, Eosin Y appears to be the main light absorbing species in the reaction mixture (bright orange line) whereas the 1-phenylethane-1,2-diol (gray dottet line) does not have any observable absorption above 300 nm. Addition of a solid diol **2.1** to a solution of Eosin Y in MeCN appears to slightly reduce the intensity of absorption on the Eosin Y's main band at 520 nm and somewhat intensify the absorption near UV-region around 300 nm. Although minor, these changes could hint towards a weak interaction between the diol **2.1** and Eosin Y.

2.5.5.2 UV-vis monitoring of Eosin Y photodegradation

Owing to the observed colour change during the first 10 minutes of the reaction, the possibility of (photo)degradation of Eosin Y was studied more closely (Figure S2.6). For this study, four vials were set up separately according to **GP1** containing either only Eosin Y (1.4 mg, 2.0 µmol) or a combination of Eosin Y (1.4 mg, 2.0 µmol) and 1-phenylethane-1,2-diol (**2.1**, 13.8 mg, 0.10 mmol) dissolved in non-dried MeCN (1 mL) under N_2 atmosphere. The reaction mixtures were then irradiated with the desired wavelengths (385 nm or 523 nm) at 20 °C (temperature controlled with a cryostate) and a 25 µL probe of the

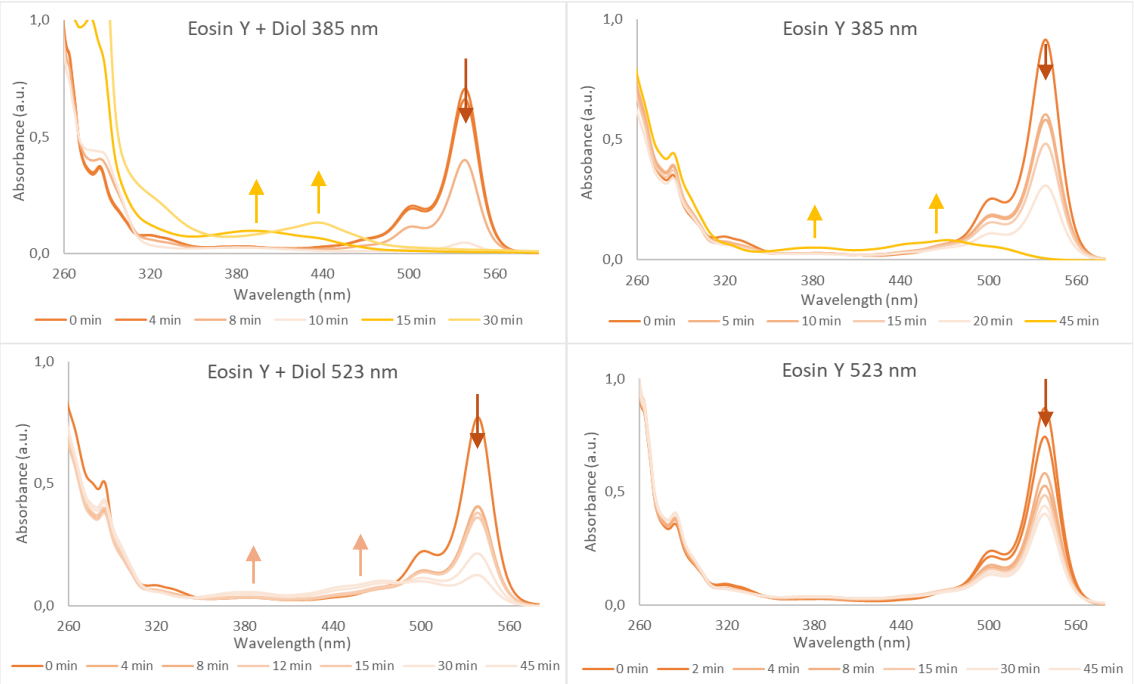

Figure S2.6. Time-dependent photodegradation of Eosin Y w/o 1-phenylethane-1,2-diol (**2.1**) under 385 nm (4.7 W) or 523 nm (0.8 W) irradiation.

reaction mixture was drawn with a Hamiltonian syringe at noted time points. These probes were diluted with 1 mL MeCN before measuring with UV-vis (quartz cuvette 10 mm × 1 mm, pathlength 10 mm, temperature 25 °C).

Taken together, the results presented in Figure S2.6 suggest that a rapid photodegradation of the original catalyst takes place under the high intensity irradiation at 385 nm. The observed changes in the UV-vis spectrum are in good agreement with the literature reported Eosin Y degradation with 520 nm laser irradiation.[3] In the literature, an inert atmosphere was found to speed up the photodegradation, perhaps by excluding an alternative relaxation pathway *via* singlet oxygen generation, whereas under our conditions the presence of diol **2.1** clearly accelerates the degradation perhaps by generating free radicals into the reaction mixture. In contrast, though, the degradation process appears to be significantly slower when irradiating the main absorption band of Eosin Y at 523 nm. This can be either owing to the inherently lowered energy of the irradiation of longer wavelength (Planck–Einstein Relation) or due direct excitation of an electron to a higher unoccupied molecular orbital with higher energy and intensity irradiation (although Kasha's rule would predict a fast relaxation to the lowest LUMO, which would correspond the orbital with excited state energy corresponding 520 nm irradiation). Meanwhile, the thermal control experiment run at 60 °C did not show any significant degradation even at prolonged time periods (1 h), ruling out the possibility of varying degrees of heating with different wavelength LEDs.

2.5.5.3 Kinetic studies

Kinetic profile of the reaction

The kinetic profile of the reaction was measured from the reaction of 1-phenylethane-1,2-diol (**2.1**) under standard reaction conditions (**GP1**). The reaction progress was monitored by taking a 25 µL sample from the reaction mixture at indicated time points, and an internal standard of mesitylene (100 µL of 0.025 M stock solution in MeCN) was added. Then, the mixtures were submitted to GC-FID analysis and the final conversion and yields were calculated from five-point calibration curves made for the starting material and product.

Based on the kinetic profile presented in Figure S2.7, three different stages of the reaction can be separated. The reaction begins with a short induction period (< 10 min) during which neither the starting material gets consumed, nor formation of product is detected. This initiation period for the reaction correlates with the Eosin Y degradation described in the previous chapter. According to the UV-vis degradation studies, the original photocatalyst bleaches within the first ten minutes of the reaction, whereas the starting material consumption starts only shortly before the 10-minute mark. These coincidences could therefore suggest that Eosin Y acts as a precatalytic species in our system, and the initial activation leads to the formation of highly efficient catalytic system.

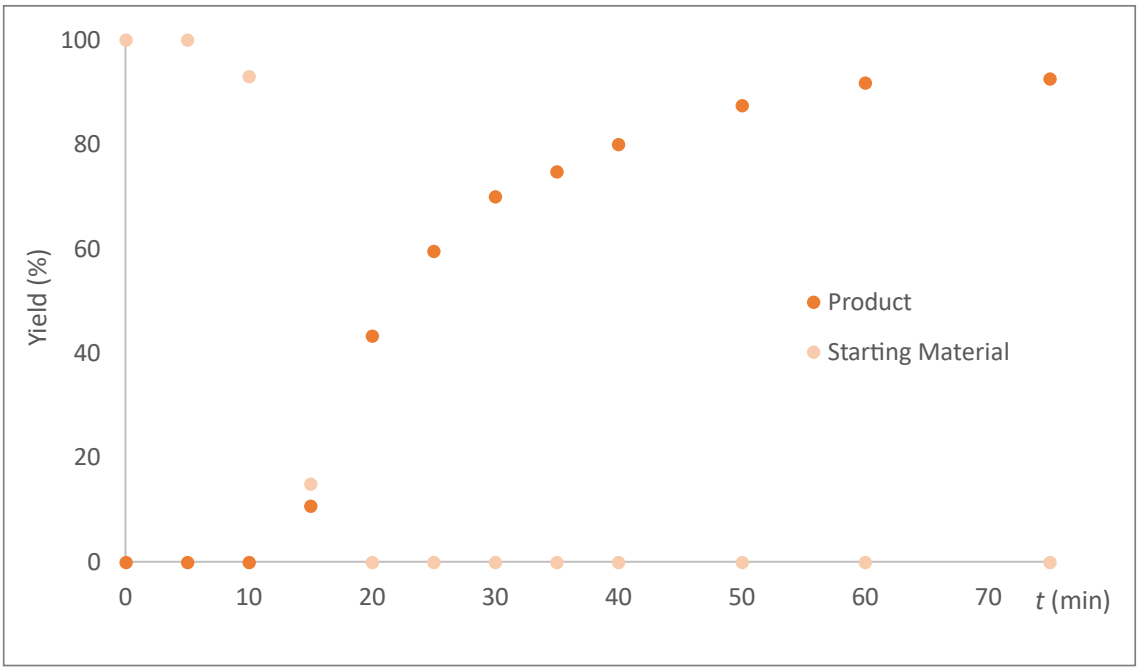

Figure S2.7. The kinetic profile of the reaction.

In the second stage of the reactions (t = 10–20 min), the starting material gets rapidly consumed and reaches full conversion at 20 minutes. During this time period the rate of the product formation displays a logarithmic kinetic, indicative of fast formation of product. However, at the point of 20 minutes where the starting material is fully consumed, the product yield has reached around 40%. In the last stage of the reaction (t = 20–60 min) the product formation is still ongoing, the rate of which starts to slowly plateau and reaching the final yield at 60 minutes.

Reaction monitoring with *ex situ* ^{1}H-NMR

As the reaction kinetic presented in Figure S2.7 indicated towards the possibility of a reaction intermediate, an *ex-situ* NMR kinetic was measured. For this, one vial was prepared according to **GP1** and the reaction was irradiated with 385 nm (4.7 W) LEDs at 20 °C. On given time points, a 50 µL sample was drawn from the reaction mixture, diluted with MeCN-d_3 and submitted to ^{1}H NMR-analysis (300 MHz) (Figure S2.8).

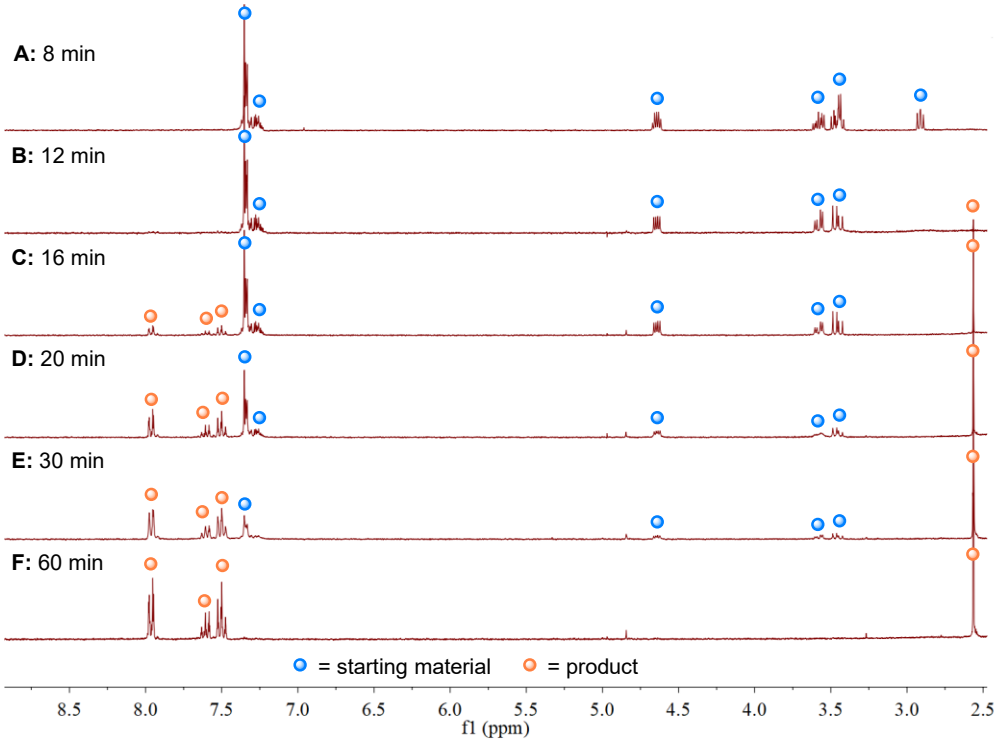

Figure S2.8. Combined ^{1}H-NMR spectra for the kinetic profile of the reaction.

Strikingly, before the onset of the reaction, the ^{1}H-NMR spectrum might not be on the first glance easily recognizable as 1-phenylethane-1,2-diol (**2.1**) due to unexpectedly complex splitting of the proton signals and the occurrence of an additional triplet around 3.0 ppm. Upon deeper analysis of spectra, the additional complexity was attributed to the hydroxy protons of **2.1** which under anhydrous conditions appeared to be rather unexchangeable (Figure S2.8, spectrum A). Furthermore, these OH protons also cause an extra order of splitting in the nearby C–H signals. However, as the reaction commences, the water released as a by-product initiates a fast exchange of the hydroxy protons, illustrated by the simplified ^{1}H-NMR spectrum at 12 minutes (spectrum B). From this point on, the formation of product becomes visible and the growth of the aromatic protons at 8 ppm belonging to the product **2.2** can be observed until 60 minutes (spectra C–F). Unfortunately, though, despite the rapid starting material consumption compared to the product formation, no prominent reaction intermediate could be distinguished.

Reaction efficiency with added acetophenone (autocatalytic pathway)

Since the acetophenone formed as the product is also known as a photocatalytic HAT reagent, the possibility of an autocatalyzed reaction was studied.[40] To this end, four reactions were set up according to **GP1** and a varying amount of acetophenone was added to each mixture before irradiating the reactions for 30 minutes with 385 nm LEDs (table S2.7). Afterwards, mesitylene (250 µL of 0.4 M stock solution) was added as an internal standard and the reaction mixtures were analysed by GC-FID. Yields were calculated against five-point calibration curve and amounts of originally added acetophenone were then subtracted to give the final corrected yields.

Table S2.7. Study of the addition of initial amounts of **2.2** to the reaction mixture.

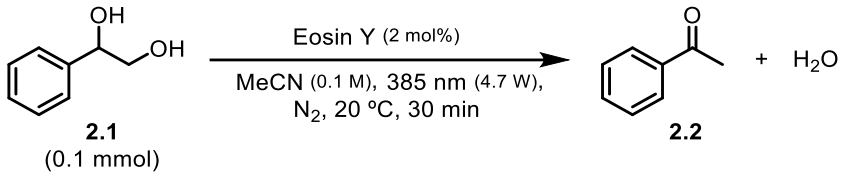

2.1 (0.1 mmol) **2.2**

Entry	**Initial loading of 2.2** (mol%)	**Corrected yield of 2.2**[a]
1	0	45
2	25	40
3	50	30
4	75	15

[a]Initial loading of acetophenone subtracted.

As can be seen from the table S2.7, the addition of the product to the reaction mixture does not present advantages to the reaction, and indeed the addition of more than 25 mol% begins to show reaction inhibition. Therefore, it seems that the formation of the product does not help to drive the reaction, but on the contrast hinders the productive reaction pathway. One possible explanation could be acetophenone acting as a competing light absorbing species, therefore diminishing the excitation efficiency of the reaction catalyzing species.

Light on/off study

To differentiate between a photoinitiated and photochemical reaction pathways, a light on/off experiment was carried out. Based on the earlier sections, degradation of the original photocatalyst was already proven to be a photodriven process but the dependency of the later reaction stages (consumption of starting material and especially the conversion of possible intermediate(s) to products) on light irradiation was still unclear. For the light on/off reaction, one vial was set up according to **GP1** and irradiated with 385 nm (4.7 W) LEDs while cycling between the light and dark periods (ten minutes each) as shown in Figure S2.9. The progress of the reaction with respect to the product formation was followed by drawing a sample of 25 µL every ten minutes (at the exact points of switching between light and dark phases) to which 250 µL of mesitylene stock solution (0.01 M in acetonitrile) was added. Then, 0.5 mL of MeCN-d_3 was added and the probes were analysed with ^{1}H-NMR (300 MHz). The integrals of the aromatic protons of mesitylene (3H, δ = 6.5 ppm) and the aliphatic methyl group of acetophenone (3H, δ = 2.3 ppm) were used for the calculation of product yield.

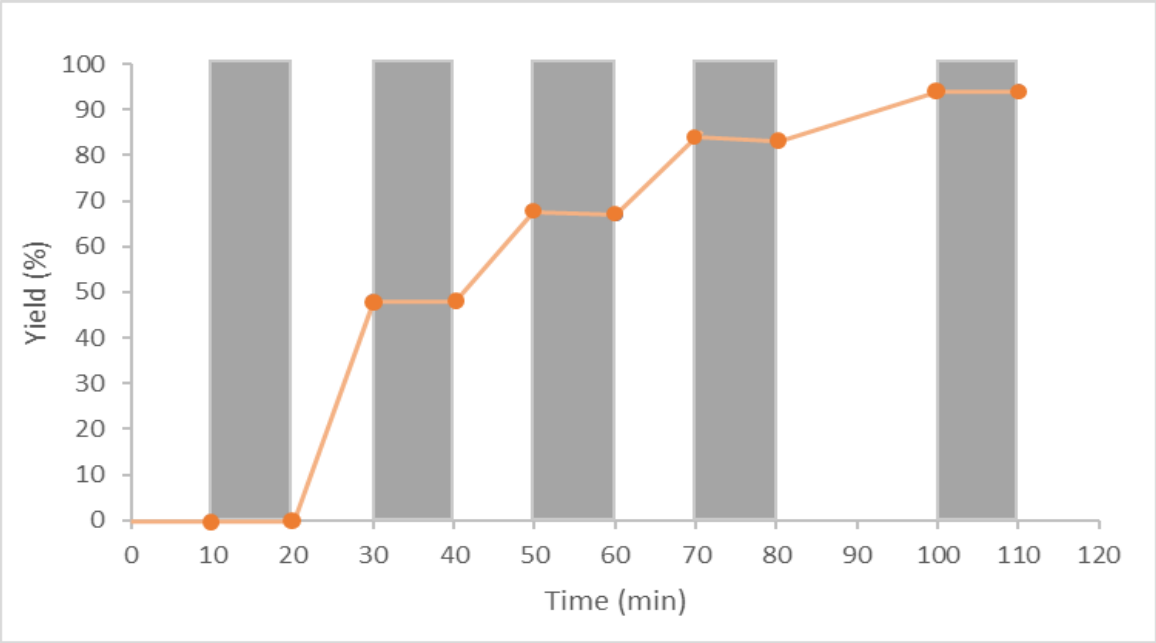

Figure S2.9. Light on/off experiment of the photocatalytic dehydration reaction of 1-phenylethane-1,2-diol (**2.1**).

The results shown in Figure S2.9 clearly show that the reaction proceeds only during the "light" phases, therefore confirming that continuous irradiation is needed for each stage of the process. The ten-minute induction period observed during the measurement of the reaction kinetic also displays in the on/off experiment causing only small amounts of the

product being formed during the first irradiation period of 10 minutes. Apart from the light-dependency of the degradation of the photocatalyst, according to the light on/off study also the consumption of starting material and the conversion of possible intermediates to the desired product are all light-dependent events.

2.5.5.4 HPLC-MS Analysis of Eosin Y photodegradation

Following up the leads on the possible photodegradation of Eosin Y in the overtime UV-vis measurement and the literature precedents, the composition of the reaction mixture was further studied with HPLC-MS. For this, one vial comprising of Eosin Y (69.2 mg, 0.1 mmol, 1.0 equiv.) and diol **2.1** (13.8 mg, 0.1 mmol, 1.0 equiv.) in MeCN (1 mL) was set up according to **GP1** and was irradiated for 10 minutes with the 390 nm (4.7 W) LEDs at 20 °C (cryostate set at 10 °C). The mixture was then filtered through a syringe filter before submitting for HPLC-QTOF analysis. Despite the simplicity of the reaction in terms of the number of reagents, a complex mixture of compounds was obtained. On the basis of the prevailing decomposition/radical addition patterns, some representative examples of the found compounds accompanied by the possible structures are combined in Figure S2.10.

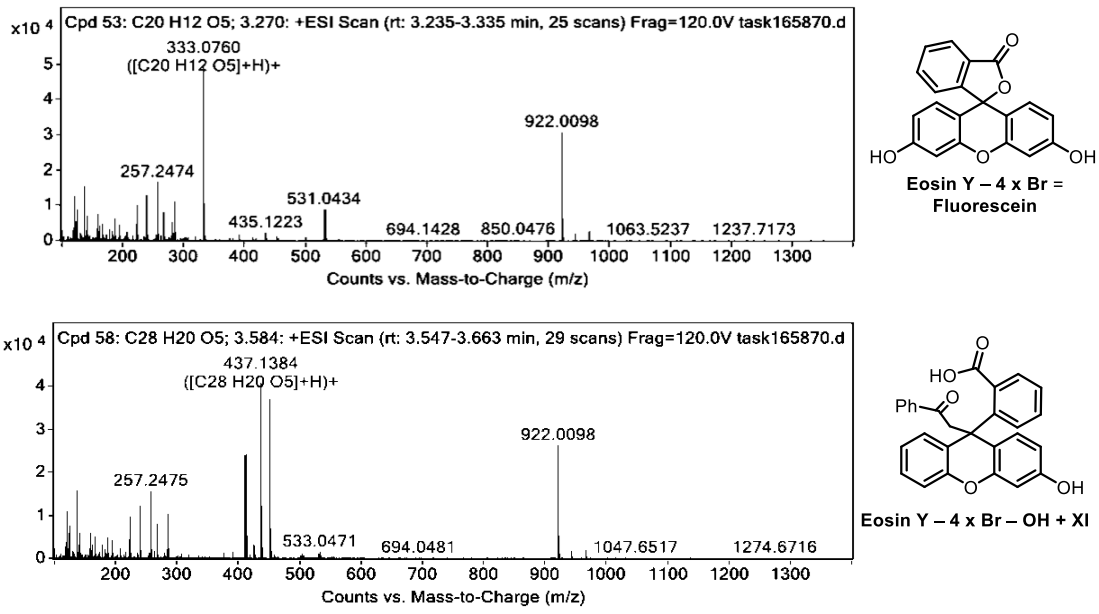

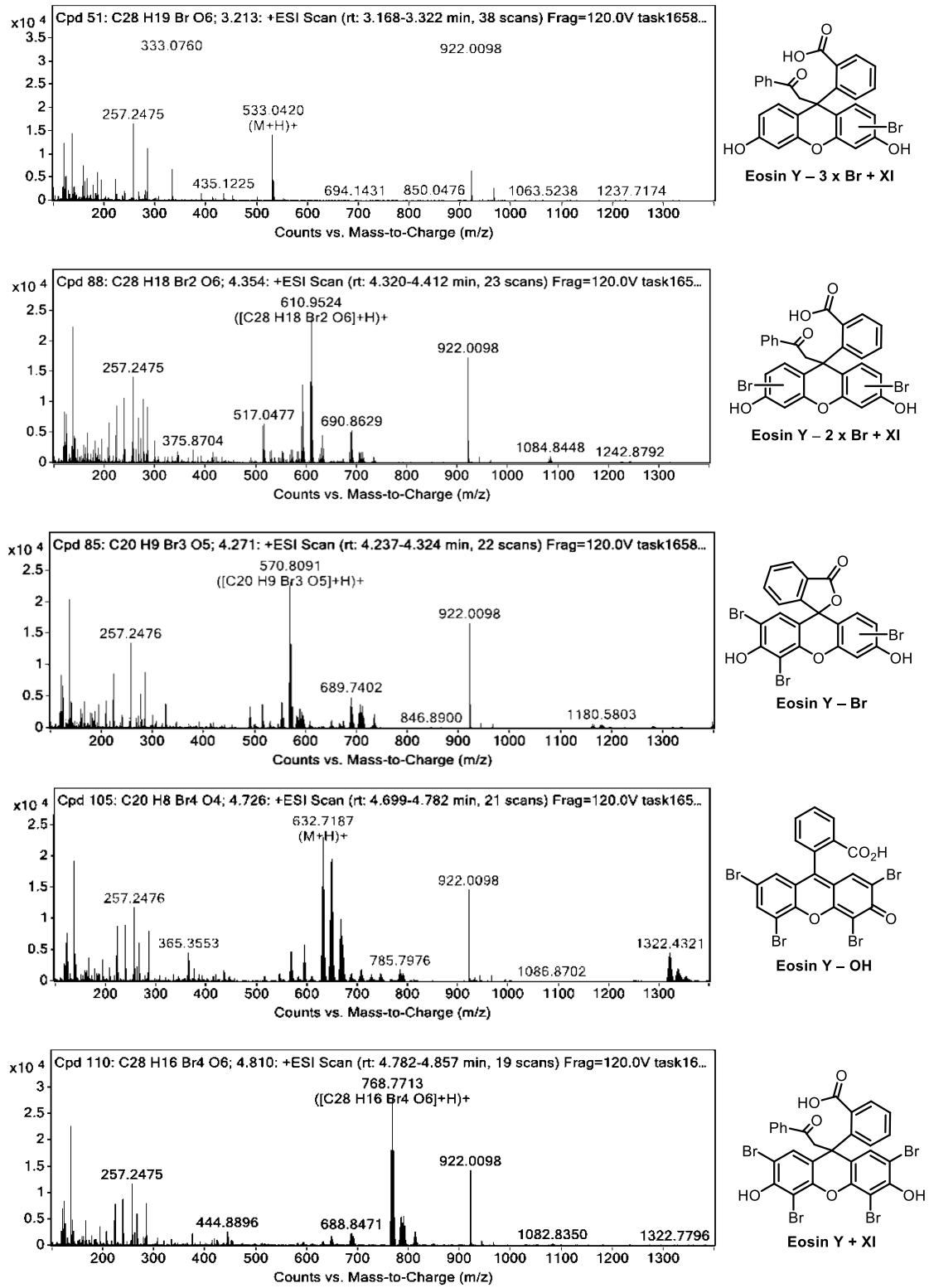

Figure S2.10. An overview of the HPLC-MS spectrum of Eosin Y and 1-phenylethane-1,2-diol photodegradation (above) combined with selected mass spectra (below). Possible structures of corresponding to each peak are shown on the right.

As can be seen from the Figure S2.10, the majority of the degradation products could be categorized corresponding to A) different degrees of Eosin Y debromination (1–4 bromines cleaved), B) addition of an α-carbonyl radical to the photocatalyst and C) further dehydration of the debrominated molecules and radical adducts. Out of these degradation pathways, debromination of Eosin Y has been well established in the literature,[3] whereas significantly less has been discussed about the possible radical addition. However, based on earlier reports disclosing the photosubstitution reactions on 4CzIPN[28] and photoadditions to Fukuzumi dye[30], analogous reactivity with Eosin Y could be imagined. This could also in part explain the increased rate of Eosin Y degradation in the presence of the diol **2.1** as observed by UV-vis spectroscopy. The questions regarding the extent and efficiency of this possible process remain outside of the frames of this study.

2.5.5.5 Studies towards Br-radical as a potential HAT catalyst

After identifying debromination as one of the main events in the photodegradation of Eosin Y during the initiation period of the reaction, the possibility of the so-generated bromide radical acting as a HAT catalyst was studied. Towards this direction, a bromine radical precursor was added in the reaction as tetrabutylammonium salt, and four photocatalysts were chosen based on literature reports to oxidize the bromide anion to a bromine radical.[31,32] Due to the very low catalyst loading of Eosin Y in the standard reaction conditions, the bromide anion loading was kept low to mimic the original reaction conditions. Therefore, we started our studies with the bromide loading of 2.0 mol%. As can be seen from the table S2.8, in the presence of 3,6-di-*tert*-butyl-9-mesityl-10-phenylylacridin-10-ium perchlorate the desired acetophenone product was obtained in an unoptimized yield of 28% indicating that the hypothesis of bromide-radical driven HAT is feasible (Entry 2). In contrast, though, (Ir[dF(CF_3)ppy]$_2$(dtbbpy)PF_6 and triphenylpyrylium tetrafluoroborate were not able to catalyze the reaction despite theoretically possessing the required redox-potentials to oxidize the bromide anion (Entries 1–3). In all the unsuccessful reaction the starting material **2.1** remained untouched. Furthermore, increasing the bromide loading to 5.0 mol% led to a positive effect on the reaction and an improved 36% yield was observed (Entry 4). As the acridinium dyes are known as strong oxidizing agents (E^*_{red} > 2.0 V) the alternative mechanistic pathway going *via* aryl oxidation followed by benzylic deprotonation was ruled out by the control experiment where no

Table S2.8. Screening of bromide anion as HAT precursor in the dehydration reaction.

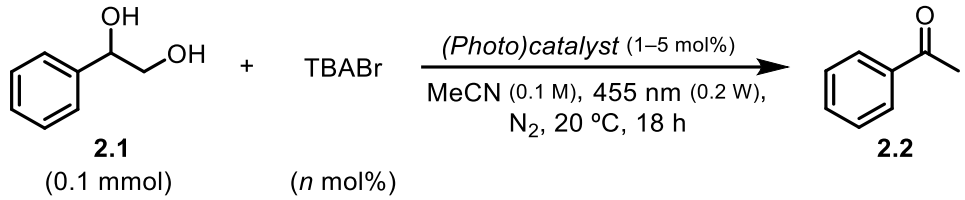

Entry	**(Photo)catalyst** (1–5 mol%)	**Br^- Loading**	**Yield** (%)
1	$Ir[dF(CF_3)ppy]_2(dtbbpy)PF_6$	2.0	n.d.
2	Mes-(^{t}Bu)$_2$Acr-Ph ClO_4	2.0	28
3	Triphenylpyrylium tetrafluoroborate	2.0	n.d.
4	Mes-(^{t}Bu)$_2$Acr-Ph ClO_4	5.0	36
5	Mes-(^{t}Bu)$_2$Acr-Ph ClO_4	–	n.d.
6	$BiBr_3$	20	46

Reaction conditions: **2.1** (13.8 mg, 0.1 mmol, 1.0 equiv.), TBABr (mol%), (photo)catalyst [Ir] 1.0 mol%, organic photocatalysts 5.0 mol%, $BiBr_3$ (20 mol%). TBABr = tetrabutylammonium bromide, Acr^+-Mes ClO_4 = 3,6-di-*tert*-butyl-9-mesityl-10-phenylylacridin-10-ium perchlorate.

product was detected in the absence of a bromide source (Entry 5). Finally, an orthogonal method for the bromide radical generation was studied and a LMCT approach with bismuth bromide was found to give 46% yield of the desired product (Entry 6).

Taken together, the productive reactions using orthogonal methods for bromine radical generation would thus hint towards the feasibility of bromine radical to catalyze our HAT/SCS sequence. However, even though the increase in bromide loading does have an advantageous effect on the reaction, the efficiency of this process still clearly falls short of that seen in the optimal reaction conditions with Eosin Y. It is therefore well likely that bromine radical is not the only HAT active species in the reaction, but other fragmentation products of Eosin Y also participate to the product formation.

2.5.5.6 TEMPO trapping

To gather information about the short-lived radical intermediates formed during the reaction, trapping of these possible intermediates were attempted with TEMPO. For the TEMPO trapping studies, one reaction was set up according to **GP1** with the addition of TEMPO (15.6 mg, 0.1 mmol, 1.0 equiv.) as a radical trapping reagent. After irradiation, the reaction mixture was filtered through a syringe filter and submitted for a LC-MS analysis.

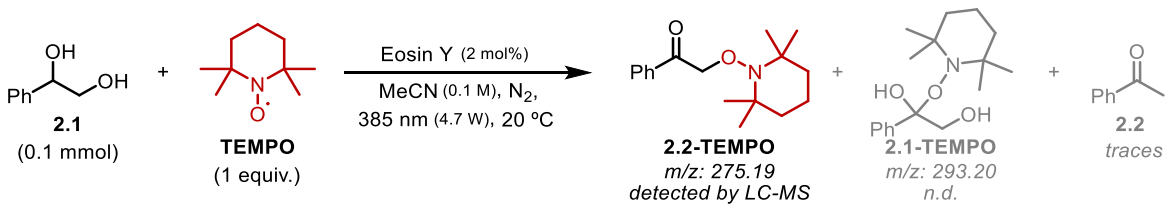

Scheme S2.1. TEMPO trapping studies with diol **2.1**.

The measured LC-MS from the crude reaction mixture containing TEMPO included several mass peaks (Figure S2.11). The base peak of the mixture corresponded to the protonated TEMPO adduct **2.2-TEMPO**, whereas the identity of higher mass peaks were unknown, and the possibility of dimerization during the reaction or measurement was not ruled out. Importantly, any mass peak potentially corresponding to the benzylic radical adduct **2.1-TEMPO** was not detected, which might indicate that the radical transfer from the benzylic position to the *alpha*-carbon during the spin center shift could be a very fast process.

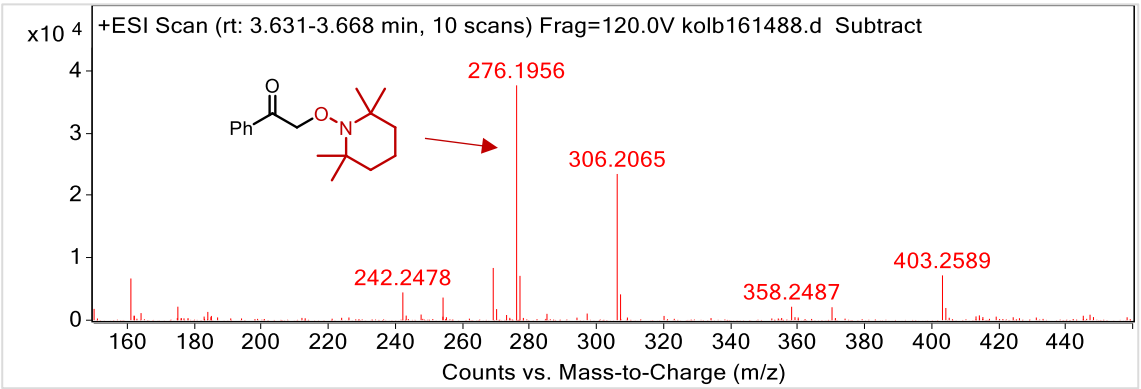

Figure S2.11. LC-MS chromatogram for the photocatalytic dehydration of **2.1** in presence of TEMPO (1 equiv.). Mass spectrum recorded with Q-TOF on positive polarization using electron spray ionization (ESI+) as ionization method.

2.5.5.7 Deuterium Labelling Studies

Finally, the mechanistic studies were concluded with deuterium labelling studies (Scheme S2.2). For these, the deuterated version of **2.1** was synthetized and otherwise the reactions were set according to the **GP1** with modifications highlighted in Scheme below. Firstly, no deuteration was observed when running the reaction in MeCN-d_3, suggesting that the solvent does not directly participate the reaction (Scheme S2.2, a). A recently disclosed publication about the superbasicity of benzylic carbanions demonstrated how, in the absence of other reaction partners, these intermediates are quenched by deprotonating the solvent.[33] In the context of the afore-mentioned study, the intermediacy of carbanions could thus be proven by deuterium transfer from the solvent to the product. Under our reaction conditions, however, similar rationalizations cannot be followed in such a straightforward manner for various reasons; the reduction of *alpha*-carbonyl radical would generate an enolate which is no longer superbasic, and substrates **2.1**, acetophenone products and Eosin Y are all more acidic than the solvent and would therefore be preferentially deprotonated. On the other hand, an intramolecular deuterium transfer from **2.1-*d*$_1$** led to a 67% deuterium incorporation to the product **2.2-*d*$_1$**, demonstrating that the species responsible of the initial HAT can react again with the intermediate and donate back the abstracted atom either in the form of a hydrogen atom or a proton (Scheme S2.2, b). The intermolecular deuterium transfer furthermore demonstrated that the H/D scrambling takes place when reacting equimolar amounts of deuterated and non-deuterated substrates (Scheme S2.2, c). This indicates that the HAT catalyst and the reaction intermediate dissociate after the first catalytic event and that other factors such as acidity, precoordination or the rate of BHAT could be more important factors than initial spatial arrangement when determining which species react together in the product forming step.

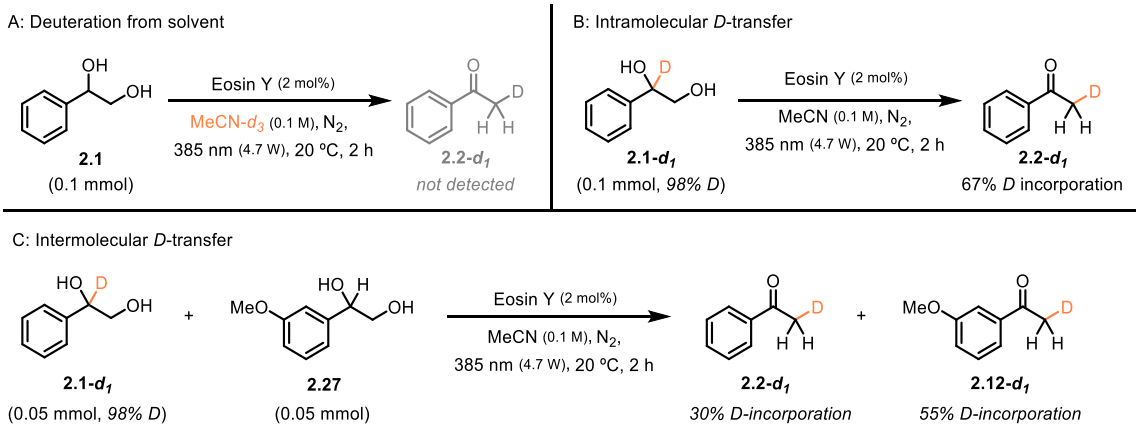

Scheme S2.2. Summary of deuterium labelling experiments.

2.6 Copies of NMR spectra and primary research data

Dear Reader,

For the copies of the NMR spectra, please open the supporting information provided at the publisher's website.
https://chemistry-europe.onlinelibrary.wiley.com/doi/10.1002/chem.202404200

Primary research data of this chapter, including experimental NMR-spectra, HRMS files and the raw data for UV-vis studies can be downloaded free of charge from the Regensburg University Library's repository: https://epub.uni-regensburg.de/58645/

2.7 Notes and References

(1) Majek, M.; Filace, F.; Wangelin, A. J. V. On the Mechanism of Photocatalytic Reactions with Eosin Y. *Beilstein J. Org. Chem.* **2014**, *10*, 981–989.

(2) Caro, H. Ueber Die Entwickelung Der Theerfarben-Industrie. *Ber. Dtsch. Chem. Ges.* **1892**, *25* (3), 955–1105.

(3) Alvarez-Martin, A.; Trashin, S.; Cuykx, M.; Covaci, A.; De Wael, K.; Janssens, K. Photodegradation Mechanisms and Kinetics of Eosin-Y in Oxic and Anoxic Conditions. *Dyes Pigments.* **2017**, *145*, 376–384.

(4) Javaeed, A.; Qamar, S.; Ali, S.; Mustafa, M. A. T.; Nusrat, A.; Ghauri, S. K. Histological Stains in the Past, Present, and Future. *Cureus* **2021**, *13*, (10), e18486.

(5) Titford, M. The Long History of Hematoxylin. *Biotech. Histochem.* **2005**, *80* (2), 73–78.

(6) Li, Y.; Li, N.; Yu, X.; Huang, K.; Zheng, T.; Cheng, X.; Zeng, S.; Liu, X. Hematoxylin and Eosin Staining of Intact Tissues via Delipidation and Ultrasound. *Sci. Rep.* **2018**, *8* (1), 12259.

(7) Cao, H.; Kong, D.; Yang, L.-C.; Chanmungkalakul, S.; Liu, T.; Piper, J. L.; Peng, Z.; Gao, L.; Liu, X.; Hong, X.; Wu, J. Brønsted Acid-Enhanced Direct Hydrogen Atom Transfer Photocatalysis for Selective Functionalization of Unactivated C(Sp3)–H Bonds. *Nat. Synth.* **2022**, *1* (10), 794–803.

(8) Fan, X.-Z.; Rong, J.-W.; Wu, H.-L.; Zhou, Q.; Deng, H.-P.; Tan, J. D.; Xue, C.-W.; Wu, L.-Z.; Tao, H.-R.; Wu, J. Eosin Y as a Direct Hydrogen-Atom Transfer Photocatalyst for the Functionalization of C−H Bonds. *Angew. Chem. Int. Ed.* **2018**, *57* (28), 8514–8518.

(9) Yan, J.; Cheo, H. W.; Teo, W. K.; Shi, X.; Wu, H.; Idres, S. B.; Deng, L.-W.; Wu, J. A Radical Smiles Rearrangement Promoted by Neutral Eosin Y as a Direct Hydrogen Atom Transfer Photocatalyst. *J. Am. Chem. Soc.* **2020**, *142* (26), 11357–11362.

(10) Schmalzbauer, M.; Marcon, M.; König, B. Excited State Anions in Organic Transformations. *Angew. Chem. Int. Ed.* **2021**, *60* (12), 6270–6292.

(11) Hari, D. P.; König, B. Synthetic Applications of Eosin Y in Photoredox Catalysis. *Chem. Commun.* **2014**, *50* (51), 6688–6699.

(12) Tripathi, J.; Gupta, H.; Sharma, A. Photoacid-Catalyzed Esterification of Carboxylic Acids Using Eosin Y. *Org. Lett.* **2025**, *27* (4), 1018–1023.

(13) Roy, V. J.; Sen, P. P.; Roy, S. R. Exploring Eosin Y as a Bimodular Catalyst: Organophotoacid Mediated Minisci-Type Acylation of *N* -Heteroarenes. *Chem. Commun.* **2022**, *58* (11).

(14) Yan, D.-M.; Chen, J.-R.; Xiao, W.-J. New Roles for Photoexcited Eosin Y in Photochemical Reactions. *Angew. Chem. Int. Ed.* **2019**, *58* (2), 378–380.

(15) Schwarz, J.; König, B. Visible-Light Mediated C–C Bond Cleavage of 1,2-Diols to Carbonyls by Cerium-Photocatalysis. *Chem. Commun.* **2019**, *55* (4), 486–488.

(16) Chen, K.; Schwarz, J.; A. Karl, T.; Chatterjee, A.; König, B. Visible Light Induced Redox Neutral Fragmentation of 1,2-Diol Derivatives. *Chem. Commun.* **2019**, *55* (87), 13144–13147.

(17) Zhu, Q.; Nocera, D. G. Catalytic C(β)–O Bond Cleavage of Lignin in a One-Step Reaction Enabled by a Spin-Center Shift. *ACS Catal.* **2021**, *11* (22), 14181–14187.

(18) Cao, Y.-X.; Zhu, G.; Li, Y.; Le Breton, N.; Gourlaouen, C.; Choua, S.; Boixel, J.; Jacquot de Rouville, H.-P.; Soulé, J.-F. Photoinduced Arylation of Acridinium Salts: Tunable Photoredox Catalysts for C–O Bond Cleavage. *J. Am. Chem. Soc.* **2022**, *144* (13), 5902–5909.

(19) Wessig, P.; Muehling, O. Spin-Center Shift (SCS) – A Versatile Concept in Biological and Synthetic Chemistry. *Eur. J. Org. Chem.* **2007**, *2007* (14), 2219–2232.

(20) Zhang, F.-L.; Li, B.; Houk, K. N.; Wang, Y.-F. Application of the Spin-Center Shift in Organic Synthesis. *JACS Au* **2022**, *2* (5), 1032–1042.

(21) Matsuo, B.; Granados, A.; Majhi, J.; Sharique, M.; Levitre, G.; Molander, G. A. 1,2-Radical Shifts in Photoinduced Synthetic Organic Transformations: A Guide to the Reactivity of Useful Radical Synthons. *ACS Org. Inorg. Au*, **2022**, *2* (6), 435–454.

(22) Kang, Y. C.; Treacy, S. M.; Rovis, T. Iron-Catalyzed Photoinduced LMCT: A 1° C–H Abstraction Enables Skeletal Rearrangements and C(Sp^3)–H Alkylation. *ACS Catal.* **2021**, *11* (12), 7442–7449.

(23) Birnthaler, D.; Narobe, R.; Lopez-Berguno, E.; Haag, C.; König, B. Synthetic Application of Bismuth LMCT Photocatalysis in Radical Coupling Reactions. *ACS Catal.* **2023**, *13* (2), 1125–1132.

(24) Lechner, R.; Kümmel, S.; König, B. Visible Light Flavin Photo-Oxidation of Methylbenzenes, Styrenes and Phenylacetic Acids. *Photochem. Photobiol. Sci.* **2010**, *9* (10), 1367–1377.

(25) Ischay, M. A.; Ament, M. S.; Yoon, T. P. Crossed Intermolecular [2 + 2] Cycloaddition of Styrenes by Visible Light Photocatalysis. *Chem. Sci.* **2012**, *3* (9), 2807–2811.

(26) Yan, D.-M.; Zhao, Q.-Q.; Rao, L.; Chen, J.-R.; Xiao, W.-J. Eosin Y as a Redox Catalyst and Photosensitizer for Sequential Benzylic C−H Amination and Oxidation. *Chem. Eur. J.* **2018**, *24* (63), 16895–16901.

(27) Kimber, P.; Plasser, F. Energy Component Analysis for Electronically Excited States of Molecules: Why the Lowest Excited State Is Not Always the HOMO/LUMO Transition. *J. Chem. Theory Comput.* **2023**, *19* (8), 2340–2352.

(28) Grotjahn, S.; König, B. Photosubstitution in Dicyanobenzene-Based Photocatalysts. *Org. Lett.* **2021**, *23* (8), 3146–3150.

(29) Kwon, Y.; Lee, J.; Noh, Y.; Kim, D.; Lee, Y.; Yu, C.; Roldao, J. C.; Feng, S.; Gierschner, J.; Wannemacher, R.; Kwon, M. S. Formation and Degradation of Strongly Reducing Cyanoarene-Based Radical Anions towards Efficient Radical Anion-Mediated Photoredox Catalysis. *Nat. Commun.* **2023**, *14* (1), 92.

(30) Cao, Y.-X.; Zhu, G.; Li, Y.; Le Breton, N.; Gourlaouen, C.; Choua, S.; Boixel, J.; Jacquot De Rouville, H.-P.; Soulé, J.-F. Photoinduced Arylation of Acridinium Salts: Tunable Photoredox Catalysts for C–O Bond Cleavage. *J. Am. Chem. Soc.* **2022**, *144* (13), 5902–5909.

(31) Wang, Z.; Ji, X.; Han, T.; Deng, G.-J.; Huang, H. LiBr-Promoted Photoredox Minisci-Type Alkylations of Quinolines with Ethers. *Adv. Synth. Catal.* **2019**, *361* (24), 5643–5647.

(32) Jia, P.; Li, Q.; Poh, W. C.; Jiang, H.; Liu, H.; Deng, H.; Wu, J. Light-Promoted Bromine-Radical-Mediated Selective Alkylation and Amination of Unactivated C(Sp3)–H Bonds. *Chem* **2020**, *6* (7), 1766–1776.

(33) Grotjahn, S.; Graf, C.; Zelenka, J.; Pattanaik, A.; Müller, L.; Kutta, R. J.; Rehbein, J.; Roithová, J.; Gschwind, R. M.; Nuernberger, P.; König, B. Reactivity of Superbasic Carbanions Generated via Reductive Radical-Polar Crossover in the Context of Photoredox Catalysis. *Angew. Chem. Int. Ed.* **2024**, *63* (18), e202400815.

(34) Gao, X.; Lin, J.; Zhang, L.; Lou, X.; Guo, G.; Peng, N.; Xu, H.; Liu, Y. Iodine-Initiated Dioxygenation of Aryl Alkenes Using *Tert* -Butylhydroperoxides and Water: A Route to Vicinal Diols and Bisperoxides. *J. Org. Chem.* **2021**, *86* (21), 15469–15480.

(35) Rygus, J. P. G.; Hall, D. G. Direct Nucleophilic and Electrophilic Activation of Alcohols Using a Unified Boron-Based Organocatalyst Scaffold. *Nat. Commun.* **2023**, *14* (1), 2563.

(36) Zeynizadeh, B.; Behyar, T. Wet THF as a Suitable Solvent for a Mild and Convenient Reduction of Carbonyl Compounds with NaBH4. *Bull. Chem. Soc. Jpn.* **2005**, *78* (2), 307–315.

(37) Dond, B. D.; Thore, S. N. NFSI/KF Mediated Mild and Chemoselective Interconversion of Aryl TBDMS Ethers to Their Benzene Sulfonate. *Tetrahedron Lett.* **2020**, *61* (13), 151660.

(38) Obaro-Best, O.; Reed ,Jack; Norfadilah ,Alya A. F. B.; Monahan ,Ryan; and Sunasee, R. Bismuth Trichloride–Mediated Cleavage of Phenolic Methoxymethyl Ethers. *Synth. Commun.* **2016**, *46* (7), 586–593.

(39) Wang, S.-K.; You, X.; Zhao, D.-Y.; Mou, N.-J.; Luo, Q.-L. Iodine-Promoted Semmler–Wolff Reactions: Step-Economic Access to Meta-Substituted Primary Anilines via Aromatization. *Chem. Eur. J.* **2017**, *23* (49), 11757–11760.

(40) Huix-Rotllant, M.; Siri, D.; Ferré, N. Theoretical Study of the Photochemical Generation of Triplet Acetophenone. *Phys. Chem. Chem. Phys.* **2013**, *15* (44), 19293–19300.

CHAPTER 3

3 Use of Anionic Bismuth Complexes for LMCT Decarboxylation

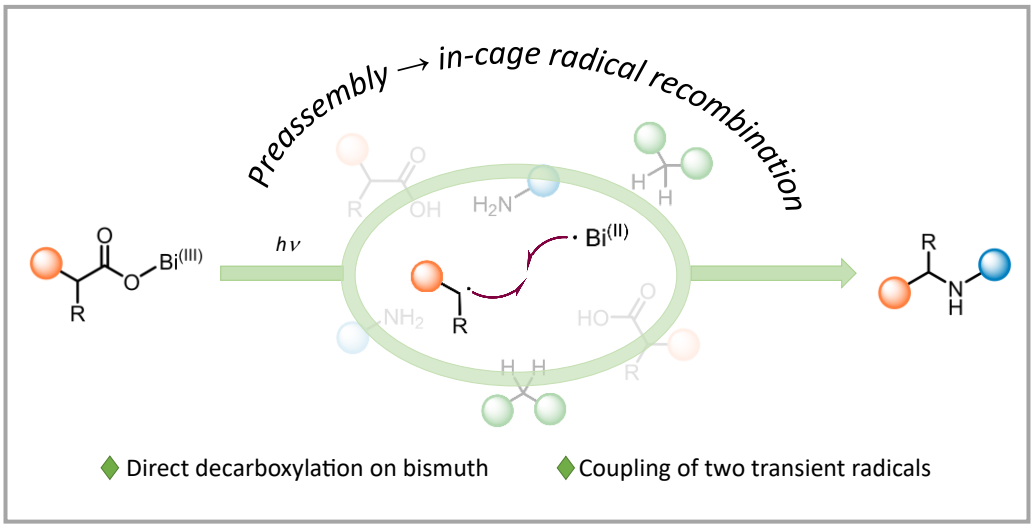

Abstract: During the past years, LMCT photocatalysis has evolved into a versatile alternative to the previously established MLCT protocols. Importantly, while the ruthenium and iridium polypyridyl complexes are cationic in nature, LMCT reactions often proceed *via* anionic assemblies. While the counterion effect in the former has been recently identified, less attention has been given to this aspect in LMCT.

Modified version of this chapter has been published. For reference, see:
E. K. Taskinen‡, D. Birnthaler‡, V. Kermelj and B. König*, Preassembly-Controlled Radical Recombination at Bismuth: Decarboxylative C–N Coupling with Sulfonamides, *Chem. Eur. J.*, **2025**, e202500396.

Author contributions: E.K.T. and D.B. contributed equally to this work. E.K.T. and D.B. developed the concept of the project. V.K. and D.B. explored the general idea. E.K.T. and D.B. optimized the reaction, synthetized the starting materials and the products, and carried out mechanistic studies. E.K.T. and D.B. wrote the manuscript and modified the draft according to the feedback from other authors. B.K. supervised the work.

3.1 Motivation

After employing fully organic photocatalysts in the first project, we wanted to look into the ion-pairing effect on the other side of the coin. Importantly, as discussed in Chapter 1, the counterion effect on the reactivity of iridium and ruthenium polypyridyl complexes has been identified in recent years. Hence, we sought to study whether indications for counter-ion effect could be found in other applications of metal-based photocatalysis.

Since 2018 ligand-to-metal charge transfer (LMCT) photocatalysis has been evolving as an efficient approach to activate various substrates.[1] Unlike with typical MLCT photocatalysts, which can catalyze single-electron or energy transfer steps, in LMCT the photolysis of the metal-ligand bond acts as a method to generate the radical intermediates. Importantly, while long excited-state lifetimes are in most cases needed for efficient MLCT catalysis, such requirements no longer hold importance in LMCT.[2] This, in turn, has enabled a facile expansion of the metals used in photocatalysis beyond rare ruthenium und iridium. For the LMCT approaches, cerium, iron, copper, titanium and most recently bismuth have been found active, and the photocatalytic complexes are typically generated spontaneously in the reaction mixture. With our group's previous background in bismuth LMCT photocatalysis[3], we decided to develop the bismuth chemistry further and investigate the possible ion-pairing interactions arising.

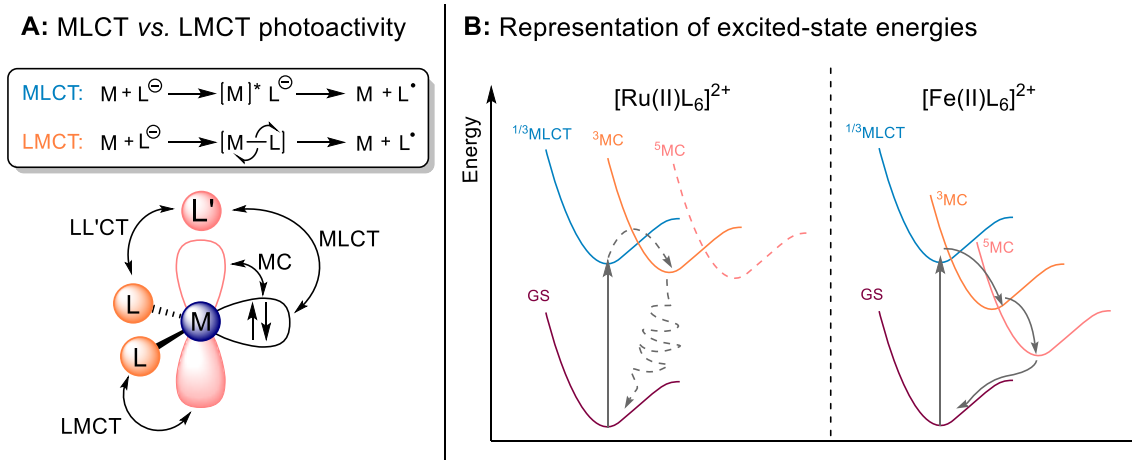

Figure 3.1. Schematic representation of MLCT and LMCT activity (a) and representation of electronic state energies (b).[2]

3.2 Introduction

Bismuth, the heaviest member of the pnictogen family (group 15) and the last stable element in the periodic system (atomic number 83), has attracted considerable attention in recent years among the synthetic chemists. Although technically a non-metal, bismuth displays many transition-metal like characters particularly in reaction settings.[5] While the bismuth salts were at first utilised as Lewis-acids akin to other metal salts, rich redox reactions of bismuth have recently emerged.[5,6] At its heart, the versatile chemistry of bismuth stems from the broad variety of oxidation states (ranging from +V to –I) and formal charges (from +3 to –3) on bismuth combined with the atom's facile shuttling between these states. Importantly, even more properties of bismuth compounds can be accessed when a *charge* is purposefully added to the complexes.[7] For instance, cationic bismuth(III) species display increased Lewis acidity, inserting to reaction partners such as aldehyde Bi–C bonds under conditions in which their neutral counterparts remain inactive.[8] In contrast, anionic bismuth complexes, such as $[BiR_2]^-$, can undergo alkylation and arylation with respective organic halides, making increased nucleophilicity over neutral compounds.[9,10] Intriguingly, a counterion-dependence has also been reported for the reaction of neutral $Bi(O\textit{t}Bu)_3$ with butylate salts; while the expected -ate complex $[KBi(O\textit{t}Bu)_4]$ was obtained with potassium *tert*-butylate, an oxoalkoxide $[Na_4Bi_2O(O\textit{t}Bu)_8]$ was isolated with sodium *tert*-butylate.[11]

While some bismuth complexes, especially those centring around a bismuth atom in its unstable oxidation state (such as +II), rely on careful ligand design[12,13], others can be formed spontaneously in solution. Our group entered the realm of bismuth chemistry in 2023 when the first application of simple bismuth salts in ligand-to-metal charge transfer (LMCT) catalysis was disclosed.[3] For this, a benchmark Giese-coupling reaction between aliphatic hydrocarbons and electron-poor alkenes was realized.[14] Importantly, this and previous literature suggests that the chlorine radical generation with LMCT mainly occurs from the anionic metal-chloride complexes. For iron, self-ionization of $FeCl_3$ to $FeCl_2^+$ and $FeCl_4^-$ is often proposed with the anionic species being the photoactive one.[15,16] With copper, the self-ionization is less efficient, and addition of a chloride salt to the reaction mixture is often needed for optimal results.[17] With bismuth, the neutral $BiCl_3$ was found unactive under 385 nm irradiation, however, in the presence of two equivalents of TBACl high yields of the Giese-coupling products could be achieved.[3] At least partially the beneficial effect of the added chloride ligand can be attributed to the enhanced UV-vis

absorption of the anionic complexes. With $FeCl_3$, addition of LiCl causes only a small increase in the intensity of the most red-shifted absorption band at 361 nm (in MeCN) due to the already efficient self-ionization.[16] With sole $CuCl_2$, though, the LMCT band at 462 nm appears as a rather weak bump just separating from the rising baseline, yet the addition of LiCl enhances this absorption feature notably (in MeCN).[17] In turn, $BiCl_3$ alone displays a broad absorption band below 350 nm (in MeCN) which then significantly sharpens and undergoes a bathochromic shift in the presence of TBACl.[3] The experimental observation of the favoured stoichiometry of 2 equivalents of Cl-ligands to one bismuth centre has also been supported computationally by the group of Hunt who identified the $[BiCl_5]^{2-}$ as the most stabile monomer of Bi^{3+} in the excess of chloride ligands (Figure 3.2).[18] Furthermore, geometry optimization within the same study suggested slight conformational changes when moving from the gas phase to an implicit solvent environment. For $[BiCl_5]^{2-}$, the optimal geometry was suggested to be square pyramidal while for bismuth bromides (which exist equally well as $[BiBr_4]^-$ and $[BiBr_5]^{2-}$) tetrahedral, sawhorse and square pyramidal conformers are possible. Bismuth iodide, which preferentially forms $[BiI_4]^-$, the tetrahedral and sawhorse complexes are both formed.

Having established the chlorine-radical generation with $BiCl_3$, we then searched to broaden the synthetic possibilities with bismuth LMCT. For this direction, we were particularly intrigued by the activation of carboxylic acids which was briefly touched upon

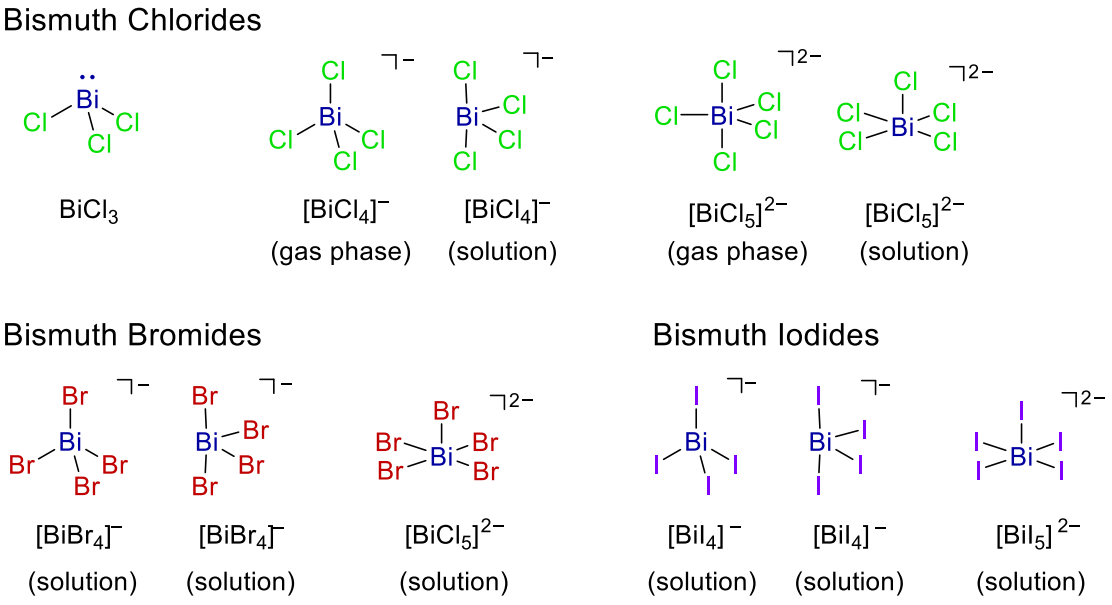

Figure 3.2. Calculated complexes and their conformers for bismuth halides.[18]

during the first publication.[3] Furthermore, the shift from HAT-protocols to decarboxylations would also allow us to move from acetonitrile to a less polar dichloromethane, which

would further favour the contact-ion pair formation. Although several bismuth carboxylates have been characterized over the years[19–22] together with the solidification of decarboxylative LMCT protocols[23], to the best of our knowledge no reports on molecular decarboxylations on bismuth have been published. Furthermore, during our initial studies we soon identified the ability of bismuth triflate to carry out what on paper seemed like a net-oxidative, decarboxylative C–N coupling. This initial hit left us both excited and puzzled. While the same overall transformation has been previously achieved with both copper and iron, the elementary reaction step with the key carbon-centred radical differs notably depending on the metal.[24,25] Copper(II), a stable radical itself, often reacts by trapping the carbon-centred radicals and converts them to (free) carbocations (Scheme 3.1, a).[24] Iron, in contrast, undergoes a radical-ligand transfer to forge a C–Cl bond which is then replaced by a nucleophilic substitution to form the products (Scheme 3.1, b).[25] In our case, however, Bi(III) as a closed-shell species was not as likely to undergo a similar radical trapping as the Cu(II)[26,27], while the Bi(II) radical had so far being known to undergo a rapid dissociation when not supported by bulky ligands.[12,28] Yet the radical-ligand transfer reactivity similarly to iron had also not been extensively described and would be unlikely on a stereoelectronic basis. Herein, we report a successful utilization of bismuth(III) triflate in decarboxylative C–N coupling reactions (Scheme 3.1, c). Our mechanistic studies lead us to proposed a spatial proximity between the reactive Bi(II) radical and organic reaction partners as the key factor enabling selective cross-couplings marking a pronounced example of preassembly in molecular catalysis.

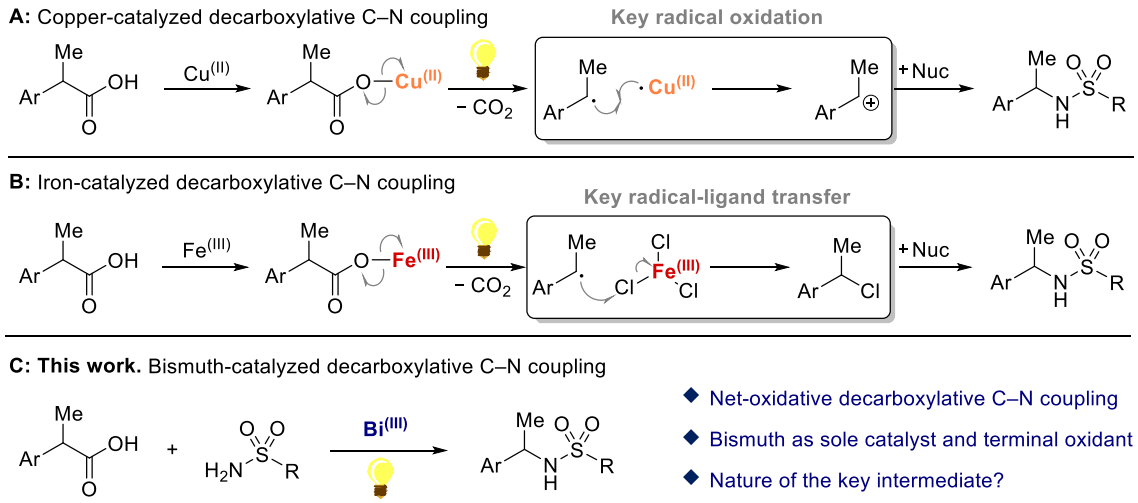

Scheme 3.1. Decarboxylative C–N cross-coupling with copper (a)[24], iron (b)[25] and bismuth (c) LMCT reactivity.

3.3 Results and Discussion

3.3.1 Optimization

We started our optimization studies by using equimolar amounts of the carboxylic acid **3.1**, sulfonamide **3.2** and a base to identify the best-performing bismuth precursor under 365 nm irradiation. Following our previous study on bismuth LMCT photoactivity[3], we decided to focus our screening on inexpensive and commercially available salts (Tables 3.1 and S3.2). We found that the reaction outcome was highly dependent on the bismuth precursor utilized. While many salts (such as $Bi(NO_3)_3$, $Bi(OAc)_3$, and BiOCl) did not give any conversion of the starting material, both $BiCl_3$ and $Bi(OTf)_3$ were able to decarboxylate the benzylic acid **3.1** (Entries 1 and 2). However, only $Bi(OTf)_3$ afforded the desired cross-coupling product **3.3**, whereas with $BiCl_3$ the homocoupling of the benzylic radical was mainly observed. Similarly to previous observations on LMCT decarboxylations, we also found the combination of a hydrogencarbonate base and DCM as a solvent

Table 3.1. Optimization of the reaction conditions.

3.1 (0.1 mmol) + **3.2** (0.1 mmol) → **3.3**

Entry		Deviation	Yield (%)[a]
1		As above	32
2		$BiCl_3$ instead of $Bi(OTf)_3$	*traces*
3[b]	**A**	Sulfonamide (3.5 equiv.)	60
4[b]	**B**	Acid (3.0 equiv.)	60
5		$Bi(OTf)_3$ (20 mol%) + NFSI (2 equiv.)	11
6		$Bi(OTf)_3$ (20 mol%) + $(NH_4)_2S_2O_8$ (2 equiv.)	*traces*
		Control Experiments	
7		No Bismuth	n.d.
8		No Light	n.d.
9		60 °C dark	n.d.

[a] Calibrated GC-FID yield. [b] $KHCO_3$ (3 equiv.). NFSI = *N*-Fluorobenzenesulfonimide.

to give the best yield.[24] After a broad screening of possible variables (see SI), a significant yield improvement was obtained when either the sulfonamide (Entry 3) or the acid (Entry 4) was used in excess. This observation led to two optimal conditions: in **conditions A** the acid partner serves as the limiting reagent combined with 3.5 equivalents of the nucleophile, whereas in **conditions B** the sulfonamide counterpart is the limiting reagent, and 3.0 equivalents of the carboxylic acid are used. Whereas conditions A worked reliably over a broad variety of carboxylic acids, conditions B proved to be particularly useful in the cases where the sulfonamides were only sparingly soluble in DCM. Apart from the solubility considerations, the dual nature of our optimized conditions leaves room for a flexible choice of the reagent in excess depending on other factors such as starting material availability and costs. Using $Bi(OTf)_3$ in catalytic amounts in combination with a chemical oxidant, such as NFSI, peroxides or persulfates, led only into trace amounts of the product (Entries 5 and 6, Table S3.8). Although the reoxidation of bismuth at the end of the product-forming sequence would be mechanistically interesting, the simplicity and economic feasibility of using stoichiometric bismuth triflate is well comparable to commonly used oxidants. Finally, control experiments confirmed the necessity of bismuth salt and photochemical nature of our transformation. In the absence of a bismuth source, no product could be detected (Entry 7). No product was also observed in the absence of light either at room temperature or upon heating to 60 °C (Entries 8 and 9).

3.3.2 Scope of the carboxylic acids

Next, we studied the scope of the transformation. (±)-2-Phenylpropanoic acid (**3.1**) was smoothly converted into the C–N coupling products with *p*-methylphenyl and *p*-methoxyphenyl sulfonamides (products **3.4** and **3.5**). Due to the improved chromatographic separation, the latter sulfonamide was chosen as the model nucleophile for the rest of the scope. Different methylation patterns were well tolerated, and particularly the *ortho*-methylated acid gave a high yield (**3.6**, **3.7** and **3.8**). A *tert*-butyl group was also compatible as an electron donating substituent in the *para*-position (**3.9**). We also noticed that the reactions of the electron rich carboxylic acids were best carried out with 385 nm irradiation to avoid undesired degradation. For electron withdrawing substituents, halogens such as fluorine (**3.10**) and chlorine (**3.11**) together with a trifluoromethoxy group (**3.12**), gave comparable yields to the standard compound. The brominated compound **3.13** was obtained in a somewhat lower yield due to the debromination accompanying the desired product-forming events.

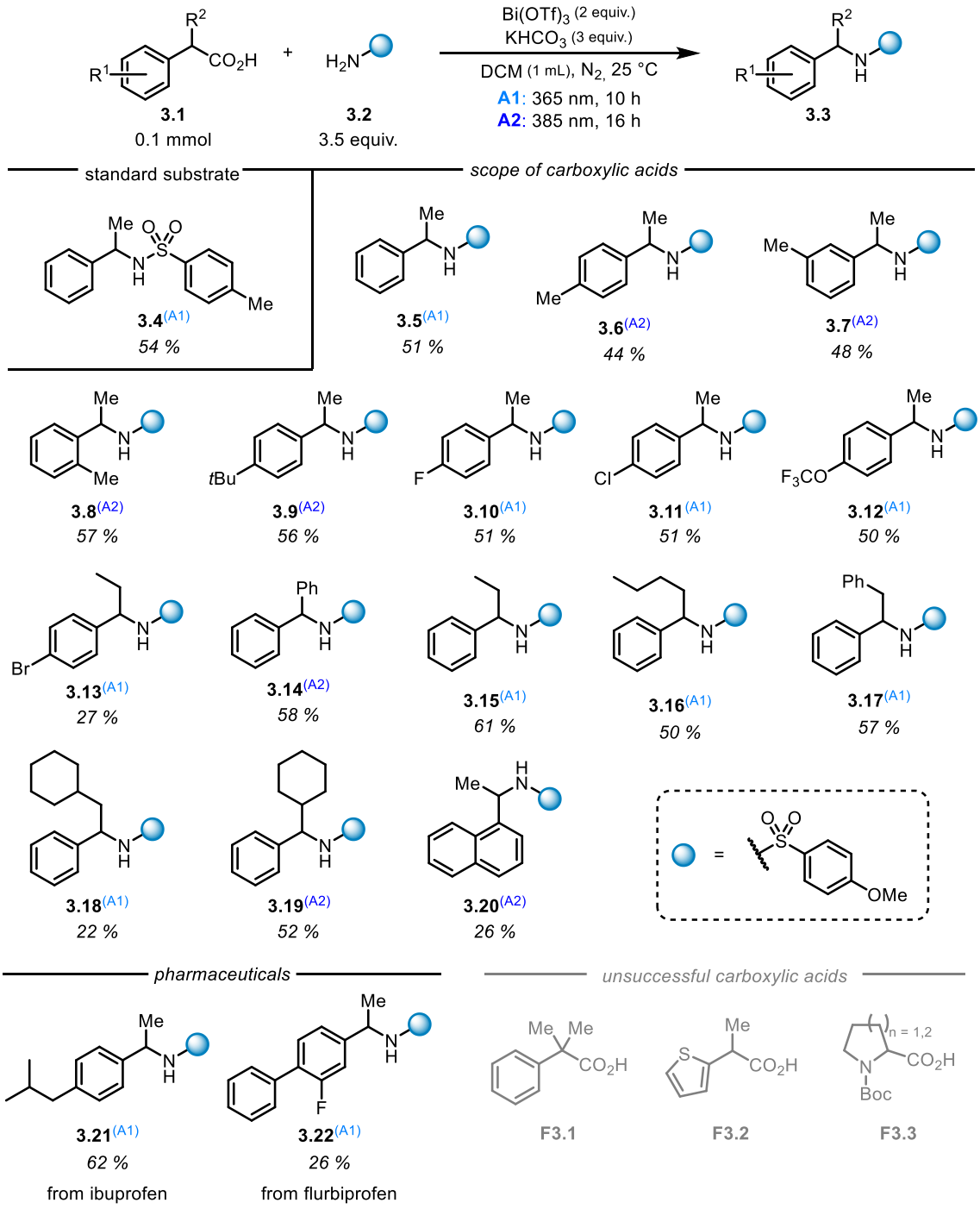

Scheme 3.2. Scope of carboxylic acids.

Several *alpha*-substituted carboxylic acids were also successfully converted to the products. A phenyl, ethyl and *n*-butyl substituents were well compatible (**3.14**, **3.15** and **3.16**). An aliphatic cyclohexyl ring was also tolerated both with a CH_2-linker (**3.18**) and when directly attached to the benzylic position (**3.19**). The positive results obtained here were particularly encouraging as they demonstrate the significant selectivity of our method towards the C–N coupling over the alternative alkene formation. Particularly worth mentioning here is the clean conversion of 2,3-diphenylpropanoic acid to the desired coupling

product **3.17** without any observable stilbene generation. The 1-napthyl substituted carboxylic acid also underwent the desired transformation, although the yield might have been slightly reduced by the direct excitation of the aromatic system (**3.20**). Finally, we applied our method for the late-stage modification of pharmaceutically active compounds, giving the products **3.21** and **3.22** stemming from ibuprofen and flurbiprofen, respectively.

Regarding the limitations, tertiary carboxylic acids (such as **F3.1**) typically underwent decarboxylation but most likely due to the steric hindrance, only homocoupling of the formed benzylic radical was observed. Unfortunately, heteroaromatic substrates also proved challenging, an no product could be observed with thiophene derivative **F3.2**. Aminoacids, such as **F3.3**, formed an insoluble species with bismuth in DCM, and no further reactivity was observed.

3.3.3 Scope of the nucleophiles

We then turned our attention to the scope of the nucleophiles. The phenyl-substituted sulfonamide yielded the desired product **3.23** in a synthetically useful 41% yield, whereas an addition of a methyl group to the *para*-position gave a higher isolated yield of **3.24**. In terms of electronic effects, *para*-trifluoromethyl and *ortho*-fluorine substituted sulfonamides (**3.25** and **3.27**) resulted in slightly lowered yields, implying that extra electron density on the sulfonamide, which would also increase the nucleophilicity, is beneficial for the reaction. When electron withdrawing substituents were placed in non-conjugated *meta*-positions, high yields were retained (**3.28**). Notably, selective coupling reactions were also obtained in the presence of a competing nucleophilic CN-group (**3.26**) or a competing electrophilic ester-group (**3.31**). For the electron donating group, a mesityl ring and 1-napthyl substituents (**3.29** and **3.30**) as well as a 4'F-biphenyl group (**3.33**) could also be included in the sulfonamide. The thiophene-derived nucleophile gave the desired product **3.32** in 22% yield. Steric demand at secondary *N*-phenyl sulfonamides was well tolerated. *N*-phenyl-methylphenyl sulfonamide gave the tertiary product **3.34** in a 55% yield. Moreover, sulfonamides with an aliphatic ring attached to the sulfonyl group were also compatible giving products **3.35** and **3.36** in over 60% yield. The highly substituted sulfonamide product **3.37** could also be obtained. Finally, the pharmaceutically

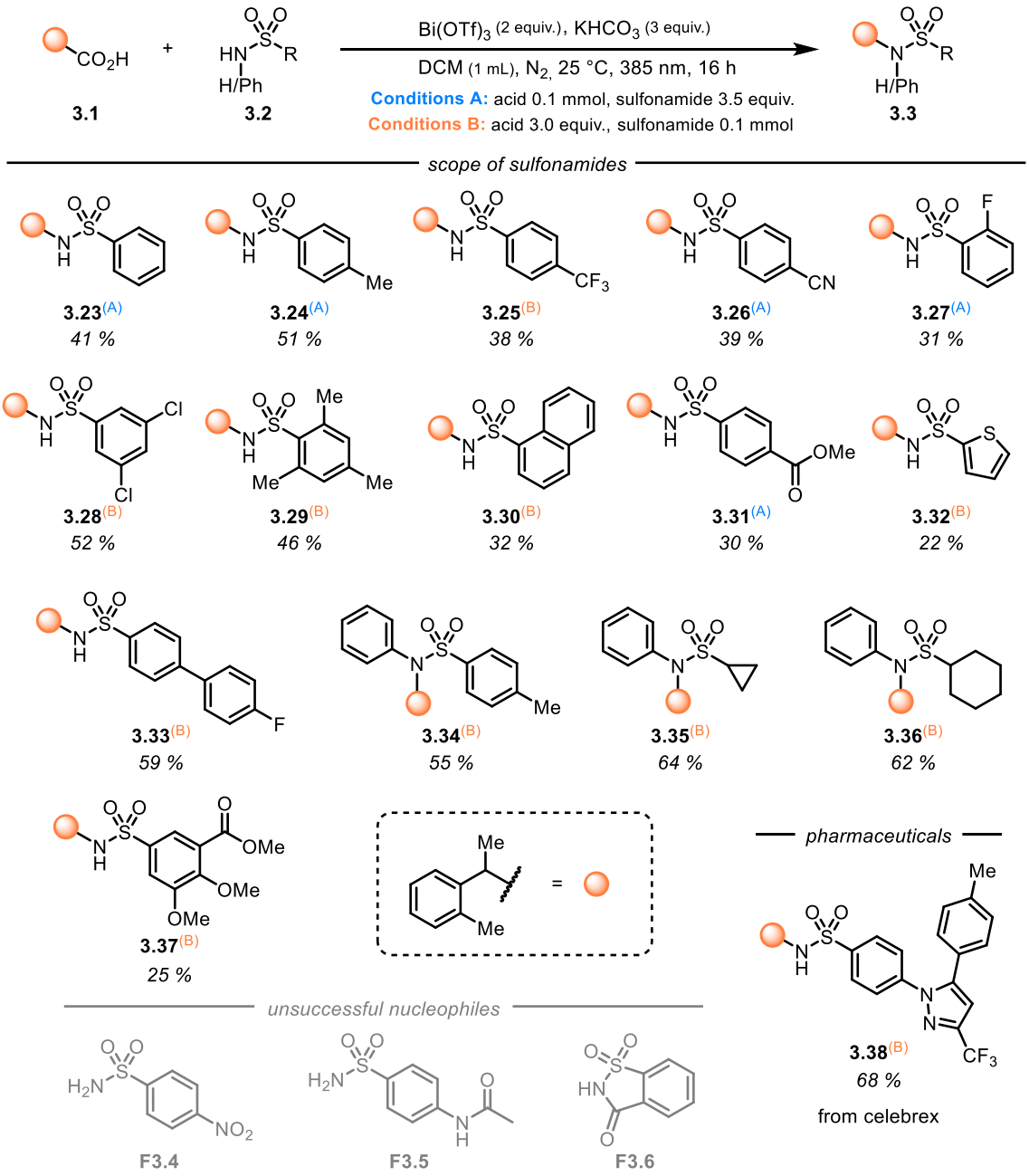

Scheme 3.3. Scope of nucleophiles.

active compound celebrex could be derivatized with our method giving the product **3.38** in a good yield of 68%. With respect to the limitations on the sulfonamide side, a nitro substituent (**F3.4**) and an amide functionality (**F3.5**) were incompatible with the reaction and no conversion of the starting materials was observed. The cyclic sulfonamide saccharin **F3.6** also failed to undergo the desired reaction perhaps by forming an unreactive chelated ligand to bismuth.

3.3.4 Mechanistic studies

To gain a better understanding of our reaction, a set of mechanistic studies was carried out. We started by measuring the UV-vis spectra of all the reaction components and their combination. As seen from Figure 3.3a, $Bi(OTf)_3$ had its absorption maximum at 230 nm and did not show any absorbance above 300 nm (grey dotted line).The carboxylic acid **3.1** (orange line) and sulfonamide **3.2** (blue line) both exhibited their absorption band between 250 nm and 280 nm, but no absorption could be detected in the range of irradiation. The addition of $Bi(OTf)_3$ to the mixture of the carboxylic acid and the sulfonamide significantly intensified the absorption features accompanied by a prolonged tailing (yellow line). Indeed, the tailing of the absorbance reached the area of the irradiation wavelength, thus confirming the role of the *in situ* formed bismuth-centred assembly as the light-harvesting species (zoom-in spectrum). We then measured the kinetic profile of our reaction (Figure 3.3b). From the measurement spanning over the first four hours of irradiation, we could see that the product formation was rapid at the beginning of the reaction (0–20 min), after which the rate of the reaction started to gradually decrease. The product formation was observed immediately upon the start of irradiation, thus supporting our hypothesis that the active bismuth assembly is pre-formed in the mixture. The initial kinetics, in turn, followed a linear trend without detectable build-up of intermediates (Figure 3.3c). The accumulation of a black solid during the reaction suggests that the full reduction of bismuth to its metallic form takes place, perhaps *via* disproportionation of bismuth(II) and/or bismuth(I), both of which are described as unstable species in the literature.[29,30]

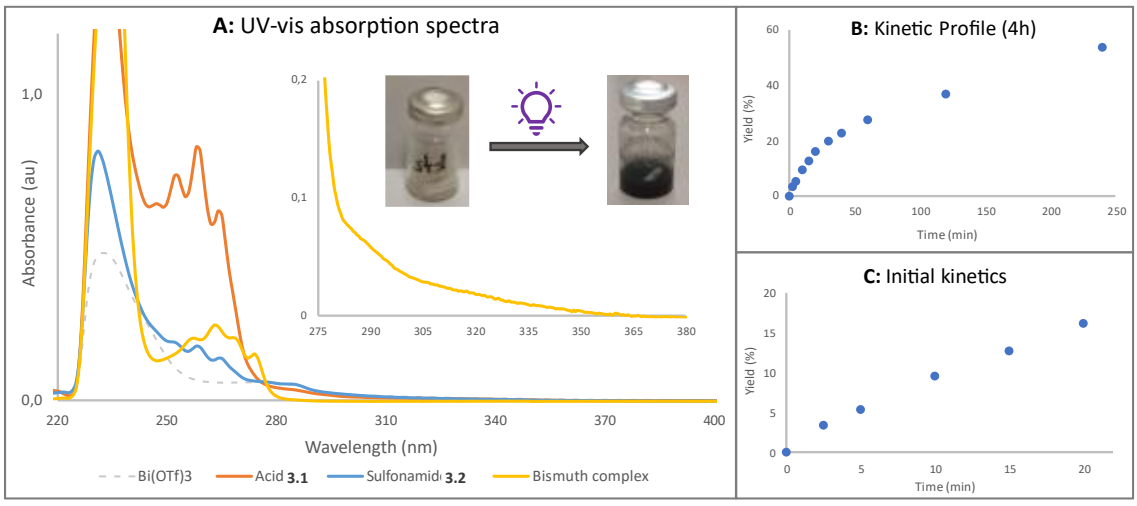

Figure 3.3. UV-vis spectrum of the reaction components and their mixture (a), kinetic profile of the reaction (b) and initial kinetics (c).

The final C–N bond-forming step could either follow an inner-sphere reductive elimination pathway or go *via* an outer-sphere mechanism. Literature reports of decarboxylative C–N coupling reactions with copper and iron suggest an outer-sphere mechanism.[24,25] To evaluate the outer-sphere ionic nucleophilic coupling mechanism proceeding *via* a carbocation, we rationalized that the presence of this intermediate would most likely lead to a broad compatibility of nucleophiles. Instead, with our bismuth system, alternative nucleophiles such as pyrazole, amides, amines, and alcohols could not be coupled so far (Scheme 3.4a). Furthermore, side-reactions like esterification or desaturation *via alpha*-deprotonation of a carbocation were rarely observed in our study. On the carboxylic acid side, sterically demanding substrates (such as **F3.1**), were not tolerated. Taken together, the C–N coupling step in our reaction most likely follows a reductive elimination pathway. When bismuth is used as a limiting reagent, the highest efficiency of bismuth as a consecutive one electron oxidant is achieved (96% yield, bismuth as limiting reagent, Scheme 3.4b). Furthermore, the radical nature of the decarboxylation process was suggested by the trapping of the benzylic radical with TEMPO (Scheme 3.4c). Finally, the light on/off experiment shows the necessity of continuous irradiation for the reaction progress, thus rendering a radical chain mechanism unlikely (Figure 3.4d).

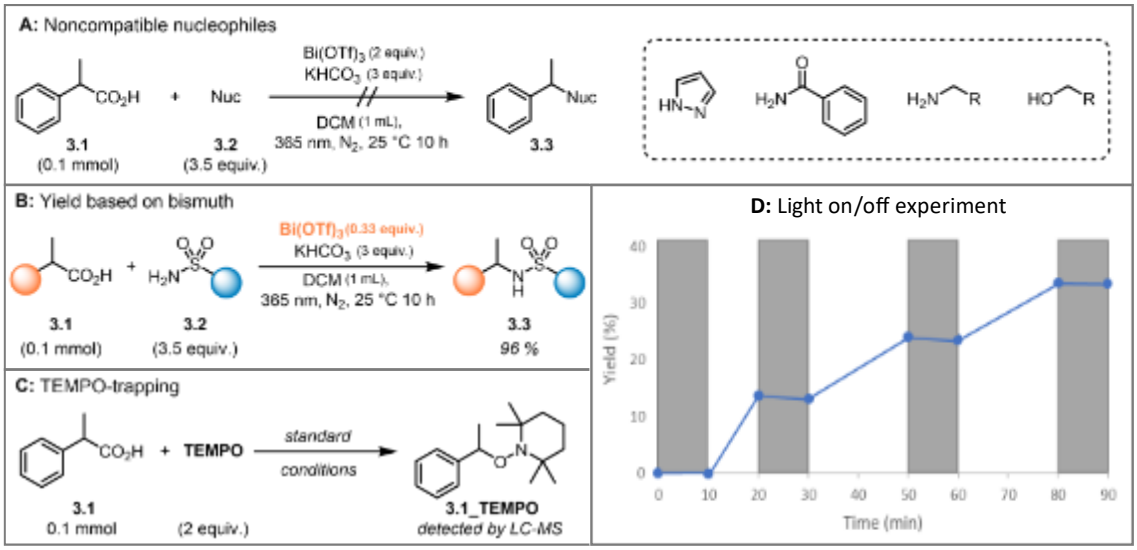

Scheme 3.4. Key mechanistic studies: investigation of alternative nucleophiles (a), reaction with bismuth as limiting reagent (b), TEMPO-trapping study (c) and light on/off experiment (d).

Despite our best efforts in the mechanistic studies, the exact coordination sphere around bismuth remains unclear. Quite notably, in both copper and iron catalysed systems strictly one equivalent of carboxylic acid had to be used for the productive reaction[24,25] whereas our system could also thrive with a significant excess of the acid. With copper, the restriction to one equivalent of carboxylic acid could be rationalized based on a UV-vis titration of the carboxylate ligand into $Cu(OTf)_2$. Therein the initially formed LMCT band around 304 nm started to diminish upon the carboxylate amount exceeding one equivalent, eventually forming a new band at 260 nm. Due to this shift in absorption maximum, only poor overlap with the LEDs emission band could be detectable. For us, though, we believe that in our system a dynamic exchange between the ligands would eventually lead to the photoactive complex, from which the decarboxylation could take place. Analogously to our observations with $BiCl_3$ with excess chloride ligand, an anionic complex could also be formed here. In that case the countercation would likely be potassium from the used base ($KHCO_3$), and in low-dielectric DCM a contact-ion pair is expected. While the exact mode of the coordination of the sulfonamide counterpart is somewhat challenging to detect, previous studies of the reactivity of bismuth(III)-amido complexes have proposed that a coordination bond would precede covalent bonding.[31,32] Herein it should also be mentioned that our attempts to crystallize the bismuth complexes using differing stoichiometries of the phenylacetic acid **3.1** and a sulfonamide nucleophile with $Bi(OTf)_3$ were unsuccessful.

Based on our mechanistic considerations and the previous literature discussed above, the following mechanism is proposed (Scheme 3.5). The product-forming sequence starts with the coordination of the respective carboxylic acid **3.1** to the bismuth centre assisted

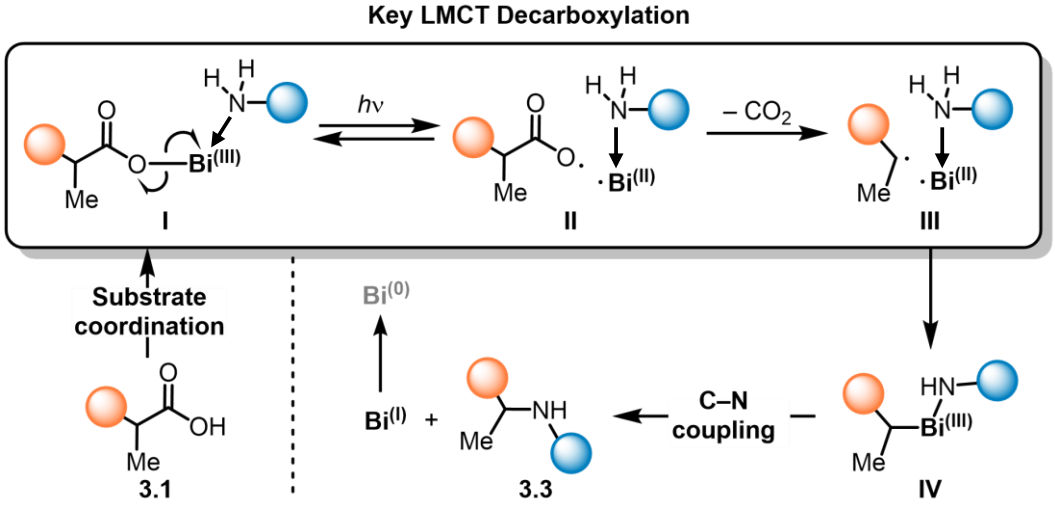

Scheme 3.5 Proposed mechanism.

by $KHCO_3$. The formed bismuth(III) carboxylate assembly **I** is irradiated resulting in the homolysis of the Bi–O bond. The formed carboxy radical **II** can then either recombine with the Bi(II) regenerating the complex **I**, or undergo an irreversible decarboxylation to the carbon-centred radical. The preassembly of the complex **I** together with the codependent manner of the radical generation ensures the spatial proximity between the bismuth(II)radical and the carbon-centred radical in **III**, thus favouring their recombination. The so-formed organobismuth compound **IV** then undergoes a reductive elimination to forge the C–N bond upon the release of the product **3.3**. The bismuth(I) formed in this process is unstable, and eventually undergoes disproportionation to metallic bismuth.

3.4 Conclusions

In summary, we report the first direct decarboxylation on bismuth, giving access to C–N cross-coupling products with sulfonamides. Our method features mild reaction conditions, tolerates either reaction partner in excess, and achieves highly selective coupling reactivity with the residual mass balance comprising mainly from the unreacted carboxylic acid. Mechanistically we believe that our reaction proceeds *via* initial coordination of the carboxylic acid to the bismuth, followed by a light-initiated Bi–O bond cleavage and decarboxylation. Preassembly enables the spatial proximity between the carbon-centred and Bi(II) radicals, and a swift radical-radical coupling takes place. Eventually, the C–N coupling products are formed perhaps by an inner-sphere reductive elimination. Although the exact nature of the photoactive bismuth complex could not be identified, based on previous reports and coordination behaviour of $BiCl_{3+n}^{n-}$, we have reason to believe that a contact-ion pair between the anionic bismuth complex and potassium countercation might be present.

3.5 Experimental

3.5.1 General

Chemicals and solvents were purchased from commercial suppliers (Sigma Aldrich, TCl, BLD Pharma, Alfa Aesar, Acros, Fluka or Thermo Fischer) and, unless otherwise noted, used without further purification. Specifically, for the benchmark reaction the following chemicals were used: $Bi(OTf)_3$ (99% purity, Thermo Scientific), (±)-2-phenylpropionic acid (98% purity, ABCR), *p*-toluenesulfonamide (99% purity, Acros), $KHCO_3$ (Merck) and DCM (99.8% purity, anhydrous, Sigma Aldrich). All air-and moisture sensitive reactions including photoreactions were set up using pre-dried N_2 as shielding gas, whereas dry solvents were obtained from commercial suppliers. Evaporation of organic solvents was carried out in a rotary evaporator at temperatures below 40 °C and under reduced pressure.

Analytical thin layer chromatography (TLC) was routinely used for the monitoring of starting material synthesis and to quantify the eluation of the product. Silica-gel precoated aluminium sheets (Macherey-Nagel, silica gel 60G/UV254, 0.2 mm) served as stationary phase, whereas the mobile phase consisted of solvents and solvent mixtures, the ratios of which are reported as v/v solutions. Visualization was performed with a 254 nm UV-light source combined with chromatographic dyes if so noted.

Flash column chromatography (FCC) was done either by hand or by a Biotage® IsoleraTM Spektra One machine. In the former case flash silica gel (Merck, particle size 40–63 μm, 230–440 mesh) was used as a stationary phase, whereas in the latter case prepacked Biotage® columns were used. For both techniques eluent mixtures, whenever possible consisting of pre-distilled petroleum ether (PE) and ethyl acetate (EtOAc), were used. For all eluents, the solvent ratios are reported as v/v ratios.

GC-FID and GC-MS measurements were performed on a GC 7890 from Agilent Technologies coupled with a FID detector. The system was equipped with a capillary column (HP-5MS UI, 30 m length, 0.25 mm diameter, 0.25 μM film) and run with He (flow rate 1mL/min) as a carrier gas. (**NOTE:** The use of H_2 as carrier gas in this project was found to result in a complex GC-spectrum, most likely due to reactions within the GC. Therefore, if change of carrier gas is desired, we recommend to test the suitability of the new

carrier by comparing against the spectrum obtained with helium). Unless otherwise noted, sample volume of 1 µL was injected (split injection, 40:1 split) at 280 °C with detector temperature 300 °C. The GC-MS measurements were done with a 7890AGC system with an Agilent 5975 MSD detector. For the GC program, the initial temperature of 40 °C was hold for 3 minutes, after which the temperature was increased on a rate of 15°C/min for over 16 minutes. The temperature was ramped until 280 °C, where the temperature was hold constant for 5 minutes. After this the temperature was increased with a rate of 25 °C/min for 48s, until the final temperature of 300 °C was reached, and hold again for 5 minutes. Finally, data accusation was done using Agilent ChemStation Rev.C.01.04.

Nuclear Magnetic Resonance Spectroscopy (NMR) was recorded at room temperature using a Bruker Avance 400 (400 MHz for ^{1}H, 101 MHz for ^{13}C, 376 MHz for ^{19}F) NMR spectrometer. All chemical shifts are reported δ-scale as part per million [ppm] (multiplicity, coupling constant *J*, number of protons) relative to the solvent residual peak. The coupling constants *J* are given in Herz [Hz] and the multiplicity of the signals are abbreviated as: singlet (s), broad singlet (br. s.), doublet (d), doublet of doublets (dd), doublet of doublet of doublets (ddd), triplet (t), doublet of triplets (dt), triplet of doublets (td), quartet (q), doublet of quartets (dq), pentet (p) and multiplet (m). For the NMR measurements deuterated solvents ($CDCl_3$ from deutero, DMSO-d_6 from Sigma Aldrich) were used. The spectra were processed using MestreNova 9.0.1.

High Resolution Mass Spectra (HRMS) were performed at the Central Analytical Laboratory of the departments of chemistry and pharmacy at the University of Regensburg. For measurements, > 1 mg of the sample submitted, which was later dissolved to acetonitrile, DCM or ethyl acetate. The samples were then injected either to a Jeol AccuTOF GCX or to an Agilent Q-TOF 6540 UHD instrument.

3.5.1.1 Photosetups

365 nm (2.0 W) setup

For the photoreactions run at 365 nm (1.5 W to 2.0 W) were performed using custom-made photoreactors depicted below (Figure S3.1). At the core of the photoreactors reside a metal block to which six single-spot LEDs of desired wavelength are mounted. On top of the LED block sits a hollow cooling block made out of stainless-steel through which a constant flow of water is possible. This cooling block also contains holes made to perfectly fit 5 mL crimp-cap vials, thus providing a sideway contact of the reaction vessels to the cooling system. Magnetic stirring for the reactions is imposed from underneath the LED blocks using Heidolph MR 3000 stirring plates. Finally, the water cooling is sustained with a Julabo Curio Co unit. **NOTE:** Due to the modular nature of these setups, they can be used to serve at any desired wavelength simply by changing the LED plate.

For safety, goggles containing UV-and blue-light filters ("orange goggles") should always be worn when working with the photoreactors. Empty vials ("dummy vials") should be placed to fill each reaction spot, and the top of the setups should be covered during the reaction to prevent exposure to diffracted light.

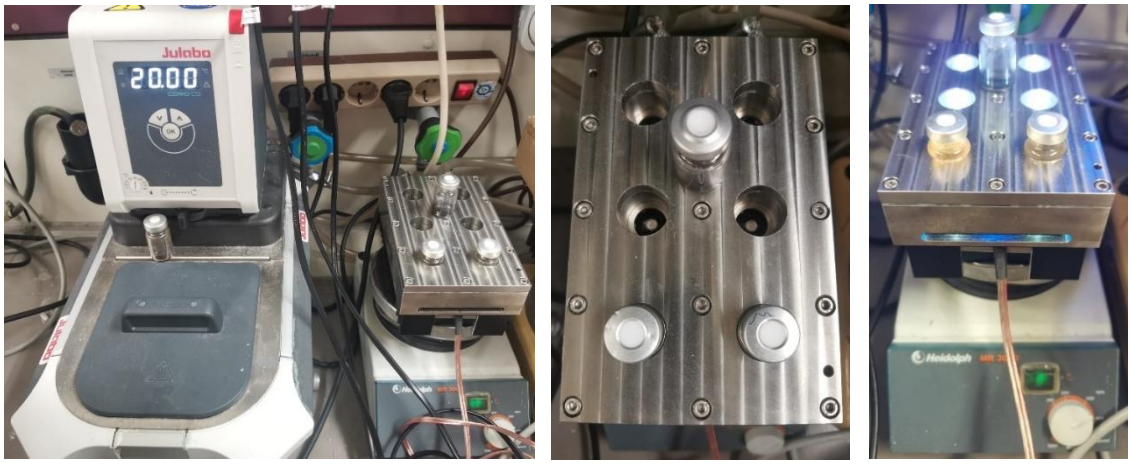

Figure S3.1. Pictures of the photosetup used for reactions run in 365 nm (1.5 W to 2.0 W optical power). General picture of the setup (left), picture from the top of the cooling block looking down to the LED plate (centre) and a sideway picture of the photosetup with lights on (right).

385 nm (0.5 W) setup

The photoreactions run at 385 nm (0.5 W) were performed using custom-made photoreactors designed to allow for an increased number of simultaneously screening (Figure S3.2). At the core of the photoreactors reside a stainless-steel block to which fifteen single-spot LEDs with emission centered around 385 nm are mounted. On top of the LED block sits a hollow cooling block made of stainless-steel, through which a constant flow of water is possible. This cooling block also contains fifteen holes made to perfectly fit 5 mL crimp-cap vials, thus providing a sideway contact of the reaction vessels to the cooling system. Magnetic stirring for the reactions is imposed from underneath the LED blocks using Cimarec i Poly 15-point stirring plates. Finally, the water cooling is sustained with a Julabo Curio Co water cooling unit. Due to the modular principle of the reactors, these several wavelengths can be utilized on these setups by changing the LED plate.

For safety, goggles containing UV-and blue-light filters ("orange goggles") should always be worn when working with the photoreactors. Empty vials ("dummy vials") should be placed to fill each reaction spot, and the top of the setups should be covered during the reaction to prevent exposure to diffracted light.

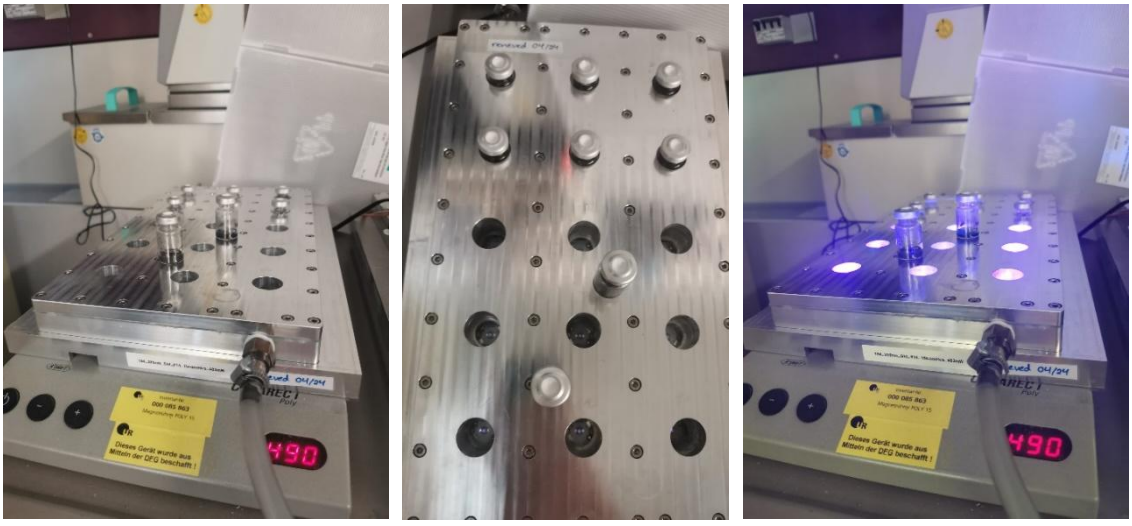

Figure S3.2. Pictures of the photosetup used for reactions run in 385 nm (0.5 W optical power). General picture of the setup (left), picture from the top of the cooling block looking down to the LED plate (centre) and a sideway picture of the photosetup with lights on (right).

3.5.1.2 Emission spectrum of the LEDs

The emission spectrum of the utilized LEDs (365 nm, Inolus and 385 nm, New Energy Luminus) was also measured to better characterize the actual emitted wavelengths of each setup. The measurement was carried out with Ocean Optics HR 2000+ spectrometer. The results are plotted in Figure S3.3.

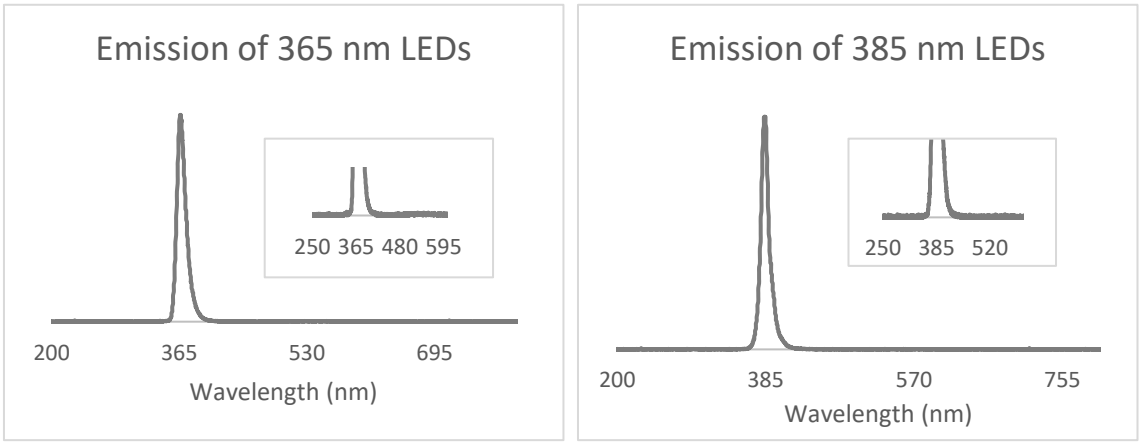

Figure S3.3. Emission spectra of the 365 nm LEDs (left) and 385 nm LEDs (right)

As can be easily observed from Figure S3.3, both of the utilized LEDs have their emission maxima around the desired wavelength, yet slight tailing is present with both LEDs. For the 365 nm LED, the actual emission starts around 350 nm and tails closer to 400 nm. For the 385 nm LEDs, on the other hand, the tailing is broader to both directions thus covering the area from around 360 nm to 440 nm.

3.5.1.3 Reaction mixtures before and after irradiation

The success of the protocol can be qualitatively assessed by the look of the reaction after the irradiation period. Before irradiation, the reaction mixture is (in most cases) a white milky solution mostly due to the incomplete solubility of $Bi(OTf)_3$ (Figure S3.4, left). After a successful reaction, the formation of fully reduced bismuth (elemental bismuth, “bismuth black”) gives the mixture a very dark, often black colour (Figure S3.4, right).

Figure S3.4. Pictures of the reaction mixture in a 5 mL crimp-cap vial before the reaction (left) and after irradiation (right).

3.5.1.4 GC-FID Calibration

For the calculation of the exact yields during the reaction optimization, a five-point calibration was carried out for the GC-FID. For this, a stock solution of the product **3.3** in DCM was prepared, five samples were taken followed by dilution to the desired concentrations (see molarities below). Equal amounts of mesitylene were then added as internal standard, and the samples were submitted for GC-FID.

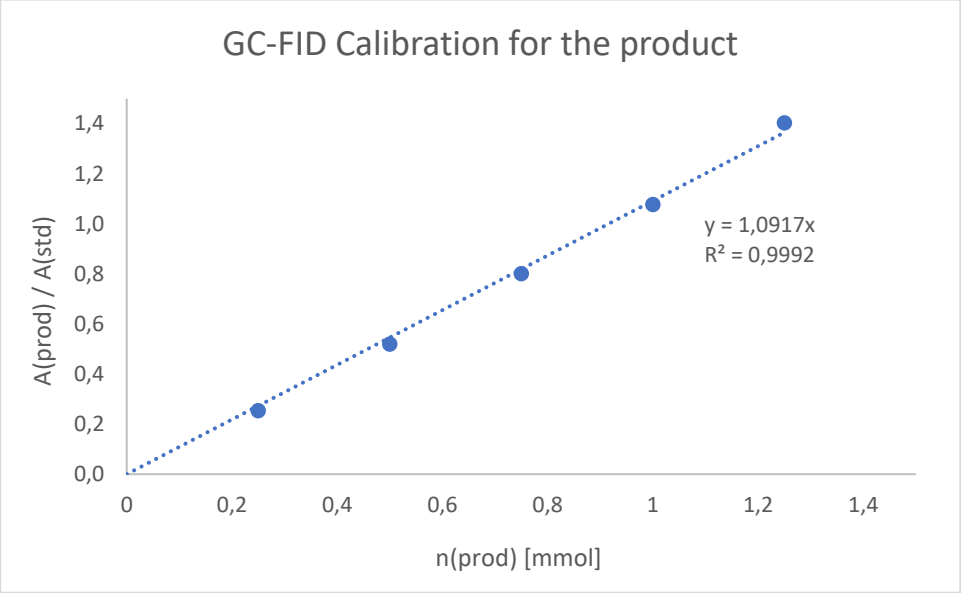

Figure S3.5. Calibration curve plotted with the ratio of product peak area to the area of internal standard as the y-axis and molar amount of the product given in each sample as x-axis as obtained from the GC-FID. Linear fit across the points and zero-point intersection added to obtain the equation for the line.

After the GC-FID analysis, the obtained areas of the peaks corresponding to the product and internal standard were then collected and plotted against the amounts of the product in moles. The linear fit was then applied, and the obtained curve set to intersect the origin. The equation of this line (y = 1,0917x) was utilized to calculate all GC-FID yields measured afterwards. Finally, the correlation coefficient (R^2) was analyzed to verify the accuracy of the calibration curve.

3.5.2 Full optimization studies

3.5.2.1 General procedure for the optimization studies

4-Methylbenzenesulfonamide (*n* equiv.) and base (*m* equiv.) and were weighed into a 5 mL crimp-cap vial equipped with a stirring bar. The vial was sealed and set under an inert atmosphere by evacuating and back-filling with N_2 three times. A 0.1 M stock solution of (±)-2-phenylpropanoic acid in a pre-dried solvent was prepared under N_2, and 1 mL of this solution was added to the reaction mixture. Residual oxygen was then removed by freeze-pump thaw (×3), after which the reaction was irradiated with 365 nm LEDs (2 W) while maintaining the temperature at 25 °C with a water-cooling block. After the given reaction time, a 100 µL of stock solution (1.0 M mesitylene in DCM) was added as internal standard and the reaction mixtures were filtered through a syringe filter. The reactions were then analyzed with GC-FID using helium as carrier gas, and the final yields were calculated against a five-point calibration curve of product **3.3** and mesitylene.

Optimization of solvent

Table S3.1. Full optimization of solvent.

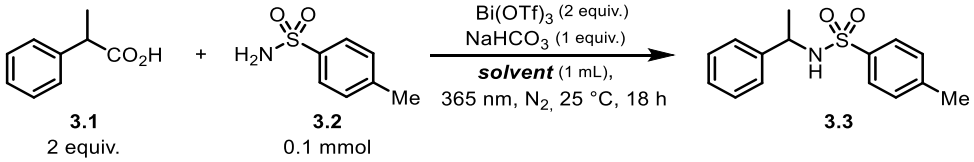

3.1 2 equiv. **3.2** 0.1 mmol **3.3**

Entry	Solvent	Yield (%)
1	DCM	28
2	DCE	11
3	$CHCl_3$	9
4	MeCN	*traces*
5	TFE	n.d.
6	HFIP	n.d.
7	Toluene	n.d.
8	H_2O	*traces*
9	DMSO	n.d.
10	DMA	n.d.
11	THF	n.d.
12	EtOAc	*traces*
13	Acetone	*traces*

Reaction conditions: $Bi(OTf)_3$ (130 mg, 0.20 mmol, 2.0 equiv.), 2-phenylpropanoic acid (30 mg, 0.20 mmol, 2.0 equiv.), $NaHCO_3$ (8.2 mg, 0.10 mmol, 1.0 equiv.) and 4-methylphenylsulfonamide (17.2 mg, 0.10 mmol, 1.0 equiv.) were dissolved into solvent in case (1 mL) under N_2. After irradiation with 365 nm (18 h) at 25 °C, internal standard was added and reactions analyzed with GC-FID. Abbreviations used: DCM = dichloromethane, DCE = dichloroethane, $CHCl_3$ = chloroform, MeCN = acetonitrile, TFE = trifluoroethanol, HFIP = hexafluoroisopropanol, DMSO = dimethylsulfoxide, DMA = dimethylacetamide, THF = tetrahydrofuran, EtOAc = ethyl acetate.

Optimization of bismuth source

Table S3.2. Full optimization of the bismuth source.

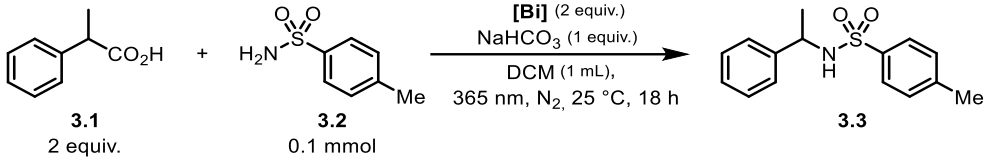

3.1 2 equiv. **3.2** 0.1 mmol **3.3**

Entry	Catalyst screening	Yield (%)
1	$Bi(OTf)_3$	28
2	$BiCl_3$	*traces*
3	BiF_3	n.d.
4	$BiBr_3$	n.d.
5	$BiPh_3$	10
6	$Bi^{(0)}$	n.d.
7	Bi_2O_3	n.d.
8	BiOCl	n.d.
9	$Bi(OAc)_3$	n.d.
10	$Bi(NO_3)_3$	n.d.

Reaction conditions: the bismuth source (0.20 mmol, 2.0 equiv.), 2-phenylpropanoic acid (30 mg, 0.20 mmol, 2.0 equiv.), $NaHCO_3$ (8.2 mg, 0.10 mmol, 1.0 equiv.) and 4-methylphenylsulfonamide (17.2 mg, 0.10 mmol, 1.0 equiv.) were dissolved into DCM (1 mL) under N_2. After irradiation with 365 nm (18 h) at 25 °C, internal standard was added and reactions analyzed with GC-FID.

Optimization of base

Table S3.3. Full optimization of bases.

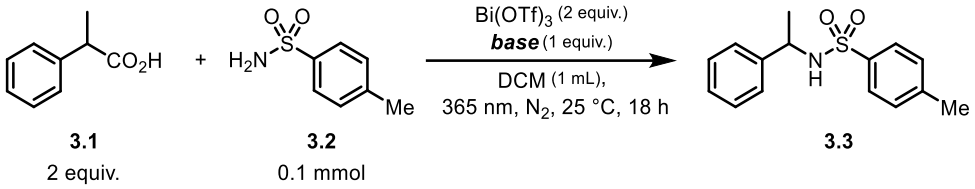

3.1 2 equiv. **3.2** 0.1 mmol **3.3**

Entry	Base	Yield (%)
1	none	*traces*
2	$NaHCO_3$	28
3	$KHCO_3$	37
4	K_2CO_3	14
5	K_3PO_4	14
6	K_2HPO_4	27
7	Na_2HPO_4	7
8	KO*t*Bu	30
9	DBU	*traces*
10	DABCO	30
11	2,6-Lutidine	5
12	TBD	*traces*
13	TMG	*traces*
14	Tetramethylpiperidine	*traces*

Reaction conditions: $Bi(OTf)_3$ (130 mg, 0.20 mmol, 2.0 equiv.), 2-phenylpropanoic acid (30 mg, 0.20 mmol, 2.0 equiv.), the base in question (0.10 mmol, 1.0 equiv.) and 4-methylphenylsulfonamide (17.2 mg, 0.10 mmol, 1.0 equiv.) were dissolved into DCM (1 mL) under N_2. After irradiation with 365 nm (18 h) at 25 °C, internal standard was added and reactions analyzed with GC-FID. Abbreviations used: DBU=1,8-diazabicyclo[5.4.0]undec-7-ene, DABCO=1,4-diazabicyclo[2.2.2]octane, TBD=1,5,7-triazabicyclo[4.4.0]dec-5-en, TMG=tetramethylguanidine.

Optimization of stoichiometry

Table S3.4. Full screening of the reaction stoichiometry.

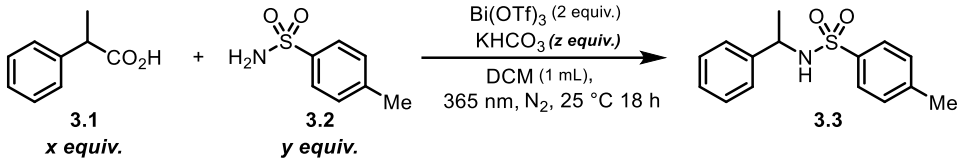

Entry	**3.1** (equiv.)	**3.2** (equiv.)	**Base** (equiv.)	**Yield** (%)
1	1.0	1.0	1.0	38
2	2.0	1.0	0.5	27
3	2.0	1.0	1.5	38
4	2.0	1.0	2.0	42
5	2.0	1.0	2.5	22
6	3.0	1.0	1.0	45
7	3.0	1.0	2.0	60
8	3.0	1.0	3.0	46
9	4.0	1.0	3.0	16
10	1.0	2.0	2.0	16
11	1.0	2.0	3.0	48
12	1.0	2.0	1.0	40
13	1.0	3.0	2.0	25
14	1.0	3.0	3.0	62
15	1.0	4.0	2.0	62
16	1.0	4.0	3.0	31
17	1.0	3.5	2.0	52
18	1.0	3.5	3.0	60

Reaction conditions: $Bi(OTf)_3$ (130 mg, 0.20 mmol, 2.0 equiv.), 2-phenylpropanoic acid (x equiv.), $KHCO_3$ (y equiv.) and 4-methylphenylsulfonamide (z equiv.) were dissolved into DCM (1 mL) under N_2. After irradiation with 365 nm (18 h) at 25 °C, internal standard was added and reactions analyzed with GC-FID.

Optimization of concentration

Table S3.5. Full screening of reaction concentration.

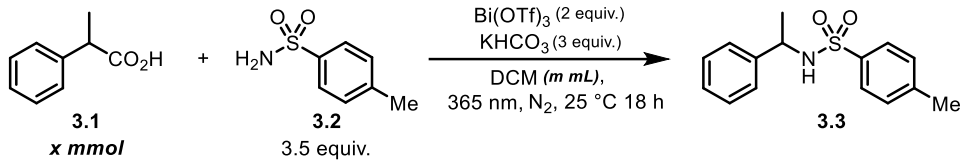

Entry	**n(acid)** (mmol)	**V(DCM)** (mL)	**Concentration** (M)	**Yield** (%)
1	0.05	1	0.05	31
2	0.075	1	0.075	33
3	0.15	1	0.15	51
4	0.2	1	0.2	30
5	0.1	0.5	0.2	20
6	0.1	0.75	0.13	31
7	0.1	1.0	0.1	60
8	0.1	1.5	0.66	49
9	0.1	2.0	0.05	47

Reaction conditions: $Bi(OTf)_3$ (2.0 equiv.), 2-phenylpropanoic acid (x mmol, 1.0 equiv.), $KHCO_3$ (3.0 equiv.) and 4-methylphenylsulfonamide (3.5 equiv.) were dissolved into DCM (m mL) under N_2. After irradiation with 365 nm (18 h) at 25 °C, internal standard was added and reactions analyzed with GC-FID.

Optimization of irradiation wavelength and temperature

Table S3.6. Full screening of irradiation wavelength and temperature.

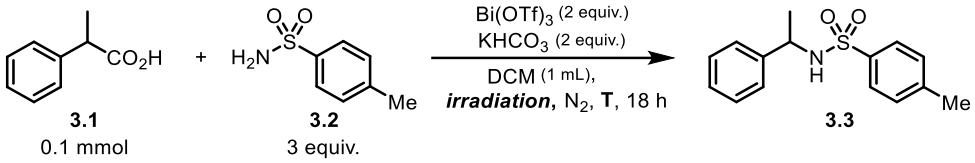

3.1 0.1 mmol + **3.2** 3 equiv. → **3.3**

Entry	**LED**	**Temperature** (°C)	**Yield** (%)
1	365 nm (3W)	25	39
2	365 nm (0.8W)	25	4
3	340 nm (0.8W)	25	6
4	385 nm (0.8W)	25	44
5	385 nm (3W)	25	43
6	365 nm (2W)	10	34
7	365 nm (2W)	15	39
8	365 nm (2W)	20	55
9	365 nm (2W)	25	60
10	365 nm (2W)	30	42

Reaction conditions: $Bi(OTf)_3$ (130 mg, 0.2 mmol, 2.0 equiv.), 2-phenylpropanoic acid (15.0 mg, 0.1 mmol, 1.0 equiv.), $KHCO_3$ (30.0 mg, 0.3 mmol, 3.0 equiv.) and 4-methylphenylsulfonamide (65.5 mg, 0.35 mmol, 3.5 equiv.) were dissolved into DCM (1 mL) under N_2. After irradiation with the wavelength in question for the given times at given temperatures, internal standard was added and reactions analyzed with GC-FID.

Optimization of bismuth loading

Table S3.7. Full optimization of bismuth triflate loading.

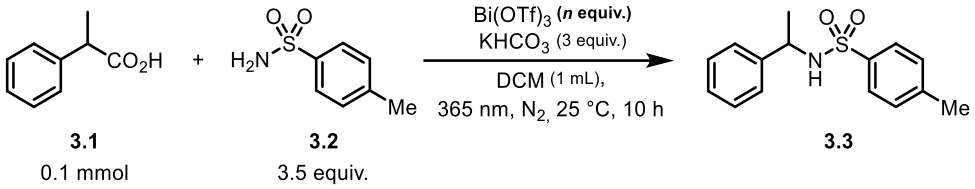

3.1 0.1 mmol | **3.2** 3.5 equiv. | **3.3**

Entry	Bi Loading	Yield (%)
1	1.0 equiv.	22
2	1.5 equiv.	44
3	1.6 equiv.	44
4	1.7 equiv.	60
5	2.0 equiv.	60
6	2.5 equiv.	52

Reaction conditions: $Bi(OTf)_3$ (n equiv.), 2-phenylpropanoic acid (15.0 mg, 0.1 mmol, 1.0 equiv.), $KHCO_3$ (30.0 mg, 0.3 mmol, 3.0 equiv.) and 4-methylphenylsulfonamide (65.5 mg, 0.35 mmol, 3.5 equiv.) were dissolved into DCM (1 mL) under N_2. After irradiation with 365 nm for 10 h at 25 °C, internal standard was added and reactions analyzed with GC-FID.

Although identical yields could be obtained with both 1.7 and 2.0 equivalents of $Bi(OTf)_3$, the conditions using 2.0 equivalents of bismuth proved better reproducible over multiple repetitions of the reaction. Hence, this stoichiometry was eventually used further on.

Screening of terminal oxidant

Table S3.8. Full optimization of the terminal oxidant.

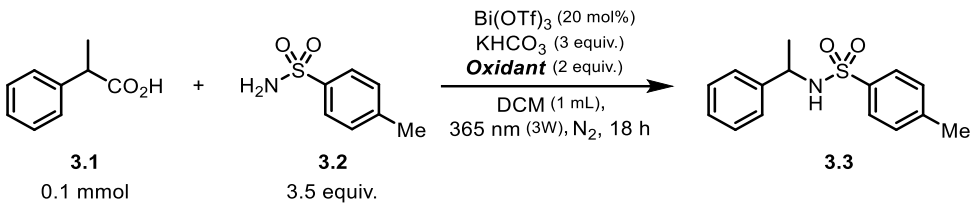

3.1 0.1 mmol **3.2** 3.5 equiv. **3.3**

Entry	Oxidant	Yield (%)
1	$Bi(OTf)_3$	60
2	none	11
3	Air	n.d.
4	Oxone	*traces*
5	$Na_2S_2O_8$	*traces*
6	$K_2S_2O_8$	*traces*
7	$(NH_4)_2S_2O_8$	5
8	NFSI	11
9	PIDA	14
10	Benzoyl peroxide	*traces*

Reaction conditions: $Bi(OTf)_3$ (13.0 mg, 0.02 mmol, 20 mol%), 2-phenylpropanoic acid (15.0 mg, 0.1 mmol, 1.0 equiv.), $KHCO_3$ (30.0 mg, 0.3 mmol, 3.0 equiv.), 4-methylphenylsulfonamide (65.5 mg, 0.35 mmol, 3.5 equiv.) and the terminal oxidant (2.0 equiv.) were dissolved into DCM (1 mL) under N_2. After irradiation with 365 nm for 18 h at 25 °C, internal standard was added and reactions analyzed with GC-FID. Abbreviations used: NFSI=*N*-fluorobenzenesulfonimide, PIDA=(diazetoxyiodo)benzene.

Control experiments

Table S3.9. Control experiments.

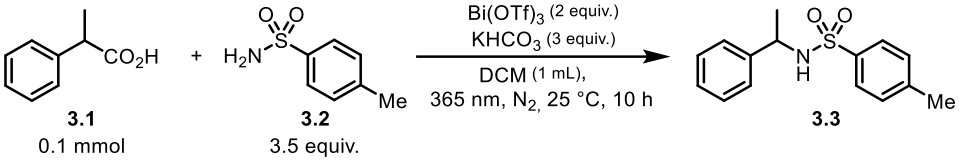

Entry	Variation	Yield (%)
1	Under air	*traces*
2[a)]	$BiBr_3$ + $Na(OTf)_3$	n.d.
3	No bismuth	n.d.
4	No light	n.d.
5	60 °C dark	n.d.

[a)] $BiBr_3$ (2 equiv.) + $Na(OTf)_3$ (2 equiv) used instead of $Bi(OTf)_3$. Reaction conditions: $Bi(OTf)_3$ (130 mg, 0.20 mmol, 0.2 equiv.), 2-phenylpropanoic acid (15.0 mg, 0.1 mmol, 1.0 equiv.), $KHCO_3$ (30.0 mg, 0.3 mmol, 3.0 equiv.) and 4-methylphenylsulfonamide (65.5 mg, 0.35 mmol, 3.5 equiv.) were dissolved into DCM (1 mL) under N_2. After irradiation with 365 nm for 10 h at 25 °C, internal standard was added and reactions analyzed with GC-FID.

3.5.3 Synthesis and characterization of products

GP1: Photocatalyzed C–N coupling, carboxylic acid as the limiting reagent

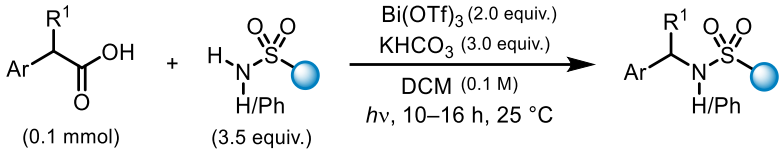

Four identical reactions were set up as following: Sulfonamide (0.35 mmol, 3.50 equiv.), $KHCO_3$ (30.0 mg, 0.30 mmol, 3.00 equiv.), $Bi(OTf)_3$ (130 mg, 0.20 mmol, 2.00 equiv.) and, if solid, the corresponding carboxylic acid (0.10 mmol, 1.00 equiv.) were weighed into a 5 mL crimp-cap vial equipped with a stirring bar. The vials were sealed and set under an inert atmosphere by evacuating and back-filling with N_2 (×3). If liquid, a stock solution of the corresponding carboxylic acid was prepared in dry DCM (0.1 M), and either 1 mL of this solution or 1 mL of dry DCM was added *via* syringe to the reaction mixture. The reaction mixture was degassed three times with a freeze-pump thaw, after which the reaction was irradiated either with 365 nm (1.8 W) for 10 hours or with 385 nm (0.5 W) for 16 hours while maintaining the temperature at 25 °C with a water-cooling block.

GP2: Photocatalyzed C–N coupling, sulfonamide as the limiting reagent

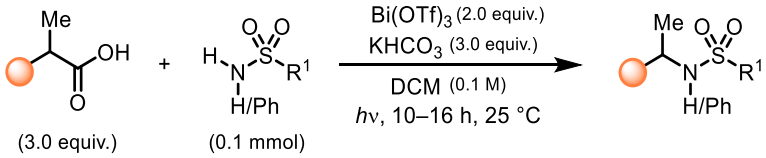

Four identical reactions were set up as following: Sulfonamide (0.10 mmol, 1.00 equiv.), $KHCO_3$ (30.0 mg, 0.30 mmol, 3.00 equiv.), $Bi(OTf)_3$ (130 mg, 0.20 mmol, 2.00 equiv.) and carboxylic acid (0.30 mmol, 3.00 equiv.) were weighed into a 5 mL crimp-cap vial equipped with a stirring bar. The vials were sealed and set under an inert atmosphere by evacuating and back-filling with N_2 (×3). If liquid, a stock solution of the corresponding carboxylic acid was prepared in dry DCM (0.3 M), and either 1 mL of this solution or 1 mL of dry DCM was added *via* syringe to the reaction mixture. The reaction mixture was degassed three times with a freeze-pump thaw, after which the reaction was irradiated either with 365 nm (1.8 W) for 10 hours or with 385 nm (0.5 W) for 16 hours while maintaining the temperature at 25 °C with a water-cooling block.

3.5.3.2 Scope of carboxylic acids

Synthesis of 4-methyl-*N*-(1-phenylethyl)benzenesulfonamide (3.4)

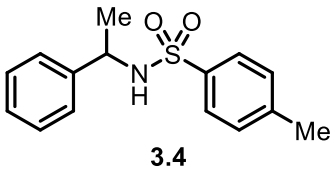

3.4

4-Methyl-*N*-(1-phenylethyl)benzenesulfonamide (**3.4**) was synthetized according to **GP1** using (±)-2-phenylpropionic acid (in total 60.0 mg, 0.40 mmol, 1.0 equiv.) as the limiting reagent and irradiated at 365 nm for 10 h. After purification with reverse-phase flash column chromatography (H_2O+0.5‰ TFA/MeCN, 10% → 100%), the title compound was obtained as a colorless oil which crystallized to a white solid upon standing under ambient conditions (59 mg, 54%).

R_f (silica, 50% EtOAc/PE): 0.87 [potassium permanganate];

^{1}H-NMR (400 MHz, $CDCl_3$): δ (ppm) 7.60–7.65 (m, 2H), 7.14–7.19 (m, 5H), 7.09–7.12 (m, 2H), 5.33 (d, *J* = 7.0 Hz, 1H), 4.45 (pent., *J* = 7.0 Hz, 1H), 2.37 (s, 3H), 1.41 (d, *J* = 7.0 Hz, 3H);

^{13}C-NMR (101 MHz, $CDCl_3$): δ (ppm) 143.1, 142.1, 137.7, 129.4, 128.5, 127.4, 127.1, 126.1, 53.7, 23.6, 21.5;

HRMS (ESI+): calc. $[M+Na]^+$ for $C_{15}H_{17}NO_2SNa$ 298.0878, found 298.0874, Δ = 0.4 mDa.

Synthesis of 4-methoxy-*N*-(1-phenylethyl)benzenesulfonamide (3.5)

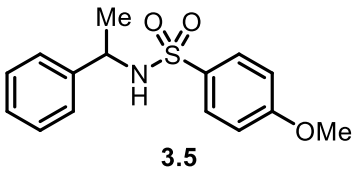

3.5

4-Methoxy-*N*-(1-phenylethyl)benzenesulfonamide (**3.5**) was synthetized according to **GP1** using (±)-2-phenylpropionic acid (in total 60.0 mg, 0.40 mmol, 1.0 equiv.) as the limiting reagent and 4-methoxybenzenesulfonamide (in total 262 mg, 1.40 mmol, 3.50 equiv.) as a nucleophile in excess. The reaction was irradiated at 365 nm for 10 h. After purification with flash column chromatography (EtOAc/PE, 20% → 40%) a colorless oil was obtained which slowly crystallized to a white solid upon standing under ambient conditions (59 mg, 51%).

R_f (silica, 50% EtOAc/PE): 0.73 [potassium permanganate];

^{1}H-NMR (400 MHz, $CDCl_3$): δ (ppm) 7.637.67 (m, 2H), 7.17–7.22 (m, 3H), 7.08–7.11 (m, 2H), 6.82–6.86 (m, 2H), 4.90 (d, *J* = 6.7 Hz, 1H), 4.45 (pent., *J* = 6.7 Hz, 1H), 3.83 (s, 3H), 1.42 (d, *J* = 6.8 Hz, 3H);

^{13}C-NMR (101 MHz, $CDCl_3$): δ (ppm) 162.7, 142.0, 132.2, 129.2, 128.6, 127.5, 126.1, 114.0, 55.6, 53.6, 23.6;

HRMS (ESI+): calc. $[M+Na]^+$ for $C_{15}H_{17}NO_3SNa$ 314.0827, found 314.0821, Δ = 0.6 mDa.

Synthesis of 4-methoxy-*N*-(1-(*p*-tolyl)ethyl)benzenesulfonamide (3.6)

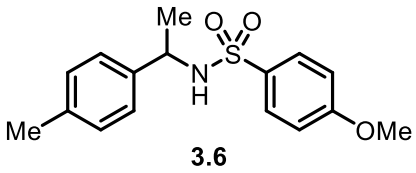

3.6

4-Methoxy-*N*-(1-(*p*-tolyl)ethyl)benzenesulfonamide (**3.6**) was synthetized according to **GP1** using 2-(4-methylphenyl)propanoic acid (in total 65.6 mg, 0.40 mmol, 1.0 equiv.) as the limiting reagent and 4-methoxybenzenesulfonamide (in total 262 mg, 1.40 mmol, 3.50 equiv.) as a nucleophile in excess. The reaction was irradiated at 385 nm for 16 h. After purification with flash column chromatography (Acetone/PE, 30%), the title compound was obtained as a pale solid (54 mg, 44%).

R$_f$ (silica, 50% EtOAc/PE): 0.80 [potassium permanganate];

^{1}H-NMR (400 MHz, $CDCl_3$): δ (ppm) 7.65–7.68 (m, 2H), 6.99 (s, 4H), 6.82–6.86 (m, 2H), 5.14 (br. s., 1H), 4.40 (pent., 6.2 Hz, 1H), 3.83 (s, 3H), 2.27 (s, 3H), 1.40 (d, *J* = 6.8 Hz, 3H);

^{13}C-NMR (101 MHz, $CDCl_3$): δ (ppm) 162.6, 139.2, 137.1, 132.3, 129.3, 129.2, 126.1, 113.9, 55.6, 53.4, 23.5, 21.0;

HRMS (ESI+): calc. $[M+Na]^+$ for $C_{16}H_{19}NO_3SNa$ 328.0983, found 328.0982, Δ = 0.1 mDa.

Synthesis of 4-methoxy-*N*-(1-(*m*-tolyl)ethyl)benzenesulfonamide (3.7)

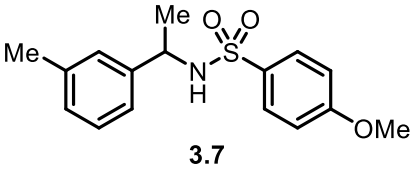

3.7

4-Methoxy-*N*-(1-(*m*-tolyl)ethyl)benzenesulfonamide (**3.7**) was synthetized according to **GP1** using 2-(4-methylphenyl)propanoic acid (in total 65.6 mg, 0.40 mmol, 1.0 equiv.) as the limiting reagent and 4-methoxybenzenesulfonamide (in total 262 mg, 1.40 mmol, 3.50 equiv.) as a nucleophile in excess. The reaction was irradiated at 385 nm for 16 h. After purification with flash column chromatography (Acetone/PE, 30%), the title compound was obtained as a colorless oil (59 mg, 48%).

R$_f$ (silica, 50% EtOAc/PE): 0.77 [potassium permanganate];

^{1}H-NMR (400 MHz, $CDCl_3$): δ (ppm) 7.63–7.67 (m, 2H), 7.08 (t, *J* = 7.5 Hz, 1H), 6.90–6.97 (m, 2H), 6.84 (br. s., 1H), 6.80–6.84 (m, 2H), 5.33 (d, *J* = 6.8 Hz, 1H), 4.40 (pent., *J* = 6.8 Hz, 1H), 3.82 (s, 3H), 2.20 (s, 3H), 1.40 (d, *J* = 6.8 Hz, 3H);

^{13}C-NMR (101 MHz, $CDCl_3$): δ (ppm) 162.6, 142.0, 138.1, 132.4, 129.2, 128.4, 128.1, 126.9, 123.2, 113.9, 55.6, 53.7, 23.6, 21.3;

HRMS (ESI+): calc. $[M+Na]^+$ for $C_{16}H_{19}NO_3SNa$ 328.0983, found 328.0978, Δ = 0.5 mDa.

Synthesis of 4-methoxy-*N*-(1-(*o*-tolyl)ethyl)benzenesulfonamide (3.8)

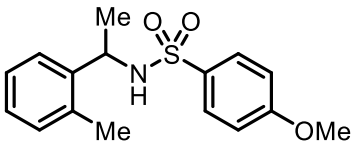

3.8

4-Methoxy-*N*-(1-(*o*-tolyl)ethyl)benzenesulfonamide (**3.8**) was synthetized according to **GP1** using 2-(4-methylphenyl)propanoic acid (in total 65.6 mg, 0.40 mmol, 1.0 equiv.) as the limiting reagent and 4-methoxybenzenesulfonamide (in total 262 mg, 1.40 mmol, 3.50 equiv.) as a nucleophile in excess. The reaction was irradiated at 385 nm for 16 h. After purification with flash column chromatography (Acetone/PE, 30%), the title compound was obtained as a pale yellowish oil (70 mg, 57%).

R_f (silica, 50% EtOAc/PE): 0.78 [potassium permanganate];

^{1}H-NMR (400 MHz, $CDCl_3$): δ (ppm) 7.60–7.65 (m, 2H), 7.11–7.14 (m, 1H), 6.99–7.05 (m, 3H), 6.77–6.82 (m, 2H), 5.40 (d, *J* = 6.8 Hz, 1H), 4.72 (pent., *J* = 6.8 Hz, 1H), 3.81 (s, 3H), 2.21 (s, 3H), 1.37 (d, *J* = 6.8 Hz, 3H);

^{13}C-NMR (101 MHz, $CDCl_3$): δ (ppm) 162.6, 140.3, 134.4, 132.3, 130.4, 129.1, 127.1, 126.4, 125.4, 113.9, 55.6, 49.7, 23.1, 19.0;

HRMS (ESI+): calc. $[M+Na]^+$ for $C_{16}H_{19}NO_3SNa$ 328.0983, found 328.0980, Δ = 0.3 mDa.

Synthesis of *N*-(1-(4-(*tert*-butyl)phenyl)ethyl)-4-methoxybenzenesulfonamide (3.9)

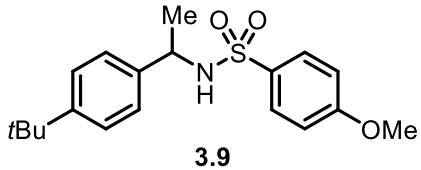

3.9

N-(1-(4-(*tert*-butyl)phenyl)ethyl)-4-methoxybenzene sulfonamide (**3.9**) was synthetized according to **GP1** using 2-(4-(*tert*-butyl)phenyl)propanoic acid (in total 82.4 mg, 0.40 mmol, 1.0 equiv.) as the limiting reagent and 4-methoxybenzenesulfonamide (in total 262 mg, 1.40 mmol, 3.50 equiv.) as a nucleophile in excess. The reaction was irradiated at 385 nm for 16 h. After purification with flash column chromatography (Acetone/PE, 30%), the title compound was obtained as an off-white solid (78 mg, 56%).

R_f (silica, 50% EtOAc/PE): 0.69 [potassium permanganate];

^{1}H-NMR (400 MHz, $CDCl_3$): δ (ppm) 7.52–7.57 (m, 2H), 7.07–7.10 (m, 2H), 6.91–6.95 (m, 2H), 6.68–6.73 (m, 2H), 5.30 (d, *J* = 6.9 Hz, 1H), 4.35 (pent., *J* = 6.9 Hz, 1H), 3.72 (s., 3H), 1.33 (d, *J* = 6.9 Hz, 3H), 1.17 (s, 9H);

^{13}C-NMR (101 MHz, $CDCl_3$): δ (ppm) 162.5, 150.2, 139.0, 132.4, 129.2, 125.9, 125.3, 113.8, 55.5, 53.4, 34.4, 31.3, 23.5;

HRMS (ESI+): calc. $[M+Na]^+$ for $C_{19}H_{25}NO_3SNa$ 370.1453, found 370.1442, Δ = 1.1 mDa.

Synthesis of *N*-(1-(4-fluorophenyl)ethyl)-4-methoxybenzenesulfonamide (3.10)

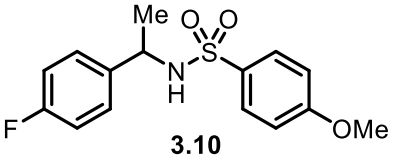

3.10

N-(1-(4-Fluorophenyl)ethyl)-4-methoxybenzenesulfonamide (**3.10**) was synthetized according to **GP1** using 2-(4-fluorophenyl)propanoic acid (in total 67.2 mg, 0.40 mmol, 1.0 equiv.) as the limiting reagent and 4-methoxybenzenesulfonamide (in total 262 mg, 1.40 mmol, 3.50 equiv.) as a nucleophile in excess. The reaction was irradiated at 365 nm for 10 h. After purification with flash column chromatography (EtOAc/PE, 20% → 40%), the title compound was obtained as a pale orange oil (62 mg, 51%).

R_f (silica, 50% EtOAc/PE): 0.75 [potassium permanganate];

^{1}H-NMR (400 MHz, $CDCl_3$): δ (ppm) 7.61–7.65 (m, 2H), 7.04–7.10 (m, 2H), 6.81–6.88 (m, 4H), 5.34 (br. s, 1H), 4.43 (q., 6.7 Hz, 1H), 3.83 (s, 3H), 1.38 (d, *J* = 6.7 Hz, 3H);

^{13}C-NMR (101 MHz, $CDCl_3$): δ (ppm) 162.7, 161.9 (d, *J* = 246 Hz), 137.9, (d, *J* = 3.1 Hz), 132.1, 129.2, 127.9 (d, *J* = 8.2 Hz), 115.2 (d, *J* = 21.7 Hz), 114.0, 55.6, 53.0, 23.6;

^{19}F-NMR (376 MHz, $CDCl_3$, $PhCF_3$ as internal standard): δ (ppm) −116.0 – (−)116.1 (m)

HRMS (ESI+): calc. $[M+Na]^+$ for $C_{15}H_{16}FNO_3SNa$ 332.0733, found 332.0727, Δ = 0.6 mDa.

Synthesis of *N*-(1-(4-chlorophenyl)ethyl)-4-methoxybenzenesulfonamide (3.11)

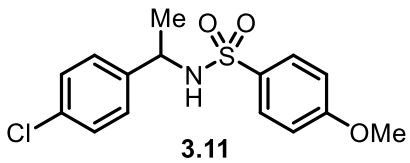

3.11

N-(1-(4-Chlorophenyl)ethyl)-4-methoxybenzenesulfonamide (**3.11**) was synthetized according to **GP1** using 2-(4-chlorophenyl)propanoic acid (in total 73.8 mg, 0.40 mmol, 1.0 equiv.) as the limiting reagent and 4-methoxybenzenesulfonamide (in total 262 mg, 1.40 mmol, 3.50 equiv.) as a nucleophile in excess. The reaction was irradiated at 365 nm for 10 h. After purification with flash column chromatography (Acetone/PE, 30% → 40%), the title compound was obtained as a white solid (67 mg, 51%).

R_f (silica, 50% EtOAc/PE): 0.78 [potassium permanganate];

^{1}H-NMR (400 MHz, $CDCl_3$): δ (ppm) 7.59–7.63 (m, 2H), 7.09–7.13 (m, 2H), 7.01–7.04 (m, 2H), 6.79–6.84 (m, 2H), 5.38–5.50 (m, 1H), 4.42 (pent., *J* = 6.9 Hz, 1H), 3.83 (s, 3H), 1.37 (d, *J* = 6.9 Hz, 3H);

^{13}C-NMR (101 MHz, $CDCl_3$): δ (ppm) 162.7, 140.77, 133.0, 132.0, 129.2, 128.5, 127.7, 124.1, 114.0, 55.6, 53.0, 23.5;

HRMS (ESI+): calc. $[M+Na]^+$ for $C_{15}H_{16}ClNO_3SNa$ 348.0437, found 348.0428, Δ = 0.9 mDa.

Synthesis of *N*-(1-(4-trifluoromethoxyphenyl)ethyl)-4-methoxybenzenesulfonamide (3.12)

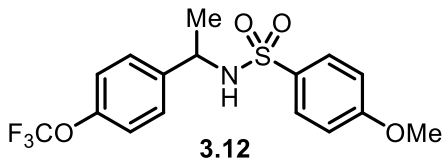

3.12

N-(1-(4-Trifluoromethoxyphenyl)ethyl)-4-methoxybenzenesulfonamide (**3.12**) was synthetized according to **GP1** using 2-(4-(trifluoromethyoxy)phenyl)propanoic acid (in total 72.9 mg, 0.30 mmol, 1.0 equiv.) as the limiting reagent and 4-methoxybenzenesulfonamide (in total 262 mg, 1.40 mmol, 3.50 equiv.) as a nucleophile in excess. The reaction was irradiated at 365 nm for 10 h. After purification with flash column chromatography (Acetone/PE, 30% → 40%), the title compound was obtained as a pale yellow solid (54 mg, 50%).

R_f (silica, 50% EtOAc/PE): 0.81 [potassium permanganate];

^{1}H-NMR (400 MHz, $CDCl_3$): δ (ppm) 7.58–7.62 (m, 2H), 7.11–7.15 (m, 2H), 6.97–7.02 (m, 2H), 6.77–6.82 (m, 2H), 5.48 (d, *J* = 7.0 Hz, 1H), 4.48 (pent., *J* = 7.0 Hz, 1H), 3.81 (s, 3H), 1.39 (d, *J* = 7.0 Hz, 3H);

^{13}C-NMR (101 MHz, $CDCl_3$): δ (ppm) 162.8, 148.2, 140.9, 132.0, 129.1, 127.7, 124.2, 121.7, 120.9, 120.3 (q, *J* = 257 Hz), 119.0, 116.6, 55.5, 53.0, 23.6;

^{19}F-NMR (376 MHz, $CDCl_3$, $PhCF_3$ as internal standard): δ (ppm) – 58.97 (s)

HRMS (ESI+): calc. $[M+Na]^+$ for $C_{16}H_{16}F_3NO_3SNa$ 398.0650, found 398.0650, Δ = 0.0 mDa.

Synthesis of *N*-(1-(4-bromophenyl)propyl)-4-methoxybenzenesulfonamide (3.13)

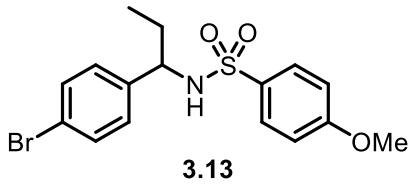

3.13

N-(1-(4-Bromophenyl)propyl)-4-methoxybenzenesulfonamide (**3.13**) was synthetized according to **GP1** using 2-(4-bromophenyl)butanoic acid (in total 97.2 mg, 0.40 mmol, 1.0 equiv.) as the limiting reagent and 4-methoxybenzenesulfonamide (in total 262 mg, 1.40 mmol, 3.50 equiv.) as a nucleophile in excess. The reaction was irradiated at 365 nm for 10 h. After purification with flash column chromatography (EtOAc/PE, 20% → 40%), the title compound was obtained as a pale yellow solid (42 mg, 27%).

R_f (silica, 50% EtOAc/PE): 0.85 [potassium permanganate];

^{1}H-NMR (400 MHz, $CDCl_3$): δ (ppm) 7.50–7.54 (m, 2H), 7.22–7.26 (m, 2H), 6.86–6.90 (m, 2H), 6.74–6.78 (m, 2H), 5.32 (d, *J* = 6.8 Hz, 1H), 4.14 (q., *J* = 7.1 Hz, 1H), 3.83 (s, 3H), 1.74 (sept., *J* = 7.1 Hz, 1H), 1.66 (sept. *J* = 7.2 Hz, 1H), 0.78 (t, *J* = 7.2 Hz, 3H);

^{13}C-NMR (101 MHz, $CDCl_3$): δ (ppm) 162.7, 139.8, 132.1, 131.4, 129.1, 128.5, 121.0, 113.8, 59.3, 55.6, 30.4, 10.4;

HRMS (ESI+): calc. $[M+Na]^+$ for $C_{16}H_{18}BrNO_3SNa$ 406.0089, found 406.0085, Δ = 0.4 mDa.

Synthesis of *N*-bezhydryl-4-methoxybenzenesulfonamide (3.14)

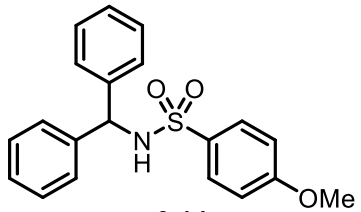

3.14

N-Bezhydryl-4-methylbenzenesulfonamide (**3.14**) was synthetized according to **GP1** using diphenyl acetic acid (in total 84.8 mg, 0.40 mmol, 1.0 equiv.) as the limiting reagent and 4-methoxybenzenesulfonamide (in total 262 mg, 1.40 mmol, 3.50 equiv.) as a nucleophile in excess. The reaction was irradiated at 385 nm for 16 h. After purification with flash column chromatography (Acetone/PE, 25%), an off-white solid was obtained (82 mg, 58%).

R_f (silica, 50% EtOAc/PE): 0.77 [potassium permanganate];

^{1}H-NMR (400 MHz, $CDCl_3$): δ (ppm) 7.58–7.62 (m, 2H), 7.18–7.24 (m, 6H), 7.10–7.13 (m, 4H), 6.77–6.80 (m, 2H), 5.56 (d, *J* = 7.2 Hz, 1H), 5.32 (d, *J* = 7.2 Hz, 1H), 3.82 (s, 3H);

^{13}C-NMR (101 MHz, $CDCl_3$): δ (ppm) 162.7, 140.6, 132.0, 129.3, 128.6, 127.6, 127.4, 113.9, 61.4, 55.6;

HRMS (ESI+): calc. $[M+Na]^+$ for $C_{20}H_{19}NO_3SNa$ 376.0983, found 376.0981, Δ = 0.2 mDa.

Synthesis of 4-methoxy-*N*-(1-phenylpropyl)benzenesulfonamide (3.15)

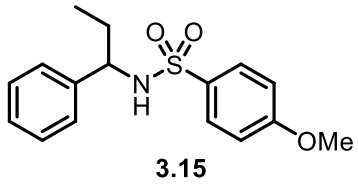

3.15

4-Methoxy-*N*-(1-phenylpropyl)benzenesulfonamide (**3.15**) was synthetized according to **GP1** using 2-phenylbutanoic acid (in total 65.6 mg, 0.40 mmol, 1.0 equiv.) as the limiting reagent and 4-methoxybenzenesulfonamide (in total 262 mg, 1.40 mmol, 3.50 equiv.) as a nucleophile in excess. The reaction was irradiated at 365 nm for 10 h. After purification with flash column chromatography (EtOAc/PE, 20% → 40%), the title compound was obtained as a white solid (74 mg, 61%).

R_f (silica, 50% EtOAc/PE): 0.81 [potassium permanganate];

^{1}H-NMR (400 MHz, $CDCl_3$): δ (ppm) 7.56–7.60 (m, 2H), 7.12–7.17 (m, 3H), 7.00–7.03 (m, 2H), 6.74–6.78 (m, 2H), 5.25–5.34 (m, 1H), 4.13–4.20 (m, 1H), 3.80 (s, 3H), 1.80 (sept., J = 7.2 Hz, 1H), 1.70 (sept., J = 7.2 Hz, 1H), 0.78 (t, J = 7.2 Hz, 3H);

^{13}C-NMR (101 MHz, $CDCl_3$): δ (ppm) 162.5, 140.8, 132.4, 129.1, 128.7, 127.3, 126.6, 113.8, 59.8, 55.6, 30.6, 10.5;

HRMS (ESI+): calc. $[M+Na]^+$ for $C_{16}H_{19}NO_3SNa^+$ 328.0983, found 328.0978, Δ = 0.5 mDa.

Synthesis of 4-methoxy-*N*-(1-phenylpentyl)benzenesulfonamide (3.16)

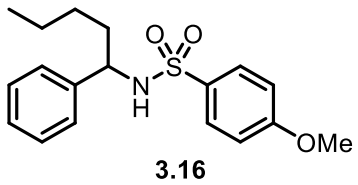

3.16

4-Methoxy-*N*-(1-phenylpentyl)benzenesulfonamide (**3.16**) was synthetized according to **GP1** using 2-phenylhexanoic acid (in total 76.8 mg, 0.40 mmol, 1.0 equiv.) as the limiting reagent and 4-methoxybenzenesulfonamide (in total 262 mg, 1.40 mmol, 3.50 equiv.) as a nucleophile in excess. The reaction was irradiated at 365 nm for 10 h. After purification with flash column chromatography (Acetone/PE, 20% → 30%), the title compound was obtained as a white solid (67 mg, 50%).

R_f (silica, 50% EtOAc/PE): 0.86 [potassium permanganate];

^{1}H-NMR (400 MHz, $CDCl_3$): δ (ppm) 7.54–7.58 (m, 2H), 7.12–7.16 (m, 3H), 6.99–7.02 (m, 2H), 6.73–6.78 (m, 2H), 5.06–5.19 (m, 1H), 4.24 (q, J = 7.2 Hz, 1H), 3.80 (s, 3H), 1.70–1.80 (m, 1H), 1.61–1.70 (m, 1H), 1.17–1.27 (m, 3H), 1.04–1.13 (m, 1H), 0.80 (t, J = 7.2 Hz, 3H);

^{13}C-NMR (101 MHz, $CDCl_3$): δ (ppm) 162.5, 141.1, 132.4, 129.1, 128.4, 127.2, 126.5, 113.8, 58.3, 55.6, 37.4, 28.0, 22.2, 13.9;

HRMS (ESI+): calc. $[M+Na]^+$ for $C_{18}H_{23}NO_3SNa^+$ 356.1296, found 356.1290, Δ = 0.6 mDa.

Synthesis of *N*-(1,2-diphenylethyl)-4-methoxybenzenesulfonamide (3.17)

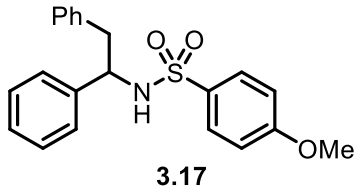

3.17

N-(1,2-Diphenylethyl)-4-methoxybenzenesulfonamide (**3.17**) was synthetized according to **GP1** using 2-phenylhexanoic acid (in total 90.4 mg, 0.40 mmol, 1.0 equiv.) as the limiting reagent and 4-methoxybenzenesulfonamide (in total 262 mg, 1.40 mmol, 3.50 equiv.) as a nucleophile in excess. The reaction was irradiated at 365 nm for 10 h. After purification with flash column chromatography (Acetone/PE, 20% → 30%), the title compound was obtained as a white solid (84 mg, 57%).

R_f (silica, 50% EtOAc/PE): 0.86 [potassium permanganate];

^{1}H-NMR (400 MHz, $CDCl_3$): δ (ppm) 7.46–7.50 (m, 2H), 7.15–7.18 (m, 6H), 7.03–7.06 (m, 2H), 6.91–6.95 (m, 2H), 6.71–6.75 (m, 2H), 5.12–5.19 (m, 1H), 4.50 (q., *J* = 6.8 Hz, 1H), 3.81 (s, 3H), 2.96–3.00 (m, 2H);

^{13}C-NMR (101 MHz, $CDCl_3$): δ (ppm) 162.5, 140.5, 136.5, 131.8, 129.3, 129.1, 128.5, 128.3, 127.4, 126.8, 126.7, 113.4, 59.3, 55.6, 44.1;

HRMS (ESI+): calc. $[M+Na]^+$ for $C_{21}H_{21}NO_3SNa$ 390.1140, found 390.1132, Δ = 0.8 mDa.

Synthesis of *N*-(2-cyclohexyl-1-phenylethyl)-4-methoxybenzenesulfonamide (3.18)

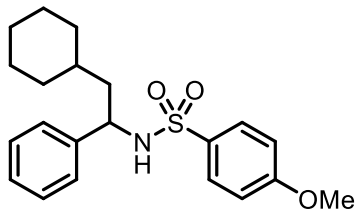

3.18

N-(2-Cyclohexyl-1-phenylethyl)-4-methoxybenzenesulfonamide (**3.18**) was synthetized according to **GP1** using 3-cyclohexyl-2-phenylpropanoic acid (in total 92.9 mg, 0.40 mmol, 1.0 equiv.) as the limiting reagent and 4-methoxybenzenesulfonamide (in total 262 mg, 1.40 mmol, 3.50 equiv.) as a nucleophile in excess. The reaction was irradiated at 365 nm for 10 h. After purification with flash column chromatography (Acetone/PE, 30%), the title compound was obtained as a pale yellowish oil (33 mg, 22%).

R_f (silica, 50% EtOAc/PE): 0.74 [potassium permanganate];

^{1}H-NMR (400 MHz, $CDCl_3$): δ (ppm) 7.54–7.58 (m, 2H), 7.11–7.16 (m, 3H), 7.00–7.03 (m, 2H), 6.74–6.78 (m, 2H), 5.04 (d, *J* = 7.5 Hz, 1H), 4.35 (q., *J* = 7.5 Hz, 1H), 3.80 (s,

3H), 1.54–1.67 (m, 6H), 1.51 (sept., *J* = 7.1 Hz, 1H), 1.02–1.19 (m, 4H), 0.75–0.92 (m, 2H);

^{13}C-NMR (101 MHz, $CDCl_3$): δ (ppm) 162.5, 141.6, 132.4, 129.1, 128.4, 127.2, 126.4, 113.8, 55.7, 55.6, 45.7, 33.9, 33.2, 32.8, 26.4, 26.1, 26.0;

HRMS (ESI+): calc. $[M+Na]^+$ for $C_{21}H_{27}NO_3SNa^+$ 396.1609, found 396.1608, Δ = 0.1 mDa.

Synthesis of *N*-cyclohexyl(phenyl)methyl-4-methoxybenzenesulfonamide (3.19)

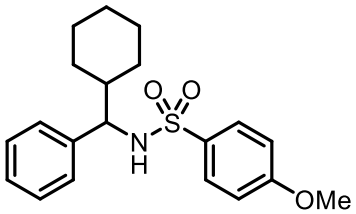

3.19

N-Cyclohexyl(phenyl)methyl-4-methoxybenzenesulfonamide (**3.19**) was synthetized according to **GP1** using 2-cyclohexyl-2-phenylacetic acid (in total 87.2 mg, 0.40 mmol, 1.0 equiv.) as the limiting reagent and 4-methoxybenzenesulfonamide (in total 262 mg, 1.40 mmol, 3.50 equiv.) as a nucleophile in excess. The reaction was irradiated at 365 nm for 10 h. After purification with flash column chromatography (Acetone/PE, 20% → 30%), the title compound was obtained as a white solid (75 mg, 52 %).

R_f (silica, 50% EtOAc/PE): 0.83 [potassium permanganate];

^{1}H-NMR (400 MHz, $CDCl_3$): δ (ppm) 7.49–7.53 (m, 2H), 7.07–7.11 (m, 3H), 6.89–6.93 (m, 2H), 6.67–6.72 (m, 2H), 5.28 (d, *J* = 8.3 Hz, 1H), 3.78 (s, 3H), 1.93–1.98 (m, 1H), 1.69–1.76 (m, 2H), 1.53–1.63 (m, 3H), 1.24–1.28 (m, 1H), 1.03–1.11 (m, 2H), 0.82–0.96 (m, 2H);

^{13}C-NMR (101 MHz, $CDCl_3$): δ (ppm) 162.4, 140.0, 132.4, 129.1, 128.1, 127.0, 126.9, 113.7, 63.5, 55.5, 43.8, 29.8, 29.5, 26.2, 25.9 (2C);

HRMS (ESI+): calc. $[M+Na]^+$ for $C_{20}H_{25}NO_3SNa$ 382.1453, found 382.1451, Δ = 0.2 mDa.

Synthesis of 4-methoxy-*N*-(1-napthalen-1-yl)ethyl)benzenesulfonamide (3.20)

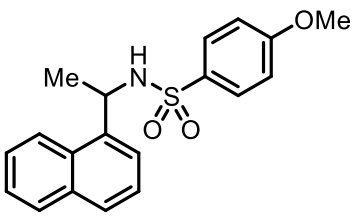

3.20

4-Methoxy-*N*-(1-napthalen-1-yl)ethyl)benzenesulfonamide (**3.20**) was synthetized according to **GP1** using 2-(naphthalen-1-yl)propanoic acid (in total 60.0 mg, 0.30 mmol, 1.0 equiv.) as the limiting reagent and 4-methoxybenzenesulfonamide (in total 262 mg, 1.40 mmol, 3.50 equiv.) as a nucleophile in excess. The reaction was irradiated at 385 nm for 16 h.

After purification with flash column chromatography (Acetone/PE, 30%), the title compound was obtained as a white solid (27 mg, 26%).

R_f (silica, 50% EtOAc/PE): 0.68 [potassium permanganate];

^{1}H-NMR (400 MHz, $CDCl_3$): δ (ppm) 7.89–7.93 (m, 1H), 7.78–7.81 (m, 1H), 7.66–7.70 (m, 1H), 7.57–7.61 (m, 2H), 7.43–7.47 (m, 2H), 7.35–7.38 (m, 1H), 7.28–7.33 (m, 1H), 6.67–6.72 (m, 2H), 5.28 (pent., *J* = 6.8 Hz, 1H), 5.14–5.20 (m, 1H), 3.78 (s, 3H), 1.59 (d, *J* = 6.8 Hz, 3H);

^{13}C-NMR (101 MHz, $CDCl_3$): δ (ppm) 162.6, 137.7, 133.8, 132.0, 130.2, 129.2, 128.8, 128.1, 126.3, 125.6, 125.3, 123.4, 122.6, 113.8, 55.5, 49.8, 23.3;

HRMS (ESI+): calc. $[M+Na]^+$ for $C_{19}H_{19}NO_3SNa$ 364.0983, found 364.0980, Δ = 0.3 mDa.

Synthesis of *N*-(1-(4-isobutylphenyl)ethyl)-4-methoxybenzenesulfonamide (3.21)

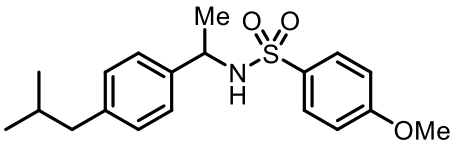

3.21

N-(1-(4-Isobutylphenyl)ethyl)-4-methylbenzene-sulfonamide (**3.21**) was synthetized according to **GP1** using 2-(4-isobutylphenyl)propanoic acid (rac. ibuprofen, in total 82.4 mg, 0.40 mmol, 1.0 equiv.) as the limiting reagent and 4-methoxybenzenesulfonamide (in total 262 mg, 1.40 mmol, 3.50 equiv.) as a nucleophile in excess. The reaction was irradiated at 385 nm for 16 h. After purification with flash column chromatography (EtOAc/PE, 5% → 50%), the title compound was obtained as a white solid (87 mg, 63%).

R_f (silica, 50% EtOAc/PE): 0.84 [potassium permanganate];

^{1}H-NMR (400 MHz, $CDCl_3$): δ (ppm) 7.62–7.67 (m, 2H), 6.95–7.01 (m, 4H), 6.81–6.85 (m, 2H), 4.92 (br. s., 1H), 4.39–4.46 (m, 1H), 3.82 (s, 3H), 2.39 (d, *J* = 6.9 Hz, 2H), 1.79 (sept., *J* = 6.9 Hz, 1H), 1.42 (d, *J* = 6.8 Hz, 3H), 0.86 (d, *J* = 6.9 Hz, 6H);

^{13}C-NMR (101 MHz, $CDCl_3$): δ (ppm) 162.6, 141.1, 139.3, 132.4, 129.2 (2C), 125.9, 113.9, 55.5, 53.4, 45.0, 30.2, 23.6, 22.3;

HRMS (ESI+): calc. $[M+Na]^+$ for $C_{19}H_{25}NO_3SNa$ 370.1453, found 370.1453, Δ = 0.0 mDa.

Synthesis of *N*-(1-(2-fluoro-[1,1'biphenyl]-4-yl)ethyl)-4-methylbenzenesulfonamide (3.22)

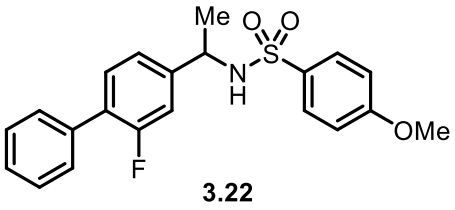

3.22

N-(1-(2-Fluoro-[1,1'biphenyl]-4-yl)ethyl)-4-methylbenzenesulfonamide (**3.22**) was synthetized according to **GP1** using 2-(2-fluoro-[1,1'biphenyl]-4-yl)propanoic acid (rac. flurbiprofen, in total 97.6 mg, 0.40 mmol, 1.0 equiv.) as the limiting reagent and 4-methoxybenzenesulfonamide (in total 262 mg, 1.40 mmol, 3.50 equiv.) as a nucleophile in excess. The reaction was irradiated at 385 nm for 16 h. After purification with flash column chromatography (EtOAc/PE, 5% → 50%), the title compound was obtained as a white solid (40 mg, 26%).

R_f (silica, 50% EtOAc/PE): 0.80 [potassium permanganate];

^{1}H-NMR (400 MHz, $CDCl_3$): δ (ppm) 7.56–7.61 (m, 2H), 7.32–7.40 (m, 4H), 7.25–7.30 (m, 1H), 7.14–7.19 (m, 1H), 6.89 (dd, *J* = 8.0, 1.8 Hz, 1H), 6.79 (dd, *J* = 11.4, 1.8 Hz, 1H), 6.73–6.77 (m, 2H), 5.13–5.20 (m, 1H), 4.38–4.45 (m, 1H), 3.69 (s, 3H), 1.36 (d, *J* = 6.9 Hz, 3H);

^{13}C-NMR (101 MHz, $CDCl_3$): δ (ppm) 162.8, 159.5 (d, *J* = 250 Hz), 143.6 (d, *J* = 7.0 Hz), 135.3 (d, *J* = 1.0 Hz), 132.1, 130.7 (d, *J* = 3.9 Hz), 129.3, 128.8 (d, *J* = 2.9 Hz), 128.4, 128.0 (d, *J* = 13.5 Hz), 127.7, 122.2 (d, *J* = 3.3 Hz), 114.0 (d, *J* = 23.7 Hz), 113.9, 55.5, 53.0, 23.4;

^{19}F-NMR (376 MHz, $CDCl_3$, $PhCF_3$ as internal standard): δ (ppm) −118.6 – (−)118.7 (m)

HRMS (ESI+): calc. $[M+Na]^+$ for $C_{21}H_{20}FNO_3SNa$ 408.1046, found 408.1037, Δ = 0.9 mDa.

3.5.3.3 Scope of nucleophiles

Synthesis of *N*-(1-(*o*-tolyl)ethyl)benzenesulfonamide (3.23)

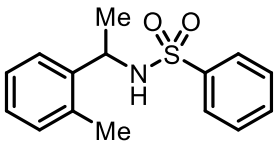

3.23

N-(1-(*o*-Tolyl)ethyl)benzenesulfonamide (**3.23**) was synthetized according to **GP1** using 2-(*o*-tolyl)propanoic acid (in total 65.7 mg, 0.40 mmol, 1.0 equiv.) as the limiting reagent and benzenesulfonamide (in total 220 mg, 1.40 mmol, 3.50 equiv.) as a nucleophile in excess. The reaction was irradiated at 385 nm for 16 h. After purification with flash column chromatography (Acetone/PE, 20% → 40%), the title compound was obtained as a colorless oil (45 mg, 41%).

R_f (silica, 50% EtOAc/PE): 0.87 [potassium permanganate];

^{1}H-NMR (400 MHz, $CDCl_3$): δ (ppm) 7.67–7.71 (m, 2H), 7.47 (tt, *J* = 7.4, 1.2 Hz, 1H), 7.32–7.37 (m, 2H), 7.08–7.11 (m, 1H), 6.98–7.05 (m, 3H), 5.10 (d, *J* = 6.7 Hz, 1H), 4.76 (pent., *J* = 6.7 Hz, 1H), 2.19 (s, 3H), 1.40 (d, *J* = 6.7 Hz, 3H);

^{13}C-NMR (101 MHz, $CDCl_3$): δ (ppm) 140.6, 140.0, 134.5, 132.3, 130.4, 128.7, 127.3, 126.9, 126.4, 125.2, 49.8, 23.2, 18.9;

HRMS (ESI+): calc. $[M+Na]^+$ for $C_{15}H_{17}NO_2SNa$ 298.0878, found 298.0874, Δ = 0.4 mDa.

Synthesis of 4-methyl-*N*-(1-(*o*-tolyl)ethyl)benzenesulfonamide (3.24)

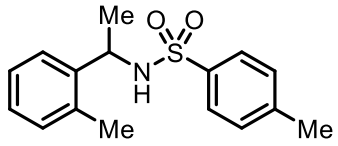

3.24

4-Methyl-*N*-(1-(*o*-tolyl)ethyl)benzenesulfonamide (**3.24**) was synthetized according to **GP1** using 2-(*o*-tolyl)propanoic acid (in total 65.7 mg, 0.40 mmol, 1.0 equiv.) as the limiting reagent and 4-methylbenzenesulfonamide (in total 240 mg, 1.40 mmol, 3.50 equiv.) as a nucleophile. The reaction was irradiated at 385 nm for 16 h. After purification with flash column chromatography (Acetone/PE, 20% → 40%) the title compound was obtained as a colorless oil (59 mg, 51%).

R_f (silica, 50% EtOAc/PE): 0.90 [potassium permanganate];

^{1}H-NMR (400 MHz, $CDCl_3$): δ (ppm) 7.58–7.62 (m, 2H), 7.12–7.15 (m, 3H), 6.98–7.06 (m, 3H), 5.37 (d, *J* = 6.6 Hz, 1H), 4.73 (pent., *J* = 6.6 Hz, 1H), 2.36 (s, 3H), 2.20 (s, 3H), 1.37 (d, *J* = 6.6 Hz, 3H);

^{13}C-NMR (101 MHz, $CDCl_3$): δ (ppm) 143.0, 140.4, 137.7, 134.4, 130.4, 129.3, 127.1, 127.0, 126.4, 125.4, 49.7, 23.1, 21.5, 19.0;

HRMS (ESI+): calc. $[M+Na]^+$ for $C_{16}H_{19}NO_2SNa$ 312.1034, found 312.1031, Δ = 0.3 mDa.

Synthesis of *N*-(1-(*o*-tolyl)ethyl)-4-(trifluoromethyl)benzenesulfonamide (3.25)

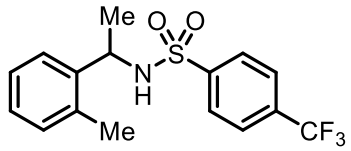

3.25

N-(1-(*o*-Tolyl)ethyl)-4-(trifluoromethyl)benzenesulfonamide (**3.25**) was synthetized according to **GP2** using 4-(trifluoromethyl)benzenesulfonamide (in total 90.0 mg, 0.40 mmol, 1.0 equiv.) as the limiting reagent and 2-(*o*-tolyl)propanoic acid (in total 197 mg, 1.20 mmol, 3.0 equiv.) as acid in excess. The reaction was irradiated at 385 nm for 16 h. After purification with flash column chromatography (Acetone/PE, 20% → 40%), the title compound was obtained as an off-white solid (52 mg, 38%).

R_f (silica, 50% EtOAc/PE): 0.95 [potassium permanganate];

^{1}H-NMR (400 MHz, $CDCl_3$): δ (ppm) 7.73 (d, *J* = 8.2 Hz, 2H), 7.53 (d, *J* = 8.2 Hz, 2H), 6.96–7.04 (m, 3H), 6.88–6.94 (m, 1H), 5.53 (d, *J* = 7.3 Hz, 1H), 4.87 (pent., *J* = 6.9 Hz, 1H), 2.26 (s, 3H), 1.43 (d, *J* = 6.9 Hz, 3H);

^{13}C-NMR (101 MHz, $CDCl_3$): δ (ppm) 144.1, 139.3, 134.4, 133.8 (q, *J* = 33 Hz), 130.4, 127.4, 127.3, 126.4, 125.6 (q, *J* = 3.7 Hz), 125.3, 123.2 (q, *J* = 272 Hz), 50.0, 29.7, 23.1, 19.0;

^{19}F-NMR (376 MHz, $CDCl_3$, $PhCF_3$ as internal standard): δ (ppm) – 63.23 (s)

HRMS (ESI+): calc. $[M+Na]^+$ for $C_{16}H_{16}F_3NO_2SNa$ 366.0752, found 366.0748, Δ = 0.4 mDa.

Synthesis of 4-cyano-*N*-(1-(*o*-tolyl)ethyl)benzenesulfonamide (3.26)

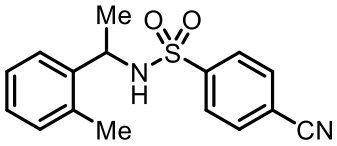

3.26

4-Cyano-*N*-(1-(*o*-tolyl)ethyl)benzenesulfonamide (**3.26**) was synthetized according to **GP1** using 2-(*o*-tolyl)propanoic acid (in total 65.7 mg, 0.40 mmol, 1.0 equiv.) as the limiting reagent and 4-cyanobenzenesulfonamide (in total 255 mg, 1.40 mmol, 3.5 equiv.) as a nucleophile in excess. The reaction was irradiated at 385 nm for 16 h. After purification with flash column chromatography (EtOAc/PE, 20% → 40%), the title compound was obtained as a pale oil which crystallized to a white solid upon standing under ambient conditions (47 mg, 39%).

R_f (silica, 50% EtOAc/PE): 0.76 [potassium permanganate];

^{1}H-NMR (400 MHz, $CDCl_3$): δ (ppm) 7.63–7.67 (m, 2H), 7.53–7.57 (m, 2H), 7.03–7.08 (m, 1H), 7.00–7.03 (m, 1H), 4.93 (d, *J* = 6.7 Hz, 1H), 4.88 (pent., *J* = 6.7 Hz, 1H), 2.25 (s, 3H), 1.44 (d, *J* = 6.7 Hz, 3H);

^{13}C-NMR (101 MHz, $CDCl_3$): δ (ppm) 144.9, 139.1, 134.7, 132.4, 130.6, 127.6, 127.4, 126.4, 125.2, 117.4, 115.8, 50.1, 23.2, 19.0;

HRMS (ESI+): calc. $[M+Na]^+$ for $C_{16}H_{16}N_2O_2SNa$ 323.0830, found 323.0826, Δ = 0.4 mDa.

Synthesis of 2-fluoro-*N*-(1-(*o*-tolyl)ethyl)benzenesulfonamide (3.27)

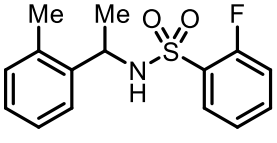

3.27

2-Fluoro-*N*-(1-(*o*-tolyl)ethyl)benzenesulfonamide (**3.27**) was synthetized according to **GP1** using 2-(*o*-tolyl)propanoic acid (in total 65.7 mg, 0.40 mmol, 1.0 equiv.) as the limiting reagent and 2-fluorobenzenesulfonamide (in total 210 mg, 1.40 mmol,

3.5 equiv.) as a nucleophile in excess. The reaction was irradiated at 385 nm for 16 h. After purification with flash column chromatography (EtOAc/PE, 20% → 40%), the title compound was obtained as a colorless oil which crystallized to white solid upon standing under ambient conditions (36 mg, 31%).

R_f (silica, 50% EtOAc/PE): 0.86 [potassium permanganate];

^{1}H-NMR (400 MHz, $CDCl_3$): δ (ppm) 7.71 (td, *J* = 7.5, 1.8 Hz, 1H), 7.38–7.41 (m, 1H), 7.13–7.16 (m, 1H), 7.10 (dt, *J* = 7.7, 0.9 Hz, 1H), 6.97–7.05 (m, 3H), 6.92–6.97 (m, 1H), 5.15 (d, *J* = 7.6 Hz, 1H), 4.81 (pent., *J* = 7.0 Hz, 1H), 2.19 (s, 3H), 1.42 (d, *J* = 7.0 Hz, 3H);

^{13}C-NMR (101 MHz, $CDCl_3$): (ppm) 158.6 (d, *J* = 252 Hz), 139.6, 134.6 (d, *J* = 8.9 Hz), 134.4, 130.4, 129.7, 128.6 (d, *J* = 12.7 Hz), 126.8 (d, *J* = 102 Hz), 124.8, 124.1 (d, *J* = 3.8 Hz), 116.5 (d, *J* = 21.1 Hz), 49.9, 23.0, 18.9;

^{19}F-NMR (376 MHz, $CDCl_3$, $PhCF_3$ as internal standard): δ (ppm) – 111.12 – (–) 111.18 (m)

HRMS (ESI+): calc. $[M+Na]^+$ for $C_{15}H_{16}FNO_2SNa$ 316.0784, found 316.0777, Δ = 0.7 mDa.

Synthesis of 3,5-dichloro-*N*-(1-(*o*-tolyl)ethyl)benzenesulfonamide (3.28)

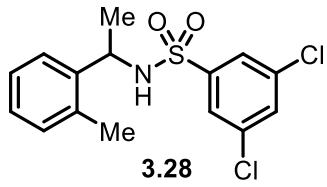

3.28

3,5-Dichloro-*N*-(1-(*o*-tolyl)ethyl)benzenesulfonamide (**3.28**) was synthetized according to **GP2** using 3,5-dichlorobenzenesulfonamide (in total 90.4 mg, 0.40 mmol, 1.0 equiv.) as the limiting reagent and 2-(*o*-tolyl)propanoic acid (in total 197 mg, 1.20 mmol, 3.0 equiv.) as an acid in excess. The reaction was irradiated at 385 nm for 16 h. After purification with flash column chromatography (Acetone/PE, 20% → 40%), the title compound was obtained as a cream-white solid (72 mg, 52%).

R_f (silica, 50% EtOAc/PE): 0.92 [potassium permanganate];

^{1}H-NMR (400 MHz, $CDCl_3$): δ (ppm) 7.40–7.42 (m, 2H), 7.33 (t, *J* = 1.8 Hz, 1H), 7.03–7.05 (m, 2H), 6.97–7.00 (m, 2H), 5.49 (br. s., 1H), 4.87 (pent., *J* = 7.0 Hz, 1H), 2.29 (s, 3H), 1.45 (d, *J* = 7.0 Hz, 3H);

^{13}C-NMR (101 MHz, $CDCl_3$): δ (ppm) 143.4, 138.9, 135.4, 134.5, 132.1, 130.5, 127.7, 126.3, 125.3, 125.2, 50.1, 23.1, 19.0;

HRMS (ESI+): calc. $[M+Na]^+$ for $C_{15}H_{15}Cl_2NO_2SNa$ 366.0098, found 366.0095, Δ = 0.3 mDa.

Synthesis of 2,4,6-trimethyl-*N*-(1-(*o*-tolyl)ethyl)benzenesulfonamide (3.29)

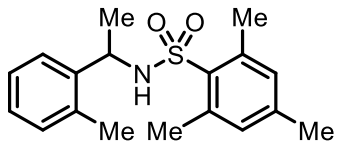

3.29

2,4,6-Trimethyl-*N*-(1-(*o*-tolyl)ethyl)benzenesulfonamide (**3.29**) was synthetized according to **GP2** using 2,4,6-trimethylbenzenesulfonamide (in total 79.7 mg, 0.40 mmol, 1.0 equiv.) as the limiting reagent and 2-(*o*-tolyl)propanoic acid (in total 197 mg, 1.20 mmol, 3.0 equiv.) as an acid in excess. The reaction was irradiated at 385 nm for 16 h. After purification with flash column chromatography (Acetone/PE, 20% → 40%), the title compound was obtained as a cream-white solid (58 mg, 46%).

R_f (silica, 50% EtOAc/PE): 0.92 [potassium permanganate];

^{1}H-NMR (400 MHz, $CDCl_3$): δ (ppm) 7.09–7.13 (m, 1H), 6.98–7.07 (m, 3H), 6.85 (s, 2H), 4.77 (d, *J* = 5.6 Hz, 1H), 4.71 (pent., *J* = 6.4 Hz, 1H), 2.53 (s, 6H), 2.26 (s, 3H), 2.17 (s, 3H), 1.36 (d, *J* = 6.4 Hz, 3H);

^{13}C-NMR (101 MHz, $CDCl_3$): δ (ppm) 141.9, 140.3, 138.8, 134.6, 134.5, 131.8, 130.5, 127.2, 126.2, 125.1, 49.5, 23.0, 22.8, 20.9, 18.8;

HRMS (ESI+): calc. $[M+Na]^+$ for $C_{18}H_{23}NO_2SNa$ 340.1347, found 340.1345, Δ = 0.2 mDa.

Synthesis of *N*-(1-(*o*-Tolyl)ethyl)naphthalene-1-sulfonamide (3.30)

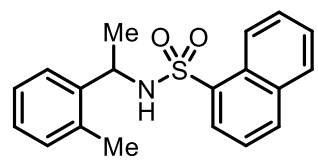

3.30

N-(1-(*o*-Tolyl)ethyl)naphthalene-1-sulfonamide (**3.30**) was synthetized according to **GP2** using napthalene-1-sulfonamide (in total 82.9 mg, 0.40 mmol, 1.0 equiv.) as the limiting reagent and 2-(*o*-tolyl)propanoic acid (in total 197 mg, 1.20 mmol, 3.0 equiv.) as an acid in excess. The reaction was irradiated at 385 nm for 16 h. After purification with flash column chromatography (Acetone/PE, 30% → 40%), the title compound was obtained as a cream-white solid (41 mg, 32%).

R_f (silica, 50% EtOAc/PE): 0.86 [potassium permanganate];

^{1}H-NMR (400 MHz, $CDCl_3$): δ (ppm) 8.22 (d, *J* = 1.4 Hz, 1H), 7.79–7.86 (m, 3H), 7.67 (dd, *J* = 8.7, 1.8 Hz, 1H), 7.54–7.63 (m, 2H), 7.06–7.10 (m, 1H), 6.98–6.95 (m, 3H), 4.94 (d, *J* = 6.6 Hz, 1H), 4.82 (pent., *J* = 6.6 Hz, 1H), 2.17 (s, 3H), 1.41 (d, *J* = 6.6 Hz, 3H);

^{13}C-NMR (101 MHz, $CDCl_3$): δ (ppm) 139.9, 137.4, 134.6, 134.5, 132.0, 130.4, 129.2, 129.1, 128.6, 128.3, 127.8, 127.3 (2C), 126.3, 125.1, 122.2, 49.9, 29.7, 23.1, 18.9;

HRMS (ESI+): calc. $[M+Na]^+$ for $C_{19}H_{19}NO_2SNa$ 348.1034, found 348.1031, Δ = 0.3 mDa.

Synthesis of methyl 4-(*N*-(1-(*o*-tolyl)ethyl)sulfamoyl)benzoate (3.31)

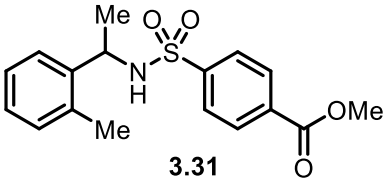

3.31

Methyl 4-(*N*-(1-(*o*-tolyl)ethyl)sulfamoyl)benzoate (**3.31**) was synthetized according to **GP1** using 2-(*o*-tolyl)propanoic acid (in total 65.7 mg, 0.40 mmol, 1.0 equiv.) as the limiting reagent and methyl 4-sulfamoylbenzoate (in total 301 mg, 1.40 mmol, 3.5 equiv.) as a nucleophile in excess. The reaction was irradiated at 385 nm for 16 h. After purification with flash column chromatography (EtOAc/PE, 20% → 40%), the title compound was obtained as an off-white solid (40 mg, 30%).

R_f (silica, 50% EtOAc/PE): 0.73 [potassium permanganate];

^{1}H-NMR (400 MHz, $CDCl_3$): δ (ppm) 7.95–8.00 (m, 2H), 7.67–7.72 (m, 2H), 6.95–7.05 (m, 4H), 4.90 (d, *J* = 6.7 Hz, 1H), 4.82 (pent., *J* = 6.7 Hz, 1H), 3.94 (s, 3H), 2.22 (s, 3H), 1.42 (d, *J* = 6.7 Hz, 3H);

^{13}C-NMR (101 MHz, $CDCl_3$): δ (ppm) 165.6, 144.7, 139.5, 134.6, 133.4, 130.6, 129.9, 127.5, 126.9, 126.4, 125.2, 52.6, 49.9, 23.1, 19.0;

HRMS (ESI+): calc. $[M+Na]^+$ for $C_{17}H_{19}NO_4SNa$ 356.0933, found 356.0927, Δ = 0.6 mDa.

Synthesis of *N*-(1-(*o*-tolyl)ethyl)thiophene-2-sulfonamide (3.32)

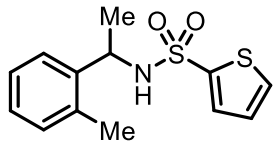

3.32

N-(1-(*o*-Tolyl)ethyl)thiophene-2-sulfonamide (**3.32**) was synthetized according to **GP2** using thiophene-2-sulfonamide (in total 65.2 mg, 0.40 mmol, 1.0 equiv.) as the limiting reagent and 2-(*o*-tolyl)propanoic acid (in total 197 mg, 1.20 mmol, 3.0 equiv.) as an acid in excess. The reaction was irradiated at 385 nm for 16 h. After purification with flash column chromatography (EtOAc/PE, 20% → 40%), the title compound was obtained as a colorless oil which crystallized to white solid upon standing under the ambient conditions (25 mg, 22%).

R_f (silica, 50% EtOAc/PE): 0.87 [potassium permanganate];

^{1}H-NMR (400 MHz, $CDCl_3$): δ (ppm) 7.46 (dd, *J* = 5.0, 1.3 Hz, 1H), 7.38 (dd, *J* = 3.8, 1.3 Hz, 1H), 7.14–7.17 (m, 1H), 7.04–7.10 (m, 3H), 5.11 (d, *J* = 5.7 Hz, 1H), 4.83 (pent., *J* = 6.6 Hz, 1H), 2.25 (s, 3H), 1.44 (d, *J* = 6.8 Hz, 3H);

^{13}C-NMR (101 MHz, $CDCl_3$): δ (ppm) 141.7, 140.0, 134.5, 132.1, 131.7, 130.5, 127.4, 127.1, 126.5, 125.1, 50.2, 23.2, 19.0;

HRMS (ESI+): calc. $[M+Na]^+$ for $C_{13}H_{15}NO_2S_2Na$ 304.0442, found 304.0434, Δ = 0.8 mDa.

Synthesis of 4'-fluoro-*N*-(1-(*o*-tolyl)ethyl-[1,1'-biphenyl]-4-sulfonamide (3.33)

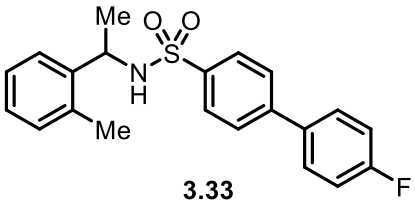

3.33

4'-Fluoro-*N*-(1-(*o*-tolyl)ethyl-[1,1'-biphenyl]-4-sulfonamide (**3.33**) was synthetized according to **GP2** using 4'-fluoro-[1,1'-biphenyl]-4-sulfonamide (in total 100.4 mg, 0.40 mmol, 1.0 equiv.) as the limiting reagent and 2-(*o*-tolyl)propanoic acid (in total 197 mg, 1.20 mmol, 3.0 equiv.) as an acid in excess. The reaction was irradiated at 385 nm for 16 h. After purification with flash column chromatography (Acetone/PE, 20% → 40%), the title compound was obtained as a white solid (87 mg, 59%).

R_f (silica, 50% EtOAc/PE): 0.73 [potassium permanganate];

^{1}H-NMR (400 MHz, $CDCl_3$): δ (ppm) 7.96–8.00 (m, 1H), 7.65–7.69 (m, 1H), 7.54–7.59 (m, 1H), 7.27–7.33 (m, 1H), 7.15–7.21 (m, 4H), 5.03 (br. s., 1H), 3.99 (q., *J* = 7.2 Hz, 1H), 2.38 (s, 3H), 1.49 (d, *J* = 7.2 Hz, 3H);

^{13}C-NMR (101 MHz, $CDCl_3$): δ (ppm) 180.0, 161.9, 144.8, 140.5, 137.0 (d, *J* = 246 Hz), 135.9, 130.6, 130.4 (d, *J* = 13.6 Hz), 129.0 (d, *J* = 8.5 Hz), 129.0 (d, *J* = 9.0 Hz), 127.4 (d, *J* = 41.3 Hz), 127.1, 126.5 (d, *J* = 9.6 Hz), 116.1 (d, *J* = 21.7 Hz), 41.0, 19.6, 17.6;

^{19}F-NMR (376 MHz, $CDCl_3$, $PhCF_3$ as internal standard): δ (ppm) −114.4 – (−)114.5 (m)

HRMS (ESI+): calc. $[M+Na]^+$ for $C_{21}H_{20}FNO_2SNa$ 392.1097, found 392.1082, Δ = 1.5 mDa.

Synthesis of 4-methyl-*N*-phenyl-*N*-(1-(*o*-tolyl)ethyl)benzenesulfonamide (3.34)

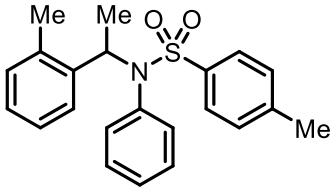

3.34

4-Methyl-*N*-phenyl-*N*-(1-(*o*-tolyl)ethyl)benzenesulfonamide (**3.34**) was synthetized according to **GP2** using 4-methyl-*N*-phenylsulfonamide (in total 98.2 mg, 0.40 mmol, 1.0 equiv.) as the limiting reagent and 2-(*o*-tolyl)propanoic acid (in total 197 mg, 1.20 mmol, 3.0 equiv.) as an acid in excess. The reaction was irradiated at 385 nm for 16 h. After purification with flash column chromatography (EtOAc/PE, 20% → 40%), the title compound was obtained as a white solid (80 mg, 55%).

R_f (silica, 50% EtOAc/PE): 0.90 [potassium permanganate];

^{1}H-NMR (400 MHz, $CDCl_3$): δ (ppm) 7.62–7.67 (m, 2H), 7.17–7.22 (m, 4H), 7.11–7.13 (m, 2H), 6.99–7.03 (m, 2H), 6.94–6.98 (m, 2H), 4.24 (q., *J* = 7.1 Hz, 1H), 2.37 (s, 3H), 2.17 (s, 3H), 1.54 (d, *J* = 7.1 Hz, 3H);

^{13}C-NMR (101 MHz, $CDCl_3$): δ (ppm) 143.7, 143.6, 143.5, 136.2, 136.0, 134.3, 130.4, 129.6, 128.5, 127.3, 126.6, 126.2, 126.1, 121.9, 40.4, 21.9, 21.6, 19.7;

HRMS (ESI+): calc. $[M+Na]^+$ for $C_{22}H_{23}NO_2SNa$ 388.1347, found 388.1345, Δ = 0.2 mDa.

Synthesis of *N*-phenyl-*N*-(1-(*o*-tolyl)ethyl)cyclopropanesulfonamide (3.35)

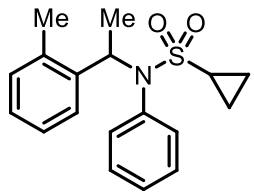

3.35

N-Phenyl-*N*-(1-(*o*-tolyl)ethyl)cyclopropanesulfonamide (**3.35**) was synthetized according to **GP2** using *N*-phenylcyclopropanesulfonamide (in total 78.9 mg, 0.40 mmol, 1.0 equiv.) as the limiting reagent and 2-(*o*-tolyl)propanoic acid (in total 197 mg, 1.20 mmol, 3.0 equiv.) as an acid in excess. The reaction was irradiated at 385 nm for 16 h. After purification with reverse-phase flash column chromatography (H_2O+0.5‰ TFA/MeCN, 10% → 100%), the title compound was obtained as a colorless oil (81 mg, 64%).

R_f (silica, 50% EtOAc/PE): 0.97 [potassium permanganate];

^{1}H-NMR (400 MHz, $CDCl_3$): δ (ppm) 7.13–7.31 (m, 9H), 6.88 (br. s., 1H), 4.33 (q., *J* = 7.2 Hz, 1H), 2.49 (tt, *J* = 8.0, 4.8 Hz, 1H), 2.26 (s, 3H), 1.63 (d, *J* = 7.2 Hz, 3H), 1.14–1.19 (m, 2H), 0.92–0.98 (m, 2H);

^{13}C-NMR (101 MHz, $CDCl_3$): δ (ppm) 143.7, 143.6, 136.0, 134.5, 130.5, 128.6, 126.6, 126.2, 126.1, 122.3, 40.5, 29.7, 22.1, 19.8, 5.6;

HRMS (ESI+): calc. $[M+NH_4]^+$ for $C_{18}H_{21}NO_2SNH_4$ 333.1637, found 333.1633, Δ = 0.4 mDa.

Synthesis of *N*-phenyl-*N*-(1-(*o*-tolyl)ethyl)cyclohexanesulfonamide (3.36)

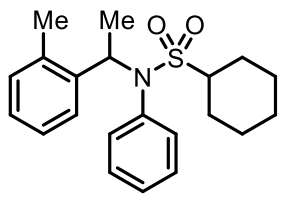

3.36

N-Phenyl-*N*-(1-(*o*-tolyl)ethyl)cyclohexanesulfonamide (**3.36**) was synthetized according to **GP2** using *N*-phenylcyclohexanesulfonamide (in total 95.7 mg, 0.40 mmol, 1.0 equiv.) as the limiting reagent and 2-(*o*-tolyl)propanoic acid (in total 197 mg, 1.20 mmol, 3.0 equiv.) as an acid in excess. The reaction was irradiated at 385 nm for 16 h. After purification with reverse-phase flash

column chromatography (H_2O+0.5‰ TFA/MeCN, 10% → 100%), the title compound was obtained as a yellow-orange oil (88 mg, 62 %).

R_f (silica, 50% EtOAc/PE): 0.95 [potassium permanganate];

^{1}H-NMR (400 MHz, $CDCl_3$): δ (ppm) 7.27–7.31 (m, 1H), 7.21–7.26 (m, 1H), 7.11–7.19 (m, 6H), 6.99 (s, 1H), 4.32 (q., *J* = 7.1 Hz, 1H), 3.02 (tt, *J* = 12.0, 3.2 Hz, 1H), 2.27 (s, 3H), 2.19 (d, *J* = 12.0 Hz, 2H), 1.88 (d, *J* = 10.6 Hz, 2H), 1.67–1.72 (m, 1H), 1.63 (d, *J* = 7.1 Hz, 3H), 1.53–1.59 (m, 2H), 1.13–1.30 (m, 3H);

^{13}C-NMR (101 MHz, $CDCl_3$): δ (ppm) 130.5, 128.7 (2C), 126.6, 126.2, 126.1, 120.5 (2C), 60.3, 40.4, 26.3, 25.1, 22.1, 19.8;

HRMS (ESI+): calc. $[M+Na]^+$ for $C_{21}H_{27}NO_2SNa$ 380.1660, found 380.1658, Δ = 0.2 mDa.

Synthesis of methyl 2,3-dimethoxy-5-(*N*-(1-(*o*-tolyl)ethyl)sulfamoylbenzoate (3.37)

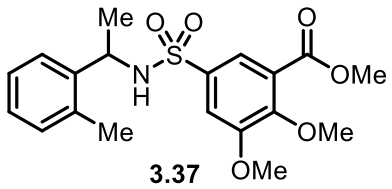

3.37

Methyl 2,3-dimethoxy-5-(*N*-(1-(*o*-tolyl)ethyl)sulfamoylbenzoate (**3.37**) was synthetized according to **GP2** using methyl 2,3-dimethoxy-5-sulfamylbenzoate (in total 110.0 mg, 0.40 mmol, 1.0 equiv.) as the limiting reagent and 2-(*o*-tolyl)propanoic acid (in total 197 mg, 1.20 mmol, 3.0 equiv.) as an acid in excess. The reaction was irradiated at 385 nm for 16 h. After purification with flash column chromatography (EtOAc/PE, 20% → 40%), the title compound was obtained as a colorless oil which crystallized to white solid upon standing under the ambient conditions (40 mg, 25%).

R_f (silica, 50% EtOAc/PE): 0.77 [potassium permanganate];

^{1}H-NMR (400 MHz, $CDCl_3$): δ (ppm) 7.65 (d, *J* = 2.2 Hz, 1H), 7.15 (d, *J* = 2.2 Hz, 1H), 6.94–7.02 (m, 4H), 5.32 (d, *J* = 7.3 Hz, 1H), 4.81 (pent., *J* = 6.9 Hz, 1H), 3.89 (s, 3H), 3.87 (s, 3H), 2.23 (s, 3H), 1.42 (d, *J* = 6.9 Hz, 3H);

^{13}C-NMR (101 MHz, $CDCl_3$): δ (ppm) 165.0, 153.3, 152.2, 139.7, 135.6, 134.4, 130.3, 127.3, 126.2, 125.3, 121.5, 113.3, 110.0, 61.6, 56.1, 52.4, 49.9, 23.4, 19.0;

HRMS (ESI+): calc. $[M+H]^+$ for $C_{19}H_{24}NO_6SNa$ 394.1324, found 394.1320, Δ = 0.4 mDa.

Synthesis of 4-(5-(*p*-tolyl)-3-(trifluoromethyl)-1*H*-pyrazol-1-yl)-*N*-(1-(*o*-tolyl)ethyl)benzenesulfonamide (3.38)

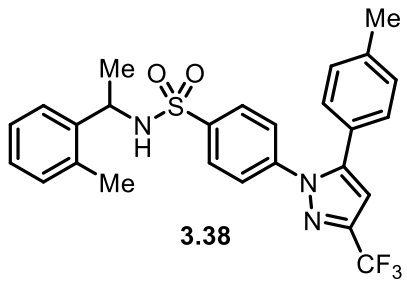

3.38

4-(5-(*p*-Tolyl)-3-(trifluoromethyl)-1*H*-pyrazol-1-yl)-*N*-(1-(*o*-tolyl) ethyl)benzenesulfonamide (**3.38**) was synthetized according to **GP2** using 4-(5-(*p*-tolyl)-3-(trifluoromethyl)-1*H*-pyrazol-1-yl)benzenesulfonamide (celebrex, in total 152.4 mg, 0.40 mmol, 1.0 equiv.) as the limiting reagent and 2-(*o*-tolyl)propanoic acid (in total 197 mg, 1.20 mmol, 3.0 equiv.) as an acid in excess. The reaction was irradiated at 385 nm for 16 h. After purification with flash column chromatography (EtOAc/PE, 20% → 40%), the title compound was obtained as a colorless oil which crystallized to white solid upon standing under the ambient conditions (136 mg, 68%).

R_f (silica, 50% EtOAc/PE): 0.95 [potassium permanganate];

^{1}H-NMR (400 MHz, $CDCl_3$): δ (ppm) 7.63–7.67 (m, 2H), 7.29–7.32 (m, 2H), 7.15–7.18 (m, 2H), 7.03–7.11 (m, 6H), 7.67 (s, 1H), 5.07 (d, *J* = 6.6 Hz, 1H), 4.79 (pent., *J* = 6.7 Hz, 1H), 2.38 (s, 3H), 2.24 (s, 3H), 1.40 (d, *J* = 6.7 Hz, 3H);

^{13}C-NMR (101 MHz, $CDCl_3$): δ (ppm) 145.1, 144.1 (q, *J* = 38 Hz), 142.2, 140.2, 139.8, 139.7, 134.5, 130.6, 129.7, 128.7, 127.9, 127.6, 126.5, 125.8, 125.3, 125.1, 121.0 (q, *J* = 268 Hz), 49.9, 23.1, 21.3, 19.1;

^{19}F-NMR (376 MHz, $CDCl_3$, $PhCF_3$ as internal standard): δ (ppm) − 63.5 (s)

HRMS (ESI+): calc. $[M+H]^+$ for $C_{26}H_{25}F_3N_3O_2S$ 500.1620, found 500.1617, Δ = 0.3 mDa.

3.5.4 Synthesis and characterization of starting materials

GP3: General Procedure for methylation of benzylic acids[32]

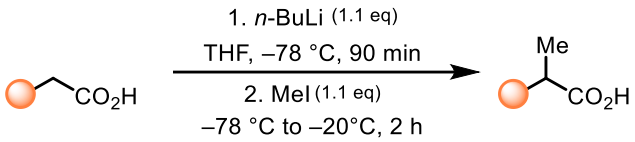

The phenyl acetic acid derivative (20 mmol, 1.00 equiv.) was added into a flame-dried Schlenk flask equipped with a stirring bar under N_2. Dry THF (100 mL, 0.2 M) was added *via* syringe, and the mixture was cooled down to −78 °C. At this temperature, *n*-butyllithium (1.6 M in hexanes, 26 mL, 42 mmol, 2.10 equiv.) was added in a dropwise manner. During the addition of the first equivalent, the reaction mixture turned white and turbid, the second equivalent gave the reaction a yellow-orange color as indication of the benzylic deprotonation. These color changes can be used to qualitatively follow the reaction progress after the addition of the electrophile. In cases where the substrate fell out of the solution due to the low solubility of the lithium carboxylate, the reaction was shaken in between the addition of the second BuLi-equivalent to improve the re-solvation of the anionic intermediate. To ensure full deprotonation, the mixture was allowed to warm to −20 °C over 1–2 hours, after which it was cooled down again to −78 °C before the addition of MeI (1.37 mL, 22 mmol, 1.10 equiv.). The reaction mixture was then stirred for two more hours while allowing to gently warm up. The reaction was quenched with sat. NH_4Cl (10 mL) and acidified with 2M HCl to pH 1. Et_2O (50 mL) was added, and the phases were separated. The aqueous layer was extracted with Et_2O (3 × 30 mL), and the combined organic layers were washed with sat. aq. sodium dithionite solution (2 × 50 mL) and brine (50 mL). The organic layers were dried over Mg_2SO_4, the drying reagent filtered off and the solvent evaporated under reduced pressure. The crude product was purified by flash column chromatography (MeOH/DCM, 5% → 10%).

GP4: General Procedure for alkylation of phenylacetic acid

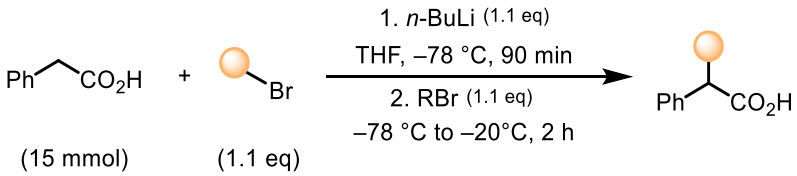

(±)2-Phenylacetic acid (2.0 g, 15.0 mmol, 1.0 equiv.) was added into a flame-dried Schlenk flask equipped with stirring bar under N_2. Dry THF (75 mL, 0.2 M) was added *via* syringe and the mixture was cooled down to −78 °C. At this temperature, *n*-butyllithium (1.6 M in hexanes, 20 mL, 21 mmol, 2.10 equiv.) was added in a dropwise manner. The reaction mixture was then stirred for 90 minutes while allowing to gently warm up, after which it was cooled back to −78 °C, and the bromide (1.1 equiv.) was added dropwise. The mixture was allowed to warm up again towards room temperature, and after (typically) two hours. The reaction was quenched with sat. NH_4Cl (10 mL) and acidified with 2M HCl to pH 1. Et_2O (50 mL) was added, and the phases were separated. The aqueous layer was extracted with Et_2O (3 × 30 mL), and the combined organic layers were washed with sat. aq. sodium dithionite solution (2 × 50 mL) and brine (50 mL). The organic layers were dried over Mg_2SO_4, the drying reagent filtered off and the solvent evaporated under reduced pressure. The crude product was purified by flash column chromatography (MeOH/DCM, 5% → 10%).

3.5.4.1 List of synthetized successful carboxylic acids

Synthesis of 2-(*m*-tolyl)propanoic acid (3.39)

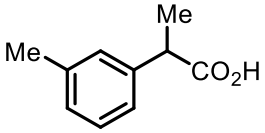

3.39

Synthetized according to **GP3** using 2-(*m*-tolyl)acetic acid (3.00 g, 20.0 mmol, 1.00 equiv.) as a starting material. After purification with flash column chromatography (MeOH/DCM, 5%), the title compound was obtained as a yellowish oil which eventually crystallized to a pale solid under ambient conditions (1.45 g, 44%).

R_f (silica, 5% MeOH/DCM) 0.26 [bromocresol green]

^{1}H-NMR (400 MHz, $CDCl_3$): δ (ppm) 11.96 (br. s., 1H), 7.34–7.39 (m, 1H), 7.21–7.30 (m, 3H), 3.85 (q, J = 7.15 Hz, 1H), 2.49 (s, 3H), 1.65 (d, J = 7.15 Hz, 3H);

^{13}C-NMR (101 MHz, $CDCl_3$): δ (ppm) 181.5, 139.9, 138.5, 128.8, 128.5, 128.3, 124.8, 45.5, 21.5, 18.2;

HRMS (EI+): calc. $[M]^{+\cdot}$ for $C_{10}H_{12}O_2^{+\cdot}$ 164.08318, found 164.08304, Δ = 0.14 mDa.

Synthesis of 2-(*o*-tolyl)propanoic acid (3.40)

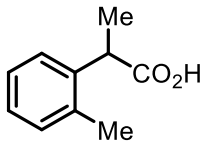

3.40

Synthetized according to **GP3** using 2-(*o*-tolyl)acetic acid (3.00 g, 20.0 mmol, 1.00 equiv.) as a starting material. After purification with flash column chromatography (MeOH/DCM, 5%), the title compound was obtained as a white hard solid (2.11 g, 64%).

R_f (silica, 5% MeOH/DCM) 0.44 [bromocresol green]

^{1}H-NMR (400 MHz, $CDCl_3$): δ (ppm) 7.28–7.31 (m, 1H), 7.16–7.23 (m, 3H), 3.99 (q, *J* = 7.15 Hz, 1H), 2.39 (s, 3H), 1.50 (d, *J* = 7.15 Hz, 3H);

^{13}C-NMR (101 MHz, $CDCl_3$): δ (ppm) 180.7, 138.3, 135.9, 130.6, 127.2, 126.6, 126.5, 41.1, 19.7, 17.5;

HRMS (EI+): calc. $[M]^{\cdot+}$ for $C_{10}H_{12}O_2^{\cdot+}$ 164.08318, found 164.08321, Δ = – 0.03 mDa.

Synthesis of 2-(4-(*tert*-butyl)phenyl)propanoic acid (3.41)

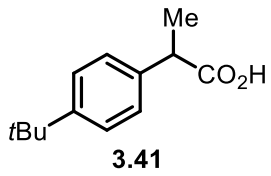

3.41

Synthetized according to **GP3** using 2-(4-*tert*-butyl)phenylacetic acid (3.85 g, 20.0 mmol, 1.00 equiv.) as a starting material. After purification with flash column chromatography (MeOH/DCM, 5%), the title compound was obtained as an off-white solid (1.20 g, 29%).

R_f (silica, 5% MeOH/DCM) 0.41 [bromocresol green]

^{1}H-NMR (400 MHz, $CDCl_3$): δ (ppm) 7.25–7.29 (m, 2H), 7.15–7.19 (m, 2H), 3.63 (q., *J* = 7.1 Hz, 1H), 1.42 (d, *J* = 7.1 Hz, 3H), 1.23 (s, 9H);

^{13}C-NMR (101 MHz, $CDCl_3$): δ (ppm) 181.0, 150.3, 136.6, 127.2, 125.6, 44.9, 34.5, 31.3, 18.0;

HRMS (EI+): calc. $[M]^{\cdot+}$ for $C_{13}H_{18}O_2^{\cdot+}$ 206.13013, found 206.13037, Δ = – 0.24 mDa.

Synthesis of 2-(4-fluorophenyl)propanoic acid (3.42)

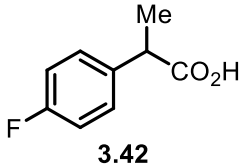

3.42

Synthetized according to **GP3** using 2-(4-fluorophenyl)acetic acid (3.80 g, 20.0 mmol, 1.00 equiv.) as starting material. After purification with flash column chromatography (MeOH/DCM, 5%) and drying in high vacuo, the title compound was obtained as a yellow oil (2.9 g, 86%).

R_f (silica, 5% MeOH/DCM) 0.64 [bromocresol green]

^{1}H-NMR (400 MHz, $CDCl_3$): δ (ppm) 11.42 (br. s., 1H), 7.27–7.33 (m, 2H), 7.00–7.05 (m, 2H), 3.70–3.77 (m, 1H), 1.49–1.53 (m, 3H);

^{13}C-NMR (101 MHz, $CDCl_3$): δ (ppm) 181.0, 162.2 (d, J = 246 Hz), 131.0 (d, J = 8.1 Hz), 129.2 (d, J = 7.8 Hz), 115.5 (d, J = 21.5 Hz), 44.7, 18.2;

^{19}F-NMR (376 MHz, $CDCl_3$, $PhCF_3$ as internal standard): δ (ppm) −115.31 – (−)115.40 (m)

HRMS (EI+): calc. $[M]^{\cdot+}$ for $C_9H_9FO_2^{\cdot+}$ 168.05811, found 168.05833, Δ = – 0.22 mDa.

Synthesis of 2-(4-chlorophenyl)propanoic acid (3.43)

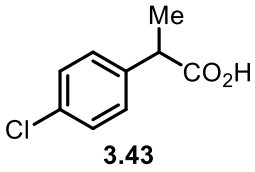

3.43

Synthetized according to a modified literature procedure over two steps.[34] 2-(4-chlorophenyl)acetonitrile (3.82 mL, 30.0 mmol, 1.00 equiv.) was dissolved to THF (30 mL) and cooled to 0 °C. NaH (60% in mineral oil, 1.32 g, 33.0 mmol, 1.10 equiv.) was added portionwise, and the reaction mixture was stirred for 3 h while allowing to warm towards room temperature. After this the mixture was cooled again to 0 °C and MeI (2.05 mL, 33.0 mmol, 1.10 equiv.) was added dropwise. Cooling bath was then removed, and the reaction was stirred overnight at room temperature. The reaction was quenched with sat. NH_4Cl (20 mL), diluted with water (200 mL) and extracted with EtOAc (3 × 50 mL). The combined organic phases were washed with water (100 mL) and brine (100 mL), dried over Mg_2SO_4, filtrated, and the solvent was removed under reduced pressure. The so-obtained crude product (3.98 g, 80 %) was used in the following step without further purification.

The crude product (3.98 g, 24.0 mmol, 1.00 equiv.) was dissolved into ethylene glycol (40 mL), and KOH (14 g, 150 mmol, 6 equiv.) was added. The reaction was then refluxed at 168 °C overnight. After cooling to room temperature, water and ethyl acetate were added, the reaction was acidified with 2M HCl (pH = 1) and the phases then separated. The aqueous phase was extracted with EtOAc (3×), the combined organic phases dried over Mg_2SO_4, filtered, and concentrated under reduced pressure. Purification with flash column chromatography (EtOAc/PE, 30%) followed by removal of the solvents afforded the title compound as a white solid (1.36 g, 31 %; overall yield over two steps 25%).

R_f (silica, 5% MeOH/DCM) 0.36 [bromocresol green]

^{1}H-NMR (400 MHz, $CDCl_3$): δ (ppm) 7.26–7.35 (m, 5H), 3.75 (q, J = 7.2 Hz, 1H), 1.53 (d, J = 7.2 Hz, 3H);

^{13}C-NMR (101 MHz, $CDCl_3$): δ (ppm) 179.9, 138.1, 133.3, 129.0, 128.8, 128.6, 127.3, 44.7, 26.2, 18.1;

HRMS (EI+): calc. $[M]^{\cdot+}$ for $C_9H_9ClO_2^{\cdot+}$ 184.02856, found 184.02935, Δ = – 0.79 mDa.

Synthesis of 2-(4-trifluoromethoxy)phenyl)propanoic acid (3.44)

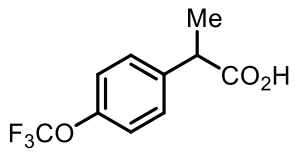

3.44

Synthetized according to **GP3** using 2-(4-trifluoromethoxy)phenyl)acetic acid (780 mg, 3.5 mmol, 1.00 equiv.) as a starting material. After purification with flash column chromatography (MeOH/DCM, 5%) and drying in high vacuo, the title compound was obtained as a yellow oil (606 mg, 73%).

R_f (silica, 5% MeOH/DCM) 0.80 [bromocresol green]

^{1}H-NMR (400 MHz, $CDCl_3$): δ (ppm) 11.52 (br. s., 1H), 7.35–7.40 (m, 2H), 7.20 (app. d., *J* = 8.0 Hz, 2H), 3.78 (q, *J* = 7.2 Hz, 1H), 1.54 (d, *J* = 7.2 Hz, 3H);

^{13}C-NMR (101 MHz, $CDCl_3$): δ (ppm) 180.8, 148.5, 138.3, 129.1, 121.1, 120.4 (q., *J* = 257 Hz) 44.8, 18.0;

^{19}F-NMR (376 MHz, $CDCl_3$, $PhCF_3$ as internal standard): δ (ppm) – 58.90 (s)

HRMS (EI+): calc. $[M]^{\cdot+}$ for $C_{10}H_9F_3O_2^{\cdot+}$ 234.04983, found 234.04999, Δ = – 0.16 mDa.

Synthesis of 2-phenylhexanoic acid (3.45)

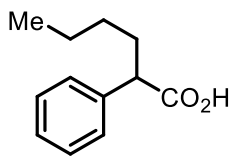

3.45

Synthetized according to **GP4** using 2-phenylacetic acid (2.0 g, 15.0 mmol, 1.0 equiv.) as limiting reagent and *n*-bromobutane (1.1 equiv.) as an electrophilic coupling partner. After purification with flash column chromatography (MeOH/DCM, 2.5%), the title compound was obtained as a yellow oil (2.29 g, 79 %).

R_f (silica, 5% MeOH/DCM) 0.75 [bromocresol green]

^{1}H-NMR (400 MHz, $CDCl_3$): δ (ppm) 11.11 (br. s, 1H), 7.28–7.37 (m, 5H), 3.57 (t, *J* = 7.7 Hz, 1H), 2.06–2.16 (m, 1H), 1.77–1.87 (m, 1H), 1.19–1.41 (m, 4H), 0.90 (t, *J* = 7.2 Hz, 3H);

^{13}C-NMR (101 MHz, $CDCl_3$): δ (ppm) 180.4, 138.6, 128.6, 128.1, 127.4, 51.6, 32.8, 29.6, 22.4, 13.8;

HRMS (EI+): calc. $[M]^{\cdot+}$ for $C_{12}H_{16}O_2^{\cdot+}$ 192.11448, found 192.11447, Δ = 0.01 mDa.

Synthesis of 2,3-diphenylpropanoic acid (3.46)

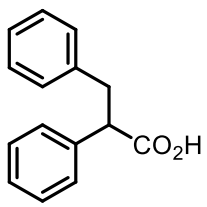

3.46

Synthetized according to **GP4** using 2-phenylacetic acid (2.0 g, 15.0 mmol, 1.0 equiv.) as a limiting reagent and benzyl bromide (1.1 equiv.) as an electrophilic coupling partner. After purification with flash column chromatography (MeOH/DCM, 2.5%), the title compound was obtained as a white solid (1.25 g, 37 %).

R_f (silica, 5% MeOH/DCM) 0.28 [bromocresol green]

^{1}H-NMR (400 MHz, $CDCl_3$): δ (ppm) 7.10–7.27 (m, 8H), 7.04–7.08 (m, 2H), 3.81 (dd, *J* = 8.7, 7.0 Hz, 1H), 3.36 (dd, *J* = 14.2, 8.4 Hz, 1H), 2.99 (dd, *J* = 14.2, 7.0 Hz, 1H);

^{13}C-NMR (101 MHz, $CDCl_3$): δ (ppm)

HRMS (EI+): calc. $[M]^{\cdot+}$ for $C_{15}H_{14}O_2^{\cdot+}$ 226.09883, found 226.09852, Δ = 0.31 mDa.

Synthesis of 3-cyclohexyl-2-phenylpropanoic acid (3.47)

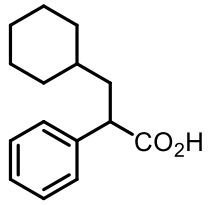

3.47

Synthetized according to **GP4** using phenylacetic acid (2.0 g, 15.0 mmol, 1.0 equiv.) as a limiting reagent and (bromomethyl)cyclohexane (1.1 equiv.) as an electrophilic coupling partner. After purification with normal phase flash column chromatography (MeOH/DCM, 5 %) on silica and a reverse-phase column chromatography (H_2O+0.5‰ TFA/MeCN, 10% → 100%), the title compound was obtained as a white solid (875 mg, 25 %).

R_f (silica, 5% MeOH/DCM) 0.45 [bromocresol green]

^{1}H-NMR (400 MHz, $CDCl_3$): δ (ppm) 7.24–7.33 (m, 5H), 3.70 (t, *J* = 7.8 Hz, 1H), 1.93–2.02 (m, 1H), 1.71–1.77 (m, 1H), 1.57–1.70 (m, 4H), 1.09–1.22 (m, 4H), 0.84–0.96 (m, 2H);

^{13}C-NMR (101 MHz, $CDCl_3$): δ (ppm) 179.0, 138.8, 128.7, 128.1, 127.4, 48.5, 40.7, 35.1, 33.3, 32.9, 26.5, 26.1, 26.0;

HRMS (EI+): calc. $[M]^{\cdot+}$ for $C_{15}H_{20}O_2^{\cdot+}$ 232.14578, found 232.14632, Δ = – 0.54 mDa.

Synthesis of 2-cyclohexyl-2-phenylacetic acid (3.48)

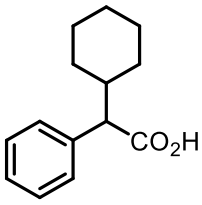

3.48

Synthetized according to **GP4** using 2-phenylacetic acid (2.0 g, 15.0 mmol, 1.0 equiv.) as a limiting reagent and cyclohexyl bromide (1.1 equiv.) as an electrophilic coupling partner. After purification with normal phase flash column chromatography (MeOH/DCM, 5 %) on silica and a reverse-phase column chromatography (H_2O+0.5‰ TFA/MeCN, 10% → 100%), the title compound was obtained as a white solid (1.03 g, 32 %).

R_f (silica, 5% MeOH/DCM) 0.38 [bromocresol green]

^{1}H-NMR (400 MHz, $CDCl_3$): δ (ppm) 10.5 (br. s., 1H), 7.28–7.39 (m, 5H), 3.26 (d, *J* = 10.9 Hz, 1H), 2.05 (qt, *J* = 10.9, 3.3 Hz, 1H), 1.91–1.98 (m, 1H), 1.75–1.82 (m, 1H), 1.60–1.70 (m, 2H), 1.29–1.41 (m, 2H), 1.06–1.24 (m, 3H), 0.73–0.83 (m, 1H);

^{13}C-NMR (101 MHz, $CDCl_3$): δ (ppm) 180.4, 137.3, 128.7, 128.5, 127.4, 58.9, 40.7, 32.0, 30.3, 26.3, 26.0, 25.9;

HRMS (EI+): calc. $[M]^{\cdot+}$ for $C_{14}H_{18}O_2$ 218.13013, found 218.13019, Δ = – 0.16 mDa.

Synthesis of 2-(naphthalen-1-yl)propanoic acid (3.49)

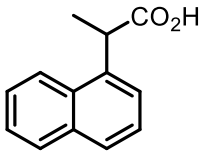

3.49

Synthetized according to **GP3** using 2-(napthalen-1-yl)acetic acid (3.72 g, 20.0 mmol, 1.00 equiv.) as a starting material. After purification with flash column chromatography (MeOH/DCM, 5%) and drying in high-vacuo, the title compound was obtained as an off-white solid (1.09 g, 18%).

R_f (silica, 5% MeOH/DCM) 0.29 [bromocresol green]

^{1}H-NMR (400 MHz, $CDCl_3$): δ (ppm) 8.10 (d, *J* = 8.4 Hz, 1H), 7.88 (dd, *J* = 7.9, 1.4 Hz, 1H), 7.79 (d, *J* = 7.9 Hz, 1H), 7.44–7.58 (m, 4H), 4.55 (q, *J* = 7.2 Hz, 1H), 1.68 (d, *J* = 7.2 Hz, 3H);

^{13}C-NMR (101 MHz, $CDCl_3$): δ (ppm) 180.7, 135.9, 133.9, 131.3, 129.0, 128.0, 126.5, 125.7, 125.5, 124.6, 123.0, 41.0, 17.8;

HRMS (EI+): calc. $[M]^{\cdot+}$ for $C_{13}H_{12}O_2^{\cdot+}$ 200.08318, found 200.08357, Δ = – 0.39 mDa.

3.5.4.2 List of synthetized unsuccessful carboxylic acids

Synthesis of 1-phenylcyclopentane-1-carboxylic acid (S3.1)

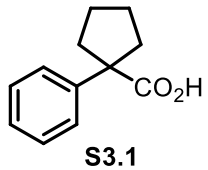

S3.1

Synthetized in a two-step manner starting from 2-phenylacetonitrile following a literature-reported procedure.[35] NaH (60% suspension in mineral oil, 1.92 g, 48 mmol, 2.4 equiv.) was suspended into DMF (14 mL) and cooled to 0 °C. A solution of 2-phenylacetonitrile (2.34 g, 20.00 mmol, 1.00 equiv.) in DMF (22 mL) was added dropwise to the suspension, and the reaction was stirred for 1 h while allowing to warm towards room temperature. 1,4-Dibromobutane (5.16 g, 24 mmol, 1.2 equiv.) was added dropwise at room temperature, after which the reaction was stirred for 5 hours. The reaction was then quenched with water (10 mL). The mixture was extracted with EtOAc (3 × 15 mL), the combined organic layers washed with brine (20 mL) and eventually dried over $MgSO_4$. The drying agent was filtered off and the solvent removed under reduced pressure. After purification with flash column chromatography (EtOAc/PE, 10%), the 1-phenylcyclopentane-1-carbonitrile was obtained as a yellow oil (1.03 g, 30%).

For the hydrolysis of the nitrile group into carboxylic acid, the previously obtained 1-phenylcyclopentane-1-carbonitrile (1.03 g, 6.00 mmol, 1.00 equiv.) was dissolved in ethylene glycol (10 mL) and KOH (2.0 g, 36.0 mmol, 6.00 equiv.) was added. The reaction was then refluxed at 168 °C overnight. After cooling to room temperature, water and ethyl acetate were added, the reaction was acidified with 2M HCl (pH = 1), and the phases then separated. The aqueous phase was extracted with EtOAc (3×), the combined organic phases dried over Mg_2SO_4, filtered, and concentrated under reduced pressure. Purification with flash column chromatography (EtOAc/PE, 30%), the 1-phenylcyclopentane-1-carboxylic acid was obtained as a white solid (0.45 g, 39%).

R_f (silica, 5% MeOH/DCM) 0.35 [bromocresol green]

^{1}H-NMR (400 MHz, $CDCl_3$): δ (ppm) 11.2 (br. s., 1H), 7.38–7.42 (m, 2H), 7.29–7.34 (m, 2H), 7.22–7.27 (m, 1H), 2.63–2.70 (m, 2H), 1.88–1.97 (m, 2H), 1.71–1.77 (m, 4H);

^{13}C-NMR (101 MHz, $CDCl_3$): δ (ppm) 182.0, 142.8, 128.3, 127.1, 110.0, 58.8, 36.0, 23.6;

HRMS (EI+): calc. $[M]^{\cdot+}$ for $C_{12}H_{14}O_2^{\cdot+}$ 190.09883, found 190.09862, Δ = 0.21 mDa.

Synthesis of 2-phenylpent-4-enoic acid (S3.2)

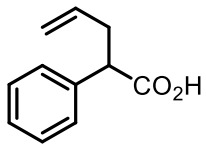

S3.2

Synthetized according to **GP4** using 2-phenylacetic acid (2.0 g, 15.0 mmol, 1.0 equiv.) as the limiting reagent and allyl bromide (1.1 equiv.) as an electrophilic coupling partner. After purification with flash column chromatography (MeOH/DCM, 2.5%) the title compound was obtained as a white solid (1.44 g, 54 %).

R_f (silica, 5% MeOH/DCM) 0.39 [bromocresol green]

^{1}H-NMR (400 MHz, $CDCl_3$): δ (ppm) 11.00 (br.s., 1H), 7.28–7.38 (m, 5H), 5.77 (ddt, *J* = 17.2, 10.3, 6.8 Hz, 1H), 5.13 (dq, *J* = 17.2, 1.6 Hz, 1H), 5.04–5.08 (m, 1H), 3.69 (dd, *J* = 8.8, 7.2 Hz, 1H), 2.83–2.91 (m, 1H), 2.54–2.62 (m, 1H);

^{13}C-NMR (101 MHz, $CDCl_3$): δ (ppm) 179.8, 137.8, 134.9, 128.7, 128.1, 127.6, 117.3, 51.4, 37.1;

HRMS (EI+): calc. $[M]^{\cdot+}$ for $C_{11}H_{12}O_2^{\cdot+}$ 176.08318, found 176.08274, Δ = 0.44 mDa.

Synthesis of 2-(thiophen-2-yl)propanoic acid (F3.2)

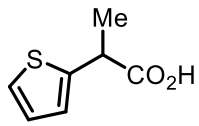

F3.2

Synthetized according to **GP3** using 2-(thiophen-2-yl)acetic acid (2.84 g, 20.0 mmol, 1.00 equiv.) as a starting material. After purification with flash column chromatography (MeOH/DCM, 5%) and drying in high-vacuo, the title compound was obtained as a yellow oil (1.09 g, 18%).

R_f (silica, 5% MeOH/DCM) 0.65 [bromocresol green]

^{1}H-NMR (400 MHz, $CDCl_3$): δ (ppm) 9.16 (br. s., 1H), 7.23 (dd, *J* = 5.1, 1.3 Hz, 1H), 6.99–7.01 (m, 1H), 6.97 (dd, *J* = 5.1, 3.5 Hz, 1H), 4.04 (q., *J* = 7.3 Hz, 1H), 1.62 (d, *J* = 7.3 Hz, 3H);

^{13}C-NMR (101 MHz, $CDCl_3$): δ (ppm) 179.7, 142.0, 126.7, 125.2, 124.6, 40.7, 19.1;

HRMS (EI+): calc. $[M]^{\cdot+}$ for $C_7H_8O_2S^{\cdot+}$ 156.02395, found 156.02396, Δ = – 0.01 mDa.

3.5.5 Synthesis of sulfonamide nucleophiles

GP5: General Procedure for the Sulfonamide Synthesis

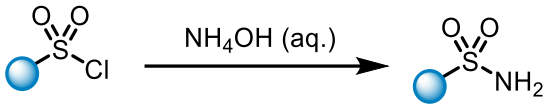

Typically, the sulfonamides were synthetized as following (see details at each sulfonamide): The respective sulfonyl chloride (1.00 equiv.) was either dissolved directly into the ammonium hydroxide (25 % solution in water) or into a noted organic solvent under ambient conditions. If not used as a solvent, ammonium hydroxide was added, and the reaction was stirred first at room temperature followed by heating up to 100 °C. The reaction was followed with thin-layer chromatography (TLC), and when full conversion of the starting material was indicated, the reaction was cooled down to room temperature and quenched by adding a 1:1 mixture of water and ethyl acetate. The phases were separated, and the aqueous phase extracted with EtOAc (3×). The combined organic phases were washed with brine, dried over $MgSO_4$, the drying agent filtered off. Removal of the solvent under reduced pressure gave a white solid. The purity of the crude product was determined with ^{1}H-NMR spectroscopy and, if needed, the product was purified by passing through a short silica plug eluating with 1:1 EtOAc/PE. Removal of the solvent then gave the final product.

3.5.5.1 List of synthetized successful sulfonamides

Synthesis of 4-trifluoromethylbenzenesulfonamide (3.50)

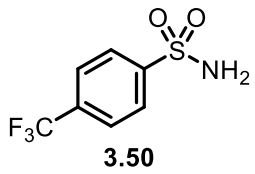

3.50

Synthetized according to a modified literature-reported procedure.[36] 4-Trifluoromethylbenzenesulfonyl chloride (2.46 g, 10.0 mmol, 1.00 equiv.) was dissolved in ammonium hydroxide (25% solution in H_2O, 4 mL) under ambient conditions. The reaction mixture was stirred overnight at room temperature, after which the reaction was quenched by addition of a mixture of water and ethyl acetate (1:1, 10 mL). The phases were separated, aqueous phase extracted with EtOAc (3 ×10 mL) and combined organic layers washed with brine (20 mL). After drying over Mg_2SO_4, the drying agent was filtered off and the solvent removed under reduced pressure. The crude product was purified by a short column (EtOAc/PE, 50%), and after removal of solvent, the title compound was obtained as a white solid (1.85 g, 82 %).

R_f (silica, 50% EtOAc/PE) 0.73 [potassium permanganate];

^{1}H-NMR (400 MHz, $CDCl_3$): δ (ppm) 8.06 (d, *J* = 8.3 Hz, 2H), 7.98 (d, *J* = 8.3 Hz, 2H), 7.64 (s, 2H);

^{13}C-NMR (101 MHz, $CDCl_3$): δ (ppm) 148.3, 132.18 (q, *J* = 32.2 Hz), 127.1, 126.7 (q, *J* = 3.8 Hz), 124.1 (q, *J* = 274.0 Hz);

^{19}F-NMR (376 MHz, $CDCl_3$, $PhCF_3$ as internal standard): δ (ppm) − 63.39 (s)

HRMS (ESI+): calc. $[M+H]^+$ for $C_7H_7F_3NO_2S^+$ 226.0150, found 226.0145, Δ = 0.5 mDa.

Synthesis of 4-cyanobenzenesulfonamide (3.51)

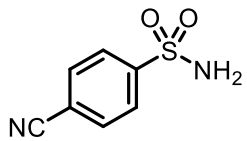

3.51

Synthetized according to a modified literature procedure.[37] 4-cyanobenzenesulfonyl chloride (1.5 g, 7.4 mmol, 1.0 equiv.) was dissolved in 25% ammonium hydroxide (10 mL) at room temperature. The mixture was then heated up and refluxed at 100 °C for 1 h. After cooling back to room temperature, the formed white precipitate was filtered, and the crude product was washed with water (3 × 10 mL). The residual water was removed *via* lyophilization after which the title compound was obtained as an off-white powder (1.0 g, 74%).

R_f (silica, 50% EtOAc/PE) 0.51 [potassium permanganate];

^{1}H-NMR (400 MHz, $CDCl_3$): δ (ppm) 8.07−8.10 (m, 2H), 7.97−8.00 (m, 2H), 7.59 (br. s., 2H), 3.43 (s, 3H);

^{13}C-NMR (101 MHz, $CDCl_3$): δ (ppm) 148.4, 133.7, 126.9, 118.3, 114.8;

HRMS (ESI+): calc. $[M+H]^+$ for $C_7H_7N_2O_2S^+$ 183.0228, found 183.0221, Δ = 0.7 mDa.

Synthesis of 3,5-dichlorobenzenesulfonamide (3.52)

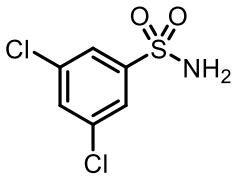

3.52

Synthetized according to a literature-reported procedure.[38] 3,5-Dichlorobenzenesulfonyl chloride (1.47 g, 6.00 mmol, 1.00 equiv.) was dissolved in ammonium hydroxide (25% solution in H_2O, 16 mL) under ambient conditions. The reaction was stirred at room temperature for 3 h, after which it was quenched by addition of a mixture of water and ethyl acetate (1:1, 12 mL). The formed layers were separated, the aqueous layer extracted with EtOAc (3 ×10 mL), and combined organic layers washed with brine (20 mL). After drying over Mg_2SO_4, the drying agent was filtered off and the solvent removed under reduced pressure. The crude product was purified by a short column (EtOAc/PE, 50%), and after removal of solvent, the title compound was obtained as a white solid (305 mg, 23 %).

R_f (silica, 50% EtOAc/PE) 0.83 [potassium permanganate];

^{1}H-NMR (400 MHz, $CDCl_3$): δ (ppm) 7.92–7.94 (m, 1H), 7.80 (d, J = 1.9 Hz, 2H), 7.65 (br. s., 2H);

^{13}C-NMR (101 MHz, $CDCl_3$): δ (ppm) 147.5, 135.2, 131.9, 124.8;

HRMS (ESI+): calc. $[M+H]^+$ for $C_6H_6Cl_2NO_2S^+$ 225.9496, found 225.9491, Δ = 0.5 mDa.

Synthesis of 2,4,6-trimethylbenzenesulfonamide (3.53)

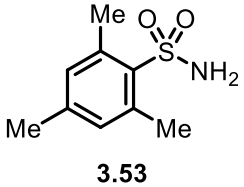

3.53

Synthetized according to a modified literature-reported procedure.[36] 2,4,6-Trimethoxybenzenesulfonyl chloride (1.09 g, 5.00 mmol, 1.00 equiv.) was dissolved in ammonium hydroxide (25% solution in H_2O, 25 mL) at 0 °C. After 15 minutes the cooling bath was removed, and the reaction was stirred for 4 hours at room temperature. The reaction was quenched by addition of a mixture of water and ethyl acetate (1:1, 10 mL), and the formed layers were separated. The aqueous layer was acidified with 2M HCl (pH=1) after which it was extracted with EtOAc (2 × 10 mL). The combined organic layers were washed with brine, dried over Mg_2SO_4, the drying agent filtered off and the solvent removed under reduced pressure. The crude product was purified by passing through a short silica plug eluting with 50% EtOAc/PE. After evaporation of the solvent, the product was obtained as an off-white solid (659 mg, 66 %).

R_f (silica, 50% EtOAc/PE) 0.75 [potassium permanganate];

^{1}H-NMR (400 MHz, $CDCl_3$): δ (ppm) 7.17 (br. s., 2H), 6.99 (s, 3H), 2.55 (s, 3H);

^{13}C-NMR (101 MHz, $CDCl_3$): δ (ppm) 141.0, 138.7, 137.6, 131.8, 23.0, 20.8;

HRMS (ESI+): calc. $[M+Na]^+$ for $C_9H_{13}NO_2SNa^+$ 222.0565, found 222.0560, Δ = 0.5 mDa.

Synthesis of naphthalene-1-sulfonamide (3.54)

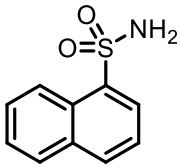

3.54

Synthetized according to a literature-known procedure.[39] Napthalene-1-sulfonyl chloride (904 mg, 4.00 mmol, 1.00 equiv.) was dissolved in THF (13 mL). Ammonium hydroxide (25% solution in H_2O, 8.7 mL) was added slowly to the mixture under ambient conditions, after which the reaction was stirred for three hours at room temperature. THF was then removed under reduced pressure, and the crude was dissolved in a mixture of EtOAc and H_2O. The layers were then separated, and the aqueous layer was extracted with EtOAc (3 × 10 mL). The combined organic layers were dried over Mg_2SO_4, the drying agent filtered off, and the solvent removed under reduced pressure. The formed pale solid was washed with hexane and Et_2O, and after drying under high vacuo, the title compound was obtained as a white solid.

R_f (silica, 50% EtOAc/PE) 0.58 [potassium permanganate];

^{1}H-NMR (400 MHz, $CDCl_3$): δ (ppm) 8.44 (d, *J* = 1.5 Hz, 2H), 8.11–8.16 (m, 2H), 8.03–8.06 (m, 1H), 7.90 (dd, *J* = 8.7, 1.8 Hz, 1H), 7.65–7.72 (m, 2H), 7.46 (br. s., 2H);

^{13}C-NMR (101 MHz, $CDCl_3$): δ (ppm) 141.7, 134.3, 132.2, 129.5 (2C), 128.9, 128.3, 127.9, 126.2, 122.6;

HRMS (ESI+): calc. $[M+Na]^+$ for $C_{10}H_9N_2O_2SNa^+$ 244.0282, found 244.0245, Δ = 3.7 mDa.

Synthesis of methyl 4-sulfamoylbenzoate (3.55)

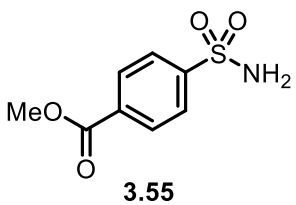

3.55

Synthetized according to a modified literature-reported procedure.[40] 4-Sulfamoylbenzoic acid (2.00 g, 9.94 mmol, 1.00 equiv.) was dissolved in MeOH (18 mL), followed by the addition of conc. H_2SO_4 (0.5 mL). The reaction was then refluxed for 7 h, after which it was cooled down to room temperature. Methanol was removed under reduced pressure, and the residue dissolved in $CHCl_3$. The organic layer was then washed with H_2O, aq. sat. Na_2CO_3 solution and finally again with H_2O. The organic phase was dried over Mg_2SO_4, the drying agent filtered off, and the solvent

removed under reduced pressure. Purification with flash column chromatography (EtOAc/PE, 20% → 80%) gave the title compound as a white solid (1.6 g, 75%).

R_f (silica, 50% EtOAc/PE) 0.54 [potassium permanganate];

^{1}H-NMR (400 MHz, $CDCl_3$): δ (ppm) 8.12–8.15 (m, 2H), 7.94–7.98 (m, 2H), 7.56 (s, 2H), 3.89 (s, 3H);

^{13}C-NMR (101 MHz, $CDCl_3$): δ (ppm) 165.7, 148.5, 132.8, 130.3, 126.5, 53.0;

HRMS (ESI+): calc. $[M+H]^+$ for $C_8H_{10}NO_4S^+$ 216.0331, found 216.0324, Δ = 0.7 mDa.

Synthesis of 4'fluoro-[1,1'-biphenyl]-4-sulfonamide (3.56)

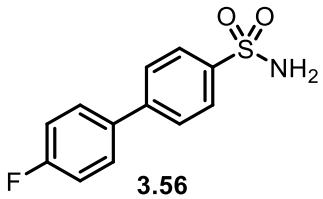

3.56

Synthetized according to a modified patented procedure.[41] 4'fluoro-[1,1'-biphenyl]-4-sulfonyl chloride (1.0 g, 3.7 mmol, 1.0 equiv.) was dissolved in 1,4-dioxane (10 mL) at room temperature. Ammonium hydroxide (25% solution in H_2O, 5.8 mL, 37.0 mmol, 10.0 equiv.) was added and the reaction was stirred for 1 h under ambient conditions. The reaction was quenched by adding a mixture of water and hexane (1:1, 10 mL) followed by solid NaCl. The mixture was further stirred for 30 minutes, after which the formed white precipitate was filtered and the washed with H_2O (3 × 10 mL). The residual water was then removed *via* lyophilization, after which the title compound was obtained as an off-white solid (678 mg, 73%).

R_f (silica, 50% EtOAc/PE) 0.63 [potassium permanganate];

^{1}H-NMR (400 MHz, $CDCl_3$): δ (ppm) 7.84–7.93 (m, 4H), 7.77–7.82 (m, 2H), 7.42 (br. s., 2H), 7.32–7.38 (m, 2H),

^{13}C-NMR (101 MHz, $CDCl_3$): δ (ppm) 162.9 (d, J = 247 Hz), 143.1 (d, J = 64 Hz), 135.6 (d, J = 3.1 Hz), 129.7, 129.6, 127.6, 126.8, 116.4 (d, J = 21.2 Hz);

^{19}F-NMR (376 MHz, $CDCl_3$, $PhCF_3$ as internal standard): δ (ppm) −116.71 – (−)116.79 (m)

HRMS (EI+): (ESI+): calc. $[M+Na]^+$ for $C_{12}H_{10}FNO_2SNa^+$ 274.0314, found 274.0310, Δ = 0.4 mDa.

Synthesis of *N*-phenylcyclopropanesulfonamide (3.57)

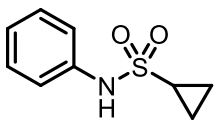

3.57

Synthetized according to a modified literature procedure.[42] Cyclopropanesulfonyl chloride (1.0 mL, 9.90 mmol, 1.0 equiv.) was dissolved to a mixture of pyridine (2 mL) and DCM (2 mL). Aniline (0.9 mL, 9.90 mmol, 1.0 equiv.) was added to the mixture under ambient

conditions, after which the reaction was heated to reflux at 50 °C overnight. After cooling down to room temperature, the mixture was diluted with Et_2O (20 mL), and the organic layer was washed with water (2 × 20 mL) and brine (20 mL). The organic layer was dried over Mg_2SO_4, the drying agent filtered off, and the organic layer concentrated under reduced pressure. The crude product was purified with flash column chromatography (EtOAc/PE), and after removal of solvents, the title compound was obtained as a white solid.

R_f (silica, 50% EtOAc/PE) 0.87 [potassium permanganate];

^{1}H-NMR (400 MHz, $CDCl_3$): δ (ppm) 7.32–7.38 (m, 2H), 7.26–7.30 (m, 2H), 7.17–7.22 (m, 1H), 6.77 (br. s., 1H), 2.46–2.54 (m, 1H), 1.15–1.21 (m, 2H), 0.93–0.99 (m, 2H);

^{13}C-NMR (101 MHz, $CDCl_3$): δ (ppm) 136.8, 129.5, 125.5, 121.8, 29.8, 5.61;

HRMS (ESI+): calc. $[M+H]^+$ for $C_9H_{12}NO_2S^+$ 198.0589, found 198.0583, Δ = 0.6 mDa.

Synthesis of *N*-phenylcyclohexanesulfonamide (3.58)

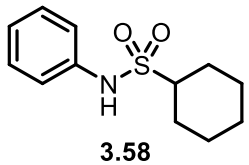

3.58

Synthetized according to a modified literature procedure.[42] Cyclohexanesulfonyl chloride (1.5 g, 8.20 mmol, 1.0 equiv.) was dissolved to a mixture of pyridine (2 mL) and DCM (2 mL). Aniline (0.84 mL, 9.20 mmol, 1.1 equiv.) was added to the mixture under ambient conditions, after which the reaction was heated to reflux at 50 °C overnight. After cooling down to room temperature, the mixture was diluted with Et_2O (20 mL), and the organic layer was washed with water (2 × 20 mL) and brine (20 mL). The organic layer was dried over Mg_2SO_4, the drying agent filtered off, and the organic layer concentrated under reduced pressure. The crude product was purified with flash column chromatography (EtOAc/PE), and after removal of solvents, the title compound was obtained as a pale yellow solid (1.51 g, 77 %).

R_f (silica, 50% EtOAc/PE) 0.74 [potassium permanganate];

^{1}H-NMR (400 MHz, $CDCl_3$): δ (ppm) 7.32–7.37 (m, 2H), 7.25–7.29 (m, 1H), 7.11–7.18 (m, 2H), 3.04 (tt, *J* = 12.1, 3.5 Hz, 1H), 2.19 (d, *J* = 13.0 Hz, 2H), 1.84–1.91 (m, 2H), 1.54–1.70 (m, 3H), 1.14–1.29 (m, 3H);

^{13}C-NMR (101 MHz, $CDCl_3$): δ (ppm) 137.4, 129.6, 124.6, 120.0, 60.4, 26.3, 25.1, 25.0;

HRMS (ESI+): calc. $[M+Na]^+$ for $C_{12}H_{17}NO_2SNa$ 262.0878, found 262.0874, Δ = 0.4 mDa.

Synthesis of methyl 2,3-dimethoxy-5-sulfamoylbenzoate (3.59)

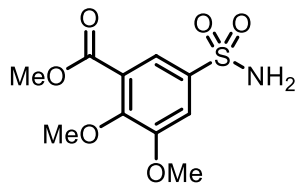

3.59

Synthetized according to a literature-reported procedure.[40] 5-(Aminosulfonyl)-2,3-dimethoxybenzoic acid (5.1 g, 20 mmol, 1.00 equiv.) was dissolved in MeOH (15 mL) followed by the addition of conc. H_2SO_4 (0.3 mL). The reaction was then refluxed for 7 h, after which it was cooled down to room temperature. Methanol was removed under reduced pressure, and the residue dissolved in $CHCl_3$. The organic layer was then washed with H_2O, aq. sat. Na_2CO_3 solution, and finally again with H_2O. The organic phase was dried over Mg_2SO_4, the drying agent filtered off, and solvent removed under reduced pressure. Recrystallization from a mixture of MeOH and H_2O yielded the final product as a white solid (1.58 g, 29% yield over three steps).

R_f (silica, 50% EtOAc/PE) 0.36 [potassium permanganate];

^{1}H-NMR (400 MHz, $CDCl_3$): δ (ppm) 7.66 (d, *J* = 16.6, 2.2 Hz, 2H), 7.42 (br. s., 2H), 3.92 (s, 3H), 3.87 (s, 3H), 3.83 (s, 3H);

^{13}C-NMR (101 MHz, $CDCl_3$): δ (ppm) 165.5, 153.7, 150.9, 140.1, 126.1, 119.3, 113.3, 61.7, 56.9, 53.0;

HRMS (ESI+): calc. $[M+H]^+$ for $C_{10}H_{14}NO_6S^+$ 276.0542, found 276.0535, Δ = 0.7 mDa.

3.5.5.2 List of synthetized unsuccessful sulfonamides

Synthesis of 4-nitrobenzenesulfonamide (U3.4)

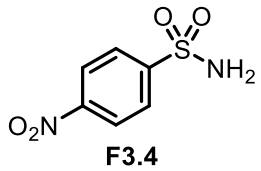

F3.4

Synthetized according to a modified literature-reported procedure.[37] 4-Nitrobenzenesulfonyl chloride (1.04 g, 5.00 mmol, 1.00 equiv.) was dissolved in ammonium hydroxide (25% solution in H_2O, 25 mL) at 0 °C. After 15 minutes the cooling bath was removed, and the reaction was stirred for 4 hours at room temperature. The reaction was quenched by addition of a mixture of water and ethyl acetate (1:1, 10 mL), and the formed layers were separated. The aqueous layer was acidified with 2M HCl (pH = 1), after which it was extracted with EtOAc (2 × 10 mL). The combined organic layers were washed with brine, dried over Mg_2SO_4, the drying agent filtered off, and the solvent removed under reduced pressure. The formed white crude product (which was not adequately pure based on ^{1}H NMR analysis) was then passed through a short silica plug (EtOAc/PE, 50%) to remove the formed sulfonic acid. After evaporation of the solvent the product was obtained as a white solid (315 mg, 31 %).

R_f (silica, 50% EtOAc/PE) 0.60 [potassium permanganate];

^{1}H-NMR (400 MHz, $CDCl_3$): δ (ppm) 8.39–8.43 (m, 2H), 8.05–8.09 (m, 2H), 7.73 (br. s., 2H);

^{13}C-NMR (101 MHz, $CDCl_3$): δ (ppm) 149.9, 149.7, 127.7, 124.9;

HRMS (ESI+): calc. $[M+H]^+$ for $C_6H_7N_2O_4S^+$ 203.0127, found 203.0120, Δ = 0.7 mDa.

3.5.6 Mechanistic Studies

3.5.6.1 UV-vis studies

UV-vis in Acetonitrile

All UV-vis measurements in MeCN were carried out in a 0.1 cm × 1.0 cm quartz cuvette with 0.1 cm light path and an internal volume of about 0.2 mL. The spectra were recorded with Agilent Cary 4000 UV-vis spectrophotometer scanning the spectral window from 900 nm to 200 nm using 11 nm data intervals. The temperature was hold constant at 25.6 °C during the measurements with water-cooling running through the probe chamber. The samples were prepared as following: $Bi(OTf)_3$ (13.0 mg, 0.2 mmol) was set under an inert atmosphere through evacuation and back-filling with N_2 (3×). Dry MeCN (1 mL) was added, and the formed stock solution was shaken to ensure even distribution of components. Then, 0.25 mL of this stock solution was transferred to another vial under N_2, and the vial was filled up to a final volume of 1.0 mL with dry MeCN. 0.2 mL from the final solution was then transferred to the afore described quartz cuvette for measurements. With respect to the other components, 2-phenylpropanoic acid (2.75 µL, 0.05 mmol) or 4-methylsulfonamide (3.0 mg, 0.05 mmol) were both dissolved into dry MeCN (1 mL) in separate vials under N_2 to form the samples of appropriate

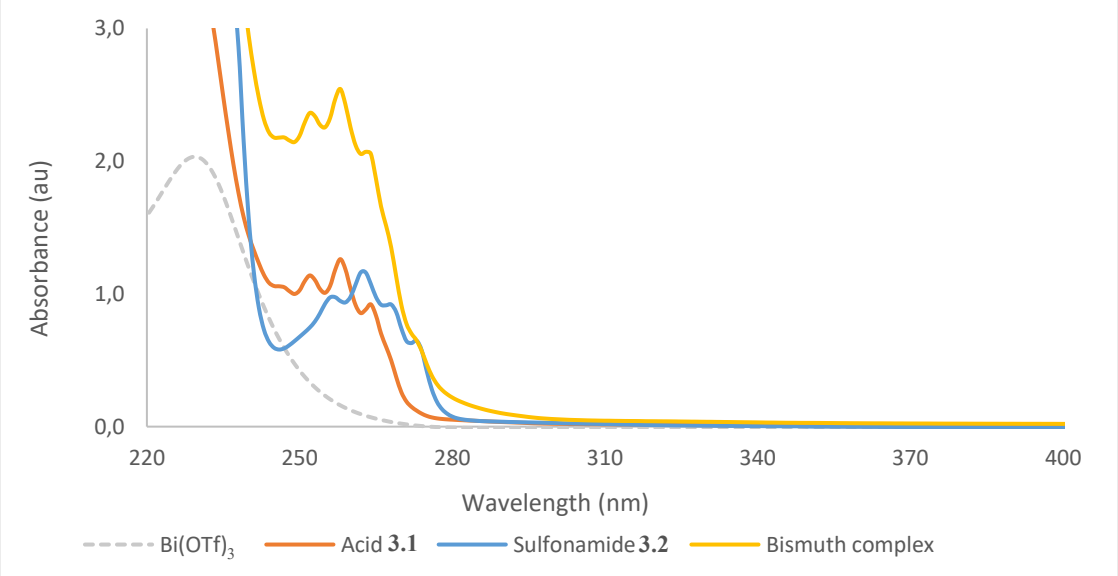

Figure S3.6. UV-vis spectrum of the reaction components: $Bi(OTf)_3$ as a gray dotted line, 2-phenylpropanoic acid (**3.1**) as an orange line, 4-methylphenylsulfonamide (**3.2**) as a blue line and the combination of the above as a yellow line. All components measured in 0.05 mmol dissolved in 0.5 mL of MeCN. Samples of acid **3.1**, sulfonamide **3.2** and complex also containing $KHCO_3$ (5 mg) as a base and H_2O (5 µL).

concentrations. Other components, $KHCO_3$ (5 mg) and H_2O (5 µL), were then added stepwise to the 1 mL sample volumes, shaken, and 0.2 mL transferred again *via* syringe to the cuvette. For the measurement of the complex, a stock solution containing 0.2 mmol of $Bi(OTf)_3$, 2-phenylpropanoic acid **3.1** and 4-methylsulfonamide **3.2** in MeCN (1 mL) was first formed followed by 1/4 dilution as described for the pure bismuth triflate. Background spectrum of pure MeCN was measured first and subtracted from other spectra.

Due to the well-soluble nature of $Bi(OTf)_3$ and other reaction components in MeCN, relatively concentrated samples could be prepared. It should be noted that polar protic solvents, such as MeCN, are known to coordinate to metal centers, and therefore the existence of acetonitrile ligands in the measured bismuth compounds cannot be ruled out. However, to enhance the coordination of the desired ligands (carboxylic acids and sulfonamides), concentrated solutions were prepared for the UV-vis studies. As can be seen from Figure S3.6, $Bi(OTf)_3$ has its broad absorption maximum around 230 nm and tails until 280 nm. The 2-phenylpropanoic acid (**3.1**) and 4-methylphenylsulfonamide (**3.2**) both have a more complex absorption spectra centered around 260 nm and tailing towards 300 nm. When $Bi(OTf)_3$ is added to the mixture containing both components, a significant enhancement in the absorbance is observed around 260 nm, with the absorption of the complex tailing to longer wavelengths than that of either components alone.

UV-vis in DCM

To obtain a better representation of the species present in the reaction mixtures, we changed the solvent to DCM. Unlike in MeCN, the bismuth species have only a limited solubility in this medium. For this reason, a notably more diluted solutions were measured combined with an increased light path length. For the measurements in DCM, a 1.0 cm × 1.0 cm quartz cuvette was utilized. Stock solutions of $Bi(OTf)_3$, carboxylic acid **3.1** and sulfonamide **3.2** were all prepared separately in 0.1 M concentration in DCM, followed by dilution with DCM to the final concentration of 0.002 M. The bismuth complex was prepared by mixing all three components in a 1:1:1 ratio (0.1 M each in DCM) followed by dilution to 0.002 M. The spectra were recorded with Agilent Cary 4000 UV-vis spectrophotometer scanning the spectral window from 900 nm to 200 nm using 11 nm data intervals. The temperature was held constant at 25.6 °C during the measurements with water-cooling running through the probe chamber.

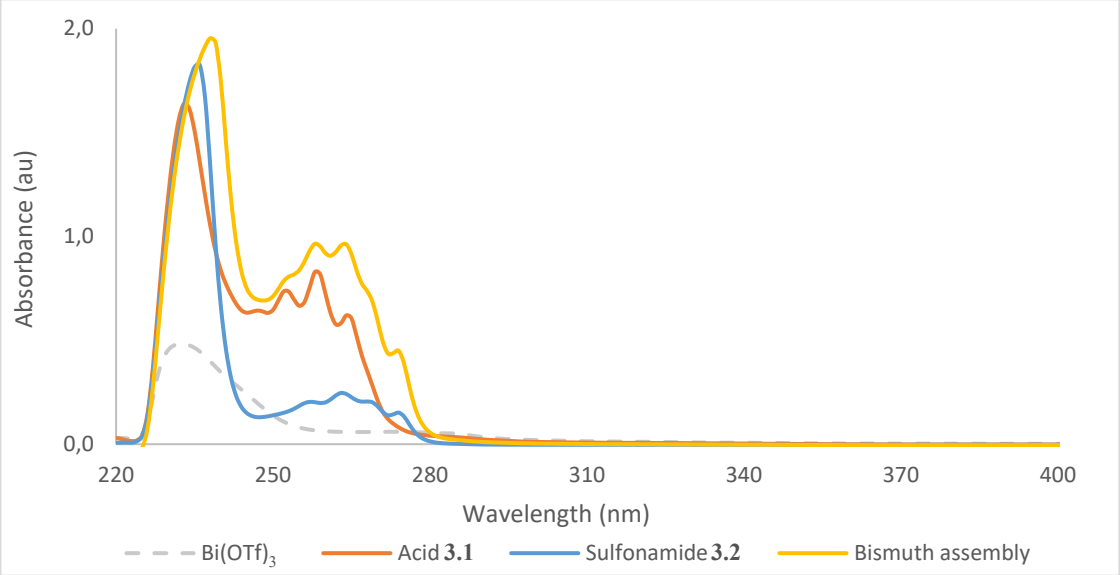

Figure S3.7. UV-vis spectrum of the reaction components in DCM: $Bi(OTf)_3$ as a gray dotted line, 2-phenylpropanoic acid (**3.1**) as an orange line, 4-methylphenylsulfonamide (**3.2**) as a blue line and the combination of the above as a yellow line. All components measured in 0.02 mmol concentrations.

As seen from Figure S3.7, the absorption spectra of each component in DCM closely resembles the respective spectra measured in MeCN both in the terms of the shape of the absorption band as well as the location of the absorption maxima. Here as well the addition of $Bi(OTf)_3$ to the mixture of acid **3.1** and sulfonamide **3.2** causes a significant enhancement of absorption at the area covering the absorption maximum. In this case, however, the exact form of the absorption band slightly differs from that seen in MeCN perhaps due to the lack of the solvent ligands in DCM.

To gain a more precise look to the absorption spectrum around the irradiation wavelength (365 nm), we decided to measure the previously formed bismuth complex (1:1:1 of acid **3.1**, sulfonamide **3.2** and $Bi(OTf)_3$, 0.002 M for each in DCM) with a 4 cm × 2 cm quartz cuvette (pathlength 4 cm, sample volume 6 mL). The measurement was carried out with Agilent Cary 60 UV-vis spectrophotometer at 25 °C in the scanning window from 1100 nm to 190 nm using the data interval of 0.5 nm. The result of this measurement can be seen in Figure S3.8.

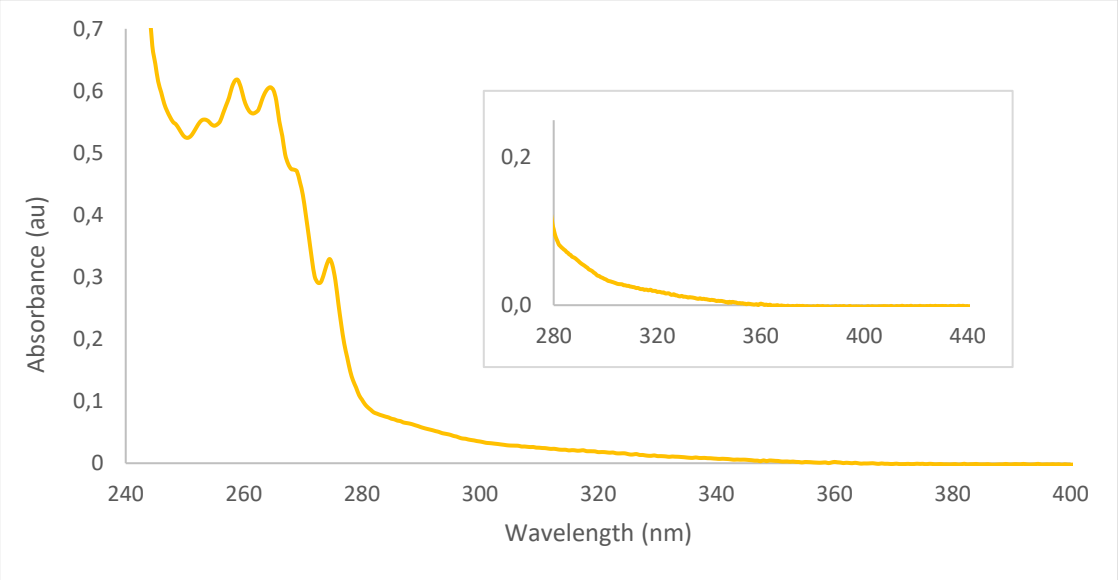

Figure S3.8. UV-vis spectrum of the bismuth complex containing $Bi(OTf)_3$, 2-phenylpropanoic acid (**3.1**) and 4-methylphenylsulfonamide (**3.2**) as 0.02 mmol concentration each in DCM. To gain a better look to the absorbance around the irradiation wavelength (365 nm), a 4.0 cm quartz cuvette was utilized.

Comparing the UV-vis spectrum obtained using the 4 cm pathlength to the one obtained with 1 cm pathlength gratifyingly shows significantly better-defined spectral region above 300 nm. Importantly, slight tailing of the UV-vis absorption of the complex can be observed starting around 360 nm, which intersects the emission spectrum of the LEDs utilized. Moreover, the low absorption coefficient around the irradiation wavelength in part accounts for the relatively high intensity needed for the product formation (Table S3.6). Although the exact intensity of the absorption around 365 nm is naturally dependent on the concentration of the complex, the UV-vis spectrum above demonstrates clearly how the absorption tails to the critical regions.

3.5.6.2 Kinetic studies

For the kinetic studies, one reaction vial was prepared as following: (±)-2-phenylpropanoic acid (15.1 mg, 0.10 mmol, 1.0 equiv.), $KHCO_3$ (30 mg, 0.30 mmol, 3.0 equiv.) and *p*-toluenesulfonamide (59 mg, 0.35 mmol, 3.5 equiv.) were weighed into a 5 mL crimp cap vial. The vial was then sealed and set under an inert atmosphere by evacuating and backfilling with pre-dried N_2 (×3). Anhydrous DCM (1 mL) was added, and the reaction mixture was degassed by freeze-pump thaw (×3). Then reaction was then irradiated with 365 nm (1.5 W) LEDs. To obtaining each data point, a 25 µL sample was drawn from the reaction mixture, to which 250 µL of the stock solution containing internal standard was added (0.01 M mesitylene in DCM). Finally, the samples were analyzed by GC-FID and the yield were calculated against the calibration curve of the product and mesitylene.

Reaction kinetics

To obtain an overall picture of the reaction kinetics, the rate of the reaction was first monitored for the first four hours, the result of which mostly resembles a logarithmic reaction kinetic (Figure S3.9). A notable feature of this reaction is indeed its rapid initial kinetics, which results in a 28 % yield during the first hour of the reaction. It thus seems like the turbidness of the reaction mixture does not prevent the adequate amounts of light from entering the reaction mixture during the first hour of the reaction time.

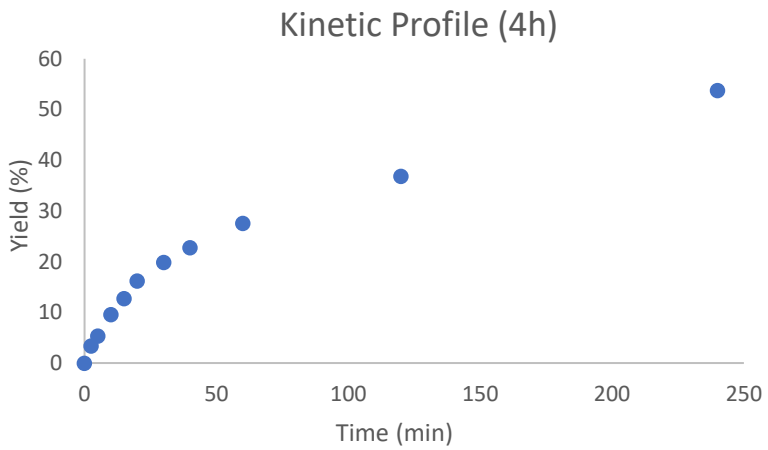

Time (min)	**Yield** (%)
0	0
2.5	3.4
5	5.4
10	9.5
15	13
20	16
30	20
40	23
60	28
120	37
240	54

Figure S3.9. Kinetic profile of the reaction during the first four hours.

As a part of the observation of the fast initial kinetic is also the significant reduction of the product forming rate after the first hour. This decrease in the productive reaction can in to at least some extend be hypothesized to come from the formation of fully reduced $Bi^{(0)}$ (also referred to as "bismuth black"), which results into a significant darkening of the reaction mixture therefore diminishing the light penetration.

Initial kinetics

To gain a deeper look to the initial kinetics of the reaction, the rate measurement was repeated during the first twenty minutes (Figure S3.10). During this time period the reaction could be said to follow a linear reaction rate although slight features of logarithmic rate could also be argued to appear. The single points obtained from each time point could also be joined with a direct line with a very high experimental correlation coefficient.

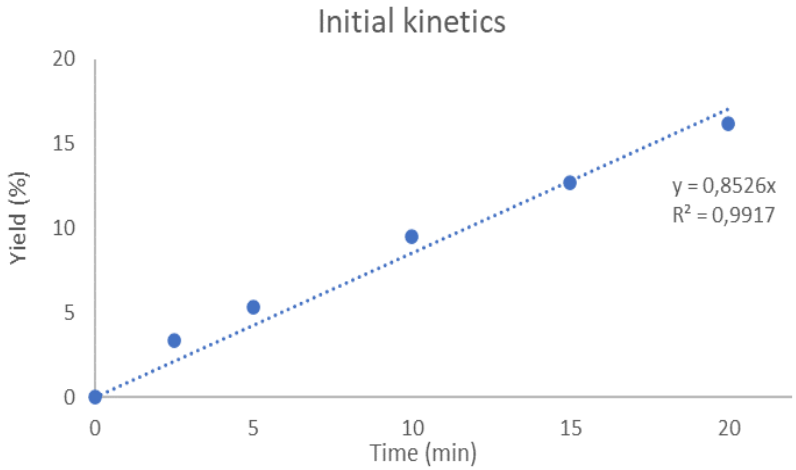

Time (min)	**Yield** (%)
0	0
2.5	3.4
5	5.4
10	9.5
15	13
20	16

Figure S3.10. Initial reaction kinetics.

Strikingly, small amounts of product can be observed already after 2.5 minutes of irradiation time implying that the reaction starts (almost) immediately when the light is turned on. Moreover, the linear kinetic is often expected in the cases where the product is directly formed from the reactants without the need to build up any intermediates or to activate a pre-catalytic species. It is worth mentioning that a linear kinetic was also observed in our previous work with the $BiCl_3$-catalyzed Giese-coupling reactions[3], which further supports the use of simple bismuth salts as efficient catalytic species requiring light as the sole source of activation.

Light on/off experiment

Finally, we concluded the kinetic experiments by carrying out a light on/off- experiment. Due to the turbid nature of our initial reaction mixture, we considered quantum yield measurement to give results that would be uncertain or difficult to interpret. Therefore,

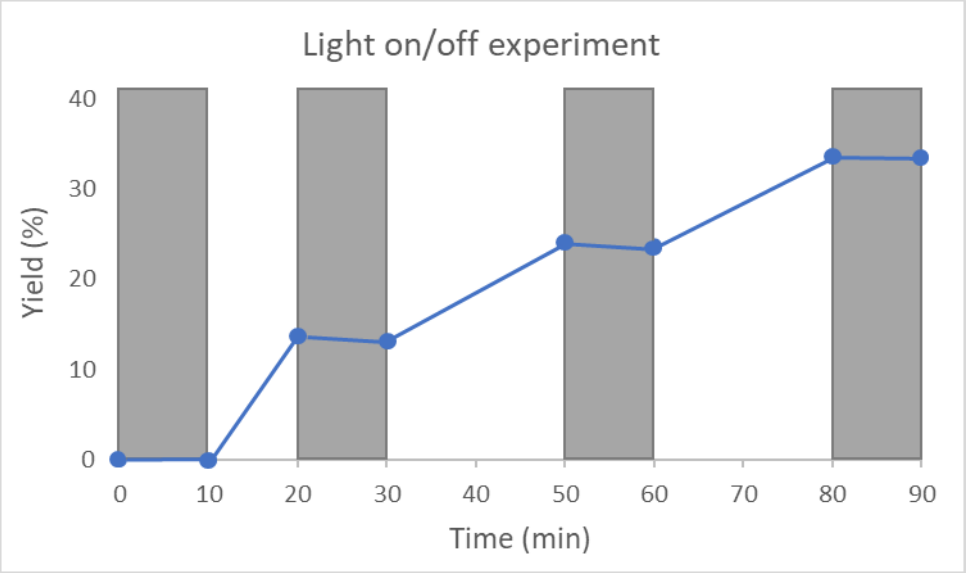

Figure S3.11. Light on/off experiment measuring the rate of product formation.

we decided to monitor the product formation by irradiating the reaction mixture 10 or 20 minutes followed by a ten-minute dark period. Results of this experiment can be seen in Figure S3.11.

As can be seen from Figure S3.11, the reaction clearly progresses only when the light is on. This in turn implies that the reaction is dependent on continuous irradiation and a radical chain, if present at all, is short and does not serve as the main product-forming mechanism. Gratifyingly, the formed product also appears to be rather stable during the dark phases and no significant degradation was observed when the light was off.

3.5.7 Experiments towards the later elementary steps

3.5.7.1 TEMPO-trapping studies

After establishing the nature of the light-harvesting species, we next turned our attention towards identification of some of the reaction intermediates. We started by carrying out a TEMPO-trapping experiment, which was set up as following: 2-phenylpropanoic acid (15.0 mg, 0.10 mmol, 1.00 equiv.), $Bi(OTf)_3$ (130 mg, 0.20 mmol, 2.00 equiv.), $KHCO_3$ (30.0 mg, 0.30 mmol, 3.00 equiv) and TEMPO (32.0 mg, 0.2 mmol, 2.00 equiv.) were weighed into a 5 mL crimp-cap vial equipped with a stirring bar. The vial was then sealed and set under an inert atmosphere by evacuating and back-filling with N_2 for three times. DCM (1 mL) was added *via* syringe against a flow of N_2, and the reaction mixture was further degassed by freeze-pump thaw (3×). The reaction was then irradiated with 365 nm LEDs for 18 hours while keeping the temperature at 25 °C by water-cooling. After completion of the reaction, the solids were removed by filtering with a syringe filter. The so-obtained crude reaction mixture was then analyzed by LC-MS.

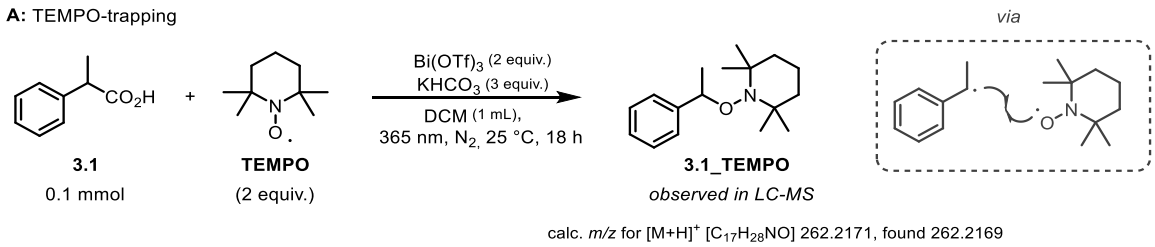

Scheme S3.1. TEMPO-trapping experiment.

As can be seen from Scheme S3.1, the TEMPO-trapping study was able to identify the expected benzylic radical formed from the radical decarboxylation. The found *m/z* of this trapped intermediate was in good agreement with the expected mass of the $[M+H]^+$ ion. Importantly, this was the only product formed during the reaction, and no traces of the radical homocoupling or Kharasch products were observed.

3.5.7.2 Studies towards presence/absence of benzylic carbocations

To gather indirect evidence on the presence or absence of a benzylic carbocation, we decided to turn towards testing different nucleophiles in our reaction. We rationalized that in the case of a "free" carbocation intermediate, nucleophilic coupling with various *N*- and *O*-centred nucleophiles should be feasible. For this, we set up the reactions according

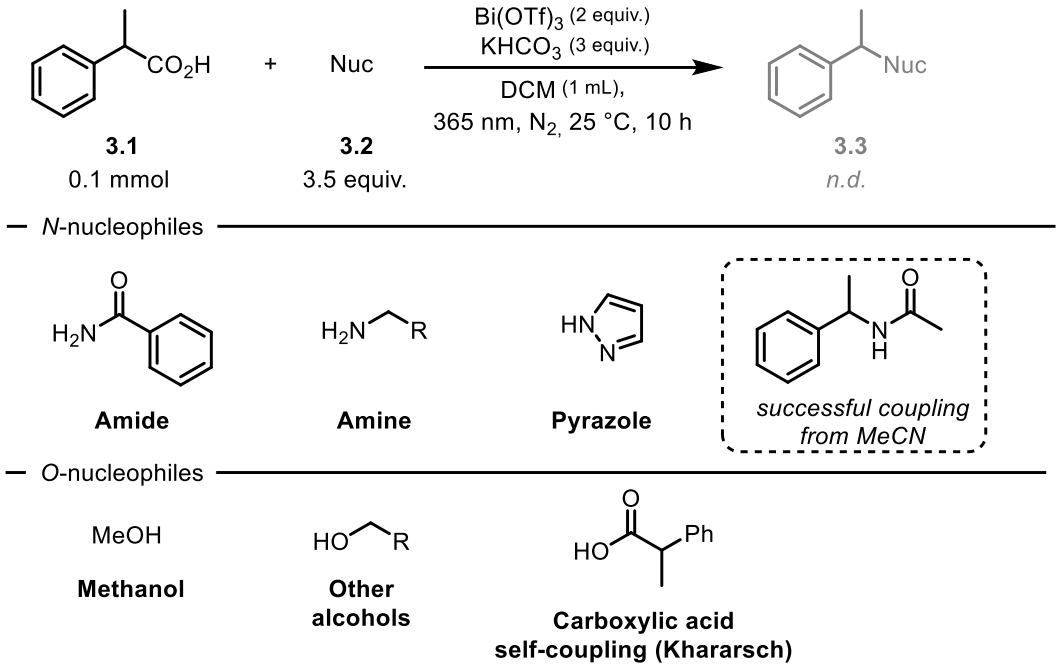

Scheme S3.2: List of unsuccessful nucleophiles.

to the **GP1** but instead of 4-methylbenzenesulfonamide we tested benzylamide, selected primary amines and pyrazole as *N*-centred nucleophiles. For the *O*-centred nucleophiles, different alcohols were set up together with the homocoupling to the 2-phenylpropanoic acid to form the benzylic ester (Kharasch product). The results are summarized in Scheme S3.2. Upon changing the sulfonamide nucleophiles other *N*-centred nucleophiles we observed clear suppression on the LMCT reactivity. Similar results were also obtained with alcohols as *O*-centred nucleophiles. While this hampering of the reactivity might stem from numerous reasons, we believe that factors worth considering include: 1) full saturation of the bismuth centre by tight coordination of alternative nucleophiles, thus leaving no room for the coordination of carboxylic acids, 2) diminished the UV-vis absorption properties *via* changing the ligands, and 3) the inability of other nucleophiles to undergo C–N coupling because no carbocation intermediates are present, and the reductive elimination strongly favours the sulfonamides. While many of the afore-mentioned factors might explain the lack of reactivity with other nucleophiles, we were also unable to observe the Kharasch product stemming from nucleophilic attack of the 2-phenylpropanoic acid – an event likely to happen in the absence of other reactants.[24] This, together with the absence of desaturation products formed by *alpha*-deprotonation of the carbocation, indicate that a carbocationic intermediate is most likely not present. It also should be noted that successful C–N coupling was observed with MeCN (Ritter amination) which also can coordinate to bismuth although in a reversible manner.

3.5.7.3 $BiCl_3$ as bismuth precatalyst

To differentiate between the possible outer-sphere mechanisms (radical-ligand transfer *vs.* radical oxidation), we set up further reactions utilizing $BiCl_3$ as bismuth precursor (Scheme S3.3). If our reaction would follow the radical-ligand transfer, benzyl chloride would be formed as an intermediate followed by nucleophilic substitution by the sulfonamides. When $BiCl_3$ was used for the decarboxylation of the acid **3.1**, the reaction yielded a low concentration of the radical homocoupling product while C–N coupling product **3.3** could not be detected (Scheme S3.3a). We then attempted to generate the chlorinated intermediate *via* a HAT reaction from ethylbenzene with over-stoichiometric amount of chlorine source (Scheme S3.3b). However, the desired product could not be observed. Taken together, these results suggest that the radical-ligand transfer, as suggested with iron chloride, did not represent the key mechanistic pathway in our reaction.

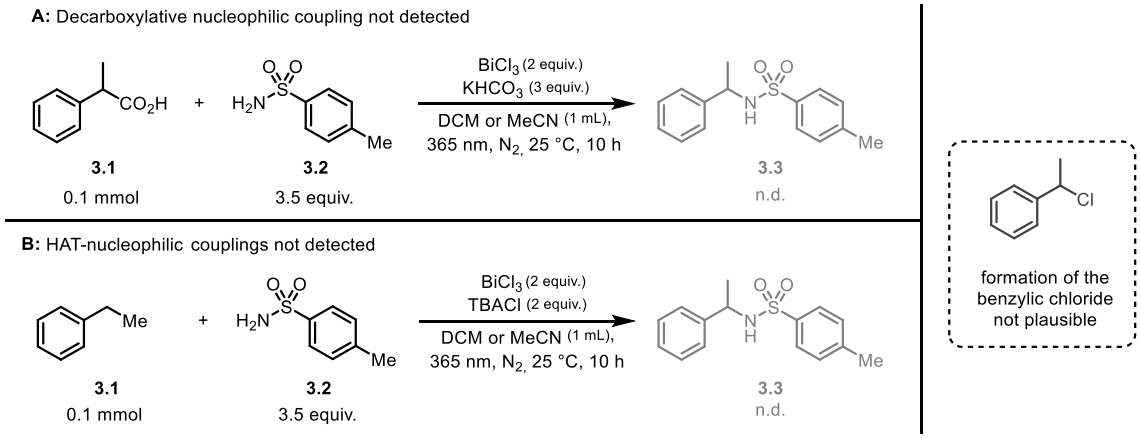

Scheme S3.3: Mechanistic studies using bismuth(III)chlorides in LMCT decarboxylation (a) and HAT coupling (b).

3.5.7.4 Reactions using substoichiometric bismuth

We set out to study the effects of using bismuth as a limiting reagent in our reaction to gain further insight into the efficiency of bismuth in our reaction. The reactions were set up following **GP1**, though lowered bismuth loading was used as described in Table S3.10.

Table S3.10: Full optimization of bismuth triflate loading.

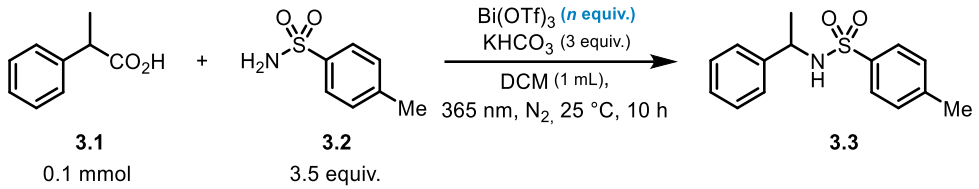

3.1 0.1 mmol | **3.2** 3.5 equiv. | **3.3**

Entry	**Bi Loading**	**Yield** (based on acid, %)	**Yield** (based on bismuth, %)
1	0.33 equiv.	31	0.94
2	0.66 equiv.	45	0.68

Reaction conditions: $Bi(OTf)_3$ (n equiv.), 2-phenylpropanoic acid (15.0 mg, 0.1 mmol, 1.0 equiv.), $KHCO_3$ (30.0 mg, 0.3 mmol, 3.0 equiv.) and 4-methylphenylsulfonamide (65.5 mg, 0.35 mmol, 3.5 equiv.) were dissolved into DCM (1 mL) under N_2. After irradiation with 365 nm for 10 h at 25 °C, internal standard was added and reactions analyzed with GC-FID.

With 0.33 equivalents of bismuth, the yield of 94% yield was obtained (Entry 1). This result suggests a high activity of bismuth, serving as an efficient subsequent one electron oxidizing agent. Moreover, this result can also be seen as supporting our mechanistic hypothesis that the bismuth centre participating the radical generation further traps the substrate radical resulting into the product formation. When 0.66 equivalents of bismuth was used, 68% yield was obtained (Entry 2).

3.6 Copies of NMR spectra and primary research data

Dear Reader,

For the copies of the NMR spectra, please open the supporting information provided at the publisher's website.

https://chemistry-europe.onlinelibrary.wiley.com/doi/10.1002/chem.202500396

Primary research data of this chapter, including experimental NMR-spectra, HRMS files and the raw data for UV-vis studies can be downloaded free of charge at Radar4Chem repository: https://www.radar-service.eu/radar/en/dataset/aygcxy5kjzu130uy

3.7 Notes and References

(1) Hu, A.; Guo, J.-J.; Pan, H.; Zuo, Z. Selective Functionalization of Methane, Ethane, and Higher Alkanes by Cerium Photocatalysis. *Science*, **2018**, *361* (6403), 668–672.

(2) Juliá, F. Ligand-to-Metal Charge Transfer (LMCT) Photochemistry at 3d-Metal Complexes: An Emerging Tool for Sustainable Organic Synthesis, *ChemCatChem*, **2022**, *14*, (19), e202200916.

(3) Birnthaler, D.; Narobe, R.; Lopez-Berguno, E.; Haag, C.; König, B. Synthetic Application of Bismuth LMCT Photocatalysis in Radical Coupling Reactions. *ACS Catal.* **2023**, *13* (2), 1125–1132.

(4) de Groot, L. H. M.; Ilic, A.; Schwarz, J.; Wärnmark, K. Iron Photoredox Catalysis–Past, Present, and Future. *J. Am. Chem. Soc.* **2023**, *145* (17), 9369–9388.

(5) Moon, H. W.; Cornella, J. Bismuth Redox Catalysis: An Emerging Main-Group Platform for Organic Synthesis. *ACS Catal.* **2022**, *12* (2), 1382–1393.

(6) Lopez, E.; Thorp, S. C.; Mohan, R. S. Bismuth(III) Compounds as Catalysts in Organic Synthesis: A Mini Review. *Polyhedron* **2022**, *222*, 115765.

(7) Heine, J.; Peerless, B.; Dehnen, S.; Lichtenberg, C. Charge Makes a Difference: Molecular Ionic Bismuth Compounds. *Angew. Chem. Int. Ed.* **2023**, *62* (24), e202218771.

(8) Lichtenberg, C. Molecular Bismuth(III) Monocations: Structure, Bonding, Reactivity, and Catalysis. *Chem. Commun.* **2021**, *57* (37), 4483–4495.

(9) Gilman, H.; Yablunky, H. L. Reactions of Organobismuth Compounds in Liquid Ammonia. *J. Am. Chem. Soc.* **1941**, *63* (1), 212–216.

(10) Rahman, Md. M.; Matano, Y.; Suzuki, H. Sodium Diarylbismuthide as a Reagent for the Bismuthanation of Reactive Arenes. Application to the Synthesis of Mixed Triarylbismuthanes Bearing a Substituent Group Incompatible with Grignard and Organolithium Reagents. *Organometallics*, **1997**, *16* (15), 3565–3568.

(11) Veith, M.; Yu, E.-C.; Huch, V. Synthesis and Structures of Alkali(Alkoxy) Antimonates and Bismuthates. *Chem. Eur. J.* **1995**, *1* (1), 26–32.

(12) Schwamm, R. J.; Harmer, J. R.; Lein, M.; Fitchett, C. M.; Granville, S.; Coles, M. P. Isolation and Characterization of a Bismuth(II) Radical. *Angew. Chem. Int. Ed.* **2015**, *54* (36), 10630–10633.

(13) Yang, X.; Reijerse, E. J.; Nöthling, N.; SantaLucia, D. J.; Leutzsch, M.; Schnegg, A.; Cornella, J. Synthesis, Isolation, and Characterization of Two Cationic Organobismuth(II) Pincer Complexes Relevant in Radical Redox Chemistry. *J. Am. Chem. Soc.* **2023**, *145* (10), 5618–5623.

(14) Chang, L.; Wang, S.; An, Q.; Liu, L.; Wang, H.; Li, Y.; Feng, K.; Zuo, Z. Resurgence and Advancement of Photochemical Hydrogen Atom Transfer Processes in Selective Alkane Functionalizations. *Chem. Sci.* **2023**, *14* (25), 6841–6859.

(15) Kang, Y. C.; Treacy, S. M.; Rovis, T. Iron-Catalyzed C(Sp3)–H Alkylation through Ligand-to-Metal Charge Transfer. *Synlett*, **2021**, *32*, 1767–1771.

(16) Kang, Y. C.; Treacy, S. M.; Rovis, T. Iron-Catalyzed Photoinduced LMCT: A 1° C–H Abstraction Enables Skeletal Rearrangements and C(Sp3)–H Alkylation. *ACS Catal.* **2021**, *11* (12), 7442–7449.

(17) Treacy, S. M.; Rovis, T. Copper Catalyzed C(Sp3)–H Bond Alkylation via Photoinduced Ligand-to-Metal Charge Transfer. *J. Am. Chem. Soc.* **2021**, *143* (7), 2729–2735.

(18) Rowe, R.; Lovelock, K. R. J.; Hunt, P. A. Bi(III) Halometallate Ionic Liquids: Interactions and Speciation. *J. Chem. Phys.* **2021**, *155* (1), 014501.

(19) Koch, T. R.; Wickham, P. P. New Method for the Preparation of Bismuth(III) Triesters. *J. Org. Chem.* **1979**, *44* (1), 157–159.

(20) C. Andrews, P.; B. Deacon, G.; C. Junk, P.; Kumar, I.; Silberstein, M. Synthetic and Structural Comparisons of Bismuth(Iii) Carboxylates Synthesised under Solvent -Free and Reflux Conditions. *Dalton Trans.* **2006**, *0* (40), 4852–4858.

(21) Anjaneyulu, O.; K. Prasad, T.; Kumara Swamy, K. C. Coordinatively Polymeric and Monomeric Bismuth(Iii) Complexes with Pyridine Carboxylic Acids. *Dalton Trans.* **2010**, *39* (8), 1935–1940.

(22) Kumar, I.; Bhattacharya, P.; Whitmire, K. H. Structural Diversity in Phenyl Bismuth(III) Bis(Carboxylate) Complexes. *J. Organomet. Chem.* **2015**, *794*, 153–167.

(23) Gavelle, S.; Innocent, M.; Aubineau, T.; Guérinot, A. Photoinduced Ligand-to-Metal Charge Transfer of Carboxylates: Decarboxylative Functionalizations, Lactonizations, and Rearrangements. *Adv. Synth. Catal.* **2022**, *364* (24), 4189–4230.

(24) Li, Q. Y.; Gockel, S. N.; Lutovsky, G. A.; DeGlopper, K. S.; Baldwin, N. J.; Bundesmann, M. W.; Tucker, J. W.; Bagley, S. W.; Yoon, T. P. Decarboxylative Cross-Nucleophile Coupling via Ligand-to-Metal Charge Transfer Photoexcitation of Cu(Ii) Carboxylates. *Nat. Chem.* **2022**, *14* (1), 94–99.

(25) Lutovsky, G. A.; Gockel, S. N.; Bundesmann, M. W.; Bagley, S. W.; Yoon, T. P. Iron-Mediated Modular Decarboxylative Cross-Nucleophile Coupling. *Chem*, **2023**, *9* (6), 1610–1621.

(26) Leifert, D.; Studer, A. The Persistent Radical Effect in Organic Synthesis. *Angew. Chem. Int. Ed.* **2020**, *59* (1), 74–108.

(27) Lutovsky, G. A.; Yoon, T. P. Cu(II) Salts as Terminal Oxidants in Visible-Light Photochemical Oxidation Reactions. *Org. Biomol. Chem.* **2023**, *22* (1), 25–36.

(28) Breunig, H. J. Organometallic Compounds with Homonuclear Bonds between Bismuth Atoms, 70 Years after Paneth' Report on the Violet Dimethyl Bismuth Compound. *Z. Anorg. Allg. Chem.* **2005**, *631* (4), 621–631.

(29) Muir, M. M. P. VI.—On Certain Bismuth Compounds. *J. Chem. Soc.* **1876**, *29* (0), 144–152.

(30) Corbett, J. D. Bismuth(I) Chloride[1]. *J. Am. Chem. Soc.* **1958**, *80* (18), 4757–4760.

(31) Yang, X.; Reijerse, E. J.; Bhattacharyya, K.; Leutzsch, M.; Kochius, M.; Nöthling, N.; Busch, J.; Schnegg, A.; Auer, A. A.; Cornella, J. Radical Activation of N–H and O–H Bonds at Bismuth(II). *J. Am. Chem. Soc.* **2022**, *144* (36), 16535–16544.

(32) Oberdorf, K.; Hanft, A.; Ramler, J.; Krummenacher, I.; Bickelhaupt, F. M.; Poater, J.; Lichtenberg, C. Bismuth Amides Mediate Facile and Highly Selective Pn–Pn Radical-Coupling Reactions (Pn=N, P, As). *Angew. Chem. Int. Ed.* **2021**, *60* (12), 6441–6445.

(33) Mandrelli, F.; Blond, A.; James, T.; Kim, H.; List, B. Deracemizing α-Branched Carboxylic Acids by Catalytic Asymmetric Protonation of Bis-Silyl Ketene Acetals with Water or Methanol. *Angew. Chem. Int. Ed.* **2019**, *58* (33), 11479–11482.

(34) Arseniyadis, S.; Kyler, K. S.; Watt, D. S. Addition and Substitution Reactions of Nitrile-Stabilized Carbanions. In *Organic Reactions*; John Wiley & Sons, Ltd, 2005; pp 1–364.

(35) Chi, H.; Li, H.; Liu, B.; Ye, R.; Wang, H.; Guo, Y.-L.; Tan, Q.; Xu, B. From Isocyanides to Iminonitriles via Silver-Mediated Sequential Insertion of C(Sp3)–H Bond. *iScience* **2019**, *21*, 650–663.

(36) Zheng, Y.; Mao, J.; Chen, J.; Rong, G.; Liu, D.; Yan, H.; Chi, Y.; Xu, X. Unexpected C[Double Bond, Length as m-Dash]N Bond Formation via NaI-Catalyzed Oxidative de-Tetra-Hydrogenative Cross-Couplings between N , N -Dimethyl Aniline and Sulfamides. *RSC Adv.* **2015**, *5* (62), 50113–50117.

(37) Curle, J. M.; Perieteanu, M. C.; Humphreys, P. G.; Kennedy, A. R.; Tomkinson, N. C. O. Alkene Syn- and Anti-Oxyamination with Malonoyl Peroxides. *Org. Lett.* **2020**, *22* (4), 1659–1664.

(38) Namba, K.; Zheng, X.; Motoshima, K.; Kobayashi, H.; Tai, A.; Takahashi, E.; Sasaki, K.; Okamoto, K.; Kakuta, H. Design and Synthesis of Benzenesulfonanilides Active against Methicillin-Resistant Staphylococcus Aureus and Vancomycin-Resistant Enterococcus. *Bioorg. Med. Chem.* **2008**, *16* (11), 6131–6144.

(39) Tilby, M. J.; Dewez, D. F.; Pantaine, L. R. E.; Hall, A.; Martínez-Lamenca, C.; Willis, M. C. Photocatalytic Late-Stage Functionalization of Sulfonamides via Sulfonyl Radical Intermediates. *ACS Catal.* **2022**, *12* (10), 6060–6067.

(40) Mishra, C. B.; Kumari, S.; Angeli, A.; Bua, S.; Buonanno, M.; Monti, S. M.; Tiwari, M.; Supuran, C. T. Discovery of Potent Anti-Convulsant Carbonic Anhydrase Inhibitors: Design, Synthesis, in Vitro and in Vivo Appraisal. *Eur. J. Med. Chem.* **2018**, *156*, 430–443.

(41) Glaettli, A.; Grammenos, W.; Mueller, B.; Lohmann, J. K.; Vrettou, M. Preparation of Heterocyclo-Fused Pyridin-4-Ylmethylsulfonamides as Agrochemical Fungicides. WO 2009/144159.

(42) Bartberger, M. D.; Beck, H. P.; Chen, X.; Connors, R. V.; Deignan, J.; Duquette, J. A.; Eksterowicz, J.; Fox, B. M.; Fu, J.; Gonzalez Buenrostro, A.; Gonzales Lopez de Turiso, F.; Gustin, D. J.; Heath, J. A.; Johnson, M. G.; Kayser, F.; Kopecky, D. J.; Li, Y.; Li, Z.; Ma, Z.; McIntosh, J.; Medina, J. C.; Mihalic, J. T.; Olson, S. H.; Rew, Y.; Roveto, P. M.; Schmitt, M. J.; Sun, D.; Wang, X.; Wanska, M.; Weathers, C.; Yan, X. Heterocyclic compounds as MDM2 inhibitors for the treatment of cancer. WO 2013/049250.

CHAPTER 4

4 Changing Photocatalytic Activity with Local Electric Fields

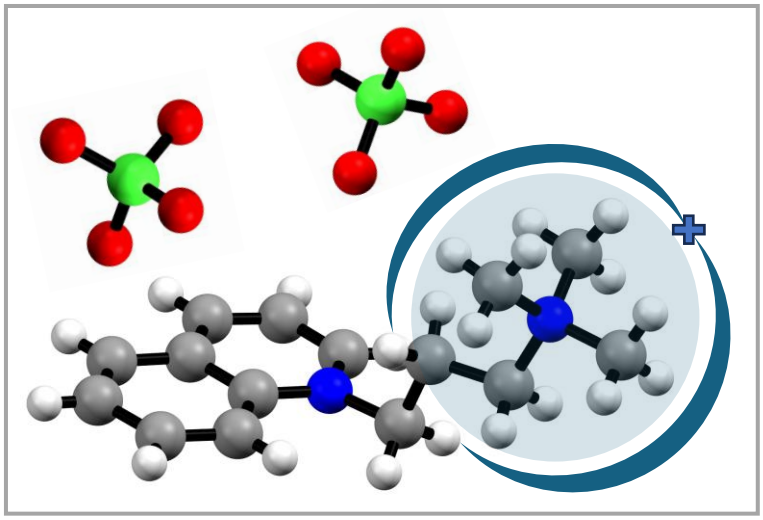

Abstract: Herein, we describe the design and synthesis of novel quinolium-based photocatalysts with *N*-substituents bearing additional charges. The second charged group creates a local electric field (LEF) at the photocatalyst which potentially changes the electron transfer kinetics and thereby the photocatalysts' reactivity.

Modified version of this chapter will be published. For reference, see:
J. Ahmed, E. K. Taskinen, C. Graf, R. J. Kutta, P. Nürnberger* and B. König*, Changing the kinetics of photoinduced electron transfer by Local Electric Fields. (*Manuscript under preparation)*

Author contributions: J.A. and B.K. formed the concept of the study. J.A. designed and synthesized the catalysts and measured the reaction kinetics and fluorescence quenching spectra. E.K.T. isolated and analyzed the C–N coupling products, assisted with reaction kinetics and fluorescence quenching measurements, and coordinated the collaboration with AK Nürnberger. C.G. carried out initial measurements. R.J.K. performed femtosecond TA measurements, analyzed the results, and derived the excited-state lifetimes and substrate oxidation rates. E.K.T. and R.J.K. wrote the manuscript with input from all authors.

4.1 Motivation

After studying anionic organophotocatalyst (Eosin Y) and a bismuth-centred LMCT-catalyst, we wanted to expand our studies of ion-pair effects in photocatalysis to yet another direction. Towards this direction, an ongoing research campaign in our group has devoted to the development of anionic organophotocatalysts with increased reduction potentials. While monoanionic catalysts, such as tetramethoxyanthrolate (TMA^{-}), did indeed possess elevated reduction potentials, the quest to even more highly reducing dianionic catalysts turned out to be more challenging.[1,2] Among various challenges, the inclusion of two anionic charges in the same conjugated system is often rather disfavoured, necessitating forcing conditions when the second charge is to be generated by deprotonation. On the other hand, embedding two non-conjugated charged groups within the same molecule appears to be a much easier task. Towards this direction, an aliphatic linker could be envisioned to simultaneously provide means to connect the second charged group and separate it from the redox-active core. As an advantage, the second charge could act by creating a constant electrostatic field around the redox-active site, thereby affecting the catalyst-substrate or catalyst-intermediate interactions. Intriguingly, studies based on these design principles have so far not been explored in the literature.

4.2 Introduction

Over the past decade, photoredox catalysis has grown into a versatile and mild method for the realization of organic reactions.[3–6] Unarguably, the current success would not have been possible without the development of molecular photoredox catalysts; compounds that can harvest the activating energy of light and mediate it to organic substrates.[7] This revolution has enabled the activation of novel starting materials, which could not be reached by direct irradiation, allowing practitioners to change their irradiation sources from far UV-light to visible-light LEDs.

The photophysical principles of the photocatalyst's function are described in Scheme 4.1a.[8,9] Absorption of light promotes an electron from the ground state of the photocatalyst (S_0) to a singlet excited state (S_1). The S_1 state is often rather short-lived, and the excited electron can undergo an intersystem crossing to a slightly lower-lying triplet state (T_1). If the T_1 state is energetically close to the S_1 state, a reverse intersystem

crossing (RISC) can be induced, for example, by thermal energy. Relaxation back to the ground-state can occur from both S_1 (fluorescence) and T_1 (phosphorescence), yet the latter process is spin-forbidden, therefore prolonging the triplet-state lifetime. Both the S_1 and T_1 states can also participate in electron transfer processes *via* a photoinduced electron transfer (PET) and a single-electron transfer (SET).[10] In the oxidative quenching, the photocatalyst donates one electron to the substrate, whereas in the reductive quenching, the photocatalyst accepts an electron.[11] Finally, the catalytic cycle must be closed *via* a single electron transfer with a reaction intermediate or a suitable terminal oxidant/reductant.

Whereas the first photoredox catalysts, for example, the $Ru(bpy)_3Cl_2$, were repurposed from their initial application in solar cells, modification of the photocatalysts soon became a powerful way of broadening the possible reactions.[7] With the ruthenium and iridium complexes, electronic modification on the ligands has emerged as a successful strategy to broaden their operative redox window and develop certain catalysts towards one mode of substrate activation.[12,13] For organic photocatalysts, the redox potentials could also be strongly modified by incorporating an electron-donating or electron-withdrawing group into their structures. Taking this strategy even further, conjugated anionic or

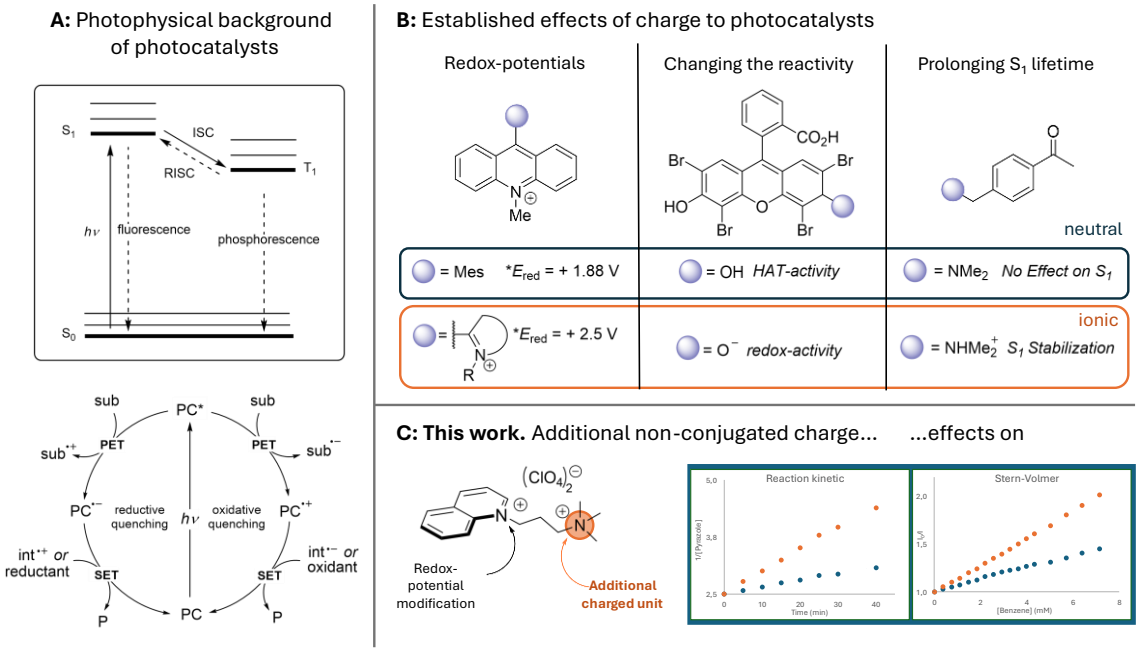

Figure 4.1. Photophysical principles in the action of photocatalysts (a), established effects of charge to photocatalysts (c) and effect of a non-conjugated charge (this work).

cationic substituents can be added to strongly modify the redox-properties, the latter approach giving rise to strongly oxidizing acridinium and pyrylium salts ($*E_{red} > 2.0$ V).[14–

[16] Recently, the charged group strategy was further harnessed in the development of dicationic acridinium/carbene hybrid photocatalysts which could achieve oxidation potentials up to +2.5 V (Figure 4.1b, left).[17] This achievement is particularly notable as the energy of blue photons (440 nm) of 270 kJ/mol defines the maximum theoretical energy threshold between the photocatalyst and substrate as +2.8 V.[18] Alternatively, the charged unit can also be introduced to the catalyst *in situ* by a simple protonation or deprotonation of a neutral compound. For example, deprotonation of the organic photocatalyst tetramethoxyanthracen-9(10*H*)-one (TMAH) leads to the appearance of a reversible oxidation peak making the catalyst suitable for uses in catalysis.[1] For Eosin Y, the neutral form is frequently utilized as hydrogen atom transfer (HAT) catalyst, whereas the deprotonated form acts as a rather strongly reducing species (Figure 4.1b, middle).[19] Furthermore, the group of Coote has established a novel strategy for prolongation of the singlet excited-state lifetime *via* stabilization of the excited-state dipole by a non-conjugated charged group (Figure 4.1, right).[20]

Despite the distinct nature of charged catalysts[21] and growing literature on ionic catalysis,[22,23] harnessing the ionic effects has remained an underutilized strategy in the field of photochemistry. In particular, we questioned whether addition of an ionic moiety to the photocatalyst could affect intermolecular electron-transfer processes, which, by definition, involve transfer of charges between the catalyst and the reactant. Towards this direction we were especially inspired by recent studies using electrostatic fields (local or external) to control reactivity and selectivity in various ground-state and excited-state reactions.[24–26] Hence, we questioned whether we could introduce a local electric field in our reaction mixtures as a part of our photocatalyst. In principle, a charged group connected to the catalyst by an aliphatic linker should not participate in the redox events but would remain in close proximity to the substrate-catalyst assembly. This, in turn, could generate *a local designed electric field (LDEF)*, potentially affecting the photoinduced electron transfer (PET) or the mechanistic steps, such as back-electron transfer (BET), occurring afterwards. Herein, we describe the design, synthesis and characterization of photocatalysts bearing a suitable group for electric field induction, as well as detailed mechanistic studies of their effects on reactivity.

4.3 Results and Discussion

4.3.1 Synthesis and characterization of the photocatalysts

We started our study by designing a series of novel quinolinium-derived photocatalysts. To reliably evaluate the effect of a non-conjugated charge on the catalyst performance, we decided to separate the additional ionic group from the redox-active core with an alkyl linker. Using the commercially available *N*-ethylquinolinium perchlorate (**PC1**) as a model catalyst, three additional catalysts differing only in the alkyl chain length and the terminal functional group were envisioned. Hence, **PC2** contains a quaternary ammonium salt linked to the core with a $(CH_2)_3$ chain, **PC3** is zwitterionic, having a sulfonate group at the end of the alkyl chain, and **PC4** corresponds to a chain-prolonged catalyst resembling structurally the dicationic catalyst (Scheme 4.1). To summarize our synthetic route, the quinone core was first *N*-alkylated with the desired alkyl bromide, through which the zwitterionic **PC3** could be directly obtained. For the other catalysts, an ion exchange process or quaternarization followed by a counter ion exchange gave the photoactive quinolinium perchlorate salts **PC1–PC4**. All catalysts were obtained as white or pale solids, and their purity was confirmed by ^{1}H-NMR and ^{13}C-NMR spectroscopy and high-resolution mass spectrometry. Furthermore, single crystals from the catalysts **PC1 – PC3** were successfully grown and analyzed by X-ray diffraction. The photocatalysts **PC1** and **PC2** both formed a monoclinic crystal system with $P2_1/c$ space group. The centre-to-centre N···P distance, indicating the separation between the quinolinium cation and the PF_6 anion, was found to be 4.83 Å in **PC1** and between 4.0 Å and 5.0 Å in **PC2**. These values indicate weak ionic interactions. Moreover, the measured $N^{+}\cdots X^{-}$ distances are in good agreement with the previously reported crystal structures of *N*-ethylquinolinium salts with iodine, bromine and hexafluorophospate counteranions.[27,28] In turn, **PC3** crystallized in

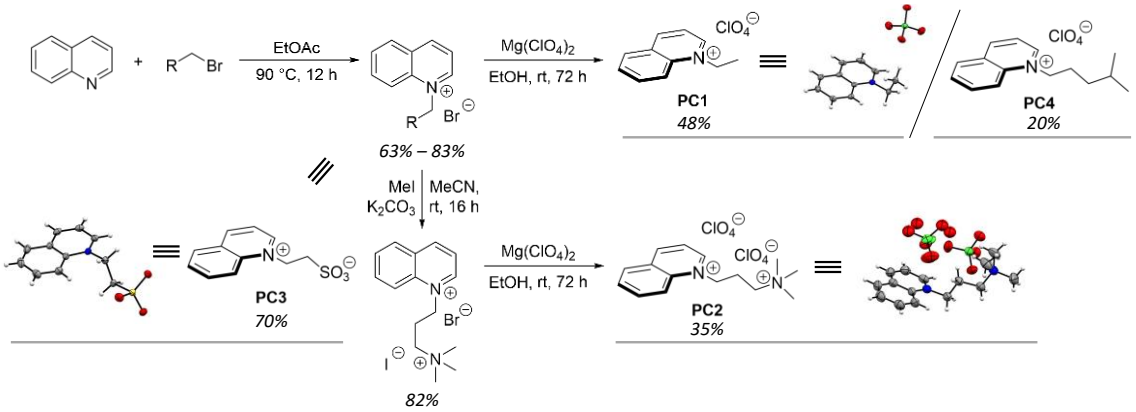

Scheme 4.1. Synthesis and X-ray structures of photocatalysts **PC1**–**PC4**.

an orthorhombic system with a Pbca space group. In all photocatalysts, the torsion angle between the quinolinium π-system and the $(R_2N)CH_2$-CH_2R alkyl chain is almost perpendicular (between 85° and 97°), making hyperconjugation possible, yet the respective bond lengths in the alkyl chain (1.52 Å and 1.54 Å) did not show notable shortening from the usual $C(sp^3)$–$C(sp^3)$ bond length of 1.54 Å.

4.3.2 UV-vis and fluorescence emission spectra

UV-vis spectroscopy of the catalysts (in MeCN) generally displayed two absorption maxima: one in the near UV-region and one in the middle UV-range (Figure 4.2). From these, the former corresponds to the first electronic transition $S_1 \leftarrow S_0$ which could be used to photoexcite the catalysts. Comparison of the catalysts with each other reveals merely subtle changes on the exact positions of the absorption maxima: the benchmark catalyst **PC1** has its maxima at 237 nm and 316 nm while the newly synthetized **PC2 – PC4** have their first absorption maximum at 237(±)1 nm and the second at 316(±)1 nm.

In contrast, slightly more shifting was observed at the fluorescence emission spectra. While the monocationic photocatalysts **PC1** and **PC4** displayed identical emission spectra having the emission maximum at 404 nm, the emission of photocatalyst **PC2** was bathochromically shifted to 409 nm. In contrast, the emission of zwitterionic **PC3** was found to be centred at 374 nm, indicating that its excited state lies a bit higher in energy as compared to the other photocatalysts.

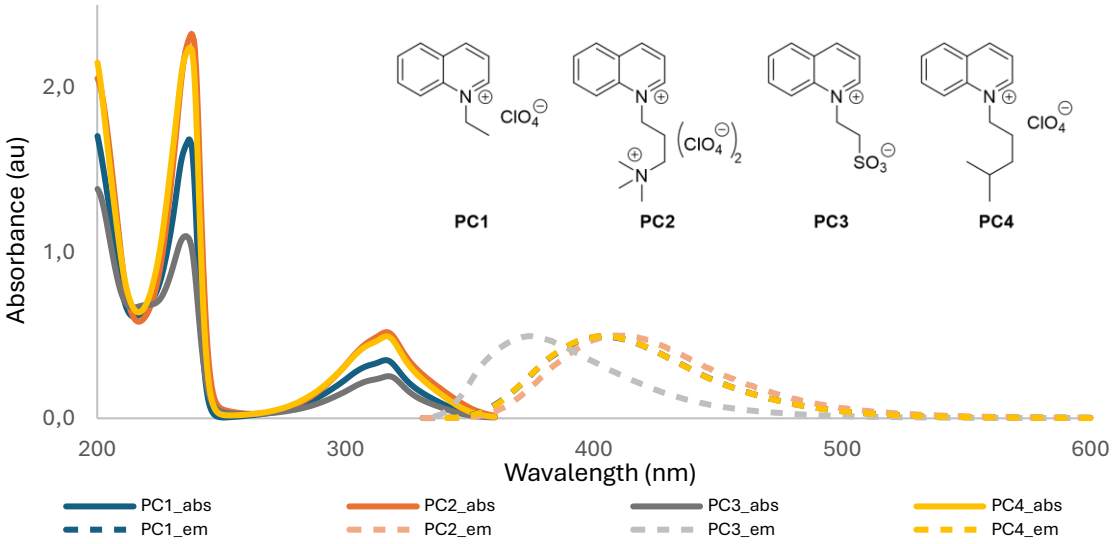

Figure 4.2. UV-vis absorption and fluorescence emission spectra of the photocatalysts.

4.3.3 Excited-state reduction potentials

The catalysts were then further characterized by cyclic voltammetry (CV) to measure their ground-state reduction potentials (for the chromatograms see section 4.5.4.2). The excited state reduction potentials were then estimated from the ground-state reduction potentials (measured against ferrocene) and the intersection point of the normalized UV-vis absorption and fluorescence emission spectra. The ground-state and excited-state redox potentials for each catalyst are summarized in Table 4.1. Following our design principles, the nature and charge of the *N*-alkyl substituent was found to have only a minor effect on the redox-abilities of the catalysts. Indeed, all catalysts exhibited highly similar ground-state reduction potentials of –0.92 eV or –0.93 eV with the sole exception being the –0.85 eV from **PC2**. In turn, the excited-state reduction potentials between 2.58 eV and 2.66 eV were obtained, making the catalysts suitable for oxidation of challenging substrates.

Table 4.1. Calculated excited-state reduction potentials of the photocatalysts.

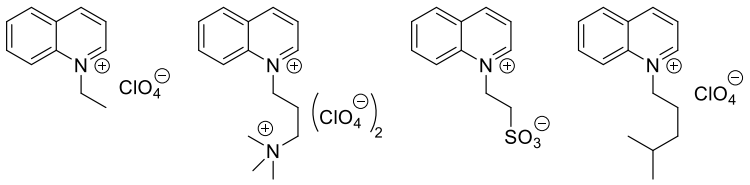

Catalyst	E^{red} vs. SCE (eV)	$E_{0,0}$ (eV)	$^*E^{red}$ (eV)
PC1	– 0.93	3.53 ($I_{0,0}$ = 351 nm)	– 2.60
PC2	– 0.85	3.49 ($I_{0,0}$ = 355 nm)	– 2.63
PC3	– 0.92	3.58 ($I_{0,0}$ = 345 nm)	– 2.66
PC4	– 0.92	3.51 ($I_{0,0}$ = 353 nm)	– 2.58

For details to the calculation of $^*E^{red}$, see section 4.5.4.2.

4.3.4 Catalyst performances

The catalysts were then tested in an aryl oxidation-nucleophilic coupling reaction which has been established as a benchmark reaction for highly oxidizing photocatalysts.[17] Choosing benzene and pyrazole as standard coupling partners, a brief screening of reaction parameters was carried out (see section 4.5.3.2). The optimal conditions were established as given in Table 4.2. Evaluating the performances of the photocatalysts under otherwise identical reaction conditions, the dicationic **PC2** afforded the highest yield of the desired product (64%) while the monocationic **PC1** gave the product in 45% yield (Entries 1 and 2). The chain-prolonged **PC4** performed slightly worse than its *N*-ethyl counterpart, yet the lowest yield (32%) was obtained with the zwitterionic **PC3** (Entries 3 and 4). In turn, variation of the aromatic reaction partner with **PC2** notably lowered the yields of the desired 1,4-difluorobenzene and toluene-derived products (Entries 5 and 6). This result was particularly surprising with toluene since the comparison of oxidation potentials should predict a more facile oxidation of this substrate. However, the productive reaction was most likely accompanied by side-reactions. Mesitylene, in turn, was found to give the highest yield of the coupling product perhaps stemming from the combination of facile oxidation and stability of the intermediate radical cation (Entry 7).

Table 4.2. Yields of the aryl oxidation- nucleophilic coupling reactions using.

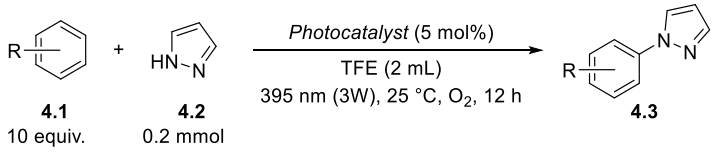

4.1 10 equiv. **4.2** 0.2 mmol **4.3**

Entry	Aryl	E^{ox} (aryl) (eV)	Cat.	Yield (%)
1	Benzene	2.57	**PC1**	45
2	Benzene	2.57	**PC2**	64
3	Benzene	2.57	**PC3**	25
4	Benzene	2.57	**PC4**	29
5	1,4-DiF-Ph	2.48	**PC2**	40
6	Toluene	2.26	**PC2**	30
7	Mesitylene	2.04	**PC2**	75

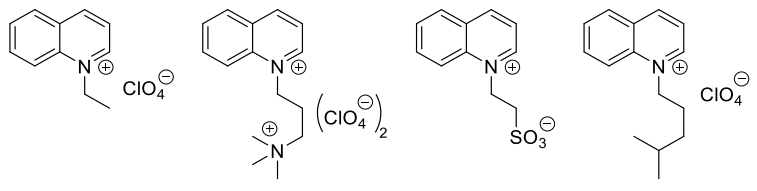

PC1 **PC2** **PC3** **PC4**

To obtain more information about the relative performances of the catalysts, reaction kinetics were studied with each combination of aromatic reaction partner and photocatalyst (Figure 4.3). Through all aromatic reactants tested, the dicationic **PC2** (orange lines) gave typically the fastest reaction rates whereas the zwitterionic **PC3** (grey lines) had the slowest rates. The relative performances of the commercially available **PC1** (blue lines) were found to be dependent on the aromatic reaction partner: with the most easily oxidizable mesitylene the reaction rate was similar to that of **PC2**, but with benzene and 1,4-difluorobenzene the reactions were notably slower. Although the excited-state reduction potentials of **PC1** and **PC2** differed only slightly (–2.60 eV *vs.* –2.63 eV), with substrates near the upper limit of the photocatalysts oxidation abilities these small differences might start to play a role in the reaction kinetic (i.e. oxidation potential of benzene 2.57 eV). The chain-prolonged monocationic catalyst **PC4** (yellow line) often gave slower reactions than its *N*-ethyl counterpart, but was more efficient both in terms of rate and yield than the zwitterionic catalyst **PC3**.

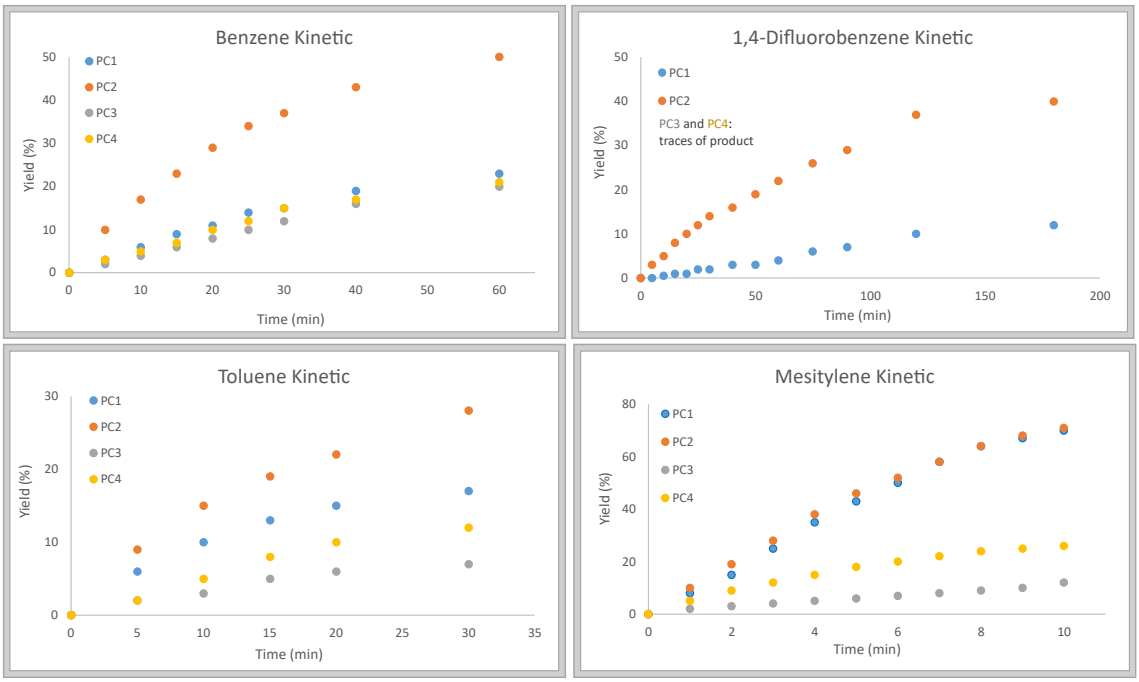

Figure 4.3. Reaction kinetics from aryl oxidation- nucleophilic substitution reaction.

4.3.5 Fluorescence quenching

The different photocatalysts were further evaluated by fluorescence quenching studies (Figure 4.4, gray background). Starting with the **PC2**, fluorescence of this catalyst was quenched efficiently by all aromatic reaction partners (orange curves). The fluorescence of **PC1** was quenched well by 1,4-difluorobenzene, toluene and mesitylene, but somewhat surprisingly, the quenching was notably less pronounced with benzene (blue curves). Fluorescence of **PC3** was well quenched only by toluene and mesitylene (grey curves), whereas the **PC4** followed similar trends to those of **PC1** albeit with slightly less quenching with 1,4-difluorobenzene (yellow curves).

The Stern-Volmer constants of each combination of the aromatic substrate and photocatalyst further demonstrated the trends above. In the case of benzene, **PC2** has significantly highest quenching rate followed by **PC1**, **PC4** and eventually **PC3**. With other aryls the lowest quenching constants were found with **PC3**. In contrast, **PC1** was found to have equal Stern-Volmer constants to **PC2** with 1,4-difluorobenzene and mesitylene, whereas with toluene **PC1** became the best-quenching.

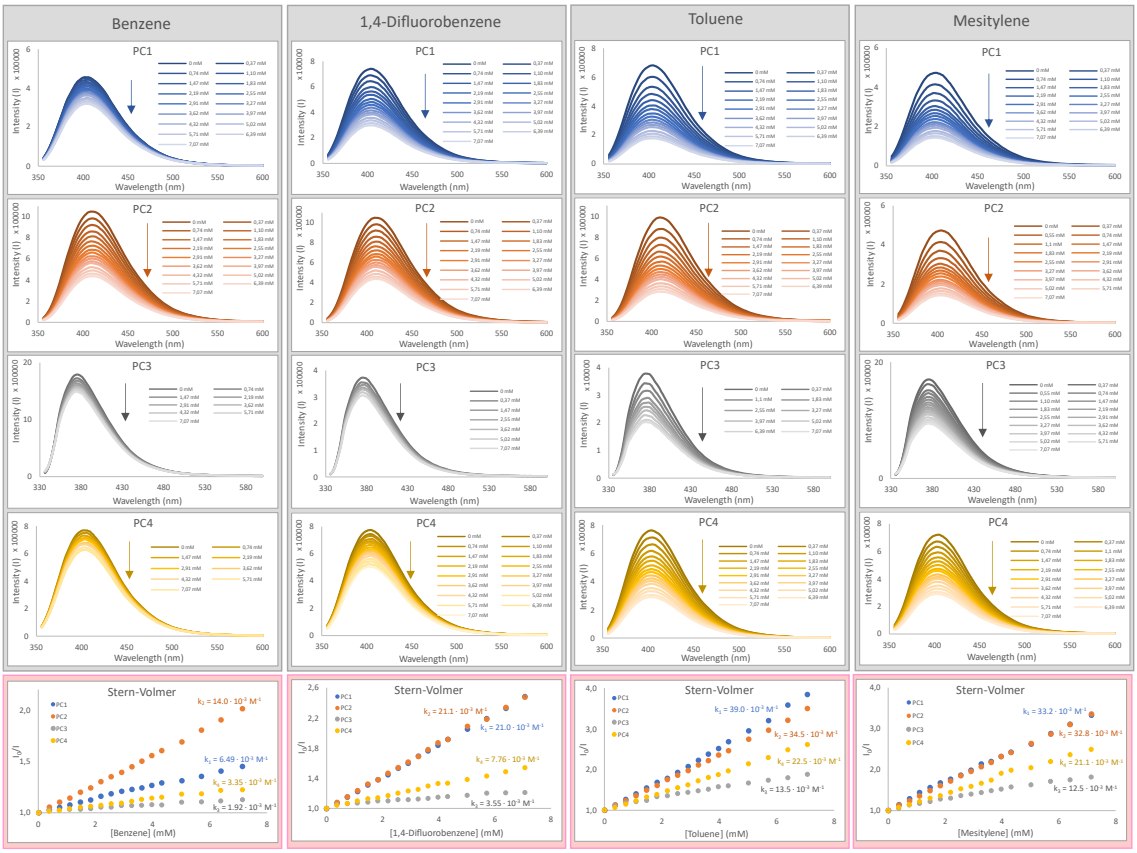

Figure 4.4. Fluorescence quenching studies with photocatalysts **PC1** – **PC4** with different aryls with the calculated Stern-Volmer quenching constants (rosa background).

Comparison of the obtained Stern-Volmer results with the reaction kinetics were particularly interesting in the cases of 1,4-difluorobenzene and toluene. While these substrates quenched the photocatalysts **PC1** and **PC2** at equal rates, the overall reactions proceeded significantly faster with **PC2** (for toluene, **PC2** $k_2 = 5.87\times10^{-4}$ M^{-1} s^{-1} **PC1** $k_1 = 3.54\times10^{-4}$ M^{-1} s^{-1}). This observation clearly suggests that other effect(s) apart from just the quenching rate affect the reaction.

4.3.6 Excited-state lifetimes and electron transfer rates

To further assess the different trends in fluorescence quenching efficiencies and reaction rates, a closer look at the excited-state lifetimes and electron transfer rates was taken. Among the photocatalysts the monocationic **PC1** and dicationic **PC2** were chosen with toluene as the representative aromatic substrate. Herein, transient absorption spectroscopy in short timescales (from 5 ps onward) proved best suitable. Although the final evaluation of the data is still ongoing, initial results clearly indicate that the excited-state lifetimes (both singlet and triplet) of **PC1** and **PC2** are very close to each other. Furthermore, in the presence of the aromatic reaction partner no triplet state of the photocatalysts could be observed, strongly indicating that the PET would take place from the singlet excited state of the catalysts.

4.4 Conclusions and outlook

In this project, we designed and synthesized four quinolinium-derived photocatalysts differentiated by their *N*-alkyl substituents; two of the catalysts contained a neutral alkyl rest, one had a cationic ammonium moiety, and one had an anionic sulfonate. This series of compounds hence offered us a platform to assess the effect of the non-conjugated charged group on the catalytic properties. According to our hypothesis, the added charge had only a minor effect on the redox potentials and excited-state lifetimes of the catalysts. In contrast, the rates of fluorescence quenching with aromatic reaction partners (benzene, toluene, mesitylene, 1,4-difluorobenzene) differed, and the kinetics of aryl oxidation-nucleophilic coupling reaction also varied depending on the catalyst. While the latter two effects mostly followed a similar trend (more efficient fluorescence quenching leading to faster reaction), particularly with toluene, this correlation did not hold for all investigated examples. Hence, it was hypothesized that the presence of a second positive charge might create a local electric field, which could repulse the newly formed toluene radical cation. In this case the back-electron transfer could be disfavoured, leading to a more efficient reaction. Mechanistic studies to address this phenomenon are ongoing.

Table 4.3. Summary of the photocatalysts **PC1** – **PC4** and their properties.

Catalyst	**$\lambda_{max,abs}$** (nm)	**$\lambda_{max,em}$** (nm)	***E*^{red}** (eV)	***E^{red}** (eV)	**Yield** (%)	**Stern-Volmer** ($\times10^{-3}$ M^{-1})	**S_1** (ns)*	**T_3** (μs)*
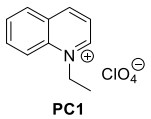 PC1	237, 316	404	– 0.93	– 2.60	45	k_{Ph} = 6.49 k_{DiF} = 21.0 k_{Tol} = 39.0 k_{Mes} = 33.2	21.8	0.73
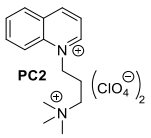 PC2	238, 316	409	– 0.85	– 2.64	64	k_{Ph} = 14.0 k_{DiF} = 21.1 k_{Tol} = 34.5 k_{Mes} = 32.8	27.2	1.0
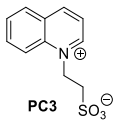 PC3	236, 317	374	– 0.92	– 2.66	32	k_{Ph} = 3.35 k_{DiF} = 7.76 k_{Tol} = 22.5 k_{Mes} = 21.1	–	–
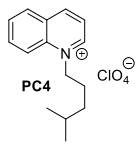 PC4	237, 316	404	– 0.92	– 2.59	–	k_{Ph} = 1.92 k_{DiF} = 3.55 k_{Tol} = 13.5 k_{Mes} = 12.5	–	–

*Excited-state lifetimes from preliminary measurements.

4.5 Experimental

4.5.1 General

Chemicals and solvents were purchased from commercial suppliers (Sigma Aldrich, TCl, BLD Pharma, Alfa Aesar, Acros, Fluka or Thermo Fischer) and, unless otherwise noted, used without further purification. All air-and moisture sensitive reactions including photoreactions were set up using pre-dried N_2 as a shielding gas, whereas dry solvents were obtained from commercial suppliers. Evaporation of organic solvents was carried out in a rotary evaporator at temperatures below 40 °C and under reduced pressure.

Analytical thin layer chromatography (TLC) was routinely used for the monitoring of starting material synthesis and to quantify the evaluation of the reactions. Silica-gel pre-coated aluminium sheets (Macherey-Nagel, silica gel 60G/UV254, 0.2 mm) served as stationary phase, whereas the mobile phase consisted of solvents and solvent mixtures, the ratios of which are reported as v/v solutions. Visualization was performed with a 254 nm UV-light source combined with chromatographic dyes if so noted.

Flash column chromatography (FCC) was done by hand using flash silica gel (Merck, particle size 40–63 μm, 230–440 mesh) as a stationary phase. Eluent mixtures consisting of pre-distilled technical grade solvents were primarily used. For all eluents, the solvent ratios are reported as v/v ratios.

Nuclear Magnetic Resonance Spectroscopy (NMR) was recorded at room temperature using a Bruker Avance 400 (400 MHz for ^{1}H, 101 MHz for ^{13}C, 376 MHz for ^{19}F) NMR spectrometer. All chemical shifts are reported δ-scale as part per million [ppm] (multiplicity, coupling constant *J*, number of protons) relative to the solvent residual peak. The coupling constants *J* are given in Herz [Hz] and the multiplicity of the signals are abbreviated as: singlet (s), broad singlet (br. s.), doublet (d), doublet of doublets (dd), doublet of doublet of doublets (ddd), triplet (t), doublet of triplets (dt), triplet of doublets (td), quartet (q), doublet of quartets (dq), pentet (p) and multiplet (m). For the NMR measurements deuterated solvents from Deutero or Sigma Aldrich were used. The spectra were processed using MestreNova 9.0.1.

High Resolution Mass Spectra (HRMS) were performed at the Central Analytical Laboratory of the departments of chemistry and pharmacy at the University of Regensburg. For measurements, > 1 mg of the sample submitted, which was later dissolved to

acetonitrile, DCM or ethyl acetate. The samples were then injected either to a Jeol AccuTOF GCX or to an Agilent Q-TOF 6540 UHD instrument.

Single Crystal X-Ray Analysis (XRD) were performed at the Central Analytical Laboratory of the departments of chemistry and pharmacy at the University of Regensburg. For measurements, the diffraction properties of each crystal were first examined under a microscope, after which a suitable crystal was mounted on a MITIGEN holder using inert oil. The diffraction data was collected with Hy-Pix Arc 150 (XtaLab Synergy R, DW System) diffractometer. Temperature was hold constant at 123 K during the measurement. Structure was solved with ShelXT 2018 program and using Olex2 1.5-alpha as the graphical interface. The model was refined with ShelXL using full matrix least squares minimization on $\boldsymbol{F}^2$. After analysis, the Cif-file was checked online with the International Union of Crystallography to provide the CheckCif- report.

UV-vis spectroscopy was measured with Agilent Cary 400 UV-Vis spectrophotometer. A quartz cuvette with a light pathlength of 10 mm was utilized as the sample container. The measurements were carried out at 25 °C. The spectral window was set to 200 nm to 700 nm with data interval of 1 nm. Before the measurement of the samples, the background consisting of pure solvent (MeCN) was measured, and the spectrum was reduced from that of the sample.

Cyclic voltammetry (CV) was performed by Regina Hoheisel at the group of Prof. König. For the measurements, a three-neck round bottom flask was equipped with a glassy carbon working electrode, a platinum wire counter electrode and a silver wire as a reference electrode. A three-electrode potentiostat galvanostat PGSTAT302N (Metrohm Autolab) was connected to the electrodes. Tetrabutylammonium hexafluorosulfate ($TBASF_6$) was utilized as supporting electrolyte as this salt allowed reliable measurements until high oxidative potentials. Before the measurements, the sample was degassed by bubbling through N_2. Potentials vs. saturated calomel electrode were recorded with ferrocene added as internal standard with $E_{1/2}(Fc/Fc^+) = 0.380$ V vs. SCE. Half-wave potentials for irreversible peaks were estimated from the first derivative of the cyclic voltammogram.

Fluorescence quenching was measurements were carried out using FluoroMax-4 spectrofluorometer (Horiba Scientific) and a quartz fluorescence cuvette with a pathlength of 10 mm. The fluorescence quenching measurements were carried out under N_2 atmosphere, and all the used solvents were carefully degassed by bubbling through N_2 for at

least 1 h before use. A stock solution of the catalyst (c = 0.0125 M) was prepared in degassed MeCN under N_2, and 10 µL of this stock solution was dissolved into 2 mL of MeCN. This mixture had the $\lambda_{max} \approx 0.1$ au on UV-vis spectrometer. The excitation wavelength was set at 340 nm (320 nm for **PC3**), slit 1 nm and emission was collected from 355 nm to 600 nm. A stock solution of the quencher (arene, 0.015 M, 5 µL or 10 µL) was added at a time and the emission spectrum was recorded. UV-vis spectroscopy was routinely measured in between of fluorescence quenching to exclude ground-state interactions. Moreover, the amount of total added quencher was kept under 100 µL to minimize dilution factors.

Emission decays were recorded by using either a commercial TCSPC device (PicoQuant GmbH, Pico Harp 300 and PLD 800-B) or a custom-build setup. The excitation wavelengths (Horiba, Nano-LED) and the detection wavelengths are displayed together with the corresponding data.

Emission quantum yields were determined *via* the total integration technique employing an Ulbricht sphere (Hamamatsu Photonics, C9920-02). The excitation wavelengths are reported together with the corresponding data.

Transient absorption (TA) spectroscopy was measured with a custom-build setup at the group of Prof. Nürnberger at Regensburg University. The setup employed a combination of a spectrograph (Bruker) and a streak camera (Hamamatsu Photonics, C7700) for detection. The sample was filled into a quartz cuvette with 10 mm light path and stirred with a micro stirring bar during the measurements. The sample was excited at 355 nm laser (Third harmonic of a Nd:YAG, Surelite^{TM} II), and orthogonally probed by a pulsed Xenon

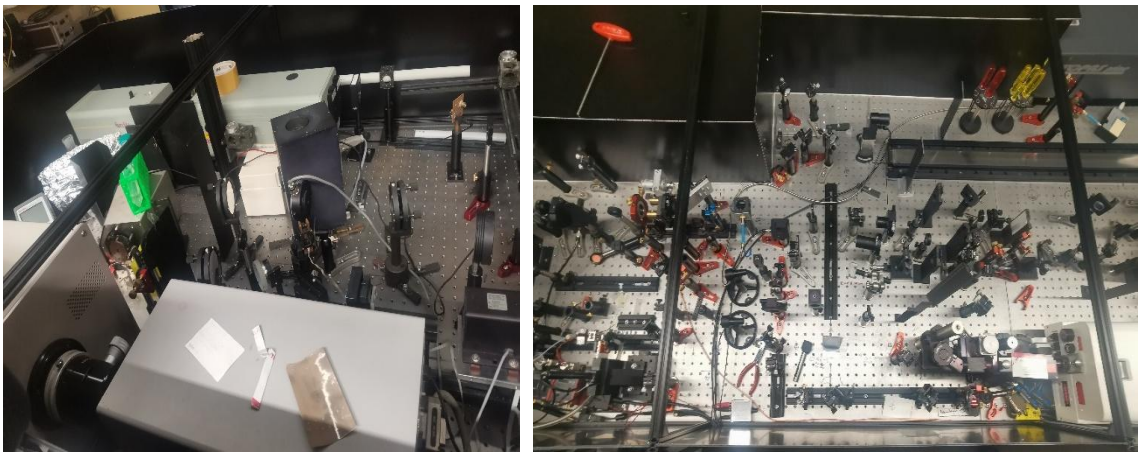

Figure S4.1. Setups for transient absorption spectroscopy

flash lamp (AppliedPhotoPhysics) along the cell's window side. The probing was done close to the excitation area to probe the volume of maximal concentration of excited molecules. UV-vis spectral range was measured before and after each TA spectrum to exclude sample decomposition and photoproduct formation.

4.5.1.2 Photosetups

The photoreactions run at 395 nm (3.0 W) were performed using custom-made photoreactors depicted in the Figure S4.2. At the core of the photoreactors reside a metal block to which six single-spot LEDs of desired wavelength are mounted. On top of the LED block sits a hollow cooling block made of stainless-steel through which a constant flow of water is possible. This cooling block also contains holes made to perfectly fit 5 mL crimp-cap vials, thus providing a sideway contact of the reaction vessels to the cooling system. Magnetic stirring for the reactions is imposed from underneath the LED blocks using Heidolph MR 3000 stirring plates. The water cooling is sustained with a Julabo Curio Co unit.

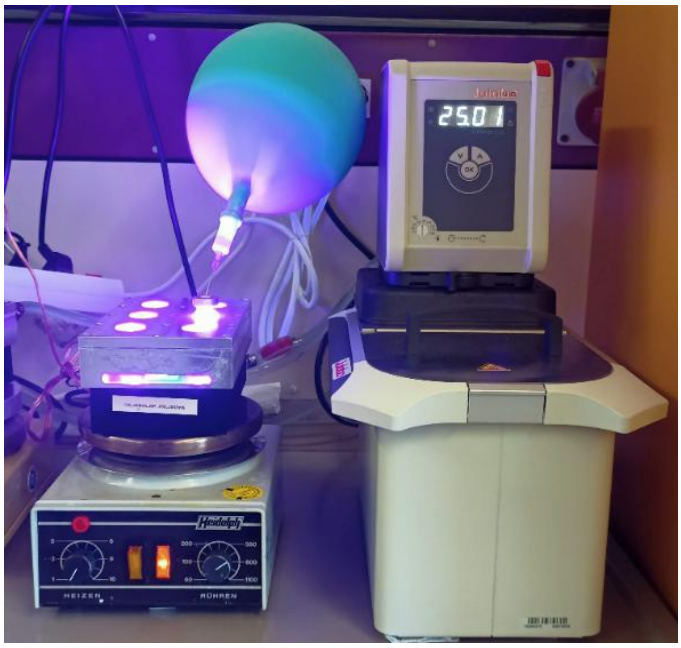

Figure S4.2. Photosetup used for this project.

4.5.1.3 Emission spectrum of the LEDs

The emission spectrum of the utilized LEDs (centred around 395 nm) was also measured to better characterize the actual emitted wavelengths of the setup. The measurement was carried out with Ocean Optics HR 2000+ spectrometer. The results are plotted in Figure S4.3.

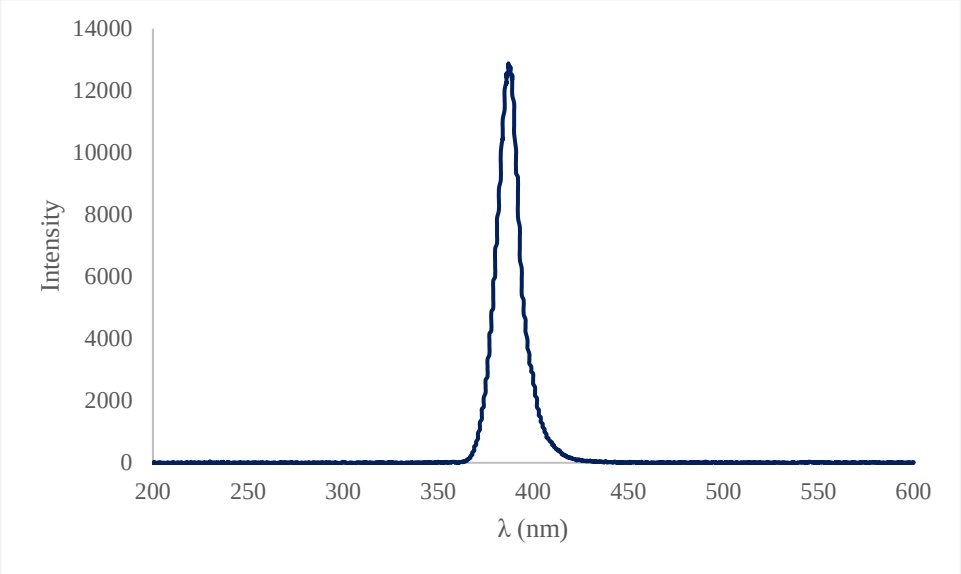

Figure S4.3. Emission spectrum of the 395 nm LEDs.

4.5.2 Synthesis of quinolinium photocatalysts

4.5.2.1 Synthesis of 1-ethyl-1 λ4-quinolinium perchlorate salt (PC1)

1-ethyl-1λ^4-quinolinium bromide

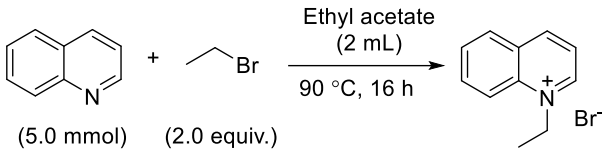

To a 20 mL sealed tube equipped with a stirring bar, quinoline (550 µL, 5.0 mmol, 1.0 equiv.) and ethyl bromide (741 µL, 10 mmol, 2.0 equiv.) were dissolved in 2 mL of ethyl acetate. The resulting reaction mixture was stirred at 90˚C for 16 hours. After completion of the reaction, the solvent was evaporated under reduced pressure. The crude reaction mixture was dissolved in minimum amount of ethanol and a good amount of precipitate was collected upon addition of diethyl ether. The precipitate was washed with minimum amount of acetone (~5 mL) and dried under vacuum to obtain the pure 1-ethyl-1 λ^4-quinolinium bromide.

^{1}H-NMR (400 MHz, DMSO-d_6) δ (ppm) 9.64 (dd, J_1 = 5.8 Hz, J_2 = 1.3 Hz, 1H), 9.31 (d, J = 8.4 Hz, 1H), 8.64 (d, J = 9.0 Hz, 1H), 8.51 (dd, J_1 = 8.2 Hz, J_2 = 1.2 Hz, 1H), 8.29 (ddd, J_1 = 8.8 Hz, J_2 = 7.0 Hz, J_3 = 1.4 Hz, 1H), 8.20 (dd, J_1 = 8.4 Hz, J_2 = 5.8 Hz, 1H), 8.06 (ddd, J_1 = 8.3 Hz, J_2 = 7.0 Hz, J_3 = 0.6 Hz, 1Hz), 5.13 (q, J = 7.2 Hz, 2H), 1.61 (t, J = 7.2 Hz, 3H);

^{13}C-NMR (101 MHz, DMSO-d_6) δ (ppm) 149.9, 147.7, 137.7, 136.1, 131.2, 130.3, 130.1, 122.8, 119.3, 53.4, 15.7;

HRMS (ESI+): calc. $[M+H]^+$ for $C_{11}H_{12}N^+$ 158.0970, found 158.0965, Δ = 0.5 mDa.

1-ethyl-1λ^4-quinolinium perchlorate

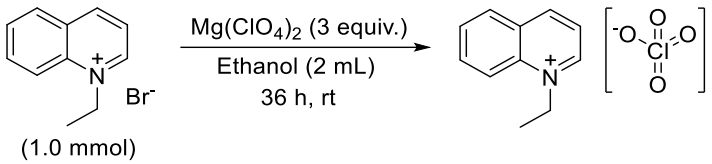

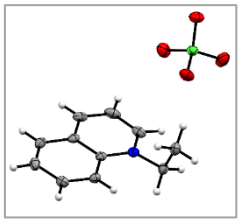

To a 50 mL sealed tube equipped with a stirring bar, 1-ethyl-1λ^4-quinolinium bromide salt (238 mg, 1.0 mmol, 1.0 equiv.) and $Mg(ClO_4)_2$ (670 mg, 3.0 mmol, 3.0 equiv.) were suspended in ethanol (2 mL). The sealed tube containing the reaction mixture was capped, and for 36 h at room temperature. A white precipitate was obtained after completion of the reaction, and the precipitate was washed with minimum amount of ethanol and finally

washed with diethyl ether. The resulting white precipitate was dried under high vacuum to obtain the final product, 1-ethyl-1λ^4-quinolinium perchlorate salt (120 mg, Yield: 48%).

^{1}H-NMR (400 MHz, DMSO-d_6) δ (ppm) 9.58 (dd, J_1 = 6.0 Hz, J_2 = 1.0 Hz, 1H), 9.29 (d, J = 8.4 Hz, 1H), 8.63 (d, J = 8.9 Hz, 1H), 8.50 (dd, J_1 = 8.4 Hz, J_2 = 1.0 Hz, 1H), 8.29 (ddd, J_1 = 9.2 Hz, J_2 = 7.0 Hz, J_3 = 1.3 Hz, 1H), 8.19 (dd, J_1 = 8.4 Hz, J_2 = 5.8 Hz, 1H), 8.06 (app. t, J_1 = 7.6 Hz, 1H), 5.11 (q, J = 7.2 Hz, 2H), 1.61 (t, J = 7.2 Hz, 3H);

^{13}C-NMR (101 MHz, DMSO-d_6) δ (ppm) 149.9, 147.7, 137.7, 136.1, 131.2, 130.3, 130.1, 122.8, 119.3, 53.4, 15.7;

HRMS (ESI+): calc. $[M+H]^+$ for $C_{11}H_{12}N^+$ 158.0970, found 158.0964, Δ = 0.6 mDa.

4.5.2.2 Synthesis of 1-(3-(trimethyl-λ4-azaneyl)propyl)-1 λ 4-quinolinium bis-perchlorate salt (PC2)

3-(1λ^4-quinolin-1-yl)propan-1-amine bromide

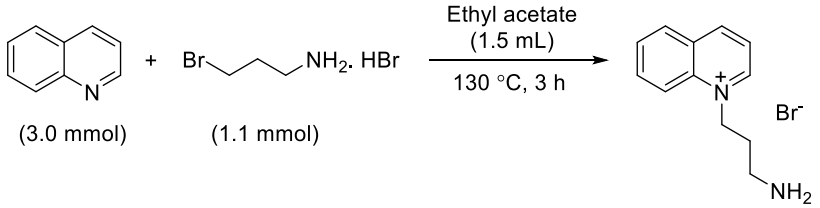

To a 20 mL sealed tube equipped with a stirring bar, quinoline (355 µL, 3.0 mmol, 1.0 equiv.), 3-bromopropan-1-amine hydrobromide (722 mg, 3.3 mmol, 1.1 equiv.) and ethyl acetate (1.5 mL) were added. The sealed tube containing the reaction mixture was capped, and the reaction mixture was heated at 130 ˚C for 3 h. A white solid precipitate was obtained after completion of the reaction. The reaction mixture was cooled to room temperature and diluted with ethanol (10 mL). A white solid was obtained as precipitate after the addition of diethyl ether. This process was repeated twice to obtain pure white precipitate after filtration. The white product was dried under vacuum to obtain white powder of the final product, 3-(1λ^4-quinolin-1-yl)propan-1-amine bromide (506 mg, Yield: 63%).

^{1}H-NMR (400 MHz, DMSO-d_6) δ (ppm) 9.67 (dd, J_1 = 5.8 Hz, J_2 = 1.1 Hz, 1H), 9.35 (d, J = 8.3 Hz, 1H), 8.72 (d, J = 9.0 Hz, 1H), 8.53 (dd, J_1 = 8.2, J_2 =1.2 Hz, 1H), 8.30 (ddd, J_1 = 8.8, J_2 = 7.0, J_3 = 1.4 Hz, 1H), 8.24 (dd, J_1 = 8.4, J_2 = 5.8 Hz, 1H), 8.07 (app. t, J = 7.6 Hz, 1H), 7.98 (br. s, 2H), 5.21 (t, J = 7.5 Hz, 2H), 3.08 – 2.97 (m, 2H), 2.36 – 2.26 (m, 2H);

^{13}C-NMR (101 MHz, DMSO-d_6) δ (ppm) 150.3, 148.2, 137.9, 136.2, 131.3, 130.4, 130.3, 122.8, 119.4, 54.9, 36.4, 27.8;

HRMS (ESI+): calc. $[M+H]^+$ for $C_{12}H_{15}N_2^+$ 187.1235, found 187.1230, Δ = 0.5 mDa.

1-(3-(trimethyl-λ^4-azaneyl)propyl)-1 λ 4-quinolinium bromide iodide salt

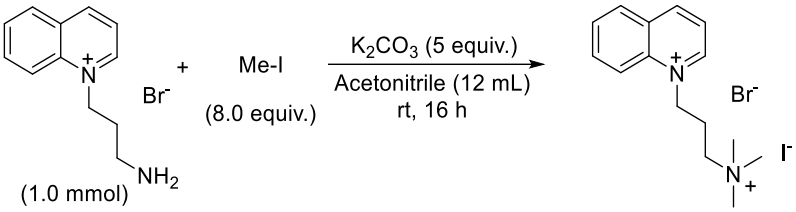

To a 50 mL sealed tube equipped with a stirring bar, 3-(1λ^4-quinolin-1-yl)propan-1-amine bromide (267 mg, 1.0 mmol, 1.0 equiv.), iodomethane (800 µL, 8.0 mmol, 8.0 equiv.) and K_2CO_3 (700 mg, 5.0 mmol, 5.0 equiv.) were taken with acetonitrile (12 mL). The sealed tube containing the reaction mixture was capped, and the reaction mixture was stirred for 16 h at room temperature. A yellow precipitate was obtained after completion of the reaction. The reaction mixture was filtered, and the residue was washed with acetonitrile until the yellow colour disappeared. After drying under high vacuum to obtain the final product, 1-(3-(trimethyl-λ^4-azaneyl)propyl)-1 λ^4-quinolinium bromide iodide salt (360 mg, Yield: 82%).

^{1}H-NMR (400 MHz, DMSO-d_6) δ (ppm) 9.63 (d, J = 5.5 Hz, 1H), 9.37 (d, J = 8.3 Hz, 1H), 8.71 (d, J = 9.0 Hz, 1H), 8.54 (d, J = 8.0 Hz, 1H), 8.37 – 8.22 (m, 2H), 8.10 (app. t, J = 7.6 Hz, 1H), 5.13 (t, J = 7.6 Hz, 2H), 3.66 – 3.54 (m, 2H), 3.14 (s, 9H), 2.49 – 2.40 (m, 2H);

^{13}C-NMR (101 MHz, DMSO-d_6) δ (ppm) 150.5, 148.3, 137.9, 136.4, 131.3, 130.5, 130.2, 122.8, 119.4, 62.5, 54.5, 53.1, 23.8;

HRMS (ESI+): calc. $[M+H]^+$ for $C_{15}H_{23}N_2^+$ 231.1861, found 231.1855, Δ = 0.6 mDa.

1-(3-(trimethyl-λ^4-azaneyl)propyl)-1λ^4-quinolinium bis-perchlorate salt

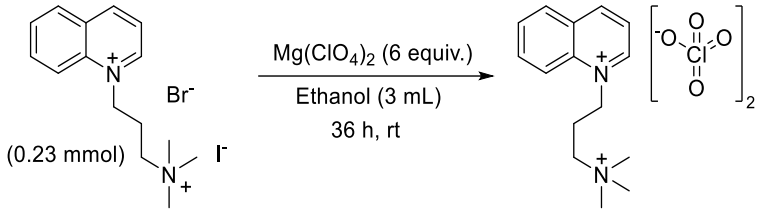

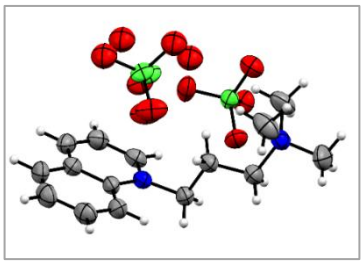

To a 50 mL sealed tube equipped with a stirring bar, 1-(3-(trimethyl-λ4-azaneyl)propyl)-1 λ4-quinolinium bromide iodide salt (100 mg, 0.23 mmol, 1.0 equiv.) and $Mg(ClO_4)_2$ (307 mg, 1.38 mmol, 6.0 equiv.) were suspended in ethanol (3 mL). The sealed tube containing the reaction mixture was capped, and the reaction mixture was stirred for 36 h at room temperature. A white precipitate was obtained after completion of the reaction, which was washed with ethanol several times and finally with diethyl ether. The resulting white precipitate was collected after drying under high vacuum to obtain the final product, 1-(3-(trimethyl-λ^4-azaneyl)propyl)-1 λ^4-quinolinium bis-perchlorate salt (67 mg, Yield: 69%).

^{1}H-NMR (400 MHz, DMSO-d_6) δ (ppm) 9.52 (dd, J_1 = 6.0, J_2 = 0.9 Hz, 1H), 9.35 (d, J = 8.3 Hz, 1H), 8.65 (d, J = 8.9 Hz, 1H), 8.53 (dd, J_1 = 8.3, J_2 = 0.9 Hz, 1H), 8.33 (ddd, J_1 = 9.1, J_2 = 7.0, J_3 = 1.2 Hz, 1H), 8.26 (dd, J_1 = 8.3, J_2 = 5.8 Hz, 1H), 8.09 (app. t, J = 7.6 Hz, 1H), 5.09 (t, J = 7.6 Hz, 2H), 3.60 – 3.47 (m, 2H), 3.07 (s, 9H), 2.49 – 2.40 (m, 2H);
^{13}C-NMR (101 MHz, DMSO-d_6) δ (ppm) 150.6, 148.4, 137.9, 136.4, 131.4, 130.5, 130.2, 122.7, 119.3, 62.6, 54.6, 53.0, 23.7;
HRMS (ESI+): calc. $[M+H]^+$ for $C_{15}H_{23}N_2^+$ 231.1861, found 231.1853, Δ = 0.8 mDa.

4.5.2.3 Synthesis of 2-(1λ⁴-quinolin-1-yl)ethane-1-sulfonate (PC3)

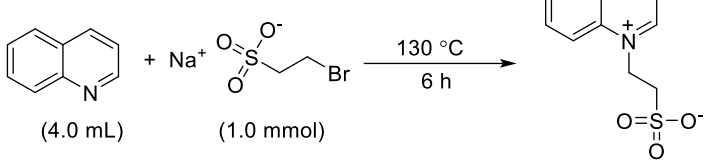

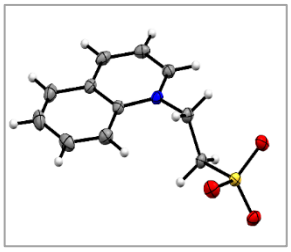

In a 20 mL sealed tube equipped with a stirring bar, 4 mL quinoline, sodium 2-bromo-ethanesulfonate (211 mg, 1.0 mmol, 1.0 equiv.) were mixed. The reaction mixture was heated to 130 ˚C and stirred for 6 hours. After completion of the reaction, the reaction mixture was cooled to room temperature. The reaction mixture of washed with diethyl ether for several times to remove excess quinoline. Solid pink powder was obtained after drying. The crude product was suspended in ethanol (5 mL) and filtered. A white undis-solved precipitate was removed, and the mother liquor was concentrated under reduced pressure. This process was repeated for another two times to get rid of unreacted sodium 2-bromoethanesulfonate and sodium bromide. Finally, the pink powder was obtained after solvent evaporation.

^{1}H-NMR (400 MHz, DMSO-d_6) δ (ppm) 9.48 (d, J = 5.6 fHz, 1H), 9.25 (d, J = 8.2 Hz, 1H), 8.55 (d, J = 8.9 Hz, 1H) 8.47 (d, J = 8.2 Hz, 1H), 8.27 (app. t., J = 7.7 Hz, 1H), 8.13 (dd, J = 8.9, 6.0 Hz, 1H), 8.04 (app. t., J = 7.7 Hz, 1H), 5.30 (t, J = 6.2 Hz, 2H), 3.15 (t, J = 6.2 Hz, 2H);

^{13}C-NMR (101 MHz, DMSO-d_6) δ (ppm) 151.7, 147.9, 137.6, 136.0, 131.2, 130.1, 129.9, 122.0, 119.2, 55.2, 49.6;

HRMS (ESI+): calc. $[M+H]^+$ for $C_{12}H_{12}NO_3S^+$ 238.0538, found 238.0536,
Δ = 0.2 mDa.

4.5.2.4 Synthesis of 1-(4-methylpentyl)-1λ⁴-quinolinium perchlorate salt (PC4)

1-(4-methylpentyl)-1 λ⁴-quinolinium bromide

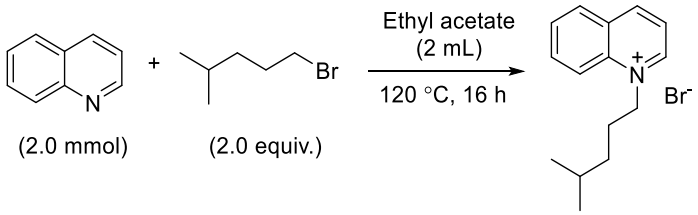

To a 20 mL sealed tube equipped with a stirring bar, quinoline (220 µL, 2.0 mmol, 1.0 equiv.) and 1-bromo-4-methylpentane (544 µL, 4.0 mmol, 2.0 equiv.) were dissolved in 2 mL of ethyl acetate. The resulting reaction mixture was stirred at 120˚C for 16 hours. After completion of the reaction, the solvent was evaporated under vacuum. The crude reaction mixture was dissolved in a minimum amount of ethanol and a precipitate was formed upon the addition of diethyl ether. The precipitate was filtered, washed with a minimum amount of acetone (~2 mL) and dried under vacuum to obtain the pure 1-(4-methylpentyl)-1 λ⁴-quinolinium bromide as purple coloured powder (480 mg, Yield: 82%).

^{1}H-NMR (400 MHz, DMSO-d_6) δ (ppm) 9.62 (dd, J = 5.8, 1.2 Hz, 1H), 9.32 (d, J = 8.3 Hz, 1H), 8.64 (d, J = 9.0 Hz, 1H), 8.51 (d, J = 8.1 Hz, 1H), 8.29 (ddd, J_1 = 8.9 Hz, J_2 = 7.1 Hz, J_3 = 1.3 Hz, 1H), 8.20 (dd, J = 8.3, 5.8 Hz, 1H), 8.06 (app. t, J = 7.6 Hz, 1H), 5.07 (t, J = 7.6 Hz, 2H), 2.02 – 1.91 (m, 2H), 1.56 (sept, J = 6.6 Hz, 1H), 1.36 – 1.23 (m, 2H), 0.85 (d, J = 6.6 Hz, 6H);

^{13}C-NMR (101 MHz, DMSO-d_6) δ (ppm) 150.1, 147.9, 137.9, 136.1, 131.2, 130.3, 130.2, 122.6, 119.4, 57.9, 35.1, 28.0, 27.7, 22.8;

HRMS (ESI+): calc. $[M+H]^+$ for $C_{15}H_{20}N^+$ 214.1596, found 214.1592, Δ = 0.4 mDa.

1-(4-methylpentyl)-1 λ^4-quinolinium perchlorate

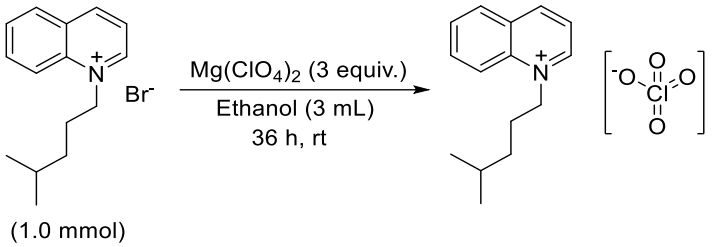

To a 50 mL sealed tube equipped with a stirring bar, 11-(4-methylpentyl)-1 λ^4-quinolinium bromide salt (294 mg, 1.0 mmol, 1.0 equiv.) and $Mg(ClO_4)_2$ (670 mg, 3.0 mmol, 3.0 equiv.) were suspended in ethanol (2 mL). The sealed tube containing the reaction mixture was capped, and the reaction mixture was stirred for 36 h at room temperature. A clear pale-yellow solution was obtained. The solution was concentrated by evaporating the solvent under vacuum, and then an off-white precipitate was obtained by adding diethyl ether. The resulting white precipitate was collected after drying under high vacuum to obtain the final product, 1-(4-methylpentyl)-1 λ^4-quinolinium perchlorate salt (140 mg, Yield: 20%).

^{1}H-NMR (400 MHz, DMSO-d_6) δ (ppm) 9.59 (dd, J_1 = 5.8 Hz, J_2 = 1.2 Hz, 1H), 9.30 (d, J = 8.3 Hz, 1H), 8.63 (d, J = 9.0 Hz, 1H), 8.50 (dd, J = 8.2, 1.1 Hz, 1H), 8.29 (ddd, J_1 = 8.8 Hz, J_2 = 7.0 Hz, J_3 = 1.4 Hz, 1H), 8.20 (dd, J = 8.4, 5.8 Hz, 1H), 8.06 (t, J = 7.5 Hz, 1H), 5.05 (t, J = 7.6 Hz, 2H), 2.05 – 1.89 (m, 2H), 1.57 (dp, J_1 = 13.2 Hz, J_2 = 6.6 Hz, 1H), 1.37 – 1.21 (m, 2H), 0.85 (d, J = 6.6 Hz, 6H);

^{13}C-NMR (101 MHz, DMSO-d_6) δ (ppm) 150.1, 147.9, 137.9, 136.2, 131.2, 130.4, 130.2, 122.6, 119.4, 57.9, 35.2, 28.0, 27.7, 22.8;

HRMS (ESI+): calc. $[M+H]^+$ for $C_{15}H_{20}N^+$ 214.1596, found 214.1590, Δ = 0.6 mDa.

4.5.3 Photocatalytic aryl oxidation nucleophilic coupling

4.5.3.1 GP1: Photocatalytic Aryl Oxidation – Nucleophilic Coupling

A 5 mL crimp capped vial was equipped with a magnetic stirring bar and pyrazole (28 mg, 0.4 mmol, 1.0 equiv.) and the quinolinium photocatalyst (5 mol%) were weighed in. The aryl partner (10 equiv.) was added, and all reactants were dissolved in a mixture of TFE/HFIP (2:1, 2 mL). The vial was then sealed, and the reaction was purged with oxygen for 2 min followed by addition of an oxygen balloon on top of the vial. The reaction was irradiated with 395 nm (3 W) LEDs for 12 h while the temperature was held at 25 ℃ by a water-cooling block.

After completion of the reaction, 1,3,5-trimethoxybenzene was added to the reaction mixture as internal standard. The reaction solvent was removed under reduced pressure, and the residue was re-dissolved into $CDCl_3$ and analysed by ^{1}H-NMR spectrum.

4.5.3.2 Optimization of the reaction

Table S4.1. Optimization of the model reaction.

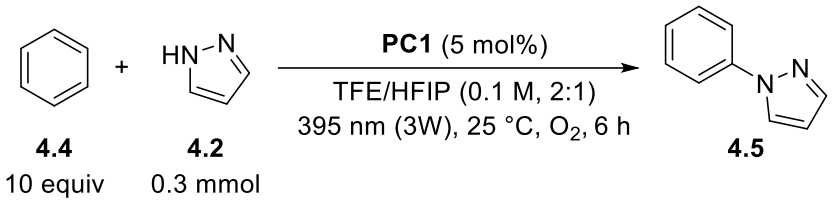

Entry	Modification to optimal	Yield (%)
1	None	45
2	Air instead of O_2	42
3	MeCN as solvent	9
4	TFE as solvent	39
5	TFE/HFIP (1:1) as solvent	*traces*
6	DMSO as solvent	n.d.
7	365 nm (3 W) LEDs	*traces*
8	395 nm (0.8 W) LEDs	*traces*

4.5.3.3 Isolation and characterization of products

Reaction with benzene

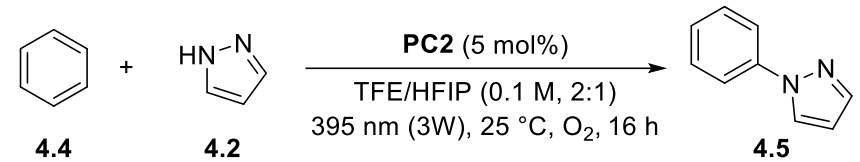

4.4 5 equiv + **4.2** 0.4 mmol → **4.5** *45%*

Pyrazole (27 mg, 0.4 mmol, 1.0 equiv.) and photocatalyst **2** (8.1 mg, 5 mol%) were weighed into a 5 mL crimp cap vial equipped with a stirring bar. The reactants were dissolved in a mixture of TFE/HFIP (2 mL, 2:1) and benzene (180 µL, 2.0 mmol, 5.0 equiv.) was added. The vial was sealed, and the reaction mixture was purged with an O_2 balloon for 1 min under stirring. The reaction was then irradiated with 395 nm (3W) LEDs at 25 °C for 16 hours while the oxygen-rich atmosphere was maintained with the O_2 balloon. After completion, solvents were removed under reduced pressure and the crude was purified with flash column chromatography (Acetone/PE, 5%). The removal of solvents gave the final product as clear oil (26 mg, 45%).

^{1}H-NMR (400 MHz, $CDCl_3$) δ (ppm) 7.93 (dd, J_1 = 2.5 Hz, J_2 = 0.4 Hz, 1H), 7.74 – 7.68 (m, 3H), 7.48 – 7.43 (m, 2H), 7.29 (tt, J_1 = 14.8 Hz, J_2 = 1.1 Hz, 1H), 6.47 (dd, J_1 = 2.5 Hz, J_2 = 1.9 Hz, 1H);

^{13}C-NMR (101 MHz, $CDCl_3$) δ (ppm) 141.1, 140.2, 129.4, 126.8, 126.5, 119.2, 107.6;

HRMS (APCI+): cal. M+H for $[C_9H_8N_2+H]^+$ 145.0766, found 145.0762, Δ = 0.4 mDa.

Reaction with toluene

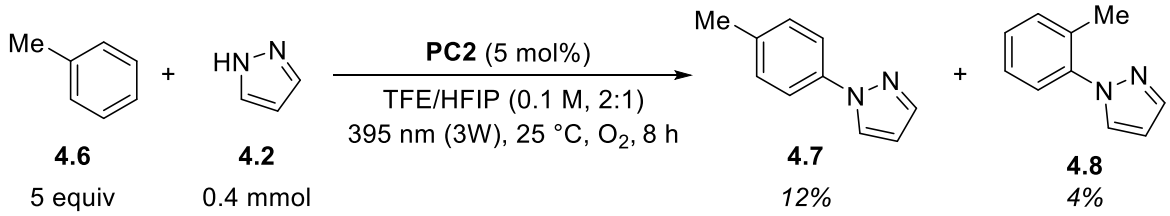

Pyrazole (27 mg, 0.4 mmol, 1.0 equiv.) and photocatalyst **2** (8.1 mg, 5 mol%) were weighed into a 5 mL crimp cap vial equipped with a stirring bar. The reactants were dissolved in a mixture of TFE/HFIP (2 mL, 2:1) and toluene (210 µL, 2.0 mmol, 5.0 equiv.) was added. The vials were sealed, and the reaction mixture was purged with an O_2 balloon for 1 min under stirring. The reaction was then irradiated with 395 nm (3W) LEDs at 25 °C for 6 hours while the oxygen-rich atmosphere was maintained with the O_2 balloon. After completion, three identical vials were combined, and solvents were removed under reduced pressure. The crude was purified with flash column chromatography (Acetone/PE, 5%), and removal of solvents gave the final product as clear oil (29 mg, 15%).

Characterization of 1-(*p*-tolyl)-1*H*-pyrazole

^{1}H-NMR (400 MHz, $CDCl_3$) δ (ppm) 7.90 (d, *J* = 2.3 Hz, 1H), 7.73 (d, *J* = 1.5 Hz, 1H), 7.61–7.57 (m, 2H), 7.26 (d, *J* = 8.8 Hz, 2H), 6.47–6.45 (m, 1H), 2.40 (s, 3H);

^{13}C-NMR (101 MHz, $CDCl_3$) δ (ppm) 140.9, 138.0, 136.2, 129.9, 126.7, 119.2, 107.3, 20.9;

HRMS (EI+): cal. $M^{\cdot+}$ for $[C_{10}H_{10}N_2]^{\cdot+}$ 158.0838, found 158.0838, Δ = 0.0 mDa.

Characterization of 1-(*o*-tolyl)-1*H*-pyrazole

^{1}H-NMR (400 MHz, $CDCl_3$) δ (ppm) 7.75 (d, *J* = 1.6 Hz, 1H), 7.62 (d, *J* = 2.2 Hz, 1H), 7.36–7.31 (m, 4H), 6.47–6.45 (m, 1H), 2.26 (s, 3H);

^{13}C-NMR (101 MHz, $CDCl_3$) δ (ppm) 140.2, 133.8, 133.7, 131.3, 130.5, 128.4, 126.5, 126.2, 106.2, 18.1;

HRMS (EI+): cal. $M^{\cdot+}$ for $[C_{10}H_{10}N_2]^{\cdot+}$ 158.0838, found 158.0838, Δ = 0.0 mDa.

Reaction with mesitylene

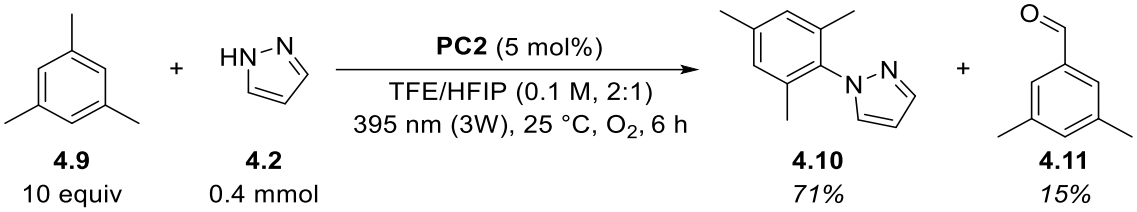

Pyrazole (27 mg, 0.4 mmol, 1.0 equiv.) and photocatalyst **2** (8.1 mg, 5 mol%) were weighed into a 5 mL crimp cap vial. The reactants were dissolved in a mixture of TFE/HFIP (2 mL, 2:1) and mesitylene (560 µL, 4.0 mmol, 10 equiv.) was added. The vial was sealed, and the reaction mixture was purged with an O_2 balloon for 1 min under stirring. The reaction was then irradiated with 395 nm (3W) LEDs at 25 °C for 16 hours while the oxygen-rich atmosphere was maintained with the O_2 balloon. After completion, solvents were removed under reduced pressure, and the crude was purified with flash column chromatography (Acetone/PE, 5%). The removal of solvents gave the product as a yellow oil (64 mg, 86%). Analysis of NMR data revealed that in addition to the expected product (71%), 3,5-dimethylbenzaldehyde was also obtained as a side product (15%).

Characterization of aryl pyrazole

^{1}H-NMR (400 MHz, $CDCl_3$) δ (ppm) 7.53 (dd, J_1 = 1.8 Hz, J_2 = 0.4 Hz, 1H), 7.26 (dd, J_1 = 2.3 Hz, J_2 = 0.4 Hz, 1H), 6.78 (d, J = 0.4 Hz, 2H), 6.27 (t, J = 2.0 Hz), 2.17 (s, 3H), 1.81 (s, 3H);

^{13}C-NMR (101 MHz, $CDCl_3$) δ (ppm) 139.9, 138.7, 136.9, 135.8, 130.8, 128.8, 127.6, 105.8, 21.1, 17.2;

HRMS (APCI+): cal. M+H for $[C_{12}H_{14}N_2+H]^+$ 187.1235, found 187.1235, Δ = 0.0 mDa.

Characterization of 3,5-dimethylbenzaldehyde

^{1}H-NMR (400 MHz, $CDCl_3$) δ (ppm) 9.77 (s, 1H), 7.32 (br. s., 2H), 7.10 (br. s., 1H), 2.23 (d, J = 0.5 Hz, 6H);

^{13}C-NMR (101 MHz, $CDCl_3$) δ (ppm) 192.7, 138.7, 136.9, 136.6, 127.6, 21.1;

HRMS (APCI+): cal. M+H for $[C_9H_{10}O+H]^+$ 135.0810, found 135.0803, Δ = 0.7 mDa.

Reaction with 1,4-difluorobenzene

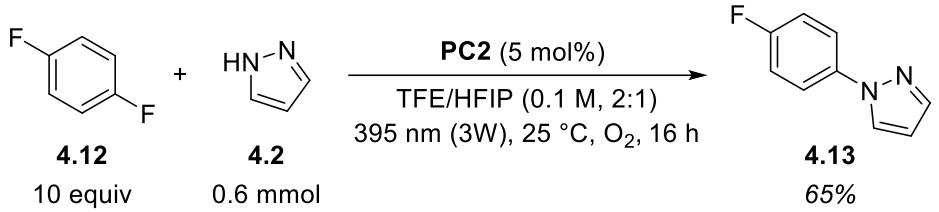

4.12 10 equiv | **4.2** 0.6 mmol | **4.13** *65%*

Pyrazole (13.5 mg, 0.2 mmol, 1.0 equiv.) and photocatalyst **2** (8.1 mg, 5 mol%) were weighed into a 5 mL crimp cap vial equipped with a stirring bar. The reactants were dissolved in a mixture of TFE/HFIP (1 mL, 2:1) and 1,4-difluorobenzene (190 µL, 2.0 mmol, 10 equiv.) was added. The vial was sealed, and the reaction mixture was purged with an O_2 balloon for 1 min under stirring. The reaction was then irradiated with 395 nm (3W) LEDs at 25 °C for 16 hours while the oxygen-rich atmosphere was maintained with the O_2 balloon. After completion, three identical vials were combined, and solvents were removed under reduced pressure. The crude was purified with flash column chromatography (Acetone/PE, 5%), and removal of solvents gave the final product as clear oil (63 mg, 65%).

^{1}H-NMR (400 MHz, $CDCl_3$) δ (ppm) 7.84 (dd, J_1 = 2.5 Hz, J_2 = 0.4 Hz, 1H), 7.70 (d, J = 1.5 Hz, 1H), 7.66 – 7.61 (m, 2H), 7.15 – 7.09 (m, 2H), 6.44 (dd, J_1 = 2.5 Hz, J_2 = 1.9 Hz, 1H);

^{13}C-NMR (101 MHz, $CDCl_3$) δ (ppm) 161.1 (J = 245 Hz), 141.1, 136.6 (d, J = 2.6 Hz), 126.9, 120.9 (d, J = 8.3 Hz), 116.1 (d, J = 22.9 Hz), 107.7;

^{19}F-NMR (376 MHz, $CDCl_3$) δ (ppm) −117.0 – (−)117.1 (m);

HRMS (APCI+): cal. M+H for $[C_9H_7FN_2+H]^+$ 163.0672, found 163.0668, Δ = 0.4 mDa.

4.5.3.4 Oxidation potentials of the aromatic substrates

Oxidation potentials of the aromatic substrates were determined by measuring cyclic voltammetry (CV) using $(n\text{-Bu})_4NPF_6$ as conducting salt in MeCN (Figure S4.4). The measurement was conducted starting into positive direction (red arrow). Ferrocene was used as internal reference, and the final potentials were reported against standard hydrogen electrode (SHE) using the ferrocene oxidation half-wave potential value of +0.380 V as a converting factor (Table S4.2).

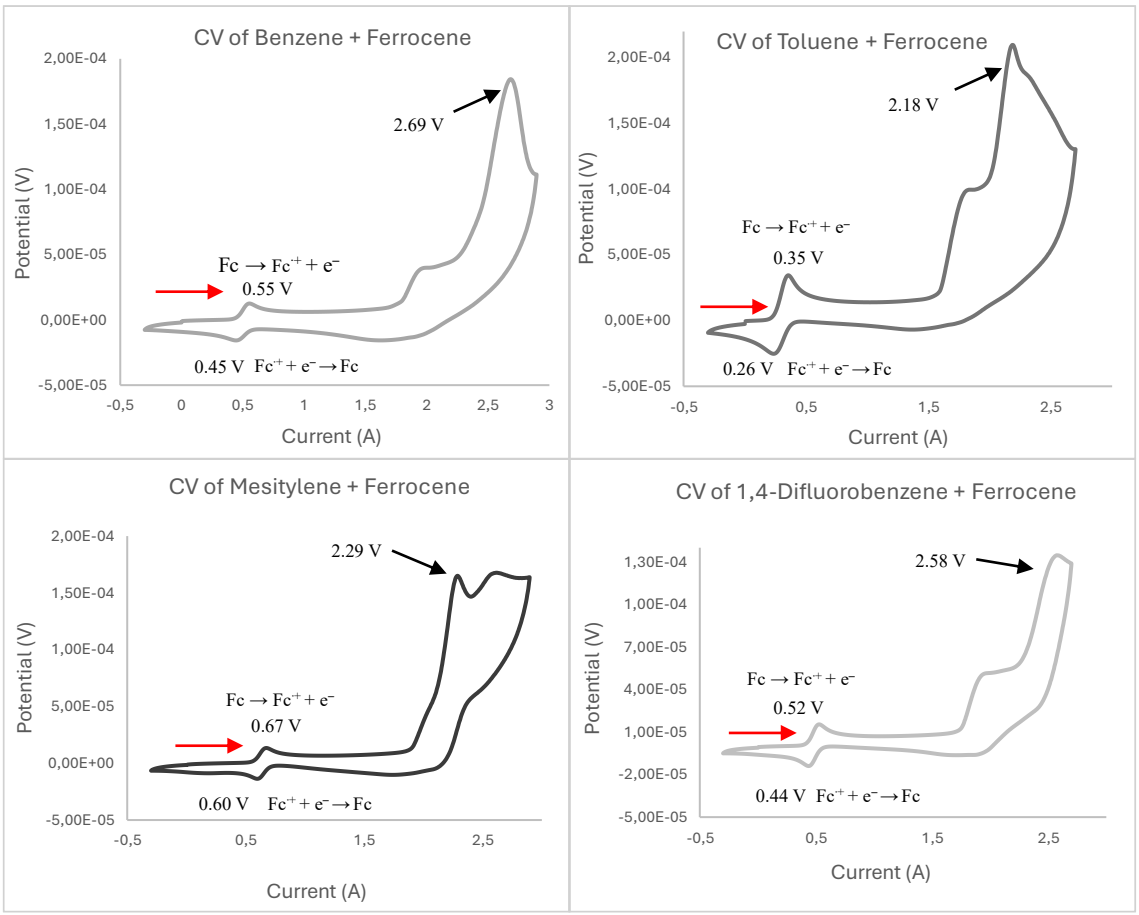

Figure S4.4. Cyclic voltammetry of used aryls with ferrocene as internal standard.

Table S4.2. Calculated oxidation potentials of aryls vs. SHE.

Aryl	E_{ox}(Aryl)	$E_{1/2}$(Fc/Fc$^+$)	$E_{1/2}$(Fc/Fc$^+$)	Correction	E_{ox}(Aryl)
Benzene	+2.69 V	+0.500 V	+0.38 V	– 0.120 V	+2.57 V
Toluene	+2.18 V	+0.305 V	+0.38 V	+ 0.075 V	+2.26 V
Mesitylene	+2.29 V	+0.635 V	+0.38 V	– 0.255 V	+2.04 V
1,4-DiFPh	+2.58 V	+0.480 V	+0.38 V	– 0.100 V	+2.48 V

4.5.4 Photophysical characterizations of the photocatalysts

4.5.4.1 UV-vis spectra

UV-vis absorption spectra of the photocatalysts were measured in MeCN (Figure S4.5). A quartz cuvette with a light pathlength of 10 mm was used for the measurements. The spectral window from 600 nm to 200 nm was set with a data interval of 1 nm (see more details in Section 1). The local absorption maxima are listed in Table S4.3.

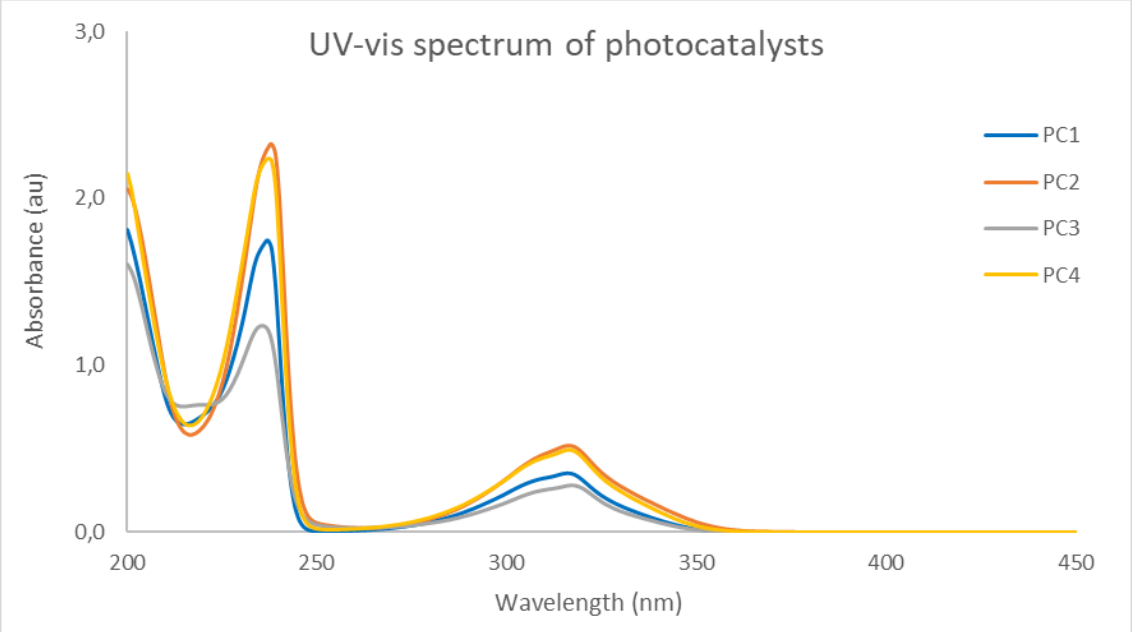

Figure S4.5. UV-vis absorption spectra of photocatalysts **PC1 – PC4**.

Table S4.3. Local UV-vis absorption maxima of photocatalysts.

Catalyst	$\lambda_{max,1}$ (nm)	$\lambda_{max,2}$ (nm)
PC1	237	316
PC2	238	316
PC3	236	317
PC4	237	316

4.5.4.2 Ground-state and excited-state reduction potentials

Cyclic voltammetry (CV) was applied to measure ground-state reduction potentials using (n-Bu)$_4$NPF$_6$ as conducting salt in MeCN. Sole catalysts were measured first starting into positive direction. Ferrocene was then added as internal standard (half-wave potential 0.380 eV vs SHE), and the specta were measured again this time starting into negative direction. The spectra with and without ferrocene were overlayed to see that no ground-state interactions took place, after which the gound-state redox potentials were calculated using the spectrum containing ferrocene.

The excited-state energy ($E_{0,0}$) was calculated from the intersection point of the UV-vis absorption spectrum and the photoluminescence spectrum according to Planck's equation (Eq. 1)

$$E_{0,0} = h \times c / \lambda \quad (1)$$

where h is Planck's constant ($h = 6.6261 \times 10^{-34}$ Js), c is the speed of light ($c = 299792458$ m/s) and λ is the wavelength of the intersection point of UV-vis absorption and photoluminescence spectrum.

The excited-state reduction potentials were then calculated from the excited-state energies obtained above and ground-state reduction potentials according to Eq. 2

$$*E^{red} = E^{red} + E_{0,0} \quad (2)$$

The so-obtained ground-state and excited-state potentials for each catalyst can be found below.

N-ethyl quinolinium perchlorate (PC1)

The ground-state reduction potential of the photocatalyst 1 was measured with cyclic voltammetry (Figure S4.6, left). The established redox-pair of ferrocene (+0.380 eV vs SHE) was used as internal standard against the measured ferrocene reduction halfwave (+0.740 eV) as follows:

E^{red} (**PC2**) = – 0.57 eV – (0.740 eV – 0.380 eV) = – 0.57 eV – 0.36 eV = – 0.93 eV

Excitation state reduction potential was then calculated according to Eq1 and Eq2. The wavelength of intersection point between the normalized UV-vis absorption and fluorescence emission was obtained from Figure S4.6 (right).

$$E_{0,0} = \frac{6.6261 \times 10^{-34}\ \text{CVs} \times 299792458\ \text{m/s}}{351 \times 10^{-9}\ \text{m}} = \frac{6.6261 \times 10^{-34}\ \text{eVs} \times 299792458\ \text{m/s}}{351 \times 10^{-9}\ \text{m} \times 1{,}602176634 \times 10^{-19}} = 3.53\ \text{eV}$$

$*E^{red}$ = – 0.93 eV + 3.53 eV = – 2.60 eV

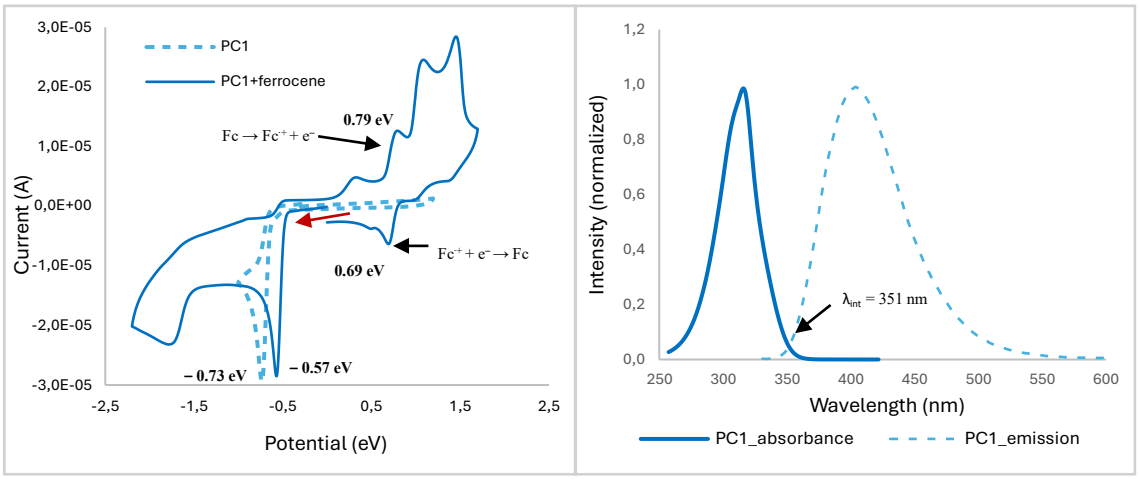

Figure S4.6. Cyclic voltammetry of **PC1** (left) and overlay of normalized UV-vis absorption and fluorescence emission spectra (right).

1-(3-(trimethyl-λ4-azaneyl)propyl)-1 λ 4-quinolinium bis-perchlorate (PC2)

The ground-state reduction potential of the photocatalyst 2 was measured with cyclic voltammetry (Figure S4.7, left). The established redox-pair of ferrocene (+0.380 eV vs SHE) was used as internal standard against the measured ferrocene reduction halfwave (+0.665 eV) as follows:

E^{red} (**PC2**) = – 0.55 eV – (0.665 eV – 0.380 eV) = – 0.55 eV – 0.285 eV = – 0.835 eV

Excitation state reduction potential was then calculated according to Eq1 and Eq2. The wavelength of intersection point between the normalized UV-vis absorption and fluorescence emission was obtained from Figure S4.7 (right).

$$E_{0,0} = \frac{6.6261 \times 10^{-34}\ \text{CVs} \times 299792458\ \text{m/s}}{355 \times 10^{-9}\ \text{m}} = \frac{6.6261 \times 10^{-34}\ \text{eVs} \times 299792458\ \text{m/s}}{355 \times 10^{-9}\ \text{m} \times 1{,}602176634 \times 10^{-19}} = 3.49\ \text{eV}$$

$^{*}E^{red}$ = – 0.84 eV + 3.49 eV = – 2.63 eV

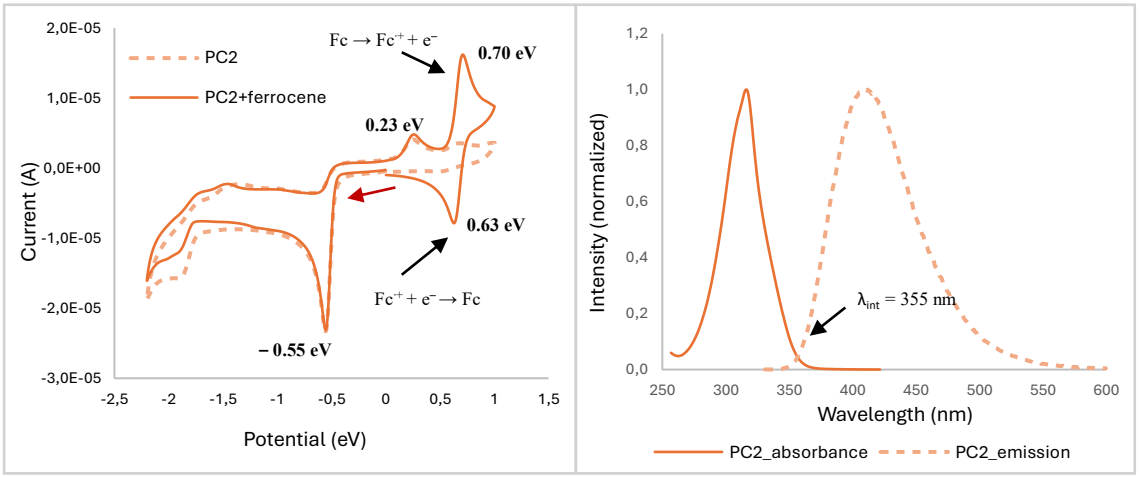

Figure S4.7. Cyclic voltammetry of **PC2** (left) and overlay of normalized UV-vis absorption and fluorescence emission spectra (right).

2-(1λ^4-quinolin-1-yl)ethane-1-sulfonate (PC3)

The ground-state reduction potential of the photocatalyst 3 was measured with cyclic voltammetry (Figure S4.8, left). The established redox-pair of ferrocene (+0.380 eV vs SHE) was used as internal standard against the measured ferrocene reduction halfwave (+0.740 eV) as follows:

E^{red} (**PC2**) = – 0.56 eV – (0.740 eV – 0.380 eV) = – 0.56 eV – 0.36 eV = – 0.92 eV

Excitation state reduction potential was then calculated according to Eq1 and Eq2. The wavelength of intersection point between the normalized UV-vis absorption and fluorescence emission was obtained from Figure S4.8 (right).

$$E_{0,0} = \frac{6.6261 \times 10^{-34}\ \text{CVs} \times 299792458\ \text{m/s}}{345 \times 10^{-9}\ \text{m}} = \frac{6.6261 \times 10^{-34}\ \text{eVs} \times 299792458\ \text{m/s}}{345 \times 10^{-9}\ \text{m} \times 1{,}602176634 \times 10^{-19}} = 3.59\ \text{eV}$$

*E^{red} = – 0.92 eV + 3.59 eV = – 2.66 eV

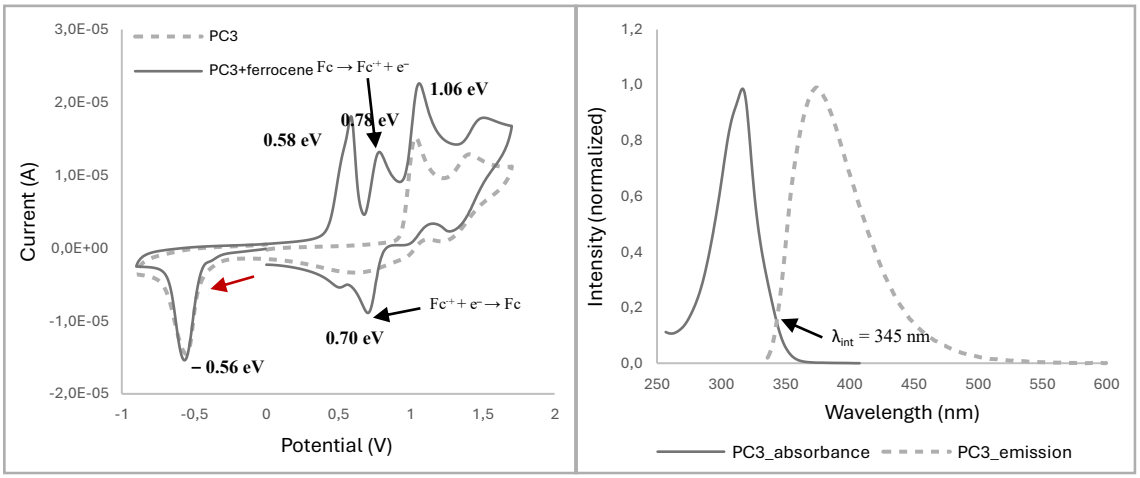

Figure S4.8. Cyclic voltammetry of **PC3** (left) and overlay of normalized UV-vis absorption and fluorescence emission spectra (right).

1-(4-methylpentyl)-1λ⁴-quinolinium perchlorate (PC4)

The ground-state reduction potential of the photocatalyst 4 was measured with cyclic voltammetry (Figure S4.9, left). The established redox-pair of ferrocene (+0.380 eV vs SHE) was used as internal standard against the measured ferrocene reduction halfwave (+0.550 eV) as follows:

E^{red} (**PC2**) = – 0.76 eV – (0.550 eV – 0.380 eV) = – 0.76 eV – 0.17 eV = – 0.93 eV

Excitation state reduction potential was then calculated according to Eq1 and Eq2. The wavelength of intersection point between the normalized UV-vis absorption and fluorescence emission was obtained from Figure S4.9 (right).

$$E_{0,0} = \frac{6.6261 \times 10^{-34}\ \text{CVs} \times 299792458\ \text{m/s}}{353 \times 10^{-9}\ \text{m}} = \frac{6.6261 \times 10^{-34}\ \text{eVs} \times 299792458\ \text{m/s}}{353 \times 10^{-9}\ \text{m} \times 1{,}602176634 \times 10^{-19}} = 3.51\ \text{eV}$$

*E^{red} = – 0.93 eV + 3.51 eV = – 2.58 eV

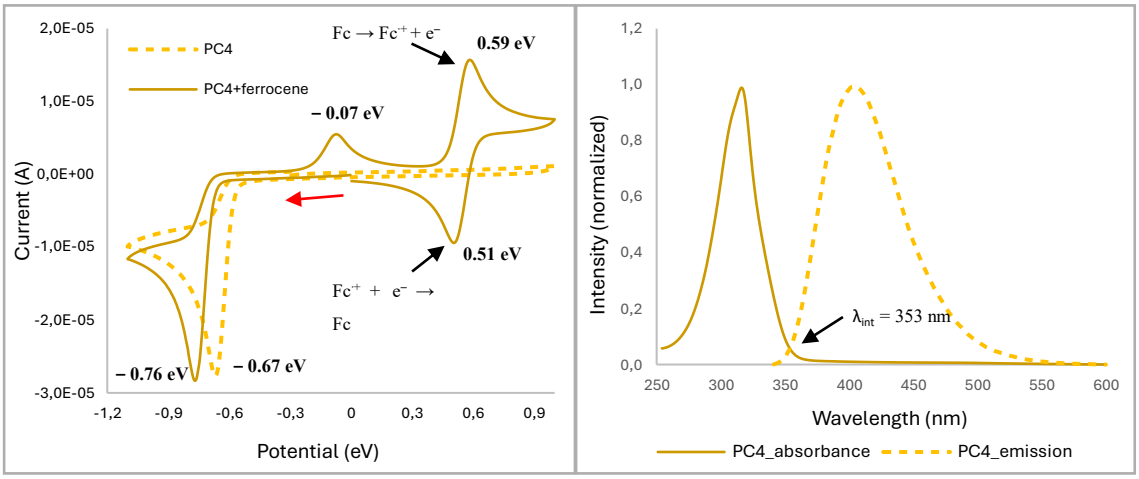

Figure S4.9. Cyclic voltammetry of **PC4** (left) and overlay of normalized UV-vis absorption and fluorescence emission spectra (right).

4.5.5 Fluorescence Quenching with Aryls

The fluorescence quenching measurements were carried out under N_2 atmosphere, and all the used solvents were carefully degassed by bubbling through N_2 for at least 1 h before use. A stock solution of the catalyst (c = 0.0125 M) was prepared in degassed MeCN under N_2, and 10 µL of this stock solution was diluted with 2 mL of MeCN. This mixture had the $\lambda_{max} \approx 0.1$ au on UV-vis spectrometer. The excitation wavelength was set at 340 nm (320 nm for **PC3**), slit 1 nm and emission was collected from 355 nm (335 nm for **PC3**) to 600 nm. A stock solution of the quencher (arene, 0.015 M, 5 µL or 10 µL) was added at a time and the emission spectrum was recorded. UV-vis spectroscopy was routinely measured in between of fluorescence quenching to exclude ground-state interactions.

The fluorescence spectra were then collected and Stern-Volmer constants calculated by plotting the ration of intensity (I_0/I) against quencher concentrations. The obtained Stern-Volmer constants are given in tables.

4.5.5.1 Fluorescence Quenching with Benzene

Results from the fluorescence quenching studies with benzene and Stern-Volmer plots are presented in Figure S4.10.

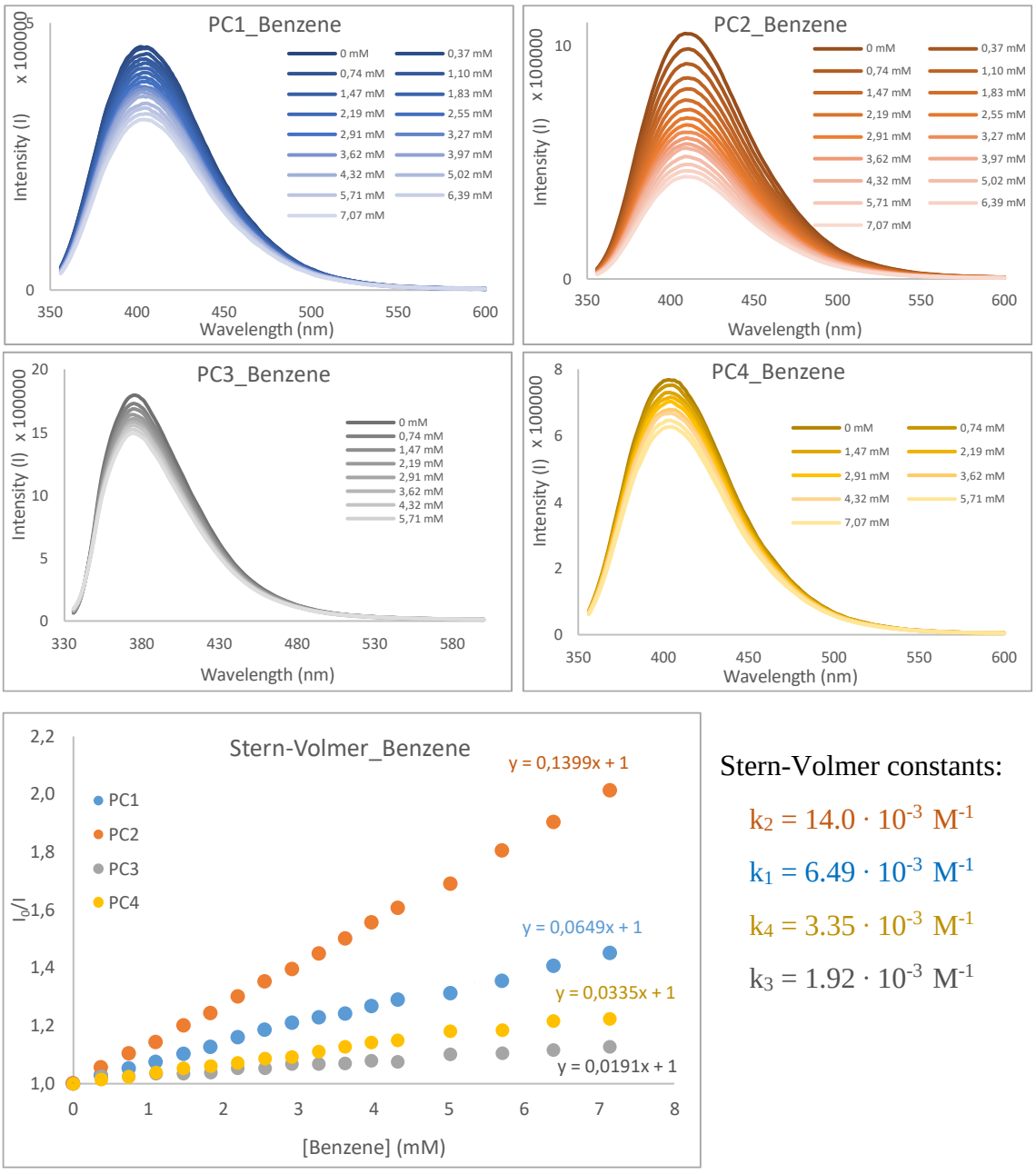

Stern-Volmer constants:

$k_2 = 14.0 \cdot 10^{-3}\ M^{-1}$

$k_1 = 6.49 \cdot 10^{-3}\ M^{-1}$

$k_4 = 3.35 \cdot 10^{-3}\ M^{-1}$

$k_3 = 1.92 \cdot 10^{-3}\ M^{-1}$

Figure S4.10. Fluorescence quenching of photocatalysts **PC1 – PC4** with benzene and respective Stern-Volmer quenching constants.

4.5.5.2 Fluorescence Quenching with 1,4-Difluorobenzene

Results from the fluorescence quenching studies with 1,4-difluorobenzene and Stern-Volmer plots are presented in Figure S4.11.

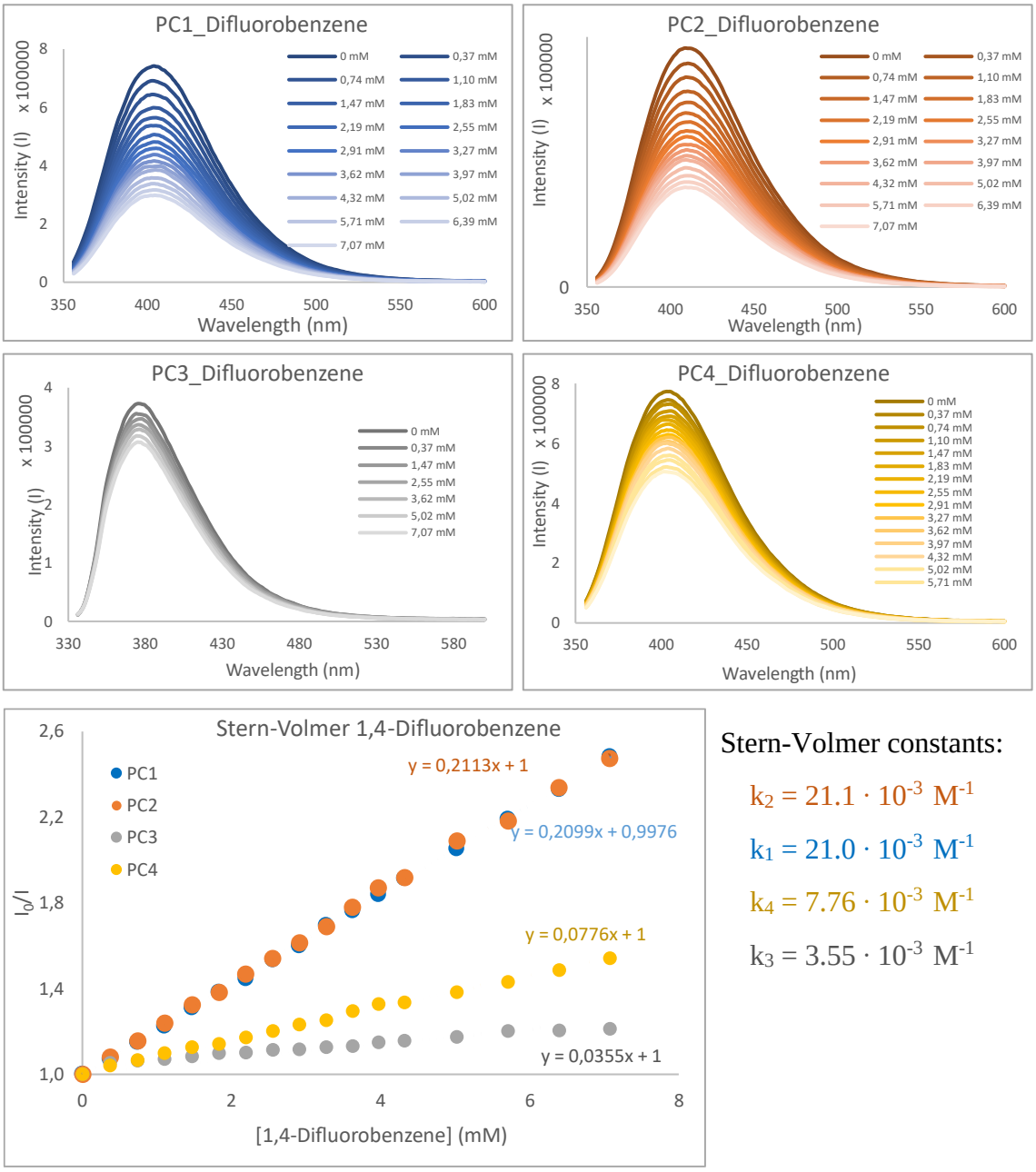

Stern-Volmer constants:

$k_2 = 21.1 \cdot 10^{-3}\ M^{-1}$

$k_1 = 21.0 \cdot 10^{-3}\ M^{-1}$

$k_4 = 7.76 \cdot 10^{-3}\ M^{-1}$

$k_3 = 3.55 \cdot 10^{-3}\ M^{-1}$

Figure S4.11. Fluorescence quenching of photocatalysts **PC1 – PC4** with 1,4-difluoro-benzene and respective Stern-Volmer quenching constants.

4.5.5.3 Fluorescence Quenching with Toluene

Results from the fluorescence quenching studies with toluene and Stern-Volmer plots are presented in Figure S4.12.

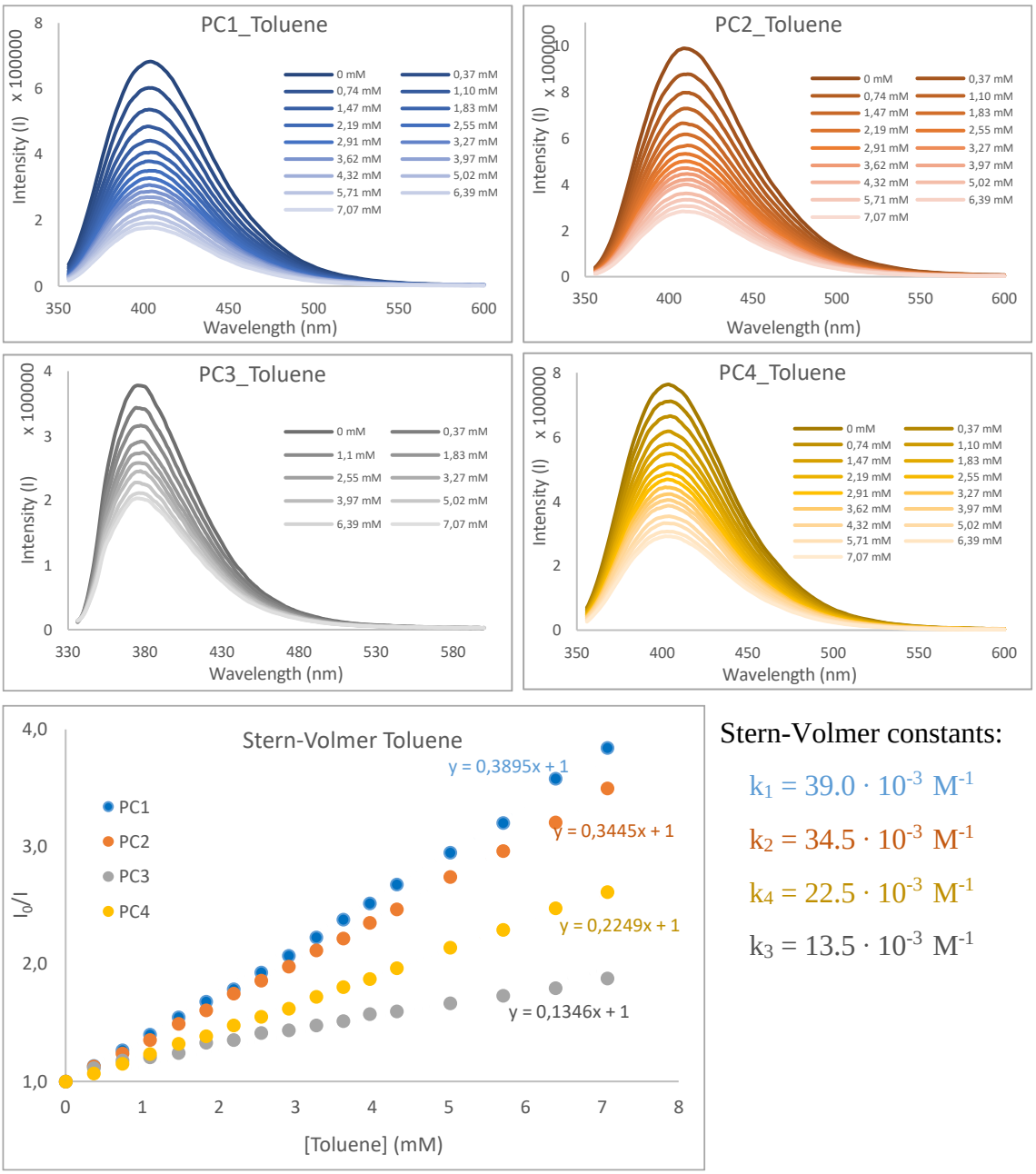

Figure S4.12. Fluorescence quenching of photocatalysts **PC1 – PC4** with toluene and respective Stern-Volmer quenching constants.

4.5.5.4 Fluorescence Quenching with Mesitylene

Results from the fluorescence quenching studies with mesitylene and Stern-Volmer plots are presented in Figure S4.13.

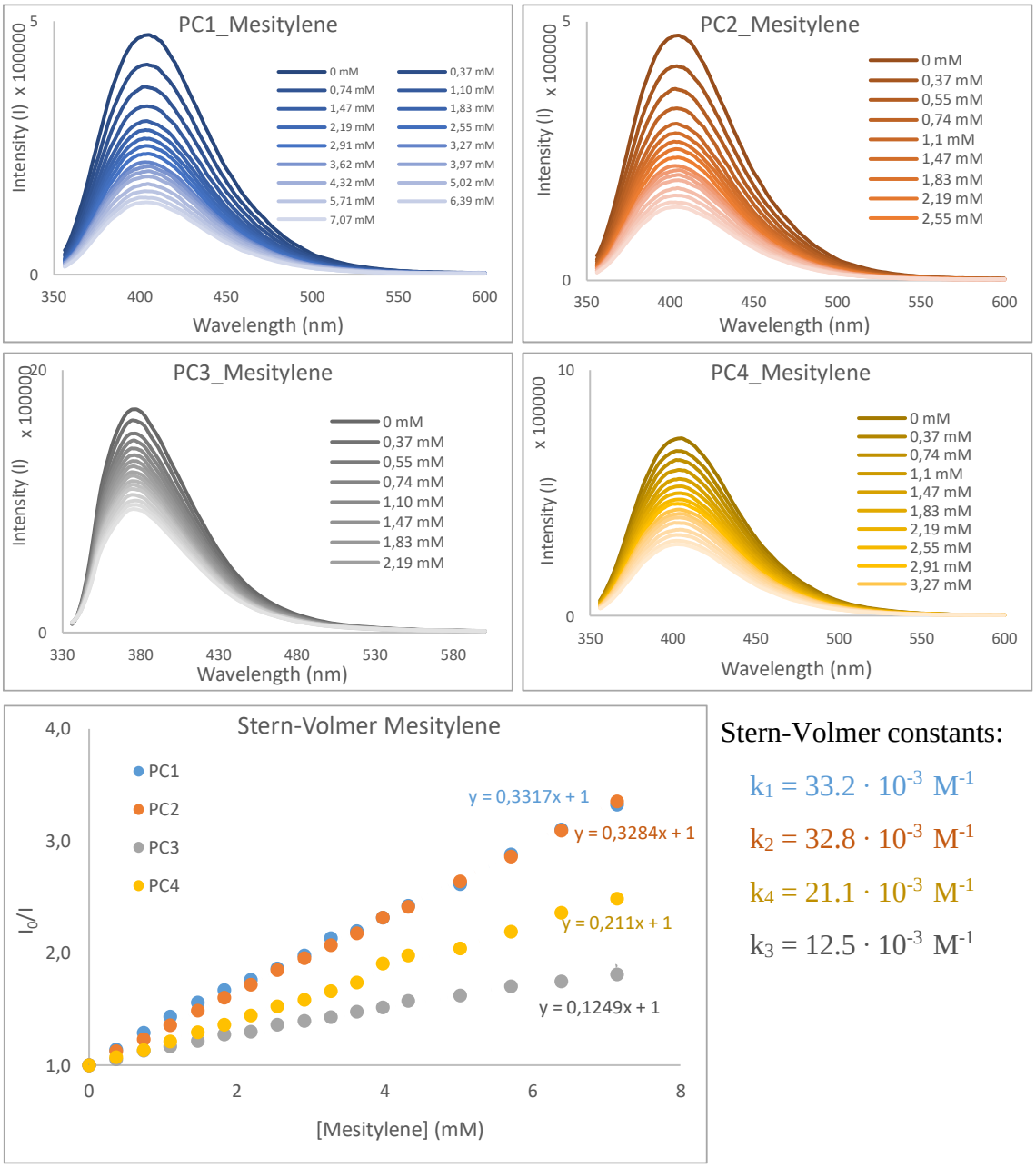

Stern-Volmer constants:

$k_1 = 33.2 \cdot 10^{-3}\ M^{-1}$

$k_2 = 32.8 \cdot 10^{-3}\ M^{-1}$

$k_4 = 21.1 \cdot 10^{-3}\ M^{-1}$

$k_3 = 12.5 \cdot 10^{-3}\ M^{-1}$

Figure S4.13. Fluorescence quenching of photocatalysts **PC1 – PC4** with mesitylene and respective Stern-Volmer quenching constants.

4.5.6 Reaction kinetics

For the measurement of reaction kinetics, one reaction was set up according to GP1. The kinetic of the reactions with different combinations of the aryl and photocatalysts were measured *ex-situ* by taking a sample every 5 minutes (benzene, 1,4-difluorobenzene and toluene) or every one minute (mesitylene) for given overall reaction times. Solvents were carefully evaporated under reduced pressure, after which the samples were dissolved in deuterated solvents and analyzed by ^{1}H-NMR. The yields were determined from the ratio of the unreacted pyrazole and the pyrazole aryl coupling product.

The initial assessments of the reaction kinetics were obtained by plotting the reaction yield against time (Figures S4.14 – S4.17). Furthermore, the rate constants for each reaction were calculated from the graphical representation of the reaction rates. Herein, reaction with mesitylene was best plotted according to first-order integrated rate law whereas benzene, toluene and 1,4-difluorobenzene were plotted according to second order integrated rate law (Equations 3 and 4).

first order: $$\ln[A] = -kt + \ln[A]_0 \quad (3)$$

second order: $$\frac{1}{[A]} = kt + \frac{1}{[A]_0} \quad (4)$$

Thus, the for the calculation of rate constants, the reciprocal of the pyrazole concentration was plotted against time resulting into a linear relationship. The rate constant was then obtained from the slope of the line and reported in M^{-1} s^{-1}.

4.5.6.1 Kinetic with benzene

Reaction kinetics with benzene as aromatic reaction partner plotted as yield against time (above) and according to second order rate law (below).

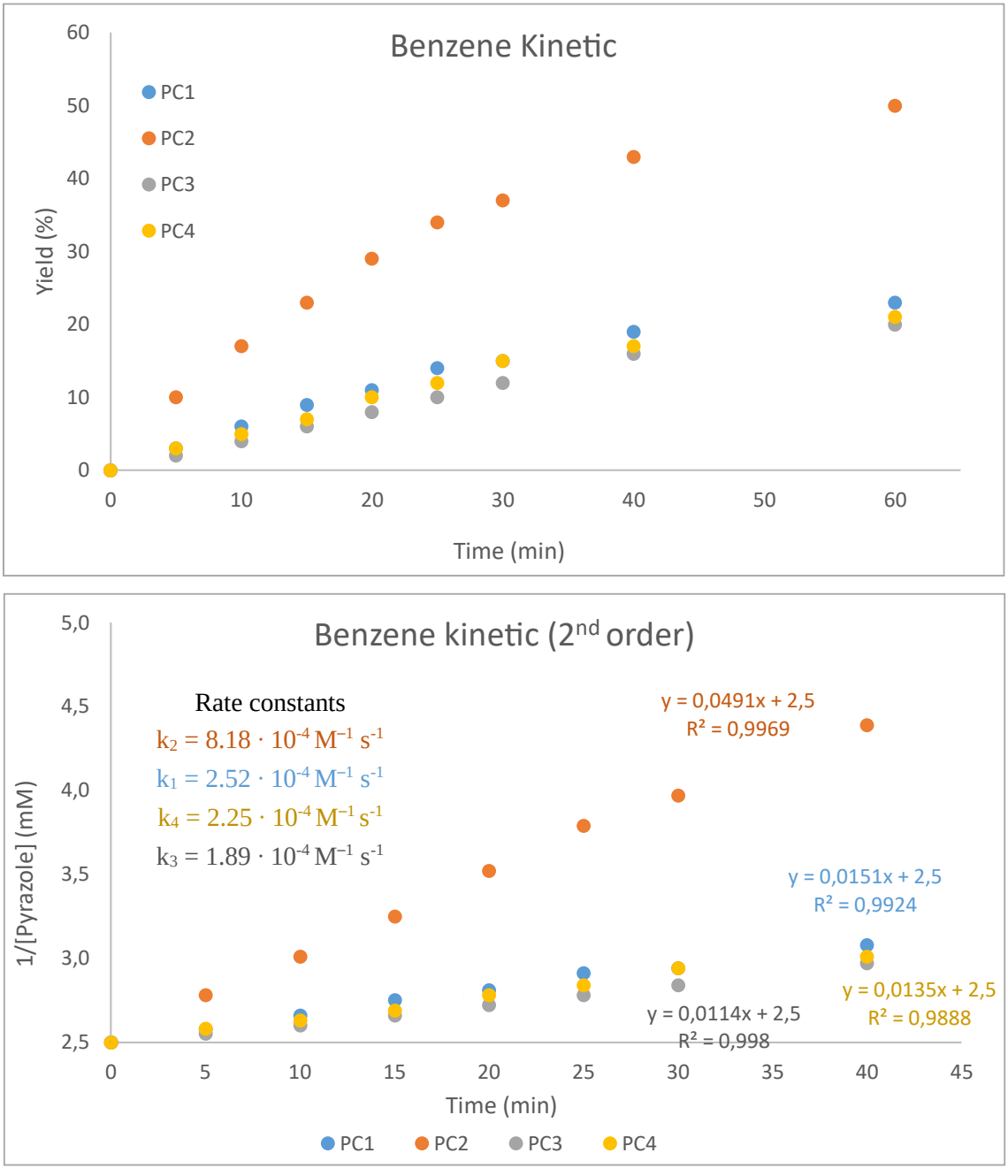

Figure S4.14. Reaction kinetic with benzene as aromatic reaction partner. Yield plotted against time (above) and the plot of reciprocal concentration of pyrazole against time (below).

4.5.6.2 Kinetic with 1,4-Difluorobenzene

Reaction kinetics with 1,4-difluorobenzene as aromatic reaction partner plotted as yield against time (above) and according to second order rate law (below).

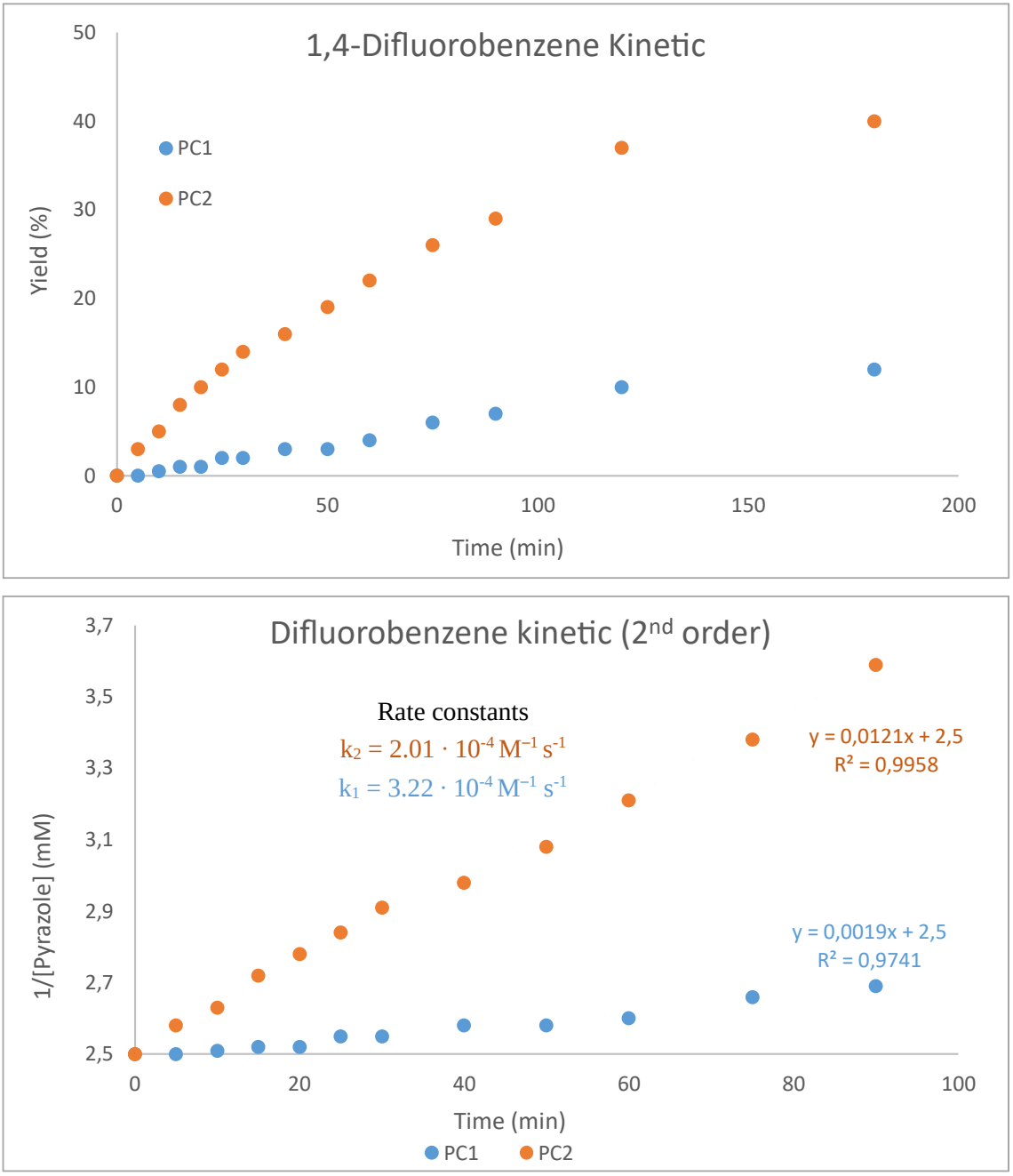

Figure S4.15. Reaction kinetic with 1,4-difluorobenzene as aromatic reaction partner. Yield plotted against time (above) and the plot of reciprocal concentration of pyrazole against time (below).

4.5.6.3 Kinetic with toluene

Reaction kinetics with toluene as aromatic reaction partner plotted as yield against time (above) and according to second order rate law (below).

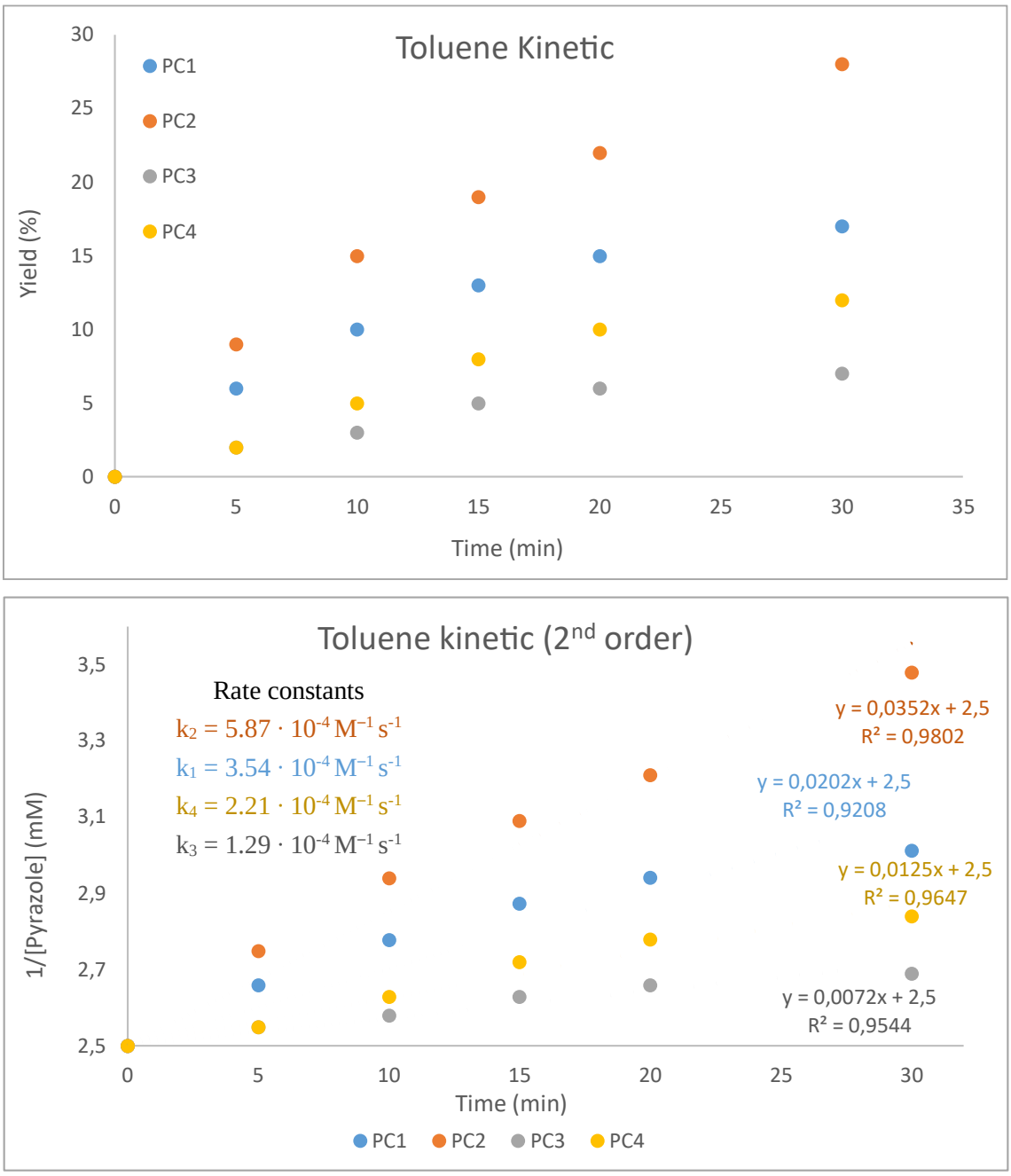

Figure S4.16. Reaction kinetic with toluene as aromatic reaction partner. Yield plotted against time (above) and the plot of reciprocal concentration of pyrazole against time (below).

4.5.6.4 Kinetic with mesitylene

Reaction kinetics with mesitylene as aromatic reaction partner plotted as yield against time (above) and according to first order rate law (below).

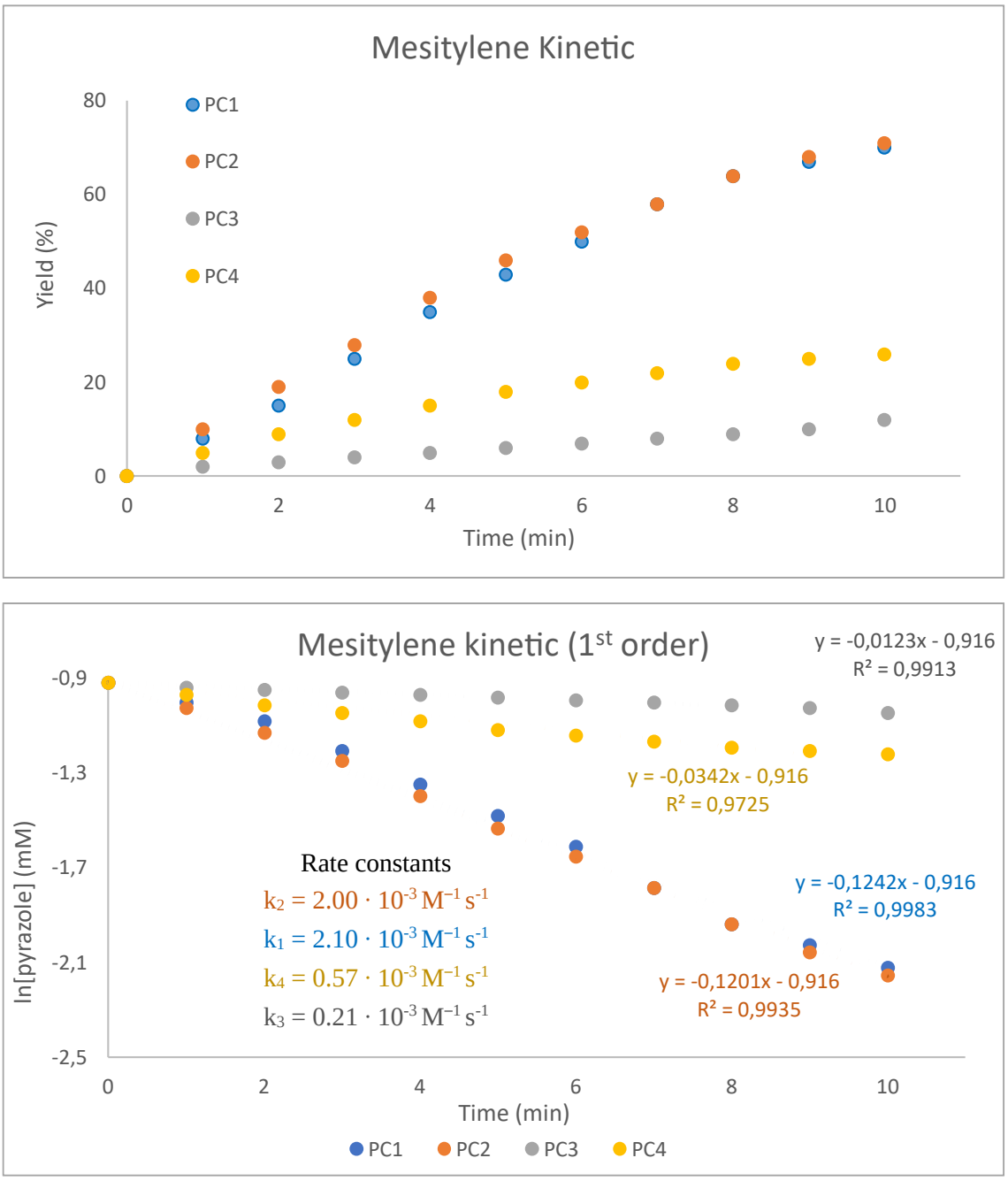

Figure S4.17. Reaction kinetic with mesitylene as aromatic reaction partner. Yield plotted against time (above) and the plot of logarithmic concentration of pyrazole against time (below).

4.6 References

(1) Schmalzbauer, M.; Svejstrup, T. D.; Fricke, F.; Brandt, P.; Johansson, M. J.; Bergonzini, G.; König, B. Redox-Neutral Photocatalytic C−H Carboxylation of Arenes and Styrenes with CO2. *Chem,* **2020**, *6* (10), 2658–2672.

(2) Müller, L.; Poll, J.; Nuernberger, P.; Ghosh, I.; König, B. Quinones as Multifunctional Scaffolds for Oxidative, Reductive, and HAT Photocatalysis. *Chem. Eur. J.* **2025**, *31* (20), e202404707.

(3) Albini, A.; Dichiarante, V. The 'Belle Époque' of Photochemistry. *Photochem. Photobiol. Sci.* **2009**, *8* (2), 248–254.

(4) Zhou, Q.-Q.; Zou, Y.-Q.; Lu, L.-Q.; Xiao, W.-J. Visible-Light-Induced Organic Photochemical Reactions through Energy-Transfer Pathways. *Angew. Chem. Int. Ed.* **2019**, *58* (6), 1586–1604.

(5) Shawn, M. H.; Twilton, J.; MacMillan, D. W. C. Photoredox Catalysis in Organic Chemistry, *J. Org. Chem.*, **2016**, *81*, (16), 6898–6926.

(6) Liao, L.-L.; Song, L.; Yan, S.-S.; Ye, J.-H.; Yu, D.-G. Highly Reductive Photocatalytic Systems in Organic Synthesis. *Trends Chem.* **2022**, *4* (6), 512–527.

(7) Bortolato, T.; Cuadros, S.; Simionato, G.; Dell'Amico, L. The Advent and Development of Organophotoredox Catalysis. *Chem. Commun.* **2022**, *58* (9), 1263–1283.

(8) M. Arias-Rotondo, D.; K. McCusker, J. The Photophysics of Photoredox Catalysis: A Roadmap for Catalyst Design. *Chem. Soc. Rev.* **2016**, *45* (21), 5803–5820.

(9) Grotjahn, S.; König, B. Common Ground and Divergence: OLED Emitters as Photocatalysts. *Chem. Commun.* **2024**, *60* (89), 12951–12963.

(10) Bhattacherjee, A.; Sneha, M.; Lewis-Borrell, L.; Amoruso, G.; Oliver, T. A. A.; Tyler, J.; Clark, I. P.; Orr-Ewing, A. J. Singlet and Triplet Contributions to the Excited-State Activities of Dihydrophenazine, Phenoxazine, and Phenothiazine Organocatalysts Used in Atom Transfer Radical Polymerization. *J. Am. Chem. Soc.* **2021**, *143* (9), 3613–3627.

(11) Medina, E.; Sandoval-Pauker, C.; Salvador, P.; Pinter, B. Mechanistic Insights into the Oxidative and Reductive Quenching Cycles of Transition Metal Photoredox Catalysts through Effective Oxidation State Analysis, *Inorg. Chem.*, **2022**, *61*, (47), 18923–18933.

(12) Sakakibara, Y.; Murakami, K. Switchable Divergent Synthesis Using Photocatalysis. *ACS Catal.* **2022**, *12* (3), 1857–1878.

(13) Shon, J.-H.; Kim, D.; D. Rathnayake, M.; Sittel, S.; Weaver, J.; S. Teets, T. Photoredox Catalysis on Unactivated Substrates with Strongly Reducing Iridium Photosensitizers. *Chem. Sci.* **2021**, *12* (11), 4069–4078.

(14) Fukuzumi, S.; Lee, Y.-M.; Nam, W. Photoredox Catalysis of Acridinium and Quinolinium Ion Derivatives. *Bull. Kor. Chem. Soc.* **2025**, *46* (1), 4–23.

(15) Konzal, J.; Murley, M.; Wolter, A.; Camou, L.; Oberbroeckling, A.; Dekker, M.; Wagner, G.; Jennejohn, K.; Peters, M.; Hayes, N.; Franklin, C.; Tobin, S.; Collier, E.; MacKenzie, I. Towards Designer Photocatalysts: Structure-Property Relationships in 2,6-Diaryl-Pyryliums. *Chem. Eur. J.* **2025**, *31* (5), e202403543.

(16) Wu, S.; Schiel, F.; Melchiorre, P. A General Light-Driven Organocatalytic Platform for the Activation of Inert Substrates. *Angew. Chem. Int. Ed.* **2023**, *135* (32), e202306364.

(17) Sau, S. C.; Schmitz, M.; Burdenski, C.; Baumert, M.; Antoni, P. W.; Kerzig, C.; Hansmann, M. M. Dicationic Acridinium/Carbene Hybrids as Strongly Oxidizing Photocatalysts. *J. Am. Chem. Soc.* **2024**, *146* (5), 3416–3426.

(18) Ghosh, I.; Ghosh, T.; Bardagi, J. I.; König, B. Reduction of Aryl Halides by Consecutive Visible Light-Induced Electron Transfer Processes. *Science*, **2014**, *346* (6210), 725–728.

(19) Majek, M.; Filace, F.; Wangelin, A. J. von. On the Mechanism of Photocatalytic Reactions with Eosin Y. *Beilstein J. Org. Chem.* **2014**, *10* (1), 981–989.

(20) Hill, N. S.; Coote, M. L. Internal Oriented Electric Fields as a Strategy for Selectively Modifying Photochemical Reactivity. *J. Am. Chem. Soc.* **2018**, *140* (50), 17800–17804.

(21) Schmalzbauer, M.; Marcon, M.; König, B. Excited State Anions in Organic Transformations. *Angew. Chem. Int. Ed.* **2021**, *60* (12), 6270–6292.

(22) Schirmer, T. E.; König, B. Ion-Pairing Catalysis in Stereoselective, Light-Induced Transformations. *J. Am. Chem. Soc.* **2022**, *144* (42), 19207–19218.

(23) Das, S.; Zhu, C.; Demirbas, D.; Bill, E.; De, C. K.; List, B. Asymmetric Counteranion-Directed Photoredox Catalysis. *Science*, **2023**, *379* (6631), 494–499.

(24) Yu, S.; Vermeeren, P.; Hamlin, T. A.; Bickelhaupt, F. M. How Oriented External Electric Fields Modulate Reactivity. *Chem. Eur. J.* **2021**, *27* (18), 5683–5693.

(25) T. Blyth, M.; L. Coote, M. Manipulation of N-Heterocyclic Carbene Reactivity with Practical Oriented Electric Fields. *Phys. Chem. Chem. Phys.* **2023**, *25* (1), 375–383.

(26) G. Nugmanova, A.; R. Sokolov, M.; E. Alexandrov, A.; A. Kniazeva, M.; Yu. Eremchev, I.; V. Naumov, A.; W. Boukhvalov, D.; König, B.; A. Kalinina, M. Electric Field-Induced Amplification of Graphene Oxide's Visible Light Photocatalytic Activity. *J. Mater. Chem. A*, **2025**, *13* (1), 200–204.

(27) Sun, X.; Zhang, B.; Li, X.; Trindle, C. O.; Zhang, G. External Heavy-Atom Effect via Orbital Interactions Revealed by Single-Crystal X-Ray Diffraction. *J. Phys. Chem. A*, **2016**, *120* (29), 5791–5797.

(28) Zhong, C.-M.; Zuo, Y.-J.; Jin, H.-S.; Liu, S.-Q.; Wang, T.-C. 1-Butyl-quinolinium Iodide. *Acta Cryst. E*, **2006**, *62* (11), 5050–5051.

CHAPTER 5

5 Harnessing Photochemistry in Natural Product Synthesis: From Strategy to Applications

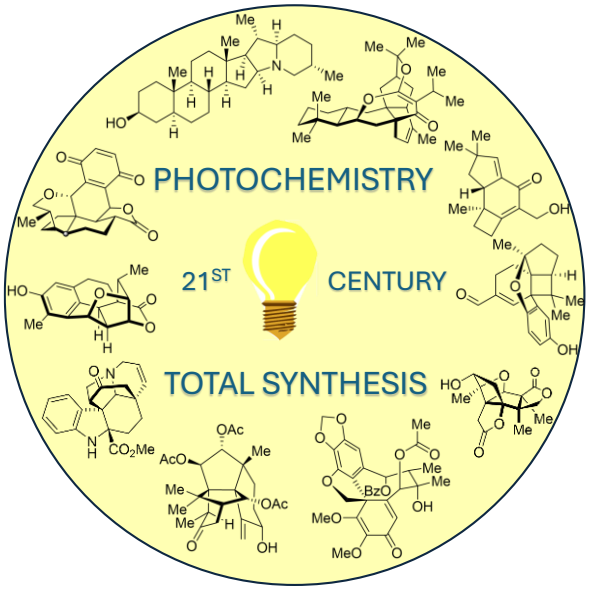

Abstract: Photochemistry and total synthesis have long roots in organic chemistry, both evolving on their own yet also crossing paths frequently. Indeed, the mild reaction conditions, versatility of transformations, and complementary selectivities to thermal methods make photochemistry a valuable tool for the synthesis of complex target molecules. In this perspective, we aim to highlight some of the total syntheses in the 21st century featuring photochemical reactions as pivotal steps. We wish that our strategic considerations help further identify cases where photochemical reactions could prove useful, and thus further encourage their use in total syntheses.

Modified version of this chapter has been published. For reference, see:
E. K. Taskinen and B. König*, Harnessing Photochemistry in Natural Product Synthesis: From Strategy to Applications. (*Manuscript submitted)*

Author contributions: E.K.T. formed the concept of the review, searched the references, draw the graphical elements and wrote the manuscript. B.K. supervised the work.

5.1 Motivation

"Modern photocatalysis enabled our work and allowed us to observe relatively slow cyclizations with remarkably high yields and selectivity"

–Lumb *et al.*, 2021–

Especially during its renaissance era, photocatalysis has gained increasing attraction among synthetic chemists. Having focused heavily on natural product total synthesis during my Masters, the advantages offered by photochemistry were easy to recognize: the mild reaction conditions, high functional group tolerance and access to complementary reactivities to that of many thermal methods do make photochemistry extremely well suitable for the synthesis of complex natural products. However, one of the factors possibly slowing down the wider-spread use of these methods in natural product synthesis might be the noticeable gap between the substrates showcased in method development papers and the substrates present in the midway of total synthesis campaigns. Despite this leap, I have been extremely delighted to see the application of various photochemical and photocatalytic reactions towards highly complex target molecules in the recent years. What's more, for many groups these recent synthetic efforts have served as an entry point to the field of photocatalysis, demonstrating that light-driven transformations are nowadays within the reach of virtually all chemists. Hence, I wanted to conclude my thesis by what I truly believe is the outlook: photochemical methods providing solutions to complex synthetic challenges and empowering the research of all fields. I wanted to particularly highlight the most recent examples (mostly around/from 2020 onwards) of syntheses including photocatalytic step(s) to further draw attention to the potential held by photochemistry. Before each example, general aspects of the reactions in question are discussed, combined with what I hope to be useful references for those interested in applying such methods in their work in the future.

5.2 Introduction

It is safe to say that no other field has shaped chemistry as much as total synthesis of natural products. For decades, tireless synthetic endeavours towards naturally occurring structures have completely reshaped the ways chemists approach their synthetic targets[1], ignited the development of numerous novel transformations, and provided access to several drug candidates[2] (Figure 5.1). Since the first synthesis of a naturally occurring molecule , the conversion of ammonium cyanate into urea in 1828[3], natural product synthesis has flourished and brought about many Nobel-prize worthy discoveries.[4,5] The beginning of the 20th century witnessed a significant leap as α-terpineol (Perkin, 1904)[6], camphor

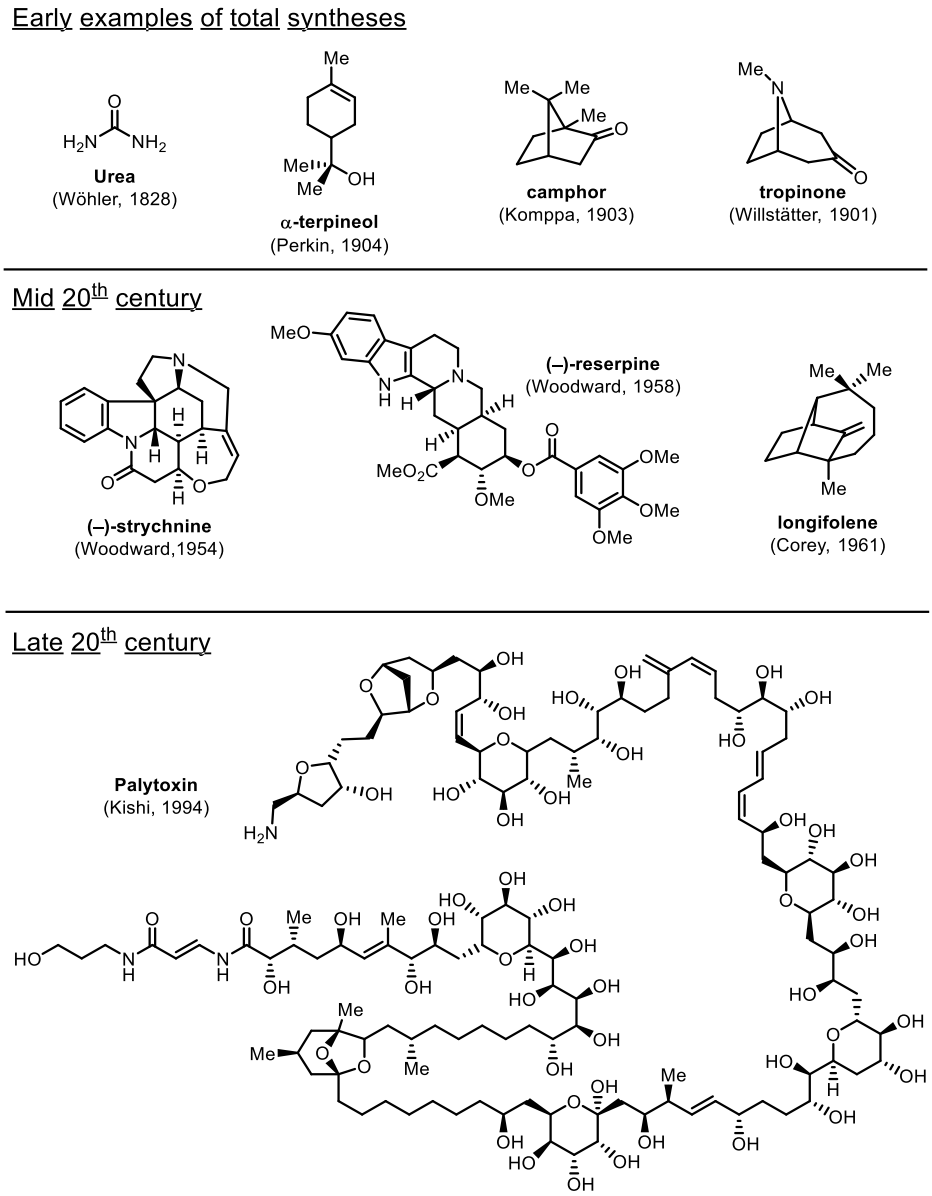

Figure 5.1. Landmarks in natural product total synthesis.

(Komppa, 1903)[7] and tropinone (Willstätter, 1901 and Robinson, 1917)[8] were all successfully prepared in the laboratory, marking the advent for precise modification of aliphatic compounds. Moving towards the 1950s, advancements in structural analysis encouraged synthetic chemists to pursue more and more complex targets. Some of the most famous accomplishments from this era include the total syntheses of (–)-strychnine and (–)-reserpine (Woodward, 1954 and 1958)[9,10] as well as the synthesis of longifolene (Corey, 1961)[11]. Eventually, the quest towards ever more complicated natural products culminated in the Kishi's breathtaking synthesis of palytoxin in 1994.[12,13]

Since the turn of the century, the goals of total synthesis have shifted once again.[14] Instead of racing towards the most complex (and synthetically demanding) targets possible, efficient and concise syntheses, sometimes as short as a few steps, have become more desirable.[15–17] To achieve the complexity of natural products in such short sequences, convergent synthetic strategies have often been employed in combination with state-of-the-art methods for fragment coupling.[18] Interestingly, in recent years, divergent syntheses have in turn gained more attention, resulting in syntheses of entire families of natural products *via* a selective late-stage modification of a common precursor.[19,20]

Photochemistry, the field focusing on light-driven transformations, also possesses a long and impressive history on its own. Importantly, though, photochemistry has also played a vital part in enabling total syntheses for decades, as, for example, the final deprotection of the palytoxin carboxylate into the natural product was only possible by photochemical means.[13] Taking into consideration the mild reaction conditions and high functional group tolerance of photochemical methods, it becomes clear why this contemporary synthetic field would be so well suited for making natural products. As compared with thermal methods, photochemistry often offers a complementary selectivity for substrate activation. Hence, functional groups such as alkenes, carboxylic acids, hydroxy anions, and nitrogen-centred anions can be activated by one-electron oxidations, thus creating electron-deficient radicals or radical cations as reactive intermediates (Figure 5.2, upper part). In contrast, one-electron reductions of functionalities like aryl (pseudo)halides, benzyl halides, alkyl iodides, α-halocarbonyls, and conjugated alkenes result in an electron-rich open-shell species (Figure 5.2, middle). Additionally, hydrogen atom abstraction (HAT) provides a facile way towards C–H activation on the hydridic positions (Figure 5.2, lower part). In this last case, acidic protons are also marked for comparison.

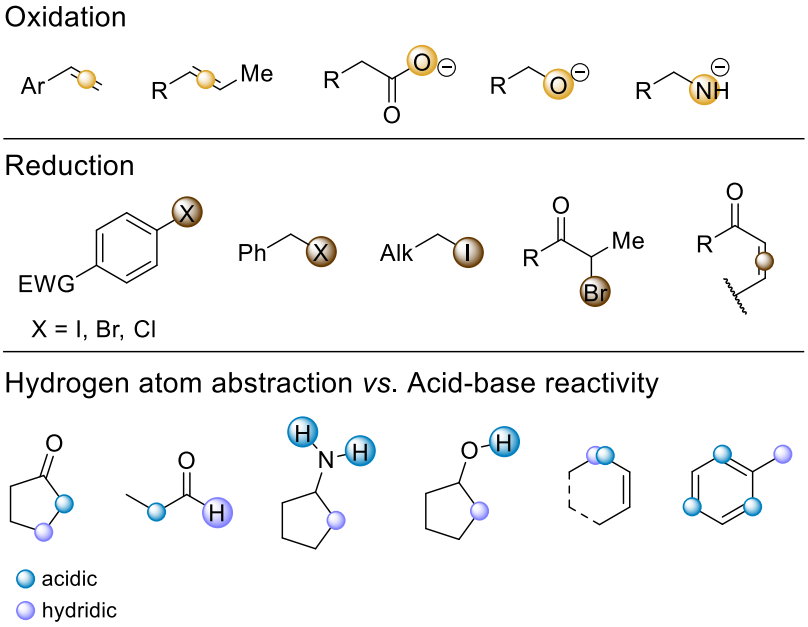

Figure 5.2. Photochemical activation of certain functional groups.

Mechanistic and photophysical principles of photochemistry are summarized in Figure 5.3. In general, photoredox catalysis can take place either *via* direct excitation of the substrate or *via* intermediacy of a photocatalyst (Figure 5.3, upper left part). In direct excitation methods the substrate acts as a light-harvesting species, and absorption of the light irradiation promotes one electron from the highest occupied molecular orbital (HOMO) to the lowest unoccupied molecular orbital (LUMO), creating a reactive singly occupied molecular orbital (SOMO). Notably, the irradiation wavelength absorbed corresponds to the energy difference of the HOMO–LUMO gap. This electronic arrangement swiftly results in productive radical reactions or back-relaxation of the excited electron. In photocatalytic methods, however, the light irradiation is initially absorbed by the photocatalyst, in which one electron is again promoted to a higher energy orbital. This generates a singlet excited state, which can be converted to a slightly longer-lived triplet excited state *via* intersystem crossing (ISC). The excited-state catalyst, whether on its singlet or triplet state, is typically a better oxidant and a better reductant than the ground-state catalyst, and a photoinduced electron transfer (PET) takes place upon engaging with a substrate. For these reactions, the reduction potential of the catalyst is the measure of how easily the catalyst gets reduced (while oxidizing the substrate), and the oxidation potential corresponds to one-electron oxidation of the catalyst (while the substrate is reduced). For closing the catalytic cycle, a complementary single-electron transfer (SET) from a reaction intermediate or terminal oxidant/reductant is needed. For clarity, the structures of the

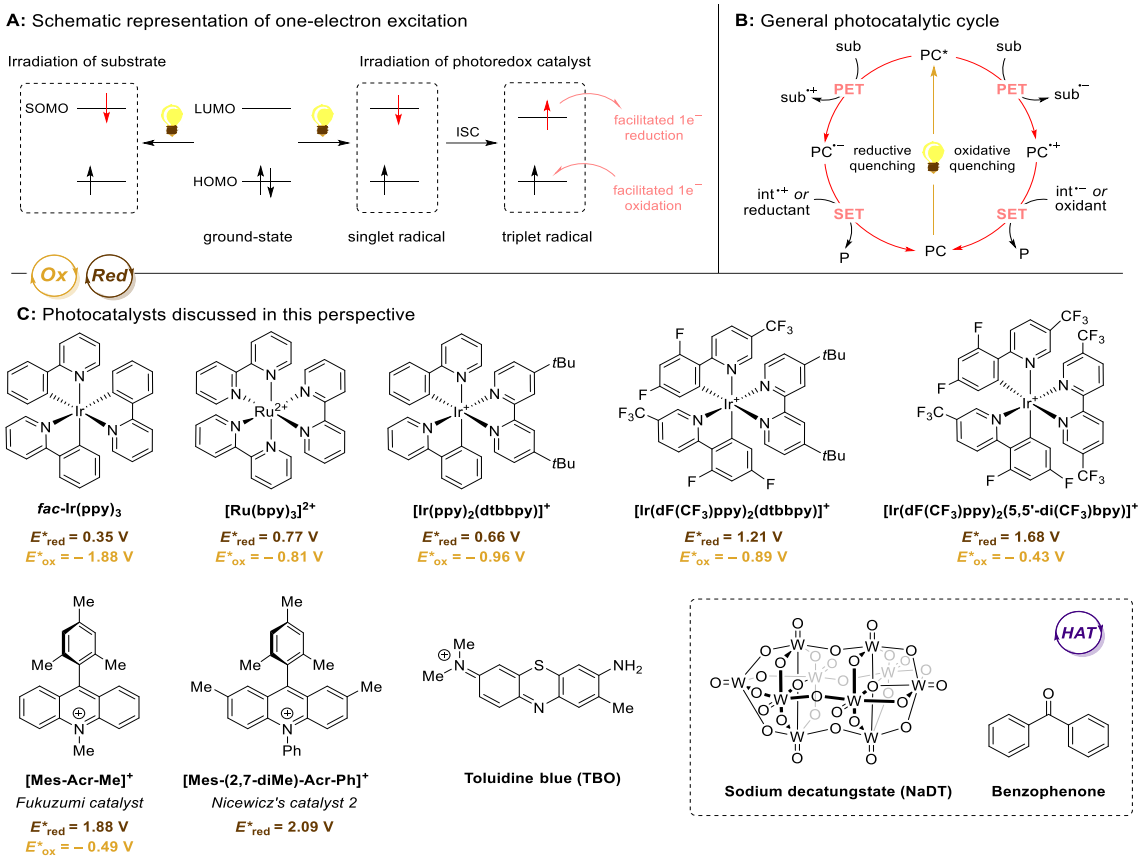

Figure 5.3. Photophysical principles of photoredox catalysis (a and b) and catalysts discussed in this perspective (c).

photocatalysts discussed in this article are shown in Figure 5.3; they will be later referred to with their names and/or acronyms. Our goal in this article is to discuss general concepts with some representative examples. More comprehensive reviews on the use of photochemistry in natural product synthesis can be found elsewhere.[21–26]

5.3 Synthetic Applications

5.3.1 [2+2]-cycloaddition

[2+2]-cycloaddition, conversion of two alkenes into a cyclobutene moiety, is one of the classical examples of a photochemical reaction (Scheme 5.1, upper part). From a synthetic perspective, the reaction holds great importance as it offers a mild and facile way to generate highly strained cyclobutane products. With its long-standing history, the [2+2]-cycloaddition, together with the similar Paternò–Büchi and de Mayo reactions, has found use in many total syntheses.[27–31] Today, the [2+2]-cycloaddition is frequently used in the synthesis of cyclobutane-containing target molecules and of compounds, in which the carbon backbone can be constructed *via* a subsequent fragmentation/rearrangement of the cyclobutane ring. While the earliest examples of this reaction were realized by direct irradiation, energy-transfer (EnT) driven processes have also been developed as a part of advancements made with photoredox catalysts.[32] Further developments include selective activation of Lewis-acid bound substrates and control over relative and absolute stereochemistries.[33–37] The generally accepted mechanism of the [2+2] cycloaddition commences with the photoexcitation of one of the alkenes (either by direct irradiation or energy transfer photocatalysis), forming a biradical which then attacks the other alkene.

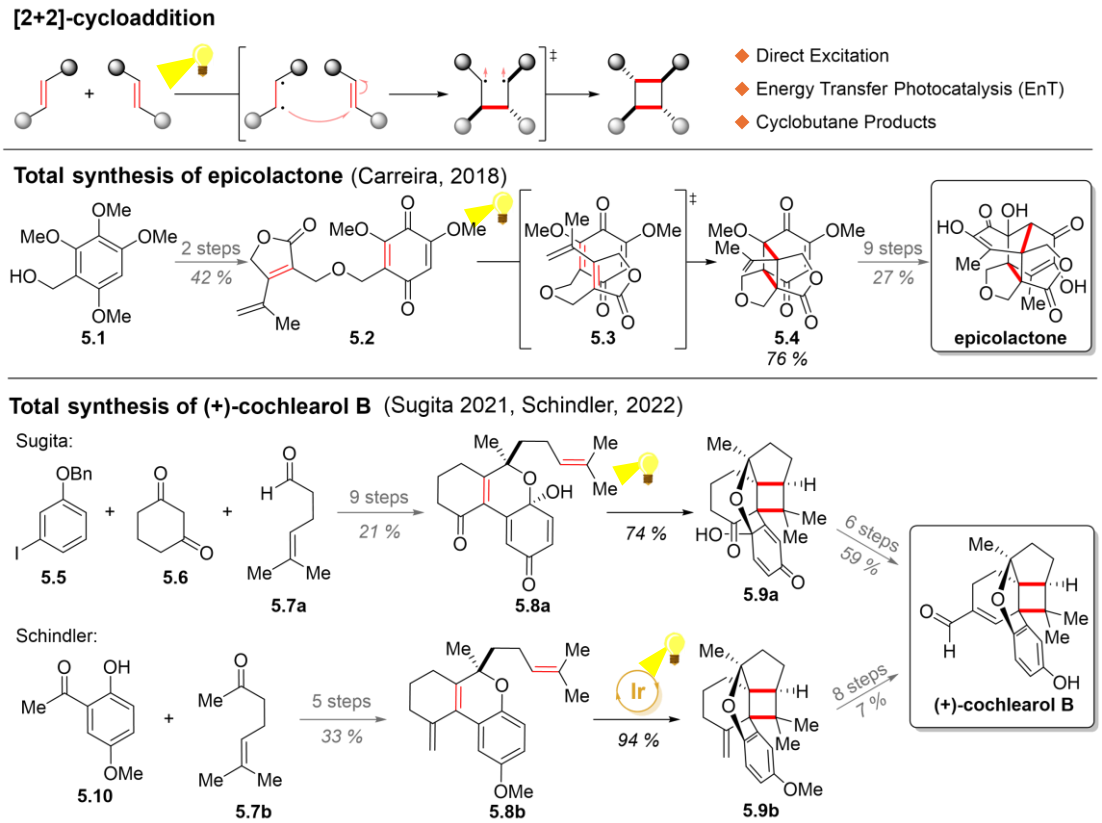

Scheme 5.1. [2+2]-cycloaddition and its use in total syntheses of epicolactone (middle)[38] and (+)-cochlearol B (lower part)[39,40]. [Ir] = $[Ir(dF(CF_3)ppy)_2(dtbbpy)]PF_6$.

While the combination of the two reagents could be a concerted cycloaddition, a stepwise mechanism, where the attack of a less-stabilized radical occurs first, has been supported by computational studies and the typical *anti*-relationship of the substituents.[41,42]

As a recent example of the use of [2+2]-cycloaddition, the Carreira group utilized the reaction as a key step *en route* to the total synthesis of epicolactone, a polycyclic secondary metabolite found in an endophytic fungus (Scheme 5.1, middle).[38] The synthesis of this compound began with the preparation of the benzylic alcohol **5.1**, which was then combined with the lactone fragment to give the quinone **5.2**. Upon direct irradiation, the desired [2+2]-cycloaddition took place, rendering the flat precursor **5.2** into a tetracyclic compound **5.4** with all three quaternary stereocentres of the target molecule in place. Particularly notable in this reaction is the possibility to directly irradiate the cyclization precursor **5.2** with blue LEDs, indicating that the substrate itself absorbs light at relatively long wavelengths. This virtue was most likely advantageous in helping to prevent undesired decomposition. The newly generated cyclobutane moiety in **5.4** was later expanded to a five-membered ring by aldol chemistry, and the last cyclohexyl ring was built to give the desired natural product in overall 12 steps.

The total synthesis of (+)-cochlearol B, a meroterpenoid natural product isolated from fungi belonging to *Ganoderma*-genus, presents another recent example (Scheme 5.1, lower part). Intriguingly, two photochemistry-driven routes for this molecule appeared consecutively in 2021 and 2022 from the groups of Sugita and Schindler, respectively.[39,40] From a strategic point of view, both groups decided to use the [2+2]-cycloaddition of the tricyclic precursors **5.8a** and **5.8b** to create the cyclobutane ring present in the natural product. The synthesis of Sugita started with iodobenzene **5.5** and cyclohexanedione **5.6** giving the tricyclic diketone **5.8a** as the precursor for the cycloaddition in 9 steps.[39] On the other hand, the optimized route of Schindler began with the acetophenone **5.10** and sulcatone (**5.7b**), yielding their tricyclic compound **5.8b** in 5 steps.[40] The interplay between structure and reactivity was then delicately demonstrated by the following photocycloaddition step. While the dienone **5.8a** underwent a smooth [2+2]-cycloaddition with direct irradiation, the chromene **5.8b** did not react in the absence of an EnT photocatalyst. Based on the precursors tested, the group of Sugita rationalized that the presence of the electron-deficient *para*-quinone unit was crucial for the direct irradiation approach. Eventually, the natural product was obtained in 15 steps (Sugita) or 14 steps (Schindler).

5.3.2 Photoenolization Diels–Alder reaction

The Diels–Alder reaction is a well-established thermal [4+2]-cycloaddition which has been extensively used in total synthesis for the generation of the carbon framework of natural products.[43] However, unless particularly reactive starting materials with a clear electronically matching nature are used, the reaction requires heating to high temperatures and prolonged reaction times (often several days). As these forcing conditions present challenges with functional group tolerance and sensitive substrates, further developments have been made to address these issues. Also here, photochemistry has been found as a compelling alternative to activate substrates under mild conditions. For example, photocatalytic oxidation of one of the reaction partners into the corresponding radical cations accelerates the reaction, particularly when both reactants are rather electron-rich in nature.[44] On the other hand, the diene counterpart can also be generated *in situ* by photoenolization, allowing the subsequent Diels–Alder reaction. Mechanistically, the

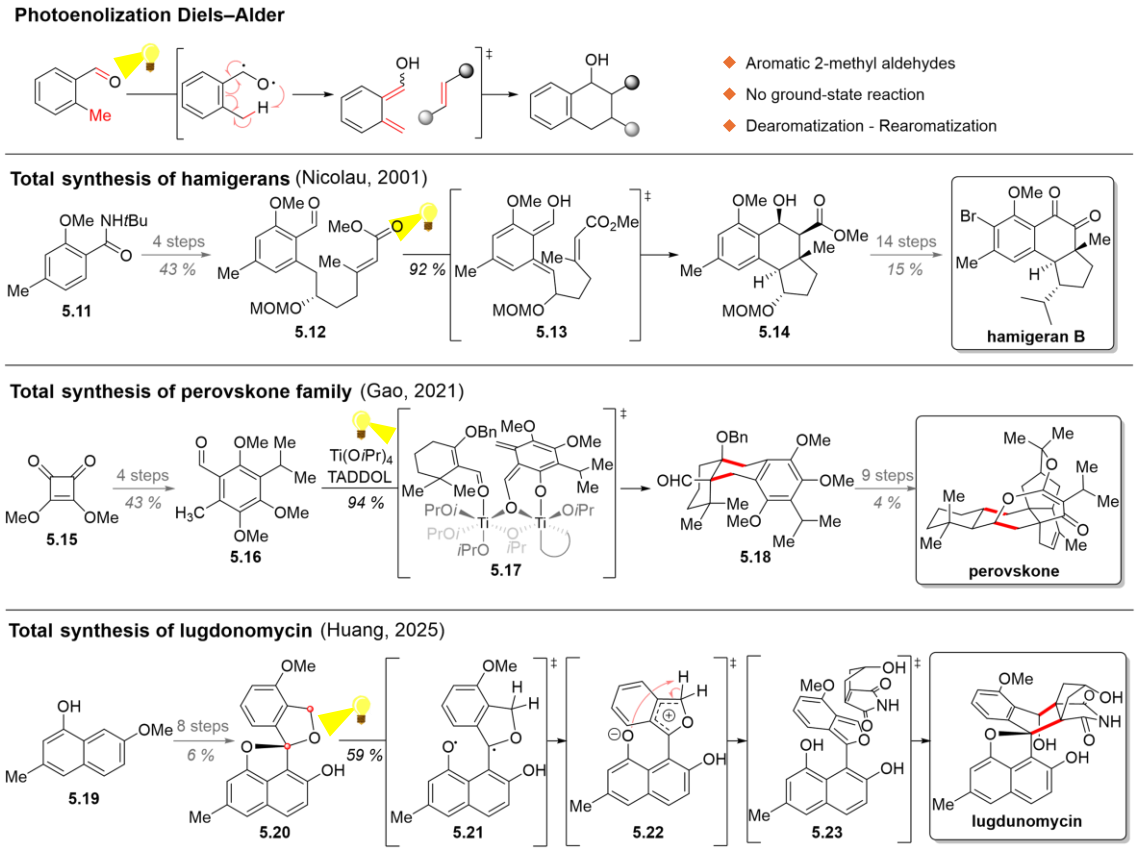

Scheme 5.2. Photoenolization/Diels–Alder reaction (upper part), its uses in the total syntheses of hamigerans (second-to-top)[46] and perovskone natural products (second-to-bottom),[47] and photocatalytic isobenzofuran generation for Diels–Alder reaction in the total synthesis of lugdunomycin (lower part)[48].

photoenolization begins with excitation of the carbonyl group of the benzaldehyde or acetophenone, leading to a biradical intermediate (Scheme 5.2, top).[45] An intramolecular 1,5-hydrogen atom transfer then forms the diene, an enol tautomer of the initial ketone/aldehyde, which then cyclizes with the dienophile. This mechanism has been supported by computational studies, and after the initial photoexcitation, the following steps have been proposed to be exergonic, driven by the conversion of a localized oxygen-centred radical into a delocalized benzylic radical. The photoenolization step can be further facilitated by the coordination of the substrate to a Lewis acid or *N*-heterocyclic carbene catalysts.[49–51] In the presence of chiral ligands, asymmetric variants of this method have also been introduced.[49,52]

The total synthesis of hamigrans by the Nicolaou group serves as a fine representation of the intertwined nature of method development and total synthesis (Scheme 5.2, second-to-top). [46,53] In 2001 the group published two communications, detailing first their method development towards a substrate-controlled stereoselective photoenolization/Diels–Alder reaction and then its utilization in the total synthesis of the hamigeran family of natural products. Indeed, their thorough study on inter- and intramolecular reactions effectively solidified their access to the tricyclic carbon core and equipped them with valuable experience of the behaviour of this reaction.[53] Their work towards the natural products commenced with the benzamide **5.11**, which was converted to the aldehyde **5.12** in 4 steps.[46] The intramolecular photoenolization/Diels–Alder reaction was then carried out with direct irradiation above 200 nm, closing the two aliphatic rings in the 6/5-fused system **5.14**. Even more importantly, the stereochemistry of the MOM-protected alcohol was found to dictate the stereochemistry of the four newly formed centres, three of them which were formed to extremely high stereoselectivity. After building the carbon skeleton of the molecule, the rest of the synthetic efforts focused on establishing the correct oxidation pattern of the cyclohexadienone unit, and addition of the remaining bromide and isopropyl substituents to give hamigeran B in 14 additional steps.

Over the past years, the group of Gao has made significant improvements to the photoenolization Diels–Alder methodology. First, the titanium isopropoxide catalyst was introduced as a means of facilitating the photoenolization and pre-organizing the diene and dienophile before the reaction.[50] Furthermore, the pre-coordination forged by titanium most likely acts to prevent the dimerization of the photoenolized aldehyde, a challenge typically requiring a notable excess of the aldehyde or its dropwise addition.[54] Soon

afterwards, the same group reported an asymmetric version of the photoenolization Diels–Alder reaction enabled by combining the aforementioned titanium catalyst with a chiral TADDOL-derived ligand.[52] This asymmetric induction was further employed in the collective total synthesis of perovskones and structurally related hydrangenones in 2021 (Scheme 5.2, second-to-bottom).[47] The longest linear sequence started with dimethyl squarate (**5.15**), which was converted into the aldehyde **5.16** in 4 steps. For the key photochemical transformation, the titanium-bridged asymmetric complex **5.17** was formed by simply adding the components together, followed by photoenolization. The desired Diels–Alder reaction rapidly took place, giving **5.18** in 94% yield and an impressive 97.7:2.3 e.r. after recrystallization. The tricyclic aldehyde **5.18** served as a common precursor for six terpenoids, the parent compound perovskone shown as a representative example.

In 2025, the group of Huang reported an alternative photochemical method to initiate a Diels–Alder reaction as a part of their synthetic studies towards lugdonomycin (Scheme 5.2, bottom).[48] Starting with the napthalenol **5.19**, the substrate for the photoinitiated Diels–Alder reaction **5.20** was prepared over 8 steps. The spiroketal **5.20** was then subjected to direct irradiation, which homolyzed the phenoxy C–O bond to give **5.21**, followed by an intermolecular electron transfer to give the zwitterionic intermediate **5.22**. Subsequent proton exchange likely gave isobenzofuran **5.23**, and a Diels–Alder reaction with *iso*-maleimycin formed the lugdomycin after regeneration of the previously broken napthol C–O bond in silica gel. The calculated reaction pathways, intermediates, and transition states supported the afore-described mechanism. Furthermore, DMSO, a widely used solvent in photochemistry, was necessary for the progress of the reaction. The authors hypothesized that the key factor here would be the hydrogen-bonding ability of DMSO, stabilizing and prolonging the lifetime of the isobenzofuran intermediate **5.23**. Notably, the generation of the isobenzofuran intermediate with neither heat nor acidic conditions could initiate the desired reaction.

5.3.3 Alkene oxidation and reduction

One-electron oxidation and reduction of alkenes give rise to interesting intermediates possessing both ionic and radical character (Scheme 5.3, upper part).[55,56] The choice of which reactivity takes place first can often be controlled by modification of the reaction conditions. As expected, one-electron oxidation of the olefins is notably facilitated by conjugation with an electron-rich substituent, whereas one-electron reduction often requires conjugation with an electron-poor group. From the strategic point of view, the one-electron oxidations and reductions of alkenes can be seen as umpolung reactivity; oxidation converts the previously electron-rich alkenes into electron-deficient radical cations, whereas reduction of the electron-poor olefins gives them radical anion character. Furthermore, while thermal alkene hydrofunctionalizations typically proceed *via* initial protonation to give Markovnikov selectivity, with alkene radical cations, the nucleophilic attack precedes, resulting in anti-Markovnikov products. This reaction has been realized with a broad variety of nucleophiles, particularly oxygen- and nitrogen-centred ones, and can be realized both intra- and intermolecularly.[57–60] Reciprocally, alkene radical anions can attack electrophiles with the same anti-Markovnikov selectivity as intriguingly shown, for example, with photocatalytic carboxylations.[61,62]

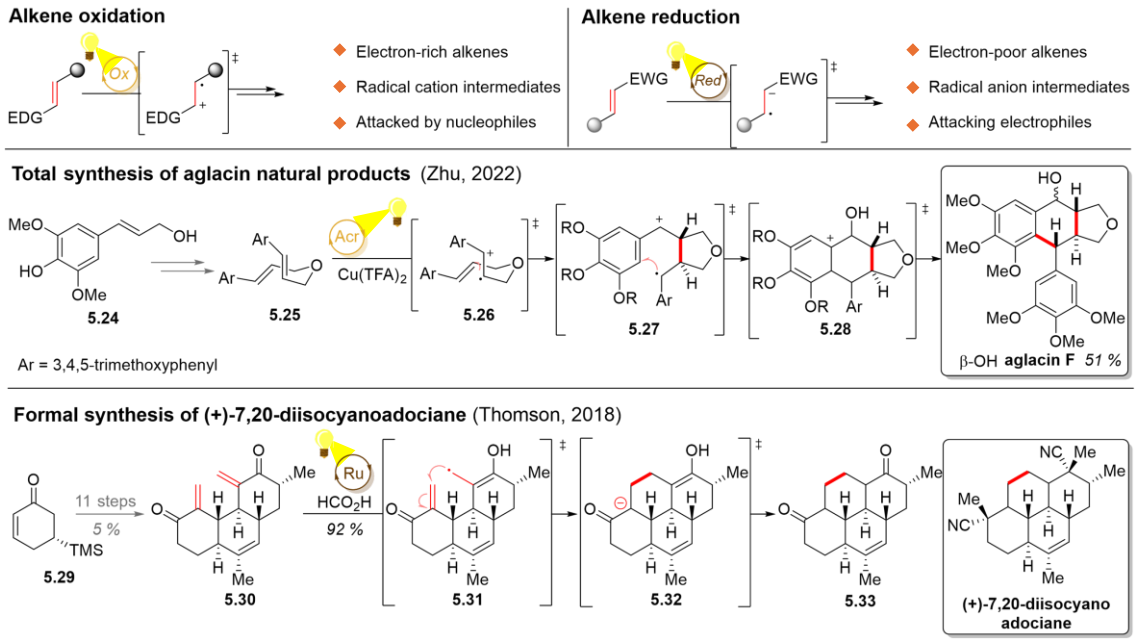

Scheme 5.3. One-electron oxidation and reduction of an alkene (upper part), and their utilizations in total synthesis of aglacin F (middle)[63] and formal synthesis of (+)-7,20-diidocyanoadociane (lower part).[64] Details for the conversion of **5.24** to **5.25** were not reported in the original publication. ACR = Fukuzumi catalyst, [Ru] = $Ru(bpy)_3Cl_2$.

The use of photocatalytic alkene oxidation in natural product chemistry has been recently demonstrated by the Zhu group in their concise synthesis of aglacins (Scheme 5.3, middle).[63] As widely distributed secondary metabolites, these dimeric compounds play diverse roles in plants, forming a defence against pathogens and pests as well as stimulating growth and development. In Nature, the biosynthesis of such products centres on a regio-, diastereo-, and enantioselective radical cyclization, and hence a related transformation was chosen as a blueprint for the laboratory synthesis. Using sinapyl alcohol (**5.24**) as a starting material, its methylated dimer **5.25** was quickly assembled for the photocatalytic key step. Photoexcitation of the highly oxidizing acridinium catalyst thus oxidized the alkene, setting the reaction cascade in motion. A fast 5-*exo*-trig cyclization forged the first new C–C bond, followed by a 6-*endo*-trig cyclization on the aryl ring (proposed transition state **5.26**). During this cyclization sequence, a molecule of water attacks the benzylic carbocation, giving the hydroxy group present in the product. The benzylic radical is eventually oxidized by the copper(II) salt to give the delocalized aryl cation **5.28**, after which aromaticity can be restored by deprotonation. Aglacin F is obtained as the major product from this cyclization cascade (β-OH 51 %) while its α-OH epimer, aglacin E is produced as a minor product (11 %).

An example of the reaction of alkene radical anions in natural product chemistry can be found from Thomsons formal synthesis of (+)-7,20-diidocyanoadociane, a marine sponge-derived diterpene (Scheme 5.3, lower part).[64] Utilizing the pseudo C_2-symmetry as a guide for their synthetic strategy, the longest linear sequence commenced with the β-TMS enone **5.29**. The bis-enone **5.30**, comprising three out of the four rings and 6 out of 8 total stereocenters, was assembled in 11 steps. For the pivotal closure of the final ring, a radical reaction was envisioned, and the photocatalytic reductive γ-coupling turned out to be a well-suited option.[65] Herein, protonation of the carbonyl group with formic acid and one-electron reduction of the alkene formed a methyl radical **5.31**, which then underwent an intramolecular Giese-coupling reaction.[64] Reduction of the second radical to the respective enolate **5.32**, followed by protonation, gave the Corey dienone **5.33** in high yield and as a single stereoisomer. As the conversion of this dienone to the (+)-7,20-diisocyanoadociane has been previously reported over three steps, the synthetic efforts of Thomson represent a 17-step formal synthesis of the said natural product.

5.3.4 Decarboxylation of carboxylic acids and oxalates

Decarboxylation, the loss of CO_2 from the (organic) starting materials, has been used for a long time for the generation of reactive intermediates. Despite having a functional handle to mark the reactive site, thermal decarboxylations often require heating to high temperatures (>100 °C),[66,67] putting sensitive substrates at risk of undesired decomposition. In contrast, under photochemical conditions, decarboxylation can be realized at room temperature using only a base and a (photo)catalyst.[68–73] While both the thermal and photochemical processes typically begin with a deprotonation of the carboxylic acid, the decarboxylative step itself is best described as a radical process in photocatalytic reactions (Scheme 5.4, upper part).[66,74] Hence, the photocatalytic decarboxylation results into a carbon-centred radical which can be easily trapped with radical acceptors.[69] If desired, the carbon-centred radicals can be converted back to the ionic regime by one-electron reduction with the photocatalyst or by one-electron oxidation with a sacrificial oxidant.

A fine example of the use of photocatalytic radical decarboxylation was developed during the total synthesis of zephycarinate alkaloids by the Ohno group (Scheme 5.4, middle).[75] Their synthesis commenced with L-serine and biphenyl carboxylic acid **5.34** as starting materials, giving the carboxylic acid **5.35** in 6 steps. This carboxylic acid was then

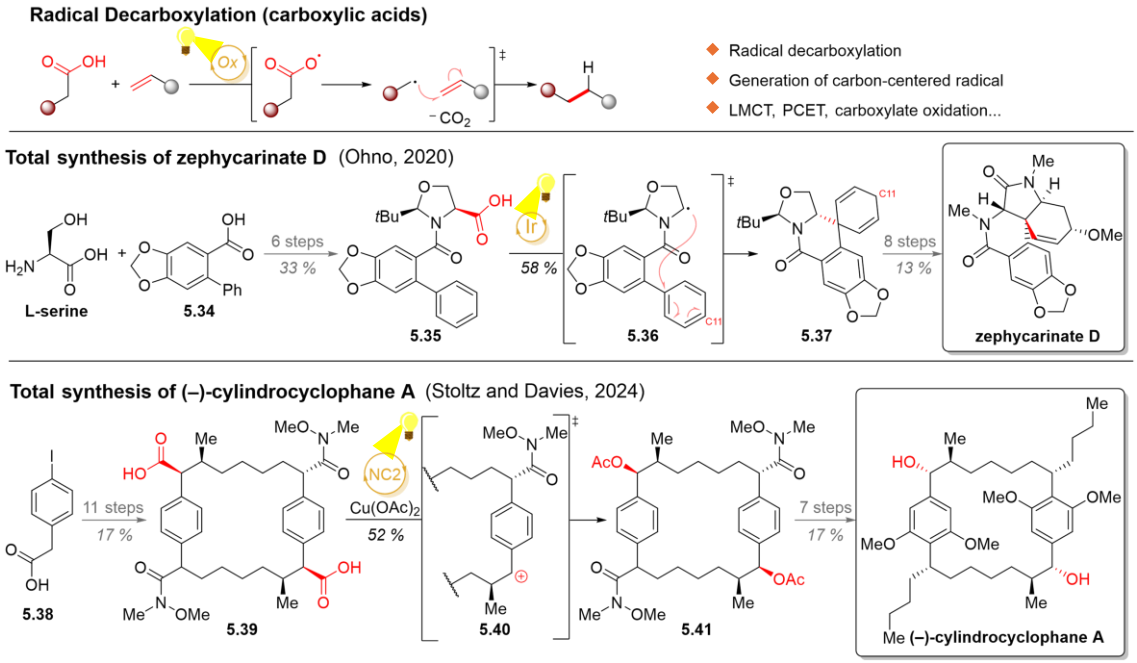

Scheme 5.4. Photocatalytic decarboxylation (upper part), and its utilization in total syntheses of zephycarinate D (middle)[75] and cylindrocyclophane A (lower part)[76]. [Ir] = $[Ir(dF(CF_3)ppy)_2(dtbbpy)]PF_6$, NC2 = Nicewicz's catalyst 2.

subjected to photocatalytic decarboxylation, which resulted in loss of CO_2 followed by a 6-*endo*-trig radical cyclization (intermediate **5.36**). The secondary radical at C11 was then most likely briefly reduced to a carbanion, after which protonation gave the spirocyclic compound **5.37**, finalizing the reductive radical *ipso*-cyclization. Further 8 steps then gave zephycarinate D, also providing an easily tunable route for its *N*-alkyl analogs.

In 2024, the groups of Stoltz and Davies published their total synthesis of (–)-cylindrocyclophane A, a peculiar C_2-symmetric macrocyclic natural product (Scheme 5.4, lower part).[76] While selective C–H functionalization strategies lay in the heart of this synthesis, photochemical "inversion" of carboxylic acids into acetates was also utilized. The synthesis started with phenylacetic acid **5.38**, which was converted into the macrocyclic compound relatively early in the synthesis (8 steps), giving the bis-carboxylic acid **5.39** after additional functional group adjustments. This acid was then decarboxylated under photocatalytic conditions, and the formed benzylic radical was oxidized to a carbocation **5.40** using copper(II)acetate as a terminal oxidant.[77] Nucleophilic attack of the acetic acid co-solvent or of an acetate released during the reduction of copper(II) then formed acetamide **5.41**. The desired natural product was achieved after seven additional steps.

Oxalates, 1,2-dicarboxylic acids, have also been found to be successful precursors for decarboxylation (Scheme 5.5, upper part). Synthetically, they represent another opportunity to utilize the oxidative decarboxylation reaction with substrates that do not initially possess a carboxylic acid group. Various alcohols, especially tertiary ones, have proven excellent precursors for oxalates, their photochemical stepwise loss of two molecules of CO_2 giving radicals on the initial *ipso*-carbon.[78] In 2016, the group of Overman used the

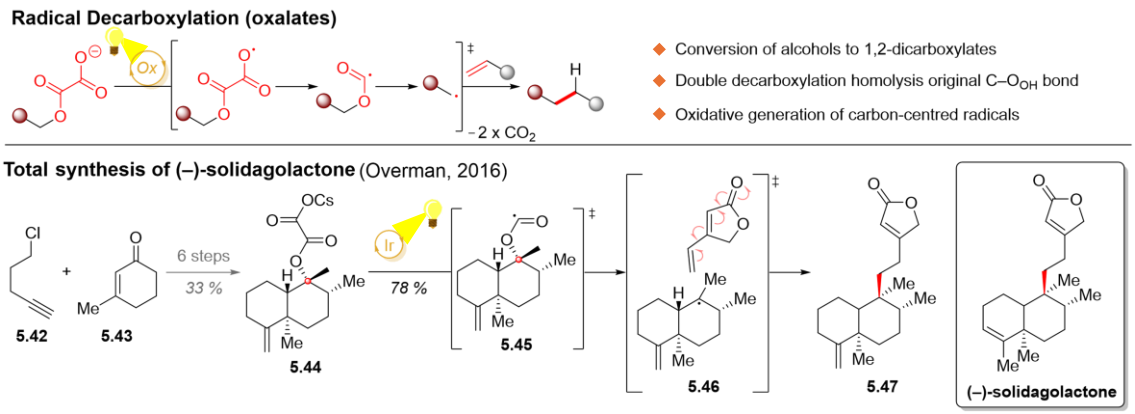

Scheme 5.5. Photocatalytic decarboxylation with oxalates (upper part) and its utilization in total synthesis of (–)-solidagolactone (lower part)[79].

photocatalytic decarboxylation of oxalates to generate the reactive radical intermediate for the coupling of two fragments in their total synthesis of (–)-solidagolactone (Scheme 5.5, lower part).[79] Their enantioselective synthesis commenced with hydroalumination of the chloroalkyne **5.42**, followed by a copper-catalyzed asymmetric conjugate addition to cyclohexenone **5.43**. Initially, a phthalimide oxalate was envisioned as a radical precursor, however, acylation of the tertiary alcohol with (*N*-phthalimidoyl)chlorooxalate proved unsuccessful. Instead, functionalization of the oxalate ester **5.44** proceeded with high yield (90 %), setting the stage for the decarboxylative coupling. Albeit the scarcity of high-yielding 1,6-conjugate addition of carbon centred radicals (such as **5.46**), optimization of this coupling step eventually delivered the desired lactone **5.47** in 78 % yield (83% ee) and in a total of seven steps. This important lactone represents the core structure of several *trans*-clerodane alkaloids, and its conversion to (–)-solidagolactone in one step has been demonstrated earlier by the same group.[80] Slight adjustments to the northeast butenolide part have enabled the synthesis of two further natural products (16-hydroxycleroda-1,13-dien-15,16-olide and annonene), shortening their total syntheses from 19–27 steps to 11 and 9 steps, respectively.[81–84]

5.3.5 Redox-active ester fragmentation

The earliest reports on the photoactivity of *N*-phthalimide esters date back to the 1970s, when Kanaoka and co-workers extensively studied light-induced reactions of their derivatives.[85] While these initial reports were mainly focused on transformations incorporating the phthalimide moiety to the product, the possibility for homolytic radical generation was demonstrated by the group of Skell with *N*–Br phthalimide esters shortly after.[86] This finding in particular paved the way for the uses of phthalimide esters for the generation of alkyl radicals and the broad variety of applications we see today.[87–90] Although many methods for direct photocatalytic decarboxylation have been established, these methods typically begin with one-electron oxidation. With phthalimide esters, in contrast, the redox moiety is first activated by one-electron reduction, followed by homolysis of the weak *N–O* bond and subsequent decarboxylation (Scheme 5.6, upper part). As the catalytic cycle commences with a reduction, the cycle-closing step becomes oxidative in nature. In this sense, phthalimide esters can be regarded as internal terminal oxidants, which are typically highly compatible with a variety of organic substrates and reaction conditions. In addition to carboxylic acids, phthalimide esters of oxalates and alcohols can also be utilized, giving an alternative access to C- and O-centered radicals.[91] So far, the

phthalimide esters have appeared to be the most favored redox-active tether, although alternatives such as 4-substituted Hanzsch esters and *N*-alkylated pyridines (Katrinzky salts) have also been developed.[92,93] This could be at least in part due to the ease and typically high yields obtained from their preparation, combined with well-studied properties and the variety of activation methods.[94]

As a synthetic example, the group of Overman used the phthalimide group towards the initiation of their key radical addition/cyclization/fragmentation cascade *en route* to (–)-chromodorolide B, a member of rearranged spongian diterpenoid (Scheme 5.6, middle).[95] Their longest linear sequence started with (*S*)-enedione **5.48**, which was converted to the phthalimide ester **5.49** over 13 steps with the vinylic chloro-substituent in place as a cascade-ending leaving group. Photocatalyzed reduction of the *N*-phthalimide moiety with ruthenium or iridium polypyridyl complex resulted in an intermolecular Giese-coupling (**5.50**), followed by an intramolecular trapping of the newly formed radical (**5.51**) and the alkene migration upon chloride elimination. Hence, this sequence achieves to couple the two main fragments together, simultaneously establishing the configuration

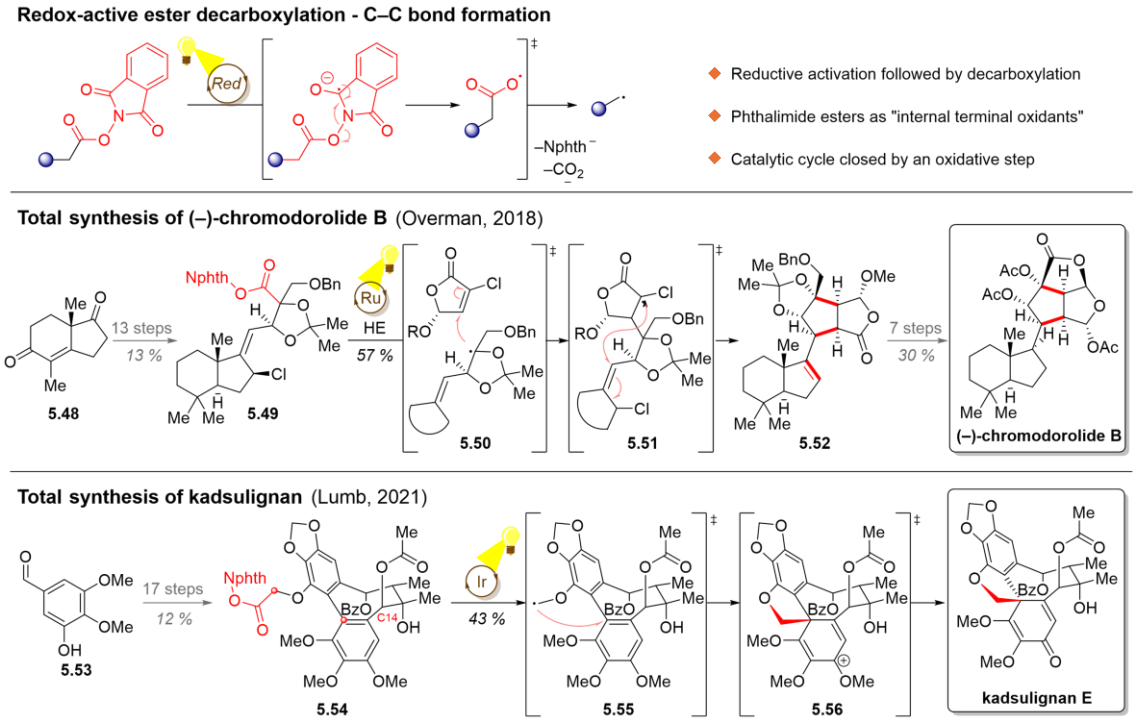

Scheme 5.6. Redox-active ester fragmentation (upper part), and its utilization in total syntheses of (–)-chromodorolide B (middle)[95] and kadsulignan (lower part)[96]. [Ru] = $[Ru(bpy)_3](PF_6)_2$, [Ir] = $[Ir(ppy)_2(dtbbpy)]PF_6$.

of two new stereocentres. Computational methods were utilized to model the desired transition states of this cascade, which eventually disclosed the importance of the chloride substituent on the butanolide for both high yield and high stereoselectivity. Importantly, after the fragment combination dechlorination could remove the α-carbonyl halogen under the same reaction conditions (see next Section). Optimized conditions of the coupling reaction gave 57% yield of the pentacyclic compound **5.52**, which could be converted into the target natural product in 7 additional steps.

Phthalimide esters were further used as a precursor to generate α-oxygen radicals in a collective synthesis of various highly oxidized dibenzocyclooctadiene (DBCOD) natural products by the group of Lumb (Scheme 5.6, lower part).[96] Compounds bearing the DBCOD core are divided into many (sub)families, yet this shared backbone has been postulated to account for their bioactivity prized in traditional Asian and Eastern European medicine. Furthermore, based on the biosynthetic hypothesis, the addition of a nucleophilic methyl radical to an electron-rich aromatic ring, similar to **5.55**, is likely to play a crucial role in the formation of these compounds. As the cyclization event is already oxidative in nature, a reductive method for the radical generation would be needed for the overall redox-neutrality. The collective synthesis towards these natural products commenced with the aldehyde **5.53**, which was converted to the phthalimide ester **5.54** over 17 steps, setting up the stage for the photocyclization. Gratifyingly, the reductive formation of the methyl radical in led to an efficient 5-*exo*-trig cyclization (**5.55**). Oxidation of the so-formed aryl radical was most likely to follow (intermediate **5.56**), after which regioselective addition of water and methanol elimination formed the desired *para*-spirodiene natural product. The strategic importance of this radical cyclization was further demonstrated by the same group as modification of the substituent pattern on the C14 acetate in **5.54** led to the synthesis of six other DBCOD natural products.

5.3.6 Dehalogenation

Photochemical dehalogenation offers a mild a regioselective method for the generation of various alkyl and aryl radicals (Scheme 5.7, upper part). The reactivity of halogens towards this transformation decreases in order I < Br < Cl < F, making many iodides and bromides photolabile under low-wavelength irradiation.[97,98] While the bromides and iodides often react under direct irradiation or *via* a single-electron reduction with a broad variety of photocatalysts,[99,100] dechlorinations and defluorinations typically require special reaction conditions, catalysts, or substrates.[101–103] In terms of the carbon skeleton, a benzyl ring, α-carbonyl group, or the presence of *para*-EWG in a phenyl ring significantly facilitates the dehalogenation process.[104] Out of these cases, the α-carbonyl one is particularly useful as this position can be first halogenated by radical bromination or iodination, followed by dehalogenative radical generation.

The group of Xia utilized the photocatalytic dehalogenation in their total synthesis of (+)-flavisiamine F, an alkaloid isolated from *Kopsia* plants featuring a highly cyclic skeleton with two all-carbon quaternary stereocentres (Scheme 5.7, middle).[105] Their synthesis started with *N*-sulfonylated carbazolone **5.57**, to which two additional rings were constructed, and iodination of the enolate position gave the compound **5.58**.

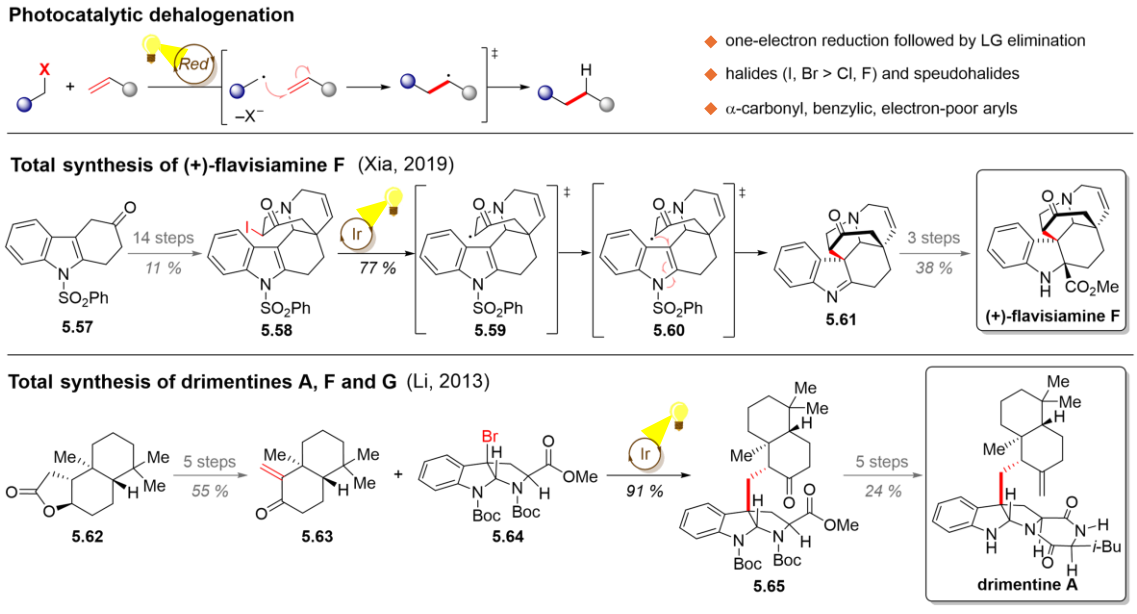

Scheme 5.7. Photocatalytic dehalogenative C–C bond formation (upper part) and its uses in total syntheses of (+)-flavisiamine F (middle)[105] and drimentine A (lower part) [107]. [Ir] = $[Ir(dF(CF_3)ppy)_2(5,5'\text{-}d(CF_3)bpy)]PF_6$ (middle), [Ir] = $[Ir(ppy)_2(dtbbpy)]PF_6$ (lower part).

Photocatalytic single-electron reduction of the α-iodocarbonyl moiety was followed by iodide elimination, giving the reactive intermediate **5.59**. This radical then cyclized to the indole (**5.60**), and desulfonylation gave the desired product of the radical cascade **5.61**. While the substrate undergoes two reductive steps (iodide elimination and desulfonylation), the catalytic cycle is most likely closed by a single-electron oxidation of the excess Et_3N. In contrast, while the α-carbonyl radical **5.59** could be generated thermally, Bu_3SnH or $(TMS)_3SiH$ quickly reduced this radical, and protonation of the formed enolate intermediate led to a simple protodehalogenation.[106] After this sterically demanding C–C bond forming step, the synthesis was completed in three further steps.[105]

A similar dehalogenative C–C coupling, yet this time intermolecular, was used by the Li group in their collective synthesis of drimentine alkaloids (Scheme 5.7, lower part).[107] The longest linear sequence commenced with (+)-scalreolide (**5.62**) with most of the stereogenic centres of the target molecule already in place. A five-step synthetic route gave the enone **5.63**, while the other fragment **5.64** was prepared in one step from L-tryptophan. The key debrominative conjugate addition then took its turn. Herein, a photocatalytic one-electron reduction of the indole moiety resulted in a rapid debromination, and the newly generated benzylic radical then added to the enone in a conjugate fashion (Giese-coupling reaction). Interestingly, also in this case, the use of alkyl tin radical initiators resulted in a premature radical quenching, highlighting their nature as fast hydrogen-atom-donating reagents. After this fragment coupling, the rest of the molecule was built in five steps from **5.65**, giving access to three drimetine alkaloids differing in substitution on the diketopiperazine. Furthermore, the drimentine carbon backbone could be further converted into indotertine skeleton in a one-step rearrangement, opening the route to yet another class of natural products.

5.3.7 Hydrogen Atom Transfer (HAT)

Photocatalytic hydrogen atom transfer (HAT) is an efficient strategy to activate C–H bonds which have low bond dissociation energy (BDE) or are even completely unactivated. Especially with intramolecular reactions, the 1,5-HAT with a six-membered transition state often prevails over other regioisomers (Scheme 5.8, upper part).[108,109] Hence, HAT offers an important complementary strategy to many two-electron methods where the C–H or X–H bond acidity is the reactivity-determining factor. As shown in Figure 5.2, weakened C–H bonds are often found, for example, *alpha* to a heteroatom (particularly O or N), at highly substituted carbons, or at allylic/benzylic positions.[110,111] As for the possible hydrogen atom abstracting species, oxygen, nitrogen, and sulfur-centred radicals typically abstract hydrogen atoms from positions with moderately strong bond dissociation energies, whereas the decatungstate anion and chlorine radical are among well-established strong hydrogen atom abstractors. Importantly, various activation strategies have been developed for the mild generation of these radical species. For the decatungstate anion, direct irradiation breaks one of the W=O bonds into a HAT-active biradical.[110] Ligand-to-metal charge transfer (LMCT) can be used to generate radicals (Cl, RO, RCO_2 etc.) by homolysis of the metal-ligand σ-bond.[112] Proton-coupled electron transfer (PCET) methods combine a simultaneous deprotonation and oxidation of the heteroatom (N, O), while similar stepwise mechanisms can also be used to oxidize nitrogen and oxygen anions.[113–115]

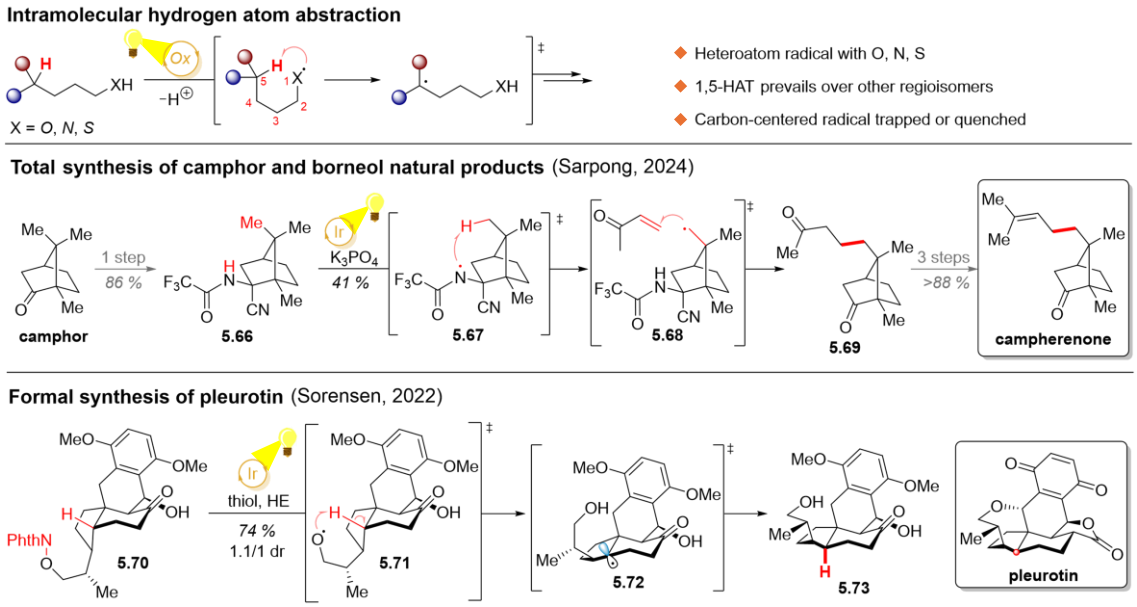

Scheme 5.8. Intramolecular 1,5-HAT (upper part) and its utilization in total syntheses of campherenone (middle)[116] and pleurotin (lower part)[54]. [Ir] = [Ir(dF(CF3)ppy)2(5,5'-d(CF3)bpy)]PF6 (middle), [Ir] = *fac*-Ir(ppy)3 (lower part), HE = Hantzsch ester.

The intramolecular 1,5-HAT was utilized as a key step in the divergent total synthesis of camphor-derived natural products by Sarpong group in 2024 (Scheme 5.8, middle).[116] In the heart of their synthetic strategy lay a selective functionalization of the bridgehead methyl group (marked in red) with the pseudo-equatorial heteroatom. Despite the 1,5-relationship between the reaction-participating substituents, the overall strained nature of the [2.2.1] bicyclic intermediate **5.67** could make the step less favourable, opening pathways for competing side-reactions. At least one of these, β-scission, could be hampered by choosing a nitrogen-centred radical over an oxygen-centred radical as HAT active moiety since the formed C=N double bond would be notably weaker than the C=O one. With these considerations in hand, the group began the optimization of the desired HAT step and collective total syntheses. Hence, camphor was converted into the aminonitrile **5.66**, and after some optimization, deprotonation of this compound at elevated temperatures (60 °C) for 3 hours was found crucial for obtaining high yields of the desired HAT. This stepwise addition of reagents supports a single-electron oxidation of the amide anion as the mechanism for the radical generation. Furthermore, the need for higher temperatures for the N–H deprotonation soon turned out to be an asset as the secondary C–H bond in the Giese-coupling product **5.69** would be weaker than the primary one in the starting material **5.66**, yet only minor amounts of double alkylation were observed. Three additional steps then furnished campherenone, a natural product which could be further converted to copacamphor.

Another example of the use of an intramolecular HAT can be drawn from the Sorensen group's formal synthesis of pleurotin (Scheme 5.8, lower part).[54] The synthesis began with the methoxyindanone, which formed the southern part of **5.70** after coupling with the northern fragment. Importantly, the photoenolization/Diels–Alder reaction (see Section 5.3.2) used for this fragment coupling inevitably produced the *cis*-fused hydroindane, whereas the *trans*-fused isomer would be needed for the natural product. Hence, an intramolecular 1,5-HAT was envisioned for this key epimerization. Strategically, this step provides a complementary way for two-electron epimerizations, which often rely on deprotonation/reprotonation of acidic positions, e.g., *alpha* to a carbonyl group. A kinetically controlled hydrogen-atom donation to **5.72** would then give the desired stereomer. *N*-alkoxyphthalimide was chosen as the radical precursor, a decision that was at least partly influenced by the need for an OH-protecting group in the previous fragment-combining step. Now, reduction of **5.70** with a photoexcited iridium catalyst delivered the short-lived alkoxy radical **5.71** as a hydrogen-atom abstracting species. Notably, the possible side

reactions, such as unproductive 1,5-HAA to the indanone methylene group or oxidation to aldehyde, could be well suppressed. In contrast, control over the site from which the hydrogen atom was back-donated to **5.72** proved more challenging. While the simple thiophenol mainly returned the *cis*-ring junction, sterically more hindered 2,4,6-triisopropylbenzenethiol gave the best diastereomeric ratio of 1.1:1 *trans*/*cis*. The diastereomers could be chromatographically separated, and two additional steps on the *trans*-isomer led to the diol **5.73**, previously converted into pleurotin in 3 steps by Hart and coworkers.[117]

A powerful demonstration for HAT on strong C–H bonds came from the Wu group's recent total synthesis of demissidine, a steroidal alkaloid isolated from several potato species (Scheme 5.9, middle).[118] The commercially available tigogenin acetate (**5.74**) serves as an attractive starting point for the synthesis, already having the steroidal backbone in place; however, as a slight drawback, the stereochemistry of the C25 methyl group needs to be inverted. Both previously reported syntheses solved this problem by inserting a carbonyl group at C26, making the base-catalyzed epimerization possible. However, the formation and removal of this carbonyl functionality notably lengthened the total syntheses.[119,120] In contrast, the absence of carbonyl intermediates made the synthesis from Wu straightforward, and the amine **5.75** could be accessed in three steps from tigogenin acetate.[118] For the key epimerization reaction, a strong HAT catalyst was needed as the desired position at C25 was unactivated, and the conditions of Wendland were chosen as a

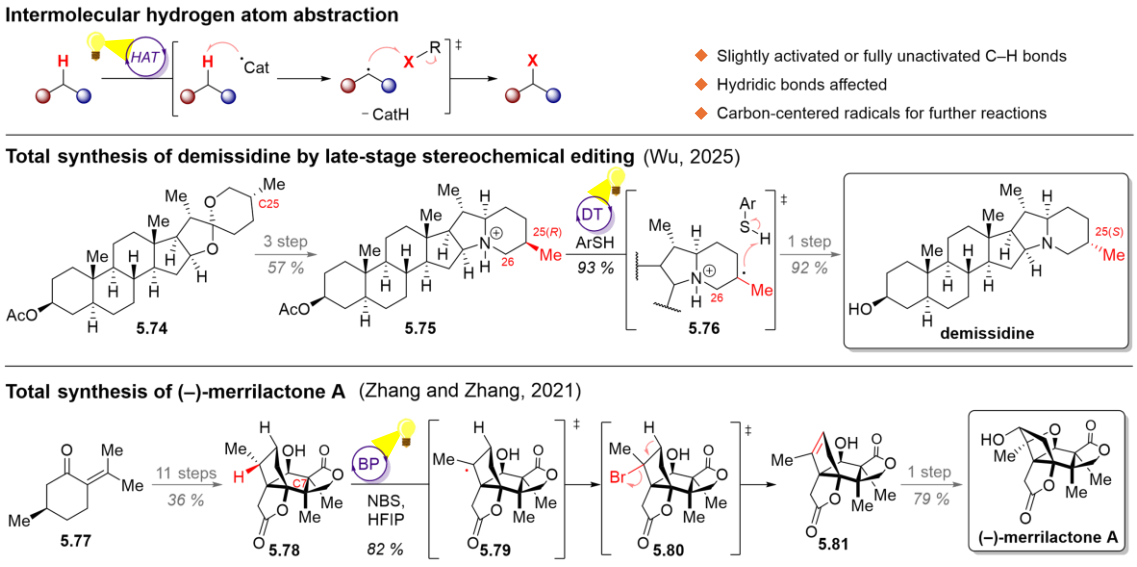

Scheme 5.9. Intermolecular HAT (upper part) and its utilization in total syntheses of demissidine (middle)[118] and (–)-merrilactone A[121]. DT = decatungstate, BP = benzophenone.

starting point.[122] As expected, protonation of the tertiary amine proved necessary to deactivate the α-amino position C26, thus shifting the regioselectivity to C25.[123] Gratifyingly, *in situ*-protonation with H_sSO_4 followed by the photocatalytic HAA/HAD-sequence afforded the desired axial-to-equatorial epimerization with 92% yield and diastereomeric ratio greater than 20:1. A simple hydrolysis of the southwest acetate group completed the total synthesis in just 5 steps and overall yield of 48%.

An intriguing utilization of HAT was recently demonstrated by groups of Zhang and Zhang in their synthesis of (–)-merrilactone A, a sesquiterpene with promising results against neurodegenerative disorders (Scheme 5.9, lower part).[121] For the endgame of this synthesis, the groups decided to utilize a somewhat unconventional strategy where an unactivated alkyl motif would be desaturated after initial hydrogen atom abstraction *via* **5.80**. To be successful, this transformation would need to overcome particularly the challenges in regioselectivity as no functional handles were planned to direct the desaturation. Using (*R*)-pulegone (**5.77**) as a starting material, the tetracyclic lactone **5.78** was built in 11 steps, setting the stage for the pivotal desaturation. However, in addition to the desired C1–H bond, the compound also possessed another weak *alpha*-OH C–H bond, thus presenting a possible regioselectivity issue in the radical bromination. Indeed, initial attempts for the bromination using AIBN as radical initiator did not give any selectivity, but the desired C1 bromination was accompanied by oxidation of the C7-hydroxy group to the corresponding ketone. The groups then decided to harness solvent effects, more precisely the addition of hexafluoroisopropanol (HFIP) as hydrogen bond donor, to reduce the electron density at C7 while creating a sterically hindering solvent shell around this position. Now irradiation of this reaction mixture in the presence of benzophenone as photocatalyst and NBS as brominating reagent gave the desaturation product **5.81** in high yield. This synthetic intermediate proved particularly valuable as late-stage modification of the oxygenation pattern could give rise to five natural products, among them the one-step conversion to (–)-merrilactone A.

5.3.8 C–C bond fragmentation

In the synthetic planning, the C–C bond fragmentation translates into a reconnection strategy during the retrosynthetic analysis. Since the stereochemistry on cyclic substrates is often easier to control compared to their linear counterparts, controlling the stereochemistry in cyclic systems before opening the ring to acyclic intermediates has proven to be a highly successful synthetic strategy. However, while the ring opening of cyclopropyl and cyclobutyl substrates is often driven by the strain-release, rings such as cyclohexyls no longer benefit from this driving force, thus making their opening less favourable. Some of the well-established thermal methods for such fragmentations include the Grob fragmentation[124], oxonolysis[125] and various pericyclic processes including (but not limited to) *retro*-Diels–Alder, Claisen rearrangement with cyclopropane fragmentation, and *retro*-ene reactions. As a notable photochemical contribution to this field, the cyclohexanol ring opening has been achieved with PCET and LMCT methods.[126,127] These methods also represent a wider reactivity pattern of alcohols: the initial generation of the oxygen-centered radical is typically followed by a β-scission, in which the formation of a strong C=O double bond makes up the energy loss of C–C σ-bond breaking (Scheme 5.10, upper part). The formed carbon-centred radical can then undergo trapping with radical acceptors

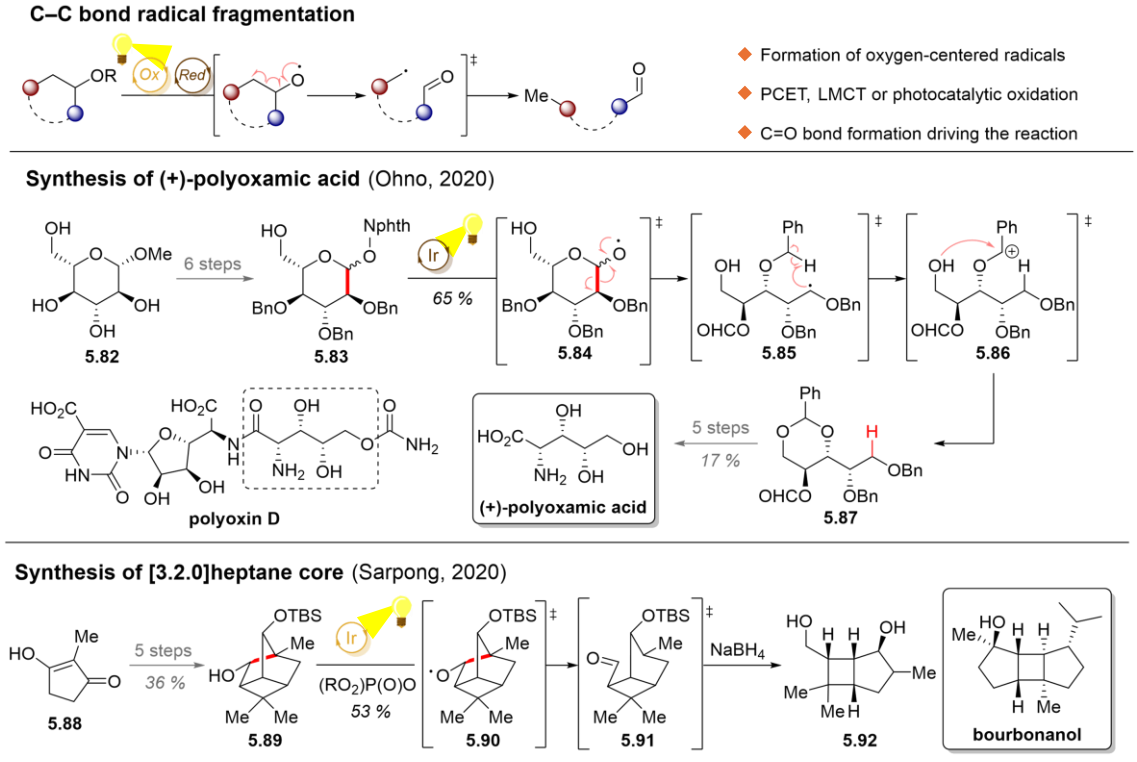

Scheme 5.10. Photochemical C–C bond fragmentation (upper part) and its uses in preparation of (+)-polyoxamic acid (middle)[128] and the [3.2.0]-heptane core (lower part)[129]. [Ir] = $Ir(ppy)_3$ (middle), [Ir] = $[Ir(dF(CF_3)ppy)_2(5,5'\text{-}d(CF_3)bpy)]PF_6$ (lower part).

or be quenched by a hydrogen-atom donor to yield the final product. As another intriguing entry, the group of Leonore developed a photochemical ozonolysis-resembling fragmentation of alkenes utilizing excited-state nitroarenes in the place of ozone.[130]

The advantage of the cyclic carbon core for stereocontrol was employed by the group of Ohno in their synthesis of (+)-polyoxamic acid, a polyhydroxy α-amino acid (Scheme 5.10, middle).[128] While this compound is not directly a natural product, it is found embedded in numerous polyoxins such as polyoxin D. Testing towards the feasibility of this synthesis was started with methyl-α-D-glucopyranose **5.82** with all stereocentres in the synthetic target already in place. After stepwise insertions of suitable protecting groups, the pyranose was converted into the phthalimide ester **5.83** in 6 steps. For the photochemical step, a reductive activation of the phthalimide ester gave the oxygen-centered radical **5.84**, which then underwent a ring-opening β-scission to **5.85**. A 1,5-HAT to the nearby oxygen protecting group then gave a benzylic radical, which was oxidized to the benzylic carbocation **5.86** by the iridium catalyst. At this stage, nucleophilic attack from the primary hydroxy group concluded the reaction sequence, giving the acetal **5.87**. Importantly, the presence of this unprotected alcohol was found crucial since, in the absence of a good nucleophile, the carbocation was attacked by adventitious water instead. Further substituent modification, followed by global deprotection, gave the (+)-polyoxamic acid. Furthermore, by using the methyl-α-L-glucopyranose (–)-polyoxamic acid, it could be accessed by the same route, representing a powerful manipulation of chiral pool substrates.

Another fine example of the use of C–C cleavage for structural diversification came from studies of highly strained tricyclooctanes by the Sarpong group (Scheme 5.10, lower part).[129] This 4/5 fused core can be found for example in the bourbon family of sesquiterpene natural products, such as bourbonanol.[131] In the synthetic direction, enone **5.88** was chosen as a starting material, and the tricyclo[3.2.1.$0^{3,6}$]octane (**5.89**) was prepared in 5 step, including a [2+2]-cycloaddition to form the four-membered ring. This alcohol was then subjected to a photocatalytic reaction with an iridium photocatalyst and a phosphate base present. The desired oxygen-centered radical **5.90** was formed either by a stepwise deprotonation-oxidation sequence or by a concerted proton-coupled electron transfer. A β-scission again took place, opening the bridged ring system to bicyclic **5.91**. As the initially generated aldehyde in was found highly unstable, it was reduced to the corresponding alcohol **5.92** before isolation. For context, a similar core can be found for example in bourbonanol natural products.

5.3.9 Borylation

In the synthetic context, borylations are important reactions as boron-containing compounds can be used as substrates for a wide variety of follow-up reactions ranging from oxidation to palladium-catalyzed cross-couplings. While Miyaura borylation[132] has been established as a go-to method for the formation of various borates, other methods starting from aryl halides and pseudohalides have also been developed.[133,134] Among the continuous development of the methodology, notable research has been devoted to replacing these (pseudo)halide handles in starting materials.[135–138] Gratifyingly for the photochemical endeavours, diboranes have proven to be efficient radical-capturing reagents. Hence, various photochemical methods can be utilized to generate the carbon-centred radical, which is then reliably trapped by the boronating reagent (Scheme 5.11, upper part).[139–142] Furthermore, mechanistic studies have demonstrated the possibility to further activate the diboron compounds by coordination of for example fluoride anions[143] or Lewis-basic solvent molecules.[144]

In 2022 Sarpong group utilized the photocatalytic aryl borylation-oxidation sequence in their collective synthesis of cephanolides and ceforalides, benzenoid members of cephalotane-type norditerpenoids (Scheme 5.11, middle).[145] Keeping Corey's guidelines for retrosynthetic analysis in mind, the group decided to disconnect the maximally bridged ring first, leading to a significant simplification of the target compound. In the forward

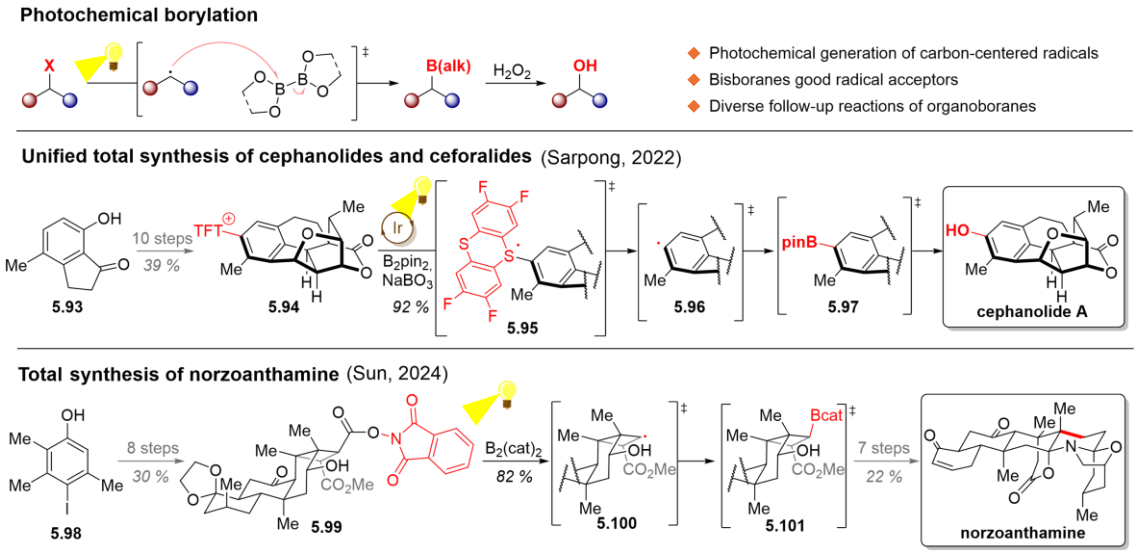

Scheme 5.11. Photochemical borylation (upper part) and its uses in total syntheses of cephanolide A (middle)[145] and norzoanthamine (lower part)[146]. [Ir] = $[Ir(dF(CF_3)ppy)_2(dtbbpy)]PF_6$.

sense, this strategy proved extremely successful as the pentacyclic carbon framework of the natural product could be accessed in just 4 steps from the hydroxyindanone **5.93**. Further modifications furnished the cyclic ether **5.94** in 6 additional steps. One-electron oxidation of the thianthrenium salt to **5.95** resulted in the degradation of the S–C_{Ar} bond to yield the phenyl radical **5.96**, which was trapped with borane to **5.**97.[147] Subsequently oxidation to a phenolic hydroxy group gave the desired natural product over 11 steps. A particularly intriguing point in this last transformation is the generation of a highly unstable phenyl radical intermediate, a rather daunting task which has been greatly facilitated in the past decade.[140,148–150]

The Sun group recently employed another variant of the photochemical alkyl borylation in their synthesis of norzoanthamine, a marine alkaloid with a broad range of biological activities (Scheme 5.11, lower part).[146] Their elegant synthesis featured altogether three photochemical steps: a dearomative-6π-desymmetrization early on in the synthesis, a [2+2]-cycloaddition for the generation of the cyclobutane moiety, and photochemical borylation to make the handle for the cyclic amine. While the entire synthesis is certainly worth reading, we will here only focus on the last one of the photochemical steps. For this transformation, the phenol **5.98** was converted into the phthalimide ester **5.99,** containing three of the rings found in the natural product. Direct excitation of the phthalimide ester led to homolysis of the weak N–O bond, and following decarboxylation gave the radical intermediate **5.100**. This radical was then trapped by $B_2(cat)_2$ to give the borylate **5.101**, and one-pot oxidation with hydrogen peroxide gave the corresponding alcohol. The natural product was then achieved in 6 additional steps, marking by far the shortest synthesis of norzoanthamine to date.

5.3.10 Miscellaneous carbon-skeleton modifications

In this final section we would like to highlight a few more examples demonstrating photochemical modification of carbon skeletons.[151,152] While the current understanding of photoreactivity often allows an accurate prediction of the reaction outcome, sometimes the cascade reactions can still be difficult to design. This can be particularly true with direct irradiation, where the first reaction might be followed by further transformations as long as the products absorb adequate amounts of light. Based on the preliminary report by Wagner[153] and their earlier experience,[154] the Bach group decided to utilize a previously established photochemical cascade as a key transformation to generate the carbon

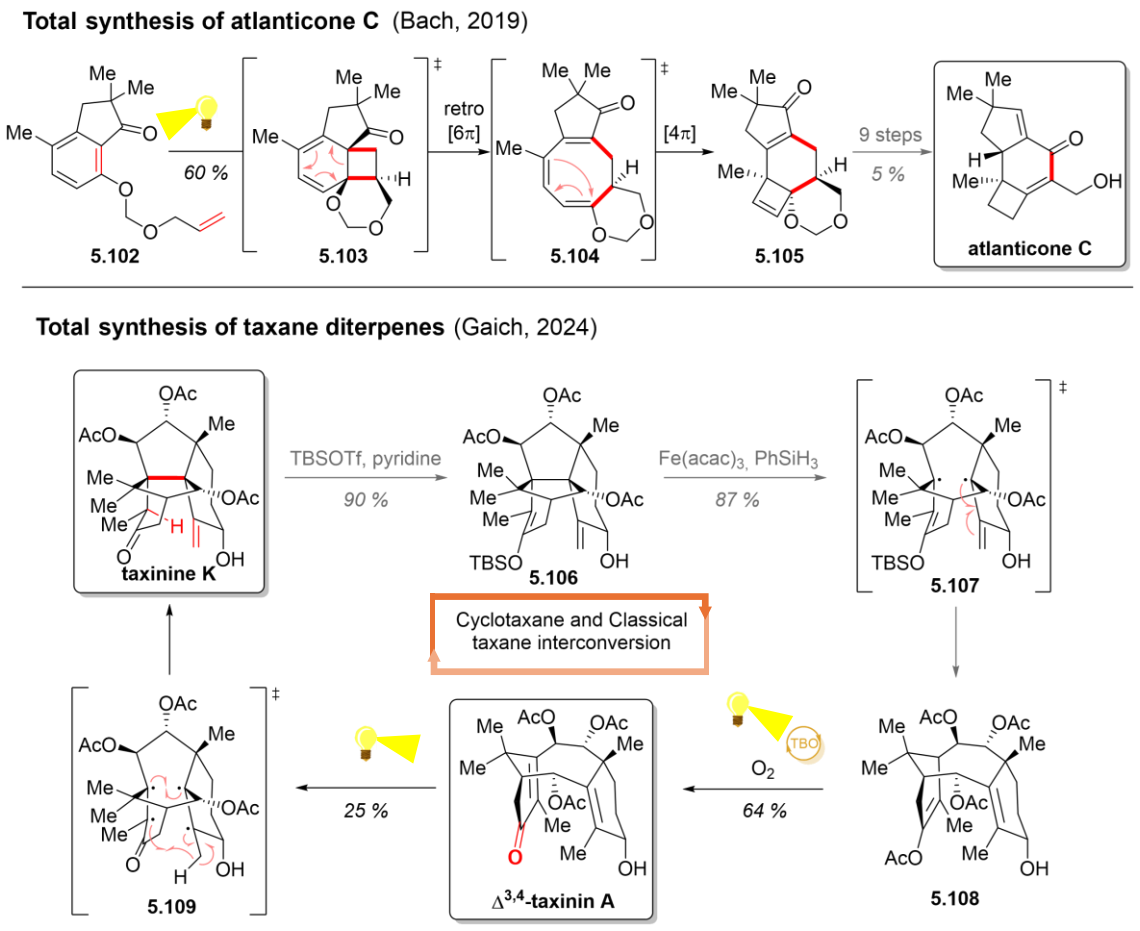

Scheme 5.12. Total synthesis of atlanticone C with photochemical cyclization cascade as a key step (upper part)[152] and collective synthesis of classical taxane and cyclotaxane natural products (lower part).[151]

backbone of atlanticone C in one step (Scheme 5.12, upper part).[152] The generation of the photocyclization precursor started with *para*-cresol, which was converted into the ketone **5.102** in four steps. Direct irradiation of this compound ($\lambda \geq 350$ nm) commenced the photocascade with a [2+2] cycloaddition. The formed cyclobutane **5.103** then underwent a subsequent retro [6π] ring opening to form the strain-released **5.104**. A following 4π cyclization then finished the tetracycle **5.105**. Further modifications on the ring substituents eventually furnished atlanticone C in 9 additional steps. Notably, an enantioselective synthesis of (+)-atlanticone C was published one year later, with racemic **5.105** serving as a focal point in kinetic resolution.[155] Therein, a Corey–Bakshi–Shibata reduction of the cyclic ketone allowed separation of the diastereomers, after which the desired one was oxidized back to the ketone and the synthesis was finished similarly to the racemic route.

As a final example, we would like to discuss a showcase of an unprecedented synthetic strategy of converting the classical taxane core into cyclotaxanes as demonstrated by the group of Gaich (Scheme 5.12, lower part).[151] The entry to this interconverting loop would be obtained from taxinine K, which was synthesized over 26 linear steps. Silylation of the taxinine K to **5.106**, which possesses the parallel alignment of π bonds for the next reaction. Metal-hydride hydrogen atom transfer (MHAT) fragmented the central C–C σ-bond in **5.107** to yield the classical taxane core **5.108**. Eventually, photochemical oxidation with single oxygen selectively furnished the ketone highlighted in $\Delta^{3,4}$-taxinin A, forming this natural product. Next, direct irradiation of this compound excited both endocyclic alkenes to their biradicals in **5.109**, after which a radical-radical combination reformed the central C–C bond in cyclotaxanes and an intramolecular 1,5-HAT built the terminal alkene in taxinine K. As a whole this synthetic campaign was highly successful, furnishing 11 members of the taxane family in 23 to 28 steps.

5.4 Summary and Outlook

In the 21st century, the use of photochemistry has established its role as a compelling tool for the synthesis of complex target molecules. While approaches based on direct irradiation have been utilized for a longer time, photocatalyzed methods have also started to find their way into natural product chemistry. As a testament to the accessibility and easy set-up, photochemical transformations have been successfully taken up by groups new to the field. While iridium and ruthenium polypyridyl complexes have mainly dominated the photocatalytic reactions in natural product synthesis so far, we anticipate that the increasing literature on organophotocatalysts will encourage their use in the future. Furthermore, we strongly believe that the HAT-driven epimerization will be recognized as a revolutionary method for stereoediting. Despite the recent advances, the utilization of photocatalyst-driven transformations in natural product synthesis is still somewhat in its infancy, and many intriguing reactions, such as ligand-to-metal charge transfer (LMCT) protocols and halogen atom abstractions (XAT), are yet to make their entrance into natural product chemistry.

5.5 References

(1) Corey, E. J.; Cheng, X. *The Logic of Chemical Synthesis*; John Wiley: New York, 1989.

(2) Nicolaou, K. C.; Rigol, S. Perspectives from Nearly Five Decades of Total Synthesis of Natural Products and Their Analogues for Biology and Medicine. *Nat. Prod. Rep.* **2020**, *37* (11),

(3) Wöhler, F. Ueber Künstliche Bildung Des Harnstoffs. *Annalen der Physik* **1828**, *88* (2), 253–256.

(4) du Vigneaud, V. A Trail of Sulfa Research: From Insulin to Oxytocin, *Science*, **1956**, *123*, (3205), 967–974.

(5) Corey, E. J. The Logic of Chemical Synthesis: Multistep Synthesis of Complex Carbogenic Molecules (Nobel Lecture). *Angew. Chem. Int. Ed.* **1991**, *30* (5), 455–465.

(6) Perkin, W. H. Jr. Experiments on the Synthesis of the Terpenes. Part I. Synthesis of Terpin, Inactive Terpineol, and Dipentene, *J. Chem. Soc., Trans*, **1904**, *85*, 654–671.

(7) Komppa, Gust. Die vollständige Synthese der Camphersäure und Dehydrocamphersäure. *Ber. Dtsch. Chem. Ges.* **1903**, *36* (4), 4332–4335.

(8) Robinson, R. A Synthesis of Tropinone. *J. Chem. Soc., Trans.* **1917**, *111*, 762–768.

(9) Woodward, R. B.; Cava, M. P.; Ollis, W. D.; Hunger, A.; Daeniker, H. U.; Schenker, K. The Total Synthesis of Strychnine. *J. Am. Chem. Soc.* **1954**, *76* (18), 4749–4751.

(10) Woodward, R. B.; Bader, F. E.; Bickel, H.; Frey, A. J.; Kierstead, R. W. The total synthesis of reserpine. *J. Am. Chem. Soc.* **1956**, *78* (9), 2023–2025.

(11) Corey, E. J.; Ohno, Masaji.; Mitra, R. B.; Vatakencherry, P. A. Total Synthesis of Longifolene. *J. Am. Chem. Soc.* **1964**, *86* (3), 478–485.

(12) Armstrong, R. W.; Beau, J. M.; Cheon, S. H.; Christ, W. J.; Fujioka, H.; Ham, W. H.; Hawkins, L. D.; Jin, H.; Kang, S. H. Total Synthesis of Palytoxin Carboxylic Acid and Palytoxin Amide. *J. Am. Chem. Soc.* **1989**, *111* (19), 7530–7533.

(13) Suh, E. M.; Kishi, Y. Synthesis of Palytoxin from Palytoxin Carboxylic Acid. *J. Am. Chem. Soc.* **1994**, *116* (24), 11205–11206.

(14) Shenvi, R. A. Natural Product Synthesis in the 21st Century: Beyond the Mountain Top. *ACS Cent. Sci.* **2024**, *10* (3), 519–528.

(15) Takeuchi, H.; Mishiro, K.; Ueda, Y.; Fujimori, Y.; Furuta, T.; Kawabata, T. Total Synthesis of Ellagitannins through Regioselective Sequential Functionalization of Unprotected Glucose. *Angew. Chem. Int. Ed.* **2015**, *54* (21), 6177–6180.

(16) Winter, N.; Trauner, D. Thiocarbonyl Ylide Chemistry Enables a Concise Synthesis of (±)-Hippolachnin A. *J. Am. Chem. Soc.* **2017**, *139* (34), 11706–11709.

(17) Serna, A. V.; Kürti, L.; Siitonen, J. H. Synthesis of (±)-Setigerumine I: Biosynthetic Origins of the Elusive Racemic Papaveraceae Isoxazolidine Alkaloids. *Angew. Chem. Int. Ed.* **2021**, *60* (52), 27236–27240.

(18) Baran, P. S. Natural Product Total Synthesis: As Exciting as Ever and Here To Stay. *J. Am. Chem. Soc.* **2018**, *140* (14), 4751–4755.

(19) Condakes, M. L.; Hung, K.; Harwood, S. J.; Maimone, T. J. Total Syntheses of (−)-Majucin and (−)-Jiadifenoxolane A, Complex Majucin-Type Illicium Sesquiterpenes. *J. Am. Chem. Soc.* **2017**, *139* (49), 17783–17786.

(20) Bakanas, I.; Lusi, R. F.; Wiesler, S.; Hayward Cooke, J.; Sarpong, R. Strategic Application of C–H Oxidation in Natural Product Total Synthesis. *Nat. Rev. Chem.* **2023**, *7* (11), 783–799.

(21) Sammes, P. G. Photochemical Reactions in Natural Product Synthesis, *Q. Rev. Chem. Soc.*, **1970**, *24*, 37−68.

(22) Singh, S. P.; Stenberg, V. I.; Parmar, S. S. Photochemistry of Alkaloids. *Chem. Rev.* **1980**, *80* (3), 269–282.

(23) Hoffmann, N. Photochemical Reactions as Key Steps in Organic Synthesis. *Chem. Rev.* **2008**, *108* (3), 1052–1103.

(24) Bach, T.; Hehn, J. P. Photochemical Reactions as Key Steps in Natural Product Synthesis. *Angew. Chem. Int. Ed.* **2011**, *50* (5), 1000–1045.

(25) Kärkäs, M. D.; Porco, J. A. Jr.; Stephenson, C. R. J. Photochemical Approaches to Complex Chemotypes: Applications in Natural Product Synthesis. *Chem. Rev.* **2016**, *116* (17), 9683–9747.

(26) Pitre, S. P.; Overman, L. E. Strategic Use of Visible-Light Photoredox Catalysis in Natural Product Synthesis. *Chem. Rev.* **2022**, *122* (2), 1717–1751.

(27) Winkler, J. D.; Bowen, C. M.; Liotta, F. [2 + 2] Photocycloaddition/Fragmentation Strategies for the Synthesis of Natural and Unnatural Products. *Chem. Rev.* **1995**, *95* (6), 2003–2020.

(28) Iriondo-Alberdi, J.; Greaney, M. F. Photocycloaddition in Natural Product Synthesis. *Eur. J. Org. Chem.* **2007**, *2007* (29), 4801–4815.

(29) Sarkar, D.; Bera, N.; Ghosh, S. [2+2] Photochemical Cycloaddition in Organic Synthesis. *Eur. J. Org. Chem.* **2020**, *2020* (10), 1310–1326.

(30) Yang, P.; Jia, Q.; Song, S.; Huang, X. [2 + 2]-Cycloaddition-Derived Cyclobutane Natural Products: Structural Diversity, Sources, Bioactivities, and Biomimetic Syntheses. *Nat. Prod. Rep.* **2023**, *40* (6),

(31) Salaverri, N.; Alemán, J.; Marzo, L. Harnessing the Power of the De Mayo Reaction: Unveiling a Photochemical and Photocatalytic Masked [2+2] Methodology for Organic Synthesis. *Adv. Synth. Catal.* **2024**, *366* (2), 156–167.

(32) Hou, S.-Y.; Yan, B.-C.; Sun, H.-D.; Puno, P.-T. Recent Advances in the Application of [2 + 2] Cycloaddition in the Chemical Synthesis of Cyclobutane-Containing Natural Products. *Nat. Prod. Bioprospect.* **2024**, *14* (1), 37.

(33) Blum, T. R.; Miller, Z. D.; Bates, D. M; Yoon, T. P. Enantioselective photochemistry through Lewis acid–catalyzed triplet energy transfer, *Science*, **2016**, *354*, (6318), 1391–1395.

(34) Genzink, M. J.; Rossler, M. D.; Recendiz, H.; Yoon, T. P. A General Strategy for the Synthesis of Truxinate Natural Products Enabled by Enantioselective [2+2] Photocycloadditions. *J. Am. Chem. Soc.* **2023**, *145* (35), 19182–19188.

(35) Sherbrook, E. M.; Genzink, M. J.; Park, B.; Guzei, I. A.; Baik, M.-H.; Yoon, T. P. Chiral Brønsted Acid-Controlled Intermolecular Asymmetric [2 + 2] Photocycloadditions. *Nat. Commun.* **2021**, *12* (1), 5735.

(36) Coote, S. C.; Pöthig, A.; Bach, T. Enantioselective Template-Directed [2+2] Photocycloadditions of Isoquinolones: Scope, Mechanism and Synthetic Applications. *Chem. Eur. J.* **2015**, *21* (18), 6906–6912.

(37) Kidd, J. B.; Fiala, T. A.; Swords, W. B.; Park, Y.; Meyer, K. A.; Sanders, K. M.; Guzei, I. A.; Wright, J. C.; Yoon, T. P. Enantioselective Paternò–Büchi Reactions: Strategic Application of a Triplet Rebound Mechanism for Asymmetric Photocatalysis. *J. Am. Chem. Soc.* **2024**, *146* (22), 15293–15300.

(38) Kravina, A. G.; Carreira, E. M. Total Synthesis of Epicolactone. *Angew. Chem. Int. Ed.* **2018**, *57* (40), 13159–13162.

(39) Mashiko, T.; Shingai, Y.; Sakai, J.; Kamo, S.; Adachi, S.; Matsuzawa, A.; Sugita, K. Total Synthesis of Cochlearol B via Intramolecular [2+2] Photocycloaddition. *Angew. Chem. Int. Ed.* **2021**, *60* (46), 24484–24487.

(40) Richardson, A. D.; Vogel, T. R.; Traficante, E. F.; Glover, K. J.; Schindler, C. S. Total Synthesis of (+)-Cochlearol B by an Approach Based on a Catellani Reaction and Visible-Light-Enabled [2+2] Cycloaddition. *Angew. Chem. Int. Ed.* **2022**, *61* (31), e202201213.

(41) Jung, H.; Hong, M.; Marchini, M.; Villa, M.; S. Steinlandt, P.; Huang, X.; Hemming, M.; Meggers, E.; Ceroni, P.; Park, J.; Baik, M.-H. Understanding the Mechanism of Direct Visible-Light-Activated [2 + 2] Cycloadditions Mediated by Rh and Ir Photocatalysts: Combined Computational and Spectroscopic Studies. *Chem. Sci.* **2021**, *12* (28), 9673–9681.

(42) Franceschi, P.; Cuadros, S.; Goti, G.; Dell'Amico, L. Mechanisms and Synthetic Strategies in Visible Light-Driven [2+2]-Heterocycloadditions. *Angew. Chem. Int. Ed.***2023**, *62* (8), e202217210.

(43) Nicolaou, K. C.; Snyder, S. A.; Montagnon, T.; Vassilikogiannakis, G. The Diels–Alder Reaction in Total Synthesis. *Angew. Chem. Int. Ed.* **2002**, *41* (10), 1668–1698.

(44) Lin, S.; Ischay, M. A.; Fry, C. G.; Yoon, T. P. Radical Cation Diels–Alder Cycloadditions by Visible Light Photocatalysis. *J. Am. Chem. Soc.* **2011**, *133* (48), 19350–19353.

(45) Wang, J. Y. J.; Blyth, M. T.; Sherburn, M. S.; Coote, M. L. Tuning Photoenolization-Driven Cycloadditions Using Theory and Spectroscopy. *J. Am. Chem. Soc.* **2022**, *144* (2), 1023–1033.

(46) Nicolaou, K. C.; Gray, D.; Tae, J. Total Synthesis of Hamigerans: Part 2. Implementation of the Intramolecular Diels–Alder Trapping of Photochemically Generated Hydroxy-o-Quinodimethanes; Strategy and Completion of the Synthesis. *Angew. Chem. Int. Ed.* **2001**, *40* (19), 3679–3683.

(47) Yang, B.; Wen, G.; Zhang, Q.; Hou, M.; He, H.; Gao, S. Asymmetric Total Synthesis and Biosynthetic Implications of Perovskones, Hydrangenone, and Hydrangenone B. *J. Am. Chem. Soc.* **2021**, *143* (17), 6370–6375.

(48) Zhu, L.; Huang, J. Total Synthesis of Lugdunomycin via Sequential Photoinduced Spiroketalization and Isobenzofuran Diels–Alder Reactions. *Angew. Chem. Int. Ed.* e202422615.

(49) Mo, Y.; Ning, L.; Luo, Z.; Yang, L.; Tang, S.; Dong, S.; Zhou, Q.-L.; Feng, X. Asymmetric Photoenolization/Diels–Alder Reaction of 2-Methylbenzaldehydes and 2-Alkylbenzophenones with Chromones. *ACS Catal.* **2024**, *14* (9), 6687–6695.

(50) Yang, B.; Lin, K.; Shi, Y.; Gao, S. Ti(Oi-Pr)4-Promoted Photoenolization Diels–Alder Reaction to Construct Polycyclic Rings and Its Synthetic Applications. *Nat Commun* **2017**, *8* (1), 622.

(51) Mavroskoufis, A.; Lohani, M.; Weber, M.; Hopkinson, M. N.; Götze, J. P. A (TD-)DFT Study on Photo-NHC Catalysis: Photoenolization/Diels–Alder Reaction of Acid Fluorides Catalyzed by *N* -Heterocyclic Carbenes. *Chem. Sci.* **2023**, *14* (15), 4027–4037.

(52) Hou, M.; Xu, M.; Yang, B.; He, H.; Gao, S. Construction of Polycyclic Structures with Vicinal All-Carbon Quaternary Stereocenters via an Enantioselective Photoenolization/Diels–Alder Reaction. *Chem. Sci.* **2021**, *12* (21), 7575–7582.

(53) Nicolaou, K. C.; Gray, D.; Tae, J. Total Synthesis of Hamigerans: Part 1. Development of Synthetic Technology for the Construction of Benzannulated Polycyclic Systems by the Intramolecular Trapping of Photogenerated Hydroxy-o-Quinodimethanes and Synthesis of Key Building Blocks. *Angew. Chem. Int. Ed.* **2001**, *40* (19), 3675–3678.

(54) Hoskin, J. F.; Sorensen, E. J. A Concise Synthesis of Pleurotin Enabled by a Nontraditional C–H Epimerization. *J. Am. Chem. Soc.* **2022**, *144* (31), 14042–14046.

(55) Luo, M.-J.; Xiao, Q.; Li, J.-H. Electro-/Photocatalytic Alkene-Derived Radical Cation Chemistry: Recent Advances in Synthetic Applications. *Chem. Soc. Rev.* **2022**, *51* (16), 7206–7237.

(56) Li, X.; Tu, Y.-L.; Chen, X.-Y. Photoinduced Single-Electron Reduction of Alkenes. *Eur. J. Org. Chem.* **2024**, *27* (2), e202301060.

(57) Hamilton, D. S.; Nicewicz, D. A. Direct Catalytic Anti-Markovnikov Hydroetherification of Alkenols. *J. Am. Chem. Soc.* **2012**, *134* (45), 18577–18580.

(58) Nguyen, T. M.; Nicewicz, D. A. Anti-Markovnikov Hydroamination of Alkenes Catalyzed by an Organic Photoredox System. *J. Am. Chem. Soc.* **2013**, *135* (26), 9588–9591.

(59) Nguyen, T. M.; Manohar, N.; Nicewicz, D. A. Anti-Markovnikov Hydroamination of Alkenes Catalyzed by a Two-Component Organic Photoredox System: Direct Access to Phenethylamine Derivatives. *Angew. Chem. Int. Ed.* **2014**, *53* (24), 6198–6201.

(60) Wu, F.; Wang, L.; Ji, Y.; Zou, G.; Shen, H.; Nicewicz, D. A.; Chen, J.; Huang, Y. Direct Synthesis of Bicyclic Acetals via Visible Light Catalysis. *iScience* **2020**, *23* (8).

(61) Schmalzbauer, M.; Svejstrup, T. D.; Fricke, F.; Brandt, P.; Johansson, M. J.; Bergonzini, G.; König, B. Redox-Neutral Photocatalytic C−H Carboxylation of Arenes and Styrenes with CO2. *Chem*, **2020**, *6* (10), 2658–2672.

(62) Czyz, M. L.; Horngren, T. H.; Kondopoulos, A. J.; Franov, L. J.; Forni, J. A.; Pham, L. N.; Coote, M. L.; Polyzos, A. Photocatalytic Generation of Alkyl Carbanions from Aryl Alkenes. *Nat. Catal.* **2024**, *7* (12), 1316–1329.

(63) Xiang, J.-C.; Fung, C.; Wang, Q.; Zhu, J. Taming the Radical Cation Intermediate Enabled One-Step Access to Structurally Diverse Lignans. *Nat. Commun.* **2022**, *13* (1), 3481.

(64) Robinson, E. E.; Thomson, R. J. A Strategy for the Convergent and Stereoselective Assembly of Polycyclic Molecules. *J. Am. Chem. Soc.* **2018**, *140* (5), 1956–1965.

(65) Du, J.; Ruiz Espelt, L.; A. Guzei, I.; P. Yoon, T. Photocatalytic Reductive Cyclizations of Enones : Divergent Reactivity of Photogenerated Radical and Radical Anion Intermediates. *Chem. Sci.* **2011**, *2* (11), 2115–2119.

(66) Brown, B. R. The Mechanism of Thermal Decarboxylation. *Q. Rev., Chem. Soc.* **1951**, *5* (2), 131.

(67) Arnold, R. T.; Danzig, M. J. Thermal Decarboxylation of Unsaturated Acids. II. *J. Am. Chem. Soc.* **1957**, *79* (4), 892–893.

(68) Miyake, Y.; Nakajima, K.; Nishibayashi, Y. Visible Light-Mediated Oxidative Decarboxylation of Arylacetic Acids into Benzyl Radicals: Addition to Electron-Deficient Alkenes by Using Photoredox Catalysts. *Chem. Commun.* **2013**, *49* (71), 7854–7856.

(69) Chu, L.; Ohta, C.; Zuo, Z.; MacMillan, D. W. C. Carboxylic Acids as A Traceless Activation Group for Conjugate Additions: A Three-Step Synthesis of (±)-Pregabalin. *J. Am. Chem. Soc.* **2014**, *136* (31), 10886–10889.

(70) Donabauer, K.; Maity, M.; Lucia Berger, A.; S. Huff, G.; Crespi, S.; König, B. Photocatalytic Carbanion Generation – Benzylation of Aliphatic Aldehydes to Secondary Alcohols. *Chem. Sci.* **2019**, *10* (19), 5162–5166.

(71) Xu, P.; Su, W.; Ritter, T. Decarboxylative Sulfoximination of Benzoic Acids Enabled by Photoinduced Ligand-to-Copper Charge Transfer. *Chem. Sci.* **2022**, *13* (45), 13611–13616.

(72) Jiang, X.; Lan, Y.; Hao, Y.; Jiang, K.; He, J.; Zhu, J.; Jia, S.; Song, J.; Li, S.-J.; Niu, L. Iron Photocatalysis via Brønsted Acid-Unlocked Ligand-to-Metal Charge Transfer. *Nat. Commun.*. **2024**, *15* (1), 6115.

(73) Taskinen, E.; Birnthaler, D.; Kermelj, V.; König, B. Preassembly-Controlled Radical Recombination at Bismuth: Decarboxylative C–N Coupling with Sulfonamides. *Chem. Eur. J.*, e202500396.

(74) Bhattacherjee, A.; Sneha, M.; Lewis-Borrell, L.; Tau, O.; Clark, I. P.; Orr-Ewing, A. J. Picosecond to Millisecond Tracking of a Photocatalytic Decarboxylation Reaction Provides Direct Mechanistic Insights. *Nat. Commun.* **2019**, *10* (1), 5152.

(75) Takeuchi, H.; Inuki, S.; Nakagawa, K.; Kawabe, T.; Ichimura, A.; Oishi, S.; Ohno, H. Total Synthesis of Zephycarinatines via Photocatalytic Reductive Radical Ipso-Cyclization. *Angew. Chem. Int. Ed.* **2020**, *132* (47), 21396–21401.

(76) Bosse, A. T.; Hunt, L. R.; Suarez, C. A.; Casselman, T. A.; Goldstein, E. L., Wright, A. C.; Park, H.; Virgil, S. C.; Yu, J.-Q.; Stoltz, B. M.; Davies, H. M. L. Total synthesis of (−)-cylindrocyclophane A facilitated by C−H functionalization, *Science*, **2024**, *386*, (6722), 641−646.

(77) Lutovsky, G. A.; Yoon, T. P. Cu(II) Salts as Terminal Oxidants in Visible-Light Photochemical Oxidation Reactions. *Org. Biomol. Chem.* **2023**, *22* (1), 25–36.

(78) Anwar, K.; Merkens, K.; Aguilar Troyano, F. J.; Gómez-Suárez, A. Radical Deoxyfunctionalisation Strategies. *Eur. J. Org. Chem.* **2022**, *2022* (26), e202200330.

(79) Slutskyy, Y.; Jamison, C. R.; Lackner, G. L.; Müller, D. S.; Dieskau, A. P.; Untiedt, N. L.; Overman, L. E. Short Enantioselective Total Syntheses of Trans-Clerodane Diterpenoids: Convergent Fragment Coupling Using a Trans-Decalin Tertiary Radical Generated from a Tertiary Alcohol Precursor. *J. Org. Chem.* **2016**, *81* (16), 7029–7035.

(80) Müller, D. S.; Untiedt, N. L.; Dieskau, A. P.; Lackner, G. L.; Overman, L. E. Constructing Quaternary Stereogenic Centers Using Tertiary Organocuprates and Tertiary Radicals. Total Synthesis of *Trans* - Clerodane Natural Products. *J. Am. Chem. Soc.* **2015**, *137* (2), 660–663.

(81) Hagiwara, H.; Inome, K.; Uda, H. A Total Synthesis of an Antibacterialclerodane, 16-Hydroxyclerodа- 3,13(14)Z-Dien-L5,16-olide, *J. Chem. Soc., Perkin. Trans. 1.*, **1995**, 757–764.

(82) Takahashi, S.; Kusumi, T.; Kakisawa, H. Total Synthesis of (±)-Annonene, a trans-clerodane diterpene. *Chem. Lett.* **1979**, *8* (5), 515–518.

(83) Tokoroyama, T.; Fujimori, K.; Shimizu, T.; Yamagiwa, Y.; Monden, M. A Versatile Method for the Synthesis of Clerodane Diterpenoids: Syntheses of Cis and Trans Representatives. *J. Chem. Soc., Chem. Commun.*, **1983**, 1516–1518.

(84) Goldsmith, D. J.; Deshpande, R. Total Synthesis of Ajugarin-IV and Annonene: A Diels-Alder Approach1. *Synlett*, **2000**, *1995*, 495–497.

(85) Kanaoka, Y. Photoreactions of Cyclic Imides. Examples of Synthetic Organic Photochemistry. *Acc. Chem. Res.* **1978**, *11* (11), 407–413.

(86) Day, J. C.; Govindaraj, N.; McBain, D. S.; Skell, P. S.; Tanko, J. M. The Chemistry of 1,8-Naphthalenedicarboximidyl and Phthalimidyl Radicals. *J. Org. Chem.* **1986**, *51* (25), 4959–4963.

(87) Okada, K.; Okamoto, K.; Morita, N.; Okubo, K.; Oda, M. Photosensitized Decarboxylative Michael Addition through N-(Acyloxy)Phthalimides via an Electron-Transfer Mechanism. *J. Am. Chem. Soc.* **1991**, *113* (24), 9401–9402.

(88) Allen, L. J.; Cabrera, P. J.; Lee, M.; Sanford, M. S. N-Acyloxyphthalimides as Nitrogen Radical Precursors in the Visible Light Photocatalyzed Room Temperature C–H Amination of Arenes and Heteroarenes. *J. Am. Chem. Soc.* **2014**, *136* (15), 5607–5610.

(89) Guo, Y.; Wang, X.; Li, C.; Su, J.; Xu, J.; Song, Q. Decarboxylation of β-Boryl NHPI Esters Enables Radical 1,2-Boron Shift for the Assembly of Versatile Organoborons. *Nat. Commun.* **2023**, *14* (1), 5693.

(90) Parida, S. K.; Mandal, T.; Das, S.; Hota, S. K.; De Sarkar, S.; Murarka, S. Single Electron Transfer-Induced Redox Processes Involving N-(Acyloxy)Phthalimides. *ACS Catal.* **2021**, *11* (3), 1640–1683.

(91) Lackner, G. L.; Quasdorf, K. W.; Pratsch, G.; Overman, L. E. Fragment Coupling and the Construction of Quaternary Carbons Using Tertiary Radicals Generated From Tert-Alkyl N-Phthalimidoyl Oxalates By Visible-Light Photocatalysis. *J. Org. Chem.* **2015**, *80* (12), 6012–6024.

(92) Faisca Phillips, A. M.; Pombeiro, A. J. L. Applications of Hantzsch Esters in Organocatalytic Enantioselective Synthesis. *Catalysts*, **2023**, *13* (2), 419.

(93) Correia, J. T. M.; Fernandes, V. A.; T. Matsuo, B.; Delgado, J. A. C.; Souza, W. C. de; Weber Paixão, M. Photoinduced Deaminative Strategies: Katritzky Salts as Alkyl Radical Precursors. *Chem. Comm.* **2020**, *56* (4), 503–514.

(94) Azpilcueta-Nicolas, C. R.; Lumb, J.-P. Mechanisms for Radical Reactions Initiating from *N*-Hydroxyphthalimide Esters. *Beilstein J. Org. Chem.* **2024**, *20*, 346–378.

(95) Tao, D. J.; Slutskyy, Y.; Muuronen, M.; Le, A.; Kohler, P.; Overman, L. E. Total Synthesis of (−)-Chromodorolide B By a Computationally-Guided Radical Addition/Cyclization/Fragmentation Cascade. *J. Am. Chem. Soc.* **2018**, *140* (8), 3091–3102.

(96) Huang, Z.; Lumb, J.-P. Mimicking Oxidative Radical Cyclizations of Lignan Biosynthesis Using Redox-Neutral Photocatalysis. *Nat. Chem.* **2021**, *13* (1), 24–32.

(97) Levy, A.; Meyerstein, D.; Ottolenghi, M. Photodissociation of Iodoaromatics in Solution. *J. Phys. Chem.* **1973**, *77* (26), 3044–3047.

(98) Tang, B.; Zhu, R.; Tang, Y.; Ji, L.; Zhang, B. Photodissociation of Bromobenzene at 267 and 234 Nm: Experimental and Theoretical Investigation of the Photodissociation Mechanism. *Chem. Phys. Lett.* **2003**, *381* (5), 617–622.

(99) Nguyen, J. D.; D'Amato, E. M.; Narayanam, J. M. R.; Stephenson, C. R. J. Engaging Unactivated Alkyl, Alkenyl and Aryl Iodides in Visible-Light-Mediated Free Radical Reactions. *Nat. Chem.* **2012**, *4* (10), 854–859.

(100) Buettner, C. S.; Schnürch, M.; Bica-Schröder, K. Photocatalytic Hydroalkylation of Aryl-Alkenes. *J. Org. Chem.* **2022**, *87* (16), 11042–11047.

(101) Wu, S.; Wong, T. H.-F.; Righi, P.; Melchiorre, P. Photochemical Organocatalytic Synthesis of Thioethers from Aryl Chlorides and Alcohols. *J. Am. Chem. Soc.* **2024**, *146* (5), 2907–2912. h

(102) Li, Y.; Ye, Z.; Lin, Y.-M.; Liu, Y.; Zhang, Y.; Gong, L. Organophotocatalytic Selective Deuterodehalogenation of Aryl or Alkyl Chlorides. *Nat. Commun.* **2021**, *12* (1), 2894.

(103) Guo, Q.; Wang, M.; Liu, H.; Wang, R.; Xu, Z. Visible-Light-Promoted Dearomative Fluoroalkylation of β-Naphthols through Intermolecular Charge Transfer. *Angew. Chem. Int. Ed.* **2018**, *57* (17), 4747–4751.

(104) Zhang, J.; Chen, J.; Chen, J.; Luo, Y.; Xia, Y. Solvent as Photoreductant for Dehalogenation of α-Haloketones under Catalyst-Free Conditions. *Tetrahedron Lett.* **2022**, *98*, 153835.

(105) Tong, X.; Shi, B.; Liang, K.; Liu, Q.; Xia, C. Enantioselective Total Synthesis of (+)-Flavisiamine F via Late-Stage Visible-Light-Induced Photochemical Cyclization. *Angew. Chem. Int. Ed.* **2019**, *58* (16), 5443–5446.

(106) Zhang, H.; Hay, E. B.; Geib, S. J.; Curran, D. P. Radical Cyclizations of Cyclic Ene Sulfonamides Occur with β-Elimination of Sulfonyl Radicals to Form Polycyclic Imines. *J. Am. Chem. Soc.* **2013**, *135* (44), 16610–16617.

(107) Sun, Y.; Li, R.; Zhang, W.; Li, A. Total Synthesis of Indotertine A and Drimentines A, F, and G. *Angew. Chem. Int. Ed.* **2013**, *52* (35), 9201–9204.

(108) Hu, A.; Guo, J.-J.; Pan, H.; Tang, H.; Gao, Z.; Zuo, Z. δ-Selective Functionalization of Alkanols Enabled by Visible-Light-Induced Ligand-to-Metal Charge Transfer. *J. Am. Chem. Soc.* **2018**, *140* (5), 1612–1616.

(109) Choi, G. J.; Zhu, Q.; Miller, D. C.; Gu, C. J.; Knowles, R. R. Catalytic Alkylation of Remote C–H Bonds Enabled by Proton-Coupled Electron Transfer. *Nature*, **2016**, *539* (7628), 268–271.

(110) Capaldo, L.; Ravelli, D.; Fagnoni, M. Direct Photocatalyzed Hydrogen Atom Transfer (HAT) for Aliphatic C–H Bonds Elaboration. *Chem. Rev.* **2022**, *122* (2), 1875–1924.

(111) Chang, L.; Wang, S.; An, Q.; Liu, L.; Wang, H.; Li, Y.; Feng, K.; Zuo, Z. Resurgence and Advancement of Photochemical Hydrogen Atom Transfer Processes in Selective Alkane Functionalizations. *Chem. Sci.* **2023**, *14* (25), 6841–6859.

(112) Juliá, F. Ligand-to-Metal Charge Transfer (LMCT) Photochemistry at 3d-Metal Complexes: An Emerging Tool for Sustainable Organic Synthesis, *ChemCatChem,* **2022**, *14*, (19), e202200916.

(113) Tsui, E.; Metrano, A. J.; Tsuchiya, Y.; Knowles, R. R. Catalytic Hydroetherification of Unactivated Alkenes Enabled by Proton-Coupled Electron Transfer. *Angew. Chem. Int. Ed.***2020**, *59* (29), 11845–11849.

(114) Ganley, J. M.; Murray, P. R. D.; Knowles, R. R. Photocatalytic Generation of Aminium Radical Cations for C–N Bond Formation. *ACS Catal.* **2020**, *10* (20), 11712–11738.

(115) Capaldo, L.; Ravelli, D. Hydrogen Atom Transfer (HAT): A Versatile Strategy for Substrate Activation in Photocatalyzed Organic Synthesis. *Eur. J. Org. Chem.* **2017**, *2017* (15), 2056–2071.

(116) Sennari, G.; Yamagishi, H.; Sarpong, R. Remote C–H Amination and Alkylation of Camphor at C8 through Hydrogen-Atom Abstraction. *J. Am. Chem. Soc.* **2024**, *146* (11), 7850–7857.

(117) Hart, D. J.; Huang, H. C.; Krishnamurthy, R.; Schwartz, T. Free-Radical Cyclizations: Application to the Total Synthesis of Dl-Pleurotin and Dl-Dihydropleurotin Acid. *J. Am. Chem. Soc.* **1989**, *111* (19), 7507–7519.

(118) Li, X.; Zhang, Z.; Wu, J. Photocatalytic Stereochemical Editing for the Concise Syntheses of (25S)-Δ7-Dafachronic Acid, Demissidine, and Smilagenin. *Angew. Chem. Int. Ed.*, e202500341.

(119) Zhang, Z.-D.; Shi, Y.; Wu, J.-J.; Lin, J.-R.; Tian, W.-S. Synthesis of Demissidine and Solanidine. *Org. Lett.* **2016**, *18* (12), 3038–3040.

(120) Rivas-Loaiza, J. A.; Baj, A.; López, Y.; Witkowski, S.; Wojtkielewicz, A.; Morzycki, J. W. Synthesis of Solanum Alkaloid Demissidine Stereoisomers and Analogues. *J. Org. Chem.* **2021**, *86* (2), 1575–1582.

(121) Shen, Y.; Li, L.; Xiao, X.; Yang, S.; Hua, Y.; Wang, Y.; Zhang, Y.; Zhang, Y. Site-Specific Photochemical Desaturation Enables Divergent Syntheses of Illicium Sesquiterpenes. *J. Am. Chem. Soc.* **2021**, *143* (8), 3256–3263.

(122) Zhang, Y.-A.; Palani, V.; Seim, A. E.; Wang, Y.; Wang, K. J.; Wendlandt, A. E. Stereochemical editing logic powered by the epimerization of unactivated tertiary stereocenters, *Science*, **2022**, *378*, (6618), 383–390.

(123) Schultz, D. M.; Lévesque, F.; DiRocco, D. A.; Reibarkh, M.; Ji, Y.; Joyce, L. A.; Dropinski, J. F.; Sheng, H.; Sherry, B. D.; Davies, I. W. Oxyfunctionalization of the Remote C−H Bonds of Aliphatic Amines by Decatungstate Photocatalysis. *Angew. Chem. Int. Ed.* **2017**, *56* (48), 15274–15278.

(124) Prantz, K.; Mulzer, J. Synthetic Applications of the Carbonyl Generating Grob Fragmentation. *Chem. Rev.* **2010**, *110* (6), 3741–3766.

(125) van Omum, S. G.; Champeau, R. M.; Pariza, R. Ozonolysis Applications in Drug Synthesis, *Chem. Rev.* **2006**, *106*, (7), 2990−3001.

(126) Yayla, H. G.; Wang, H.; Tarantino, K. T.; Orbe, H. S.; Knowles, R. R. Catalytic Ring-Opening of Cyclic Alcohols Enabled by PCET Activation of Strong O–H Bonds. *J. Am. Chem. Soc.* **2016**, *138* (34), 10794–10797.

(127) Guo, J.-J.; Hu, A.; Chen, Y.; Sun, J.; Tang, H.; Zuo, Z. Photocatalytic C−C Bond Cleavage and Amination of Cycloalkanols by Cerium(III) Chloride Complex. *Angew. Chem. Int. Ed.* **2016**, *55* (49), 15319–15322.

(128) Matsuoka, T.; Inuki, S.; Miyagawa, T.; Oishi, S.; Ohno, H. Total Synthesis of (+)-Polyoxamic Acid via Visible-Light-Mediated Photocatalytic β-Scission and 1,5-Hydrogen Atom Transfer of Glucose Derivative. *J. Org. Chem.* **2020**, *85* (12), 8271–8278.

(129) Bakanas, I.; Tang, J. C.; Sarpong, R. Skeletal Diversification by C–C Cleavage to Access Bicyclic Frameworks from a Common Tricyclooctane Intermediate. *Chem. Commun.* **2023**, *59* (26), 3858–3861.

(130) Ruffoni, A.; Hampton, C.; Simonetti, M.; Leonori, D. Photoexcited Nitroarenes for the Oxidative Cleavage of Alkenes. *Nature*, **2022**, *610* (7930), 81–86.

(131) Křepinský, J.; Samek, Z.; Šorm, F.; Lamparsky, D.; Ochsner, Naves, Y.-R. The Structure and Absolute Configuration of α- and β-Bourbonene, Sesquiterpenic Hydrocarbons from the Essential Oil of Geranium Bourbon. *Tetrahedron*, **1966**, *22*, 53–70.

(132) Ishiyama, T.; Murata, M.; Miyaura, N. Palladium(0)-Catalyzed Cross-Coupling Reaction of Alkoxydiboron with Haloarenes: A Direct Procedure for Arylboronic Esters. *J. Org. Chem.* **1995**, *60* (23), 7508–7510.

(133) Yao, W.; Fang, H.; Peng, S.; Wen, H.; Zhang, L.; Hu, A.; Huang, Z. Cobalt-Catalyzed Borylation of Aryl Halides and Pseudohalides. *Organometallics*, **2016**, *35* (10), 1559–1564.

(134) Daley-Dee, P.; Clarke, J.; Monfette, S.; Bedford, R. B. Iron-Catalyzed Miyaura Borylation of Aryl Chlorides and Triflates. *Org. Lett.* **2025**, *27* (1), 197–201.

(135) Willis, D. M.; Strongin, R. M. Palladium-Catalyzed Borylation of Aryldiazonium Tetrafluoroborate Salts. A New Synthesis of Arylboronic Esters. *Tetrahedron Lett.* **2000**, *41* (45), 8683–8686.

(136) Liu, C.; Ji, C.-L.; Hong, X.; Szostak, M. Palladium-Catalyzed Decarbonylative Borylation of Carboxylic Acids: Tuning Reaction Selectivity by Computation. *Angew. Chem. Int. Ed.* **2018**, *57* (51), 16721–16726.

(137) Tan, X.; Wang, X.; Li, Z. H.; Wang, H. Borenium-Ion-Catalyzed C–H Borylation of Arenes. *J. Am. Chem. Soc.* **2022**, *144* (51), 23286–23291.

(138) Furukawa, T.; Tobisu, M.; Chatani, N. Nickel-Catalyzed Borylation of Arenes and Indoles via C–H Bond Cleavage. *Chem. Commun.* **2015**, *51* (30), 6508–6511.

(139) Wang, S.; Wang, H.; König, B. Photo-Induced Thiolate Catalytic Activation of Inert Caryl-Hetero Bonds for Radical Borylation. *Chem*, **2021**, *7* (6), 1653–1665.

(140) Hari, D. P.; Schroll, P.; König, B. Metal-Free, Visible-Light-Mediated Direct C–H Arylation of Heteroarenes with Aryl Diazonium Salts. *J. Am. Chem. Soc.* **2012**, *134* (6), 2958–2961.

(141) Matsuo, K.; Yamaguchi, E.; Itoh, A. Halogen-Bonding-Promoted Photoinduced C–X Borylation of Aryl Halide Using Phenol Derivatives. *J. Org. Chem.* **2023**, *88* (9), 6176–6181.

(142) Candish, L.; Teders, M.; Glorius, F. Transition-Metal-Free, Visible-Light-Enabled Decarboxylative Borylation of Aryl N-Hydroxyphthalimide Esters. *J. Am. Chem. Soc.* **2017**, *139* (22), 7440–7443.

(143) Tian, Y.; Pu, X.; Sánchez, A. H.; Silva, W.; Gschwind, R. M.; König, B. Photoinduced Radical Borylation of Robust Carbon–Heteroatom Bonds. *Adv. Synth. Catal.* **2025**, *367* (2), e202400547.

(144) Wu, J.; He, L.; Noble, A.; Aggarwal, V. K. Photoinduced Deaminative Borylation of Alkylamines. *J. Am. Chem. Soc.* **2018**, *140* (34), 10700–10704.

(145) Sennari, G.; Gardner, K. E.; Wiesler, S.; Haider, M.; Eggert, A.; Sarpong, R. Unified Total Syntheses of Benzenoid Cephalotane-Type Norditerpenoids: Cephanolides and Ceforalides. *J. Am. Chem. Soc.* **2022**, *144* (41), 19173–19185.

(146) Sun, Y.; Zhang, X.; Jiang, F.; Zhang, M.; Wu, W.; Sun, Y. Concise Synthesis of Norzoanthamine Enabled by a Set of Photochemical Transformations. *J. Am. Chem. Soc.* **2024**, *146* (47), 32305–32310.

(147) Berger, F.; Plutschack, M. B.; Riegger, J.; Yu, W.; Speicher, S.; Ho, M.; Frank, N.; Ritter, T. Site-Selective and Versatile Aromatic C−H Functionalization by Thianthrenation. *Nature*, **2019**, *567* (7747), 223–228.

(148) Nguyen, J. D.; D'Amato, E. M.; Narayanam, J. M. R.; Stephenson, C. R. J. Engaging Unactivated Alkyl, Alkenyl and Aryl Iodides in Visible-Light-Mediated Free Radical Reactions. *Nat. Chem.* **2012**, *4* (10), 854–859.

(149) Xu, P.; López-Rojas, P.; Ritter, T. Radical Decarboxylative Carbometalation of Benzoic Acids: A Solution to Aromatic Decarboxylative Fluorination. *J. Am. Chem. Soc.* **2021**, *143* (14), 5349–5354.

(150) Li, J.; Chen, J.; Sang, R.; Ham, W.-S.; Plutschack, M. B.; Berger, F.; Chabbra, S.; Schnegg, A.; Genicot, C.; Ritter, T. Photoredox Catalysis with Aryl Sulfonium Salts Enables Site-Selective Late-Stage Fluorination. *Nat. Chem.* **2020**, *12* (1), 56–62.

(151) Pan, L.; Schneider, F.; Ottenbruch, M.; Wiechert, R.; List, T.; Schoch, P.; Mertes, B.; Gaich, T. A General Strategy for the Synthesis of Taxane Diterpenes. *Nature*, **2024**, *632* (8025), 543–549.

(152) Zech, A.; Jandl, C.; Bach, T. Concise Access to the Skeleton of Protoilludane Sesquiterpenes through a Photochemical Reaction Cascade: Total Synthesis of Atlanticone C. *Angew. Chem. Int. Ed.* **2019**, *58* (41), 14629–14632.

(153) Wagner, P. J.; Smart, R. P. Acetone Sensitized Intramolecular Ortho Photocyclization of Substituted 4-Phenoxy-1-Butenes and 5-Phenoxypent-1-Enes. *Tetrahedron Lett.* **1995**, *36* (29), 5135–5138.

(154) Zech, A.; Bach, T. Photochemical Reaction Cascade from O-Pent-4-Enyl-Substituted Salicylates to Complex Multifunctional Scaffolds. *J. Org. Chem.* **2018**, *83* (6), 3069–3077.

(155) Proessdorf, J.; Zech, A.; Jandl, C.; Bach, T. Concise Total Synthesis of (+)-Atlanticone C. *Synlett*, **2020**, *31*, 1598–1602.

6 Summary

In this thesis, the photochemistry of ion-pairs and ionic interactions have been studied. Both organic and LMCT-metal catalysis are considered together with the literature.

Chapter 1 serves as an introduction to the ion-pairing theme. First, general concepts and definitions are established, followed by a discussion of the photophysical properties and reactivities of photoactive ion-pairs. Eventually, methods for transferring stereoinformation from chiral counterions to prochiral substrates are presented.

Chapter 2 describes studies towards dual photoacid/HAT catalysis with Eosin Y, an easily ionizable organocatalyst. This reactivity blueprint was initially envisioned to enable a photocatalytic dehydration of unfunctionalized 1,2-diols. Mechanistically, initial protonation of the leaving hydroxy group would be followed by HAT-initiated 1,2-spin center shift . However, during our studies we observed a rapid photodegradation of Eosin Y, leading to a highly active mixture efficiently driving the desired reaction.

In **Chapter 3**, anionic bismuth complexes are utilized for net-oxidative, decarboxylative C–N coupling reactions. Herein, the photoactive species is formed *in situ* from neutral $Bi(OTf)_3$, deprotonated carboxylate ligands and sulfonamides. After the photolysis of the $Bi–O_2CR$ bond, a rapid decarboxylation follows. Bi(II) radical then recombines with the carbon-centred radical, forging the sulfonamide products. To the best of our knowledge this exemplifies the first direct decarboxylation on molecular bismuth and demonstrates the radical trapping ability of Bi(II).

Chapter 4 explores the effect of designed local electric field (D-LEF), which would be generated by a secondary charged group attached to the quinolinium core by an alkyl chain. As hypothesized, the non-conjugated charge did not notably affect the photophysical properties of the catalysts. However, the redox-inactive charge was envisioned to generate a repulsive force to the newly oxidized aryl radical cations, which could hinder unproductive back-electron transfer. Mechanistic studies on this hypothesis are ongoing.

Chapter 5 gives an outlook for the utilization of photochemistry in natural product synthesis. Recent literature examples are discussed with strategic considerations at the forefront and in the context of recent advances with the utilized reactions.

7 Zusammenfassung

In dieser Dissertation wurde die Photochemie von Ion-Paaren und ionischen Wechselwirkungen untersucht. Sowohl organische als auch LMCT-Metallkatalyse wurden zusammen mit der Literatur betrachtet.

Kapitel 1 dient als Einführung in das Thema von Ion-Paaren. Allgemeine Konzepte und Definitionen werden festgelegt, gefolgt von der Diskussion der photophysikalischen Eigenschaften und Reaktivitäten von photoaktiven Ion-Paaren. Schieβlich werden Methoden zur Übertragung von Stereoinformation aus chiralen Gegenionen vorgestellt.

Kapitel 2 beschreibt Studien zur dualen Photoacid-/HAT-Katalyse mit Eosin Y, einem leicht ionisiebaren Organokatalysator. Die Reaktivität wurde in der photokatalytischen Dehydratisierung von unfunktionalisierten 1,2-Diolen getestet. In dieser Reaktion könnte die abgehende Hydroxygruppe protoniert werden, wonach ein HAT-initiierter 1,2-spin center shift stattfindet. Eine schnelle Zersetzung des Katalysators wurde bei Belichtung beobachtet; die aktiven Zersetzungsprodukte katalysieren die Reaktion eventuell.

Im **Kapitel 3** werden die Ergebnisse zu anionischen Bismut-Komplexen für die oxidative, decarboxilierende C–N Kreuzkupplungen beschrieben. Hierbei wird die photoaktive Spezies *in situ* aus neutralem $Bi(OTf)_3$, Carboxylat-Liganden und Sulfonamiden gebildet. Nach der Photolyse der $Bi–O_2CR$ Bindung folgt eine schnelle Decarboxylierung, wonach sich das Bi(II) Radikal mit dem Kohlenstoffzentrierten Radikal rekombiniert und zu Produkten führt. Nach unserem Wissen stellt dies die erste direkte Decarboxylierung an molekularem Bismut dar und demonstriert die Abfangen von Radikale mit Bi(II).

Kapitel 4 fasst die Ergebnisse lokaler elektrischer Felder, die durch eine sekundäre geladene Gruppe erzeugt werden, auf die Reaktionskinetik zusammen. Die nicht-konjugierte Ladung beeinflusst die photophysikalischen Eigenschaften der Katalysatoren nicht signifikant, doch wurden Effekte auf die Reaktivität beobachtet. Mechanistische Studien zu diesem Projekt sind noch nicht vollständig abgeschlossen.

Kapitel 5 gibt einen Ausblick auf die Nutzung von Photochemie in der Naturstoffsynthese. An aktuellen Beispielen aus der Literatur werden strategischen Überlegungen zur Synthese und mit Fortschritte der verwendeten Reaktionen diskutiert.

8 Appendix

8.1 List of Abbreviations

°C	degrees Celsius
λ	wavelength
Ac	acetate
APCI	atmospheric-pressure chemical ionization
Ar	aryl
BDE	bond dissociation energy
BET	back electron transfer
bpy	bipyridyl
bpz	bipyrazine
btfmb	bistrifluoromethylbipyridyl
calc.	calculated
CFL	compact fluorescent lightbulb
CL	chain length (in radical chain reactions)
CN	cyano
CPA	chiral phosphoric acid
CV	cyclic voltammetry
DABCO	1,4-diazabicyclo[2.2.2]octane
DAT	deuterium atom transfer
DBCOP	dibenzocyclooctadiene
DBU	1,8-diazabicyclo[5.4.0]undec-7-ene
DCE	dichloroethane
DCM	dichloromethane
deep	4,4'-diethylester-2,2'-bipyrididne
DL	dielectric loss (spectroscopy)
DMA	dimethylacetamide
DMF	dimethylformamide
DMSO	dimethylsulfoxide
DT	decatungstate (anion)
EDA	electron donor-acceptor (complex)
e.g.	for example (*lat. exempli gratia*)
EI	electron ionization
EnT	energy transfer
equiv.	equivalent
ESI	electronspray ionization
Et_2O	diethylether
et al.	and others (*lat. et alii*)
EtOAc	ethyl acetate
EY	Eosin Y
Fc	ferrocene
FCC	flash column chromatography

fp	flash photolysis
FID	flame ionization detector
GC	gas chromatography
h	hour(s)
HAT	hydrogen atom transfer
HFIP	hexafluoroisopropanol
HOMO	highest occupied molecular orbital
HPLC	high performance liquid chromatography
HRMS	high resolution mass spectrometry
hν	incident photon energy
i.e.	that is (*lat. id est*)
IR	infrared spectroscopy
ISC	intersystem crossing
J	coupling constant
K	degrees Kelvin
LED	light-emitting diode
LEF	local electric field
LMCT	ligand-to-metal charge transfer
ln	natural logarithm
LUMO	lowest unoccupied molecular orbital
MeCN	acetonitrile
MHAT	metal-hydride hydrogen atom transfer
mes	mesityl/mesitylene
min	minute(s)
MLCT	metal-to-ligand charge transfer
MOM	methoxymethyl
MS	mass spectrometry
n-Bu	*n*-butyl
n.d.	not detected
NFSI	*N*-fluorobenzenesulfonimide
NMR	nuclear magnetic resonance
n.r.	no reaction
PC	photocatalyst
PCET	proton-coupled electron transfer
PE	petroleum ether
PET	photoinduced electron transfer
PG	protecting group
Ph	phenyl
phen	1,10-phenanthroline
PIDA	(Diacetoxyiodo)benzene
pK_a	acid dissociation constant at logarithmic scale
ppm	parts per million
ppy	2-phenylpyridyl
R	organic rest
RISC	reverse intersystem crossing

rt	room temperature
s	second(s)
SCS	spin-center shift
SET	single electron transfer
SCE	saturated calomel electrode
SHE	standard hydrogen electrode
TA	transient absorption spectroscopy
TBA	tetra-*n*-butyl ammonium
TBD	triazabicyclodecene
TBS	*tert*-butyldimethylsilyl ether
t-Bu	*tert*-butyl
TEMPO	2,2,6,6-tetramethyl-1-pipeidinyloxyl
TFA	trifluoroacetic acid
Tf	trifluoromethyl
TFE	trifluoroethanol
THF	tetrahydrofuran
TLC	thin layer chromatography
TMA^-	tetramethoxyanthrolate
TMAH	tetramethoxyanthracen-9(10*H*)-one
TMG	1,1,3,3-tetramethylguanidine
TMS	trimethylsilyl
TR	time-resolved
Ts	tosyl
TS	transition state
TTEnT	triplet-triplet energy transfer
Uv	ultraviolet (light)
Vis	visible (light)
vs.	against (*lat. versus*)
XAT	halogen atom transfer
XRD	single crystal X-ray analysis

8.2 Curriculum Vitae

ELINA KAROLIINA TASKINEN

21.08.1995 | Hollola, Finland | Finnish

EDUCATION

01/21 – 09/25	**Ph.D., Organic Chemistry** University of Regensburg (Germany) Thesis: "*Ionic Effects in Molecular Photocatalysis"* Supervisor: Prof. Dr. Burkhard König
09/18 – 06/20	**Master of Science, Organic Chemistry** University of Jyväskylä (Finland) Master thesis: *"Directed ortho-lithiation and its utilization in the total synthesis of Waltherione C"* Supervisor: Prof. Dr. Petri Pihko
09/14 – 0518	**Bachelor of Science, Chemistry** University of Jyväskylä (Finland) Bachelor thesis: *"Stable carbocation catalysts"* Supervisor: Prof. Dr. Petri Pihko

AWARDS

09/2024	**Poster Prize** ORChem, Regensburg University
05/2021	**Award for an outstanding Master's thesis** University of Jyväskylä
06/2016	**Award for excellence in chemistry studies** Finnish Chemical Society

PUBLICATIONS

(6)	Jasimuddin Ahmed, Elina K. Taskinen, Christina Graf, Roger-Jan Kutta, Patrick Nürnberger, Burkhard König. Changing Photocatalytic Activity with Local Electric Fields. *Manuscript under preparation*.
(5)	Elina K. Taskinen, Burkhard König. Harnessing Photochemistry in Natural Product Synthesis: From Strategy to Applications. *Manuscript submitted.*
(4)	Ferdinand L. Pointner, Jonas Poll, Elina K. Taskinen, Vincent George, Tristan Ruff, Florian Rott, Gabriel Mayer, Niklas Gessner, Roger-Jan Kutta, Burkhard König, Patrick Nürnberger, Christian Ochselfeld, Regina de Vivie-Riedle. Mechanistic Study of the Light-Initiated Generation of Free Diazoalkanes: Towards Photo-Orthogonal Synthesis. *Manuscript accepted.*
(3)	Elina K. Taskinen[‡], Dominik Birnthaler[‡], Vid Kermelj, Burkhard König. Preassembly-Controlled Radical Recombination at Bismuth: Decarboxylative CN Coupling with Sulfonamides, *Chem. Eur. J.*, **2025**, *31*, (28), e202500396.
(2)	Elina K. Taskinen, Daniel Kolb, Martin Morgenstern, Burkhard König. Photocatalyzed Dehydration of 1-Aryl-1,2-Ethanediols to Methyl Ketones Driven by Eosin Y Fragmentation Products, *Chem. Eur. J.*, **2025**, *31*, (9), e202404200.
(1)	Kristian L. Mears, Cary R. Stennett, Elina K. Taskinen, Caroline E. Knapp, Claire J. Carmalt, Heikki M. Tuononen, Philip P. Power. Molecular Complexes Featuring Unsupported Dispersion-Enhanced Aluminium–Copper and Gallium–Copper Bonds, *J. Am. Chem. Soc.*, **2020**, *142*, 19874–19878.

9 Acknowledgements

First and foremost, I would like to address my gratitude to Prof. König for allowing me to do my PhD in his group and giving me the freedom to follow my research interests. The RTG2620 is acknowledged for providing the funding for my doctoral studies and a versatile group to learn about different aspects of photochemistry.

None of my publications were solo work; I could not have done them alone. My warmest thanks go to my collaborators in these publications: Daniel, Martin, Vincent, Dominik, Jasimuddin, Vid, Jonas and Ferdinand for giving your input and accepting mine in the making of these projects. I also had the privilege to work with many motivated and highly skilled students (Markus, Lisa, Simon, Viték) to whom I am very grateful for their contribution to my projects and brightening my days.

I wish to thank Lea and Nico for the warm welcome I got upon joining the group (and downstairs lab 32.0.06). Becky has been a truly amazing labmate in 32.1.26, sharing not just the chemistry but life. I was lucky to also meet Jessica, who became a very dear friend to me. I am happy I got to share the RTG experience with Vincent, it would not have been as much fun without you. From the academically older members I would like to thank, among others, Indra, Matthias, Rok and Martin for the enlightening and inspiring discussions. To all of the younger members, keep up the good spirit! You all made this journey worth remembering.

The permanent staff is truly thanked for keeping the day-to-day worklife going. Barbara has been an irreplaceable help to me during all my questions regarding administrative things and so much more. Thank you to Regina for her CV measurements, Julia for the technical help (particularly with the LEDs), Rudi for keeping the GCs and GC-MS running, Britta for fast and reliable handling of chemical orders and Simone for keeping everything stocked-up and maintained. Finally, Ernst receives special thanks for his tireless all-around work for keeping our equipment and laboratories, and therefore the whole group, running. I hope you all know how important the work you put in is!

I would like to thank Taylor Swift for her amazing music which accompanied me through every step of my PhD. I would like to thank my boyfriend for his constant encouragement and for the beautiful experiences (travels, hikes etc.) I got to experience outside the lab. Finally, thank you to my family for their unconditional love and support. I was able to follow my dreams because I knew if I fell, you would always catch me. Kiitos.

Eidesstattliche Erklärung

Familienname: Taskinen
Vorname: Elina Karoliina
Geburtsdatum: 21.08.1995

Ich erkläre hiermit an Eides statt, dass ich die vorliegende Arbeit ohne unzulässige Hilfe Dritter und ohne Benutzung anderer als der angegebenen Hilfsmittel angefertigt habe; die aus anderen Quellen direkt oder indirekt übernommenen Daten und Konzepte sind unter Angabe des Literaturzitats gekennzeichnet.

Bei der Auswahl und Auswertung folgenden Materials haben mir die nachstehend aufgeführten Personen in der jeweils beschriebenen Weise entgeltlich/unentgeltlich geholfen:

1. ……

2. ……

3. ……

Weitere Personen waren an der inhaltlich-materiellen Herstellung der vorliegenden Arbeit nicht beteiligt. Insbesondere habe ich hierfür nicht die entgeltliche Hilfe eines Promotionsberaters oder anderer Personen in Anspruch genommen. Niemand hat von mir weder unmittelbar noch mittelbar geldwerte Leistungen für Arbeiten erhalten, die im Zusammenhang mit dem Inhalt der vorgelegten Dissertation stehen.

Die Arbeit wurde bisher weder im In- noch im Ausland in gleicher oder ähnlicher Form einer anderen Prüfungsbehörde vorgelegt.

Ich versichere an Eides statt, dass ich nach bestem Wissen die reine Wahrheit gesagt und nichts verschwiegen habe.

Vor Aufnahme der obigen Versicherung an Eides statt wurde ich über die Bedeutung der eidesstattlichen Versicherung und die strafrechtlichen Folgen einer unrichtigen oder unvollständigen eidesstattlichen Versicherung belehrt.

…… ……...…….
(Ort, Datum) (Unterschrift)

Unterschrift des die Versicherung an Eides statt aufnehmenden Beamten.

…… ……...…….
(Ort, Datum) (Unterschrift)